AD_____

Award Number: DAMD17-00-1-0459

TITLE: Non-Invasive Monitoring of Breast Tumor Oxygenation: A Key to Tumor Therapy Planning and Tumor Prognosis

PRINCIPAL INVESTIGATOR: Hanli Liu, Ph.D.

CONTRACTING ORGANIZATION: The University of Texas at Arlington
Arlington, Texas 76019-0145

REPORT DATE: September 2004

TYPE OF REPORT: Final

PREPARED FOR: U.S. Army Medical Research and Materiel Command
Fort Detrick, Maryland 21702-5012

DISTRIBUTION STATEMENT: Approved for Public Release;
Distribution Unlimited

The views, opinions and/or findings contained in this report are those of the author(s) and should not be construed as an official Department of the Army position, policy or decision unless so designated by other documentation.

20050415 059

REPORT DOCUMENTATION PAGE

Form Approved
OMB No. 074-0188

Public reporting burden for this collection of information is estimated to average 1 hour per response, including the time for reviewing instructions, searching existing data sources, gathering and maintaining the data needed, and completing and reviewing this collection of information. Send comments regarding this burden estimate or any other aspect of this collection of information, including suggestions for reducing this burden to Washington Headquarters Services, Directorate for Information Operations and Reports, 1215 Jefferson Davis Highway, Suite 1204, Arlington, VA 22202-4302, and to the Office of Management and Budget, Paperwork Reduction Project (0704-0188), Washington, DC 20503

1. AGENCY USE ONLY (Leave blank)	2. REPORT DATE	3. REPORT TYPE AND DATES COVERED
	September 2004	Final (1 Sep 2000 - 31 Aug 2004)

4. TITLE AND SUBTITLE
Non-Invasive Monitoring of Breast Tumor Oxygenation: A Key to Tumor Therapy Planning and Tumor Prognosis

5. FUNDING NUMBERS
DAMD17-00-1-0459

6. AUTHOR(S)
Hanli Liu, Ph.D.

7. PERFORMING ORGANIZATION NAME(S) AND ADDRESS(ES)
The University of Texas at Arlington
Arlington, Texas 76019-0145

E-Mail: hanli@uta.edu

8. PERFORMING ORGANIZATION REPORT NUMBER

9. SPONSORING / MONITORING AGENCY NAME(S) AND ADDRESS(ES)
U.S. Army Medical Research and Materiel Command
Fort Detrick, Maryland 21702-5012

10. SPONSORING / MONITORING AGENCY REPORT NUMBER

11. SUPPLEMENTARY NOTES

12a. DISTRIBUTION / AVAILABILITY STATEMENT
Approved for Public Release; Distribution Unlimited

12b. DISTRIBUTION CODE

13. ABSTRACT (Maximum 200 Words)

The overall goal of this research project is to develop and evaluate a new approach to monitoring of oxygenated hemoglobin concentration (HbO_2) of breast tumors under respiratory interventions using near infrared (NIR) spectroscopy and imaging techniques. The aims have included (1) to evaluate a single-channel, dual wavelength, NIR, frequency-domain oximeter and the algorithms for obtaining tumor HbO_2 against tumor pO_2 measured by ^{19}F magnetic resonance imaging (MRI), (2) to modify the single-channel system into a 3-channel NIR system, (3) to investigate heterogeneity of HbO_2 in breast tumors using the 3-channel NIR system, and (4) to study the influence of three interventions on HbO_2 and pO_2 of the breast tumors. We have accomplished all of the proposed aims and compared the optical method with concurrent measurements of tumor oxygen tension using oxygen needle electrodes, fiber optic needle systems (FOXY), and ^{19}F MRI. Overall, we conclude that NIR techniques could be a useful non-invasive monitoring tool for breast tumor oxygenation, which is a key to breast tumor therapy planning and tumor prognosis. Furthermore, the need for NIR imaging is obvious and is our current research development in order to fully characterize static and dynamic heterogeneity of breast tumor vasculature under therapeutic interventions.

14. SUBJECT TERMS
Technology development, radiological sciences, tumor therapy planning and prognosis, tumor physiology monitoring

15. NUMBER OF PAGES
202

16. PRICE CODE

17. SECURITY CLASSIFICATION OF REPORT	18. SECURITY CLASSIFICATION OF THIS PAGE	19. SECURITY CLASSIFICATION OF ABSTRACT	20. LIMITATION OF ABSTRACT
Unclassified	Unclassified	Unclassified	Unlimited

Table of Contents

Cover 1

SF 298 2

Table of Contents 3

Introduction 5

Body of Report 5

Key Research Accomplishments 7

Reportable Outcomes 8

Conclusions 10

List of personnel receiving pay from the research effort 11

Appendix 12

A 1: J. G. Kim, et al., "Interplay of Tumor Vascular Oxygenation and Tumor pO_2 Observed Using Near Infrared Spectroscopy, an Oxygen Needle Electrode, and ^{19}F MR pO_2 Mapping," *J. of Biomedical Optics* 8(1), 53-62 (2003). ..... (A1: 12-21)

A 2: Y. Gu, et al., "Dynamic Response of Breast Tumor Oxygenation to Hyperoxic Respiratory Challenge Monitored with Three Oxygen-Sensitive Parameters," *Applied Optics*, 42(16), 2960-2967 (2003). ..... (A2: 22-29)

A 3: Hanli Liu, et al., "Near Infrared Spectroscopy and Imaging of Tumor Vascular Oxygenation," *Methods in Enzymology: Imaging,* ed. by Michael Conn, vol. 385-386, 349-378 (2004). ..... (A3: 30-46)

A 4: Y. Gu, et al., "Effect of Photothermal therapy on breast tumor vascular contents: non-invasive monitoring by near infrared spectroscopy," under revision after submitted to *Photochemistry and Photobiology* (2004). ..... (A4: 47-79)

A 5: Y. Gu, et al., "Estimation of blood volume fraction sampled by near infrared spectroscopy and ^{19}F magnetic resonance spectroscopy," under revision after submitted to *Optics Express* (2004). ..... (A5: 80-89)

A 6: Y. Gu, et al., "Vascular oxygen dynamics of rat breast tumors in response to physiological interventions monitored by near-infrared spectroscopy," under revision after submitted to *Int J Radiat Oncol Biol Phys* (2004). ..... (A6: 90-122)

A 7: M. Xia, et al., "Tumour oxygen dynamics measured simultaneously by near infrared spectroscopy and ^{19}F magnetic resonance imaging in rats," submitted to *British J. of Cancer*, (2004). ..... (A7: 123-158)

A 8: Yulin Song, et al., "Investigation of breast tumor oxygen consumption by near infrared spectroscopy," submitted to *Journal of Physics D: Applied Physics*, (2004). ... (A8: 159-190)

A 9: Jae G. Kim and Hanli Liu, "Investigation of breast tumor hemodynamics using tumor vascular phantoms and FEM simulations," *OSA Biomedical Topical Meetings*, in Biomedical Topical Meetings on CD-ROM (The Optical Society ofAmerica, Washington, DC, 2004), WF16. ..... (A9: 191-193)

A 10: J. G. Kim et al., "Non-Uniform Tumor Vascular Oxygen Dynamics Monitored By Three-Channel Near-Infrared Spectroscopy", *Proc. SPIE-Int. Soc. Opt. Eng.* 4955, 388-396 (2003). ..... (A10: 194-202)

2000-2004 FINAL REPORT

This report presents the specific aims and accomplishments of our breast cancer research project during the entire period of funding sponsored by the U.S. Department of the Army. It covers our activities from September 1, 2000 to October 31, 2004.

Introduction

The overall goal of this research project is to develop and evaluate a new approach to monitoring of oxygenated hemoglobin concentration (HbO_2) of breast tumors under respiratory interventions using near infrared (NIR) spectroscopy and imaging techniques. Furthermore, we wish to compare and validate the optical method with concurrent measurements of tumor oxygen tension with the use of ^{19}F EPI relaxation of hexafluorobenzene (HFB). Once we have rigorously established the integrated approach to tumor physiology, we will explore the influence of three interventions expected to modify tumor physiology. A better understanding of the interplay of these parameters in the natural history of a tumor could lead to enhanced therapeutic approaches and provide a novel diagnostic/prognostic tool for breast cancer research and clinical practice.

The overall project has four specific aims:
Aim 1: To evaluate a single-channel, dual wavelength, NIR, frequency-domain oximeter and the algorithms for obtaining tumor HbO_2 against tumor pO_2 measured by ^{19}F EPI relaxation of HFB.
Aim 2: To modify the single-channel system into a 3-channel NIR system.
Aim 3: To investigate heterogeneity of HbO_2 in breast tumors using the 3-channel NIR system.
Aim 4: To study the influence of three interventions on HbO_2 and pO_2 of the breast tumors.

Body of the Report

The PI and her graduate students, Mr. Jae Kim and Ms. Mengna Xia, have made significant efforts in the last 4 years to accomplish the proposed aims, resulting in multiple published journal papers and manuscripts that are under revision or submission. This report is organized in such a way that we will use our published papers and manuscripts to give detailed descriptions of specific aspects of the research studies, while the papers and manuscripts are organized as Appendixes 1 to 10 for referral, as listed below:

Appendix 1: J. G. Kim, et al., "Interplay of Tumor Vascular Oxygenation and Tumor pO_2 Observed Using Near Infrared Spectroscopy, an Oxygen Needle Electrode, and ^{19}F MR pO_2 Mapping," *J. of Biomedical Optics* 8(1), 53-62 (2003).

Appendix 2: Y. Gu, et al., "Dynamic Response of Breast Tumor Oxygenation to Hyperoxic Respiratory Challenge Monitored with Three Oxygen-Sensitive Parameters," *Applied Optics*, 42(16), 2960-2967 (2003).

Appendix 3: Hanli Liu, et al., "Near Infrared Spectroscopy and Imaging of Tumor Vascular Oxygenation," *Methods in Enzymology: Imaging,* ed. by Michael Conn, vol. 385-386, 349-378 (2004).

Appendix 4: Y. Gu, et al., "Effect of Photothermal therapy on breast tumor vascular contents: non-invasive monitoring by near infrared spectroscopy," under revision after submitted to *Photochemistry and Photobiology* (2004).

Appendix 5: Y. Gu, et al., "Estimation of blood volume fraction sampled by near infrared spectroscopy and ^{19}F magnetic resonance spectroscopy," under revision after submitted to *Optics Express* (2004).

Appendix 6: Y. Gu, et al., "Vascular oxygen dynamics of rat breast tumors in response to physiological interventions monitored by near-infrared spectroscopy," under revision after submitted to *Int J Radiat Oncol Biol Phys* (2004).

Appendix 7: M. Xia, et al., "Tumour oxygen dynamics measured simultaneously by near infrared spectroscopy and ^{19}F magnetic resonance imaging in rats," submitted to *British J. of Cancer*, (2004).

Appendix 8: Yulin Song, et al., "Investigation of breast tumor oxygen consumption by near infrared spectroscopy," submitted to *Journal of Physics D: Applied Physics*, (2004).

Appendix 9: Jae G. Kim and Hanli Liu, "Investigation of breast tumor hemodynamics using tumor vascular phantoms and FEM simulations," *OSA Biomedical Topical Meetings*, in Biomedical Topical Meetings on CD-ROM (The Optical Society ofAmerica, Washington, DC, 2004), WF16.

Appendix 10: J. G. Kim et al., "Non-Uniform Tumor Vascular Oxygen Dynamics Monitored By Three-Channel Near-Infrared Spectroscopy", *Proc. SPIE-Int. Soc. Opt. Eng.* 4955, 388-396 (2003).

Aim 1: *To evaluate a single-channel, dual wavelength, NIR, frequency-domain oximeter and the algorithms for obtaining tumor HbO_2 against tumor pO_2 measured by ^{19}F EPI relaxation of HFB.*

For Aim 1, we have conducted a variety of experimental measurements to compare tumor vascular oxygenation with tumor tissue pO_2 using oxygen needle electrodes, fiber optic needle systems (FOXY), and ^{19}F magnetic resonance imaging system. The detailed descriptions can be found in **Appendixes 1, 2,** and 7, respectively.

Aim 2: *To modify the single-channel system into a 3-channel NIR system.*
Aim 3: *To investigate heterogeneity of HbO_2 in breast tumors using the 3-channel NIR system.*

For both Aims 2 and 3, we have performed computer simulations, laboratory phantoms, and experimental study to investigate breast tumor heterogeneity; **Appendixes 3, 9** and **10** are giving details for this aspect.

Aim 4: *To study the influence of three interventions on HbO_2 and pO_2 of the breast tumors.*

For Aim 4, we have reported our experimental results in **Appendixes 2, 3, 6,** and **7** with respiratory interventions of pure oxygen (100% O_2), carbogen (5% CO_2 and 95% O_2), and hypercarbic air mixture (only in **Appendix 6**). We have also conducted extra experiments with

administration of hydralazine to study therapeutic effects of the drug on tumor vasculature (also see **Appendix 6**).

Furthermore, during the course of conducting the proposed research tasks, we have explored new extra findings, as listed below:

1) During the process of scarifying the experimental tumor-bearing rats by i.v. injection of KCl, we found that the dynamic profiles of tumor vascular deoxygenation could be used to quantify tumor oxygen consumption rate after an appropriate mathematical model was developed. The detailed derivation for such a model and calculation of tumor oxygen consumption rate are given in **Appendix 8**.
2) While we were conducting ^{19}F magnetic resonance spectroscopy (MRI) measurements, we realized that it was important to calibrate and compare the tumor blood volumes sampled by both NIR and ^{19}F MRI. We found out that the blood volumes estimated by the two methods are different, revealing an important finding to better understand the potential use of NIR for breast tumor prognosis (see **Appendix 5**).
3) We have investigated the capability of using the NIR technique to monitor effects of photo-thermal therapy on breast tumor vascular contents in conjunction simultaneously with multi-channel temperature measurements. The data have clearly demonstrated that the NIR technique could provide insight into tumor vascular oxygenation and their association with thermal effects during photo-thermal therapy (see **Appendix 4**).

Key Research Accomplishments

1) We have obtained and tested both single-channel and multi-channel NIRS systems for simultaneous dynamic tumor oxygenation measurements at different locations of breast tumors.
2) We have developed breast tumor hemodynamic phantoms and conducted multi-channel NIRS measurements on the newly developed phantoms to simulate the dynamic HbO_2 changes of rat breast tumors under hyperoxic inhalations. This study supports our earlier dynamic model to explain the bi-phasic dynamic oxygenation process of breast tumors under hyperoxic interventions.
3) We have further implemented and utilized FEMLAB computer software to mimic dynamic light distribution in a simulated tissue vasculature so as to understand the effects of tumor heterogeneity on the multi-channel NIR measurements.
4) We have performed a variety of animal experiments under different respiratory interventions to correlate tumor vascular and tissue oxygenations using both NIR and various pO_2 measurements.
5) Overall, <u>we have accomplished all of our proposed aims</u> to demonstrate that NIR techniques could be a useful non-invasive monitoring tool for breast tumor oxygenation, which is a key to tumor therapy planning and tumor prognosis.

Reportable Outcomes

Peer-reviewed Journals:

1. Jae Gwan Kim, Yulin Song, Dawen Zhao, Anca Constantinescu, Ralph P. Mason, and **Hanli Liu**, "Interplay of Tumor Vascular Oxygenation and Tumor pO_2 Observed Using Near Infrared Spectroscopy, an Oxygen Needle Electrode, and ^{19}F MR pO_2 Mapping," *J. of Biomedical Optics* 8(1), 53-62 (2003).
2. Yueqing Gu, Vincent Bourke, Jae Kim, Anca Constantinescu, Ralph P. Mason, **Hanli Liu**, "Dynamic Response of Breast Tumor Oxygenation to Hyperoxic Respiratory Challenge Monitored with Three Oxygen-Sensitive Parameters," *Applied Optics*, 42(16), 2960-2967 (2003).
3. **Hanli Liu**, Yueqing Gu, Jae G. Kim, and Ralph P. Mason, "Near Infrared Spectroscopy and Imaging of Tumor Vascular Oxygenation," *Methods in Enzymology: Imaging*, ed. by Michael Conn, vol. 385-386, 349-378 (2004).
4. Yueqing Gu, Wei R. Chen, Mengna Xia, Sang W. Jeong, and **Hanli Liu**, "Effect of Photothermal therapy on breast tumor vascular contents: non-invasive monitoring by near infrared spectroscopy," under revision after submitted to *Photochemistry and Photobiology* (2004).
5. Yueqing Gu, Ralph Mason, and **Hanli Liu**, "Estimation of blood volume fraction sampled by near infrared spectroscopy and ^{19}F magnetic resonance spectroscopy," under revision after submitted to *Optics Express* (2004).
6. Yueqing Gu, Yulin Song, A. Contantinescu, **Hanli Liu**, and Ralph P. Mason, "Vascular oxygen dynamics of rat breast tumors in response to physiological interventions monitored by near-infrared spectroscopy," under revision after submitted to *Int J Radiat Oncol Biol Phys* (2004).
7. Mengna Xia, Vikram Kodibagkar, **Hanli Liu** and Ralph P. Mason, "Tumour oxygen dynamics measured simultaneously by near infrared spectroscopy and ^{19}F magnetic resonance imaging in rats," submitted to *British J. of Cancer*, (2004).
8. Yulin Song, Jae G. Kim, Ralph P. Mason, and **Hanli Liu**, "Investigation of breast tumor oxygen consumption by near infrared spectroscopy," submitted to *Journal of Physics D: Applied Physics*, (2004).
9. Jae G. Kim, Mengna Xia, and **Hanli Liu**, "Hemoglobin extinction coefficients: importance of correct values for tissue near-infrared spectroscopy," to be submitted to *IEEE in Medicine and Biology Magazine* (2004).
10. Jae G. Kim and **Hanli Liu**, "Investigation of breast tumor hemodynamics: dynamic phantoms and finite element simulations," to be submitted to *Applied Optics* (2004).

Conference Presentations and Proceeding Papers:

1. Jae G. Kim and **Hanli Liu**, "Investigation of breast tumor hemodynamics using tumor vascular phantoms and FEM simulations," *OSA Biomedical Topical Meetings*, in Biomedical Topical Meetings on CD-ROM (The Optical Society ofAmerica, Washington, DC, 2004), WF16.

2. Mengna Xia, Yueqing Gu, **Hanli Liu**, Vikram Kodibagkar, Anca Constantinescu, Ralph Mason, "Tumor oxygen dynamics measured simultaneously by near-infrared spectroscopy and MR EPI imaging," in Biomedical Topical Meetings on CD-ROM (The Optical Society ofAmerica, Washington, DC, 2004), ThF33.

3. Yueqing Gu, Mengna Xia, **Hanli Liu**, Vikram Kodibagkar, Anca Constantinescu, Ralph P. Mason, "Correlation of NIR spectroscopy with BOLD MR imaging of assessing breast tumor vascular oxygen status," in Biomedical Topical Meetings on CD-ROM (The Optical Society ofAmerica, Washington, DC, 2004), FB6.

4. V. A. Bourke, Y Gu, A. Constantinescu, **H. Liu** and R. P. Mason, "Dynamic Optical Interrogation Of Oxygenation In The Tumor Microenvironment", The Eighth International Conference on Tumor Microenvironment and Its Impact on Cancer Therapies, Miami (South Beach), Florida, May, 2003.

5. Y. Song, K. L.Worden, X. Jiang, D. Zhao, A. Constantinescu, **H. Liu** and R. P. Mason, "Tumor Oxygen Dynamics: Comparison between ^{19}F MR-EPI of hexafluorobenzene and Frequency Domain NIR Spectroscopy," Oxygen Transport to Tissue XXIV. Proceedings of the 27th annual meeting of the International Society on Oxygen Transport to Tissue. (Dunn, J. F. and H. M. Swartz Eds.), Advances in Experimental Medicine and Biology 530, Kluwer Acad. New York, pp225-236 (2003).

6. Jae G. Kim, Yueqing Gu, Anca Constantinescu, Ralph P. Mason, **Hanli Liu,** "Non-Uniform Tumor Vascular Oxygen Dynamics Monitored By Three-Channel Near-Infrared Spectroscopy", *Proc. SPIE-Int. Soc. Opt. Eng.* 4955, 388-396 (2003).

7. Yueqing Gu, Vikram Kodibagkar, Mengna Xia, Zhiyu Qian, Jae. G. Kim, Anca Constantinescu, Ralph P. Mason, **Hanli Liu** "Simultaneous determination of breast tumor vascular oxygenation and blood volume measured with near infrared spectroscopy and ^{19}F MRS and ^{1}H MRI," presented in *SPIE, Photonics West*, San Jose, CA, Jan. 26-29, 2003.

8. Jae G. Kim, Yuling Song, **Hanli Liu**, Anca Constantinescu, and Ralph P. Mason, "Investigation of tumor oxygen consumption and tumor vascular oxygen dynamics in response to pharmacological interventions by NIRS," *OSA Biomedical Topical Meetings*, Technical Digest, SuH2, Miami Beach, FL, April 7-10, 2002.

9. Yulin Song, Yueqing Gu, Jae G. Kim, **Hanli Liu**, Anca Constantinescu, and Ralph P. Mason, "Correlation between total hemoglobin concentration and blood volume of breast tumors measured by NIR spectroscopy and ^{19}F MRS of PFOB," *OSA Biomedical Topical Meetings*, Technical Digest, SuH5, Miami Beach, FL, April 7-10, 2002.

10. J. G. Kim, , Y. Song, D. Zhao, A. Constantinescu, R. P. Mason, and **Hanli Liu,** "Interplay of Tumor Vascular Oxygenation and pO_2 in Tumors Using NIRS and Needle Electrode," *Proc. SPIE-Int. Soc. Opt. Eng.* 4250, 429-436 (2001).

Invited Talks:

1. **Hanli Liu**, "Near Infrared Spectroscopy and Imaging for Tumor Prognosis and Therapy Monitoring," 4th Annual Symposium, Southwestern in vivo Cancer Cellular and Molecular Imaging Program, Dallas, Texas, November 17, 2003.

2. **Hanli Liu**, "The Physics of Biomedical Optical Imaging," Department of Physics, Wake Forest University, Winston-Salem, NC, October 9, 2003.

3. **Hanli Liu**, "Optical Spectroscopy and Imaging for Tumor Oximetry and Assisting Neurosurgery in vivo," National CLEO/QELS Annual Conference, Baltimore Convention Center, Baltimore, Maryland, June 3-4, 2003.

4. **Hanli Liu**, "Optical Imaging/Sensing with Near Infrared Light: *from organ functions to cellular structures.*" Department of Biomedical Engineering, Texas A&M University, College Station, Texas, March 25, 2003.

5. **Hanli Liu**, "Phantom and Computer Simulation for Tumor Hemodynamic Study," Department of Biochemistry and Molecular Biophysics, University of Pennsylvania, Philadelphia, PA, Nov. 18, 2002.

6. **Hanli Liu**, "Near-Infrared Spectroscopy Used in vivo for Assisting Neurosurgery and Tumor Oximetry," Progress in Electromagnetics Research Symposium (PIERS) 2002, Cambridge, Massachusetts, July 1-5, 2002.

Conclusions

From the work that we have conducted over the last four years, we can draw the following conclusions:

1) With a multi-channel NIRS system and the newly developed tumor hemodynamic phantoms, we have experimentally demonstrated that the previously observed, bi-phasic temporal changes in HbO_2 of breast tumors under carbogen intervention can be associated with two perfusion rates or two blood flow rates.
2) The newly developed hemodynamic phantoms are helpful to simulate the hemodynamic processes undertaken within the tumor tissues, and the phantoms will be further used for future breast tumor studies.
3) After having performed multiple animal experiments under simultaneous measurements of NIR and pO_2, we are convinced that breast tumor vascular oxygenation could be correlated with tumor oxygen tension; in particular, dynamic parameters of tumor vasculature under interventions are more associated with tumor pO_2 (Appendix 7).
4) Overall, we conclude that NIR techniques could be a useful non-invasive monitoring tool for breast tumor oxygenation, which is a key to tumor therapy planning and tumor prognosis. However, NIR imaging would be the desired further development in order to fully characterize static and dynamic heterogeneity of breast tumor vasculature under therapeutic interventions.

List of personnel (not salaries) receiving pay from the research effort:

Hanli Liu,	the PI;
Jae G. Kim,	a graduate research assistant and a Ph.D. candidate;
Mengna Xia,	a graduate research assistant and a Ph.D. candidate.

Journal of Biomedical Optics 8(1), 53–62 (January 2003)

Interplay of tumor vascular oxygenation and tumor pO_2 observed using near-infrared spectroscopy, an oxygen needle electrode, and ^{19}F MR pO_2 mapping

Jae G. Kim
University of Texas at Arlington/University of Texas Southwestern Medical Center at Dallas
Joint Graduate Program in Biomedical Engineering
Arlington, Texas 76019

Dawen Zhao
University of Texas Southwestern Medical Center at Dallas
Advanced Radiological Sciences
Department of Radiology
Dallas, Texas 75390

Yulin Song
University of Texas at Arlington/University of Texas Southwestern Medical Center at Dallas
Joint Graduate Program in Biomedical Engineering
Arlington, Texas 76019
and
University of Texas Southwestern Medical Center at Dallas
Advanced Radiological Sciences
Department of Radiology
Dallas, Texas 75390

Anca Constantinescu
Ralph P. Mason
University of Texas Southwestern Medical Center at Dallas
Advanced Radiological Sciences
Department of Radiology
Dallas, Texas 75390

Hanli Liu
University of Texas at Arlington/University of Texas Southwestern Medical Center at Dallas
Joint Graduate Program in Biomedical Engineering
Arlington, Texas 76019

Abstract. This study investigates the correlation of tumor blood oxygenation and tumor pO_2 with respect to carbogen inhalation. After having refined and validated the algorithms for calculating hemoglobin concentrations, we used near-infrared spectroscopy (NIRS) to measure changes of oxygenated hemoglobin concentration ($\Delta[HbO_2]$) and used an oxygen needle electrode and ^{19}F MRI for pO_2 measurements in tumors. The measurements were taken from Dunning prostate R3327 tumors implanted in rats, while the anesthetized rats breathed air or carbogen. The NIRS results from tumor measurements showed significant changes in tumor vascular oxygenation in response to carbogen inhalation, while the pO_2 electrode results showed an apparent heterogeneity for tumor pO_2 response to carbogen inhalation, which was also confirmed by ^{19}F MR pO_2 mapping. Furthermore, we developed algorithms to estimate hemoglobin oxygen saturation, sO_2, during gas intervention based on the measured values of $\Delta[HbO_2]$ and pO_2. The algorithms have been validated through a tissue-simulating phantom and used to estimate the values of sO_2 in the animal tumor measurement based on the NIRS and global mean pO_2 values. This study demonstrates that the NIRS technology can provide an efficient, real-time, noninvasive approach to monitoring tumor physiology and is complementary to other techniques, while it also demonstrates the need for an NIR imaging technique to study spatial heterogeneity of tumor vasculature under therapeutic interventions. © *2003 Society of Photo-Optical Instrumentation Engineers.*
[DOI: 10.1117/1.1527049]

Keywords: frequency-domain spectroscopy; NIR spectroscopy; ^{19}F MRI; tumor vascular oxygenation; pO_2 electrode; oxygen; oximetry.

Paper 01078 received Nov. 13, 2001; revised manuscript received June 25, 2002; accepted for publication Aug. 26, 2002.

1 Introduction

It has long been known that hypoxic tumor cells are more resistant to radiation therapy than well-oxygenated tumor cells.[1] Breathing elevated oxygen (100%) or carbogen (95% O_2, 5% CO_2) has been used during therapy for an attempt to improve tumor oxygenation.[2,3] To monitor tumor tissue oxygen tension[4] and its dynamic changes under respiratory interventions, various methods are available, including fiber optic sensors,[5] oxygen electrodes,[6] and electron spin resonance.[7] MRI has the further advantage of providing dynamic maps of pO_2, which can reveal tumor heterogeneity.[8] While NIRS does not quantify pO_2, it can indicate dynamic changes in vascular oxygenation and has the advantage of being entirely noninvasive, providing real-time measurements, and being cost-effective and portable. Furthermore, it would be important to correlate the changes between tissue pO_2 and vascular oxygenation of the tumors since little is known about oxygen transfer from the tumor vasculature to tumor tissue.

The basic principle of NIRS rests on the fact that oxygenated and deoxygenated hemoglobin molecules are major chromophores in tissue in the near-infrared region (700 to 900 nm), and they exhibit distinct absorption characteristics. In principle, the concentrations of oxygenated hemoglobin $[HbO_2]$, deoxygenated hemoglobin [Hb], and oxygen saturation of hemoglobin sO_2 can be determined by measuring light absorption and scattering in tissue based on diffusion theory. However, the theory works well only for large and homogeneous media.[9,10] Accurate quantification of tumor oxygenation in our approach is currently limited to relative changes in $[HbO_2]$ and [Hb] due to considerable heterogeneity and finite size of tumors.

The goal of this study was to investigate the correlation of tumor blood oxygenation and tumor pO_2 in response to car-

Address all correspondence to Hanli Liu. Tel: 817-272-2054; Fax: 817-272-2251; E-mail: hanli@uta.edu

1083-3668/2003/$15.00 © 2003 SPIE

bogen intervention and to develop a suitable algorithm to estimate the hemoglobin oxygen saturation of the tumor under the intervention. Specifically, in Sec. 2 of this paper, we derive accurate expressions for calculating changes in $[HbO_2]$ and [Hb] to compensate for the differences in optical path length at two wavelengths and an algorithm to estimate absolute sO_2 values of the tumor during gas intervention. The algorithms are validated through tissue-simulating phantoms and used to estimate tumor sO_2 in the animal measurement using the NIRS and mean pO_2 values, as mentioned in Secs. 3 and 4. In Sec. 4, we will show that while NIRS results tended to be similar for several tumors, pO_2 electrode measurements showed considerable variation even in the same tumor type, suggesting distinct tumor heterogeneity. In Sec. 5, we discuss the need to develop an NIR imaging technique in order to study spatial heterogeneity of tumor vasculature under oxygen interventions. Finally, we conclude that the NIRS technology can provide an efficient, real-time, noninvasive approach to monitoring tumor physiology and is complementary to other techniques.

2 Theory and Algorithm Development

2.1 Algorithms to Quantify Changes in $[HbO_2]$ and [Hb]

NIR spectroscopy can be used to measure hemoglobin concentrations and oxygen saturation since light absorptions of HbO_2 and Hb are different at the wavelengths selected (758 and 785 nm). In common with our previous work,[11] we assumed that HbO_2 and Hb are the only significant absorbing materials in tumors within the selected NIR range of 700 to 900 nm. Based on Beer-Lambert's law, the absorption coefficients μ_a comprise the extinction coefficients for deoxyhemoglobin (ε_{Hb}) and oxyhemoglobin (ε_{HbO2}) multiplied by their respective concentrations:

$$\mu_a^{758}=2.3\{\varepsilon_{Hb}^{758}[Hb]+\varepsilon_{HbO2}^{758}[HbO_2]\}, \tag{1}$$

$$\mu_a^{785}=2.3\{\varepsilon_{Hb}^{785}[Hb]+\varepsilon_{HbO2}^{785}[HbO_2]\}, \tag{2}$$

where the factor of 2.3 results from the different definitions of μ_a and ε in relation to the incident and detected optical intensities. The conventional definitions for μ_a and ε are $I=I_0\exp(-\mu_a L)$ and $I=I_0 10^{-\varepsilon CL}$, respectively, where I_0 and I are the incident and detected optical intensities in transmission measurement of a nonscattering medium, C is the concentration of hemoglobin measured in millimoles per liter, and L is the optical path length through the medium in centimeters. Therefore, we should have a relationship of $\mu_a=2.3\,\varepsilon C$.

We have not yet completed a suitable algorithm to compute μ_a of rat tumors due to their finite size and high heterogeneity. Instead of diffusion theory, we modified Beer-Lambert's law, i.e., $\mu_a=2.3\varepsilon C=(2.3/L)\log(I_0/I)$, to analyze the data using only amplitude values to quantify changes in $[HbO_2]$ and [Hb]. In this case, I_0 is the detected light intensity when no absorption is present. Specifically, changes in absorption coefficient of the tumor, $\Delta\mu_a$, between baseline and transient conditions under respiratory intervention can be expressed as

$$\Delta\mu_a=\mu_{aT}-\mu_{aB}=2.3\log(A_B/A_T)/L, \tag{3}$$

where L is the optical path length and A_B and A_T are baseline and transient amplitudes of the measured optical signals, respectively.

By manipulating Eqs. (1) to (3), changes of $[HbO_2]$ and [Hb] due to an intervention can be expressed using the transmitted amplitudes of the light through the tumor as:

$$\Delta[HbO_2]=-11.73*\frac{\log(A_B/A_T)^{758}}{L^{758}}+14.97*\frac{\log(A_B/A_T)^{785}}{L^{785}}, \tag{4}$$

$$\Delta[Hb]=8.09*\frac{\log(A_B/A_T)^{758}}{L^{758}}-6.73*\frac{\log(A_B/A_T)^{785}}{L^{785}}, \tag{5}$$

where L^{758} and L^{785} are optical path lengths between the source and detector at 758 and 785 nm, respectively. The units of $\Delta[HbO_2]$ and Δ[Hb] in Eqs. (4) and (5) are in millimolar. The constants given in the equations were computed with the extinction coefficients for oxygenated and deoxygenated hemoglobin at the two wavelengths used.[12] The constant values are slightly different from our previous report[11] due to a slight shift in wavelength (782 to 785 nm) from one laser source, but the actual differences between the values of $\Delta[HbO_2]$ and Δ[Hb] calculated from our previous report and from Eqs. (4) and (5) are little and negligible.

In principle, L^{758} and L^{785} given in Eqs. (4) and (5) are not constants, depending on both the source-detector separation and the optical properties of the measured medium. Optical path length in a scattering medium L has been expressed[13] as the source-detector separation d multiplied by a differential pathlength factor (DPF), i.e., $L=d*DPF$. DPF values of blood-perfused tissues should be wavelength- and oxygenation-dependent, and they have been studied intensively for muscles[14] and brains[15] with approximate values of 4 to 6 and 5 to 6, respectively. Little is known about DPF for tumors although a DPF value of 2.5 has been used by others.[16] In our approach, we define two parameters, β_{HbO2} and β_{Hb}, as ratios between DPF^{758} and DPF^{785} for oxygenated blood and deoxygenated blood, respectively, as given below:

$$\beta_{HbO2}=\left(\frac{DPF^{758}}{DPF^{785}}\right)_{HbO2}=\left(\frac{L^{758}}{L^{785}}\right)_{HbO2},$$

$$\beta_{Hb}=\left(\frac{DPF^{758}}{DPF^{785}}\right)_{Hb}=\left(\frac{L^{758}}{L^{785}}\right)_{Hb}. \tag{6}$$

Substituting Eq. (6) into Eqs. (4) and (5) leads to

$$\Delta[HbO_2]=\frac{-\frac{11.73}{\beta_{HbO2}}\log\left(\frac{A_B}{A_T}\right)^{758}+14.97\log\left(\frac{A_B}{A_T}\right)^{785}}{d\times DPF_0}, \tag{7}$$

$$\Delta[\mathrm{Hb}]=\frac{\frac{8.09}{\beta_{\mathrm{Hb}}}\log\left(\frac{A_B}{A_T}\right)^{758}-6.73\log\left(\frac{A_B}{A_T}\right)^{785}}{d\times DPF_0}, \quad (8)$$

where DPF_0 is a mean DPF at 785 nm for both oxygenated and deoxygenated states, i.e., $DPF_0=DPF_{\mathrm{HbO2}}^{785}=DPF_{\mathrm{Hb}}^{785}$, which is assumed to be the same for both $\Delta[\mathrm{HbO_2}]$ and $\Delta[\mathrm{Hb}]$. This assumption is based on the fact that the absorption difference between oxygenated and deoxygenated blood at 785 nm is much smaller than that at 758 nm. The maximal relative error caused by this assumption in tumor oxygen interventions was estimated to be less than 12%, and detailed justification and discussion were given in Ref. 11. Since our focus is on dynamic changes in tumor $[\mathrm{HbO_2}]$ under carbogen intervention, we simplify Eqs. (7) and (8) to Eqs. (9) and (10) by including DPF_0 in the unit:

$$\Delta[\mathrm{HbO_2}]=\frac{-\frac{11.73}{\beta_{\mathrm{HbO2}}}\log\left(\frac{A_B}{A_T}\right)^{758}+14.97\log\left(\frac{A_B}{A_T}\right)^{785}}{d}, \quad (9)$$

$$\Delta[\mathrm{Hb}]=\frac{\frac{8.09}{\beta_{\mathrm{Hb}}}\log\left(\frac{A_B}{A_T}\right)^{758}-6.73\log\left(\frac{A_B}{A_T}\right)^{785}}{d}, \quad (10)$$

where the units for Eqs. (9) and (10) become $\mathrm{mM/DPF_0}$.

To further quantify β_{HbO2} and β_{Hb}, we associate L to μ_a by $L=(\sqrt{3}/2)d\,(\mu_s'/\mu_a')^{1/2}$, where μ_s' is the reduced scattering coefficient, according to Sevick et al.[10] and Liu.[17] Equation (6) becomes

$$\beta_{\mathrm{HbO2}}=\left(\frac{L^{758}}{L^{785}}\right)_{\mathrm{HbO2}}=\left[\left(\frac{\mu_a^{785}}{\mu_a^{758}}\right)^{1/2}\right]_{\mathrm{HbO2}}=\left[\left(\frac{\varepsilon^{785}}{\varepsilon^{758}}\right)^{1/2}\right]_{\mathrm{HbO2}}, \quad (11)$$

$$\beta_{\mathrm{Hb}}=\left(\frac{L^{758}}{L^{785}}\right)_{\mathrm{Hb}}=\left[\left(\frac{\mu_a^{785}}{\mu_a^{758}}\right)^{1/2}\right]_{\mathrm{Hb}}=\left[\left(\frac{\varepsilon^{785}}{\varepsilon^{758}}\right)^{1/2}\right]_{\mathrm{Hb}}, \quad (12)$$

where $\mu_a=2.3\,\varepsilon C$ and μ_s' values at two wavelengths are canceled, assuming that μ_s' (758 nm)$\cong\mu_s'$ (785 nm). By calculating the hemoglobin extinction coefficients at 758 and 785 nm,[12] we obtained $\beta_{\mathrm{HbO2}}=1.103$ and $\beta_{\mathrm{Hb}}=0.9035$. Substituting these values into Eqs. (9) and (10) results in the final expressions for $\Delta[\mathrm{HbO_2}]$ and $\Delta[\mathrm{Hb}]$:

$$\Delta[\mathrm{HbO_2}]=\frac{-10.63\log\left(\frac{A_B}{A_T}\right)^{758}+14.97\log\left(\frac{A_B}{A_T}\right)^{785}}{d}, \quad (13)$$

$$\Delta[\mathrm{Hb}]=\frac{8.95\log\left(\frac{A_B}{A_T}\right)^{758}-6.73\log\left(\frac{A_B}{A_T}\right)^{785}}{d}. \quad (14)$$

$\Delta[\mathrm{Hb_{total}}]$ can also be obtained by adding Eqs. (13) and (14):

$$\Delta[\mathrm{Hb_{total}}]=\Delta[\mathrm{HbO_2}]+\Delta[\mathrm{Hb}]=\frac{-1.68\log\left(\frac{A_B}{A_T}\right)^{758}+8.24\log\left(\frac{A_B}{A_T}\right)^{785}}{d}. \quad (15)$$

Equations (13) to (15) will be used in calculating $\Delta[\mathrm{HbO_2}]$, $\Delta[\mathrm{Hb}]$, and $\Delta[\mathrm{Hb_{total}}]$ in tissue phantoms and tumors during gas interventions in this paper.

The units for $\Delta[\mathrm{HbO_2}]$, $\Delta[\mathrm{Hb}]$, and $\Delta[\mathrm{Hb_{total}}]$ in Eqs. (13) to (15) are $\mathrm{mM/DPF_0}$, which is still a variable, depending on the optical properties of the tumor at a particular wavelength. Since our study involves changes in $[\mathrm{HbO_2}]$ due to respiratory challenges, we can obtain a normalized $\Delta[\mathrm{HbO_2}]$ at its maximal value, i.e., $\Delta[\mathrm{HbO_2}]/\Delta[\mathrm{HbO_2}]_{\max}$, to eliminate the unit so as to minimize the effect of DPF on our results. Next, we will show that a normalized $\Delta[\mathrm{HbO_2}]$ has a close relationship with hemoglobin oxygen saturation $\mathrm{sO_2}$.

2.2 Relationship Among Normalized $\Delta[\mathrm{HbO_2}]$, $\mathrm{sO_2}$ and Blood $\mathrm{pO_2}$

We define $\mathrm{sO_2}$ values of the measured sample at the baseline, transient state, and maximal state, i.e., $(\mathrm{sO_2})_{\mathrm{base}}$, $(\mathrm{sO_2})_t$, and $(\mathrm{sO_2})_{\max}$, respectively:

$$(\mathrm{sO_2})_{\mathrm{base}}=\frac{[\mathrm{HbO_2}]_{\mathrm{base}}}{[\mathrm{Hb_{total}}]_{\mathrm{base}}}, \quad (16)$$

$$(\mathrm{sO_2})_t=\frac{[\mathrm{HbO_2}]_t}{[\mathrm{Hb_{total}}]_t}, \quad (17)$$

$$(\mathrm{sO_2})_{\max}=\frac{[\mathrm{HbO_2}]_{\max}}{[\mathrm{Hb_{total}}]_{\max}}, \quad (18)$$

where $[\mathrm{HbO_2}]_{\mathrm{base}}$, $[\mathrm{HbO_2}]_t$, and $[\mathrm{HbO_2}]_{\max}$ are corresponding to oxygenated hemoglobin concentrations at the respective state. Mathematically, it follows that

$$\frac{\Delta\mathrm{sO_2}}{\Delta\mathrm{sO_2}_{\max}}=\frac{(\mathrm{sO_2})_t-(\mathrm{sO_2})_{\mathrm{base}}}{(\mathrm{sO_2})_{\max}-(\mathrm{sO_2})_{\mathrm{base}}}=\frac{\left(\frac{[\mathrm{HbO_2}]_t}{[\mathrm{Hb_{total}}]_t}-\frac{[\mathrm{HbO_2}]_{\mathrm{base}}}{[\mathrm{Hb_{total}}]_{\mathrm{base}}}\right)}{\left(\frac{[\mathrm{HbO_2}]_{\max}}{[\mathrm{Hb_{total}}]_{\max}}-\frac{[\mathrm{HbO_2}]_{\mathrm{base}}}{[\mathrm{Hb_{total}}]_{\mathrm{base}}}\right)}. \quad (19)$$

During a cycle of oxygenation and deoxygenation in a blood-perfused tissue, if the total concentration of hemoglobin remains constant, we have the following condition: $[\mathrm{Hb_{total}}]_{\max}=[\mathrm{Hb_{total}}]_t=[\mathrm{Hb_{total}}]_{\mathrm{base}}$. In the case of tumors under gas intervention, total hemoglobin concentration does not always remain constant, but the changes in $[\mathrm{Hb}]_{\mathrm{total}}$ appeared relatively small in comparison to the changes in $[\mathrm{HbO_2}]$.[11,18] It is reasonable to assume that $\Delta[\mathrm{Hb_{total}}]\ll[\mathrm{Hb_{total}}]$, i.e., the condition of $[\mathrm{Hb_{total}}]_{\max}=[\mathrm{Hb_{total}}]_t=[\mathrm{Hb_{total}}]_{\mathrm{base}}$ still holds for the tumor under oxygen/carbogen interventions. Then, Eq. (19) becomes

$$\frac{\Delta sO_2}{\Delta sO_{2\,max}}=\frac{(sO_2)_t-(sO_2)_{base}}{(sO_2)_{max}-(sO_2)_{base}}=\frac{\Delta[HbO_2]}{\Delta[HbO_2]_{max}}. \tag{20}$$

To further make correlation between the normalized $\Delta[HbO_2]$ and blood pO_2, Hill's equation[19] can be combined with Eq. (20) to characterize oxygen transport in the tissue vasculature:

$$\frac{\Delta[HbO_2]}{\Delta[HbO_2]_{max}}=\frac{\dfrac{(pO_2^B)^n}{(P_{50}^B)^n+(pO_2^B)^n}-(sO_2)_{base}}{(sO_2)_{max}-(sO_2)_{base}}=\frac{\dfrac{(pO_2^B)^n}{(P_{50}^B)^n+(pO_2^B)^n}-b}{a-b}, \tag{21}$$

where pO_2^B is the oxygen partial pressure in blood, P_{50}^B is the oxygen partial pressure in blood at $sO_2=50\%$, n is the Hill coefficient, $a=(sO_2)_{max}$, and $b=(sO_2)_{base}$. This equation associates the normalized ΔHbO_2 to blood pO_2 in tissues. It indicates that normalized $\Delta[HbO_2]$ measured from tissues/tumors under gas interventions is associated with normalized sO_2 between $(sO_2)_{base}$ and $(sO_2)_{max}$ of the tissue/tumor, and it predicts the relationship between the normalized $\Delta[HbO_2]$ and blood pO_2 values in the tissue/tumor vasculature.

In our phantom studies, the measured pO_2 values are considered as blood pO_2 in tissue vasculature since blood is well mixed in the solution (see details in Sec. 3.4). Therefore, values of P_{50}^B, n, a, and b in Eq. (21) can be fitted to the experimental data, allowing us to determine the initial, transient, and maximal values of sO_2 of the simulating tissue due to oxygen/nitrogen interventions.

2.3 Relationship Between Normalized $\Delta[HbO_2]$ and Tissue/Tumor pO_2

In principle, blood pO_2 and tissue pO_2 are different, depending on the relative distance between a capillary vessel, oxygen consumption, and the location where pO_2 is measured.[19] It is shown that there exists a constant pressure drop between blood pO_2 and tissue pO_2 as the blood passes through a capillary vessel. Therefore, it is reasonable to assume

$$pO_2^B=\alpha\cdot pO_2^T, \tag{22}$$

where pO_2^B and pO_2^T are blood pO_2 and tissue pO_2 values, respectively, and α is a constant representing an oxygen partial pressure drop from blood pO_2 to a local tissue pO_2. Substituting Eq. (22) in Eq. (21) results in

$$\frac{\Delta[HbO_2]}{\Delta[HbO_2]_{max}}=\frac{\dfrac{(pO_2^T)^n}{(P_{50}^T)^n+(pO_2^T)^n}-b}{a-b}, \tag{23}$$

where P_{50}^T is the oxygen partial pressure in tissue resulting from P_{50}^B, and the meanings of n, a, and b remain the same as in Eq. (21). This equation shows how normalized $\Delta[HbO_2]$ measured from tissue under gas interventions is associated with both tissue pO_2 and normalized sO_2 between $(sO_2)_{base}$ and $(sO_2)_{max}$ in the tissue vasculature.

Ideally, when both $\Delta[HbO_2]$ and tissue pO_2 are measured at the same physical location, the maximal and initial oxygen saturations, i.e., a and b in Eq. (23), of the measured tissue vasculature can be obtained by fitting Eq. (23) to the measured data. In our tumor study, we then can estimate the maximal and initial hemoglobin oxygen saturations of the tumor by fitting the measured values of global normalized $\Delta[HbO_2]$ and global tissue pO_2, which result from adding up all local pO_2 values obtained from ^{19}F MR pO_2 mapping.

3 Materials and Methods

3.1 Tumor Model

Dunning prostate rat tumors (eight R3327-HI and four R3327-AT1)[20] were implanted in pedicles on the foreback of adult male Copenhagen rats, as described in detail previously.[21] Once the tumors reached approximately 1 cm in diameter, the rats were anesthetized with 0.2 ml ketamine hydrochloride (100 mg/mL; Aveco, Fort Dodge, IA) and maintained under general gaseous anesthesia with isoflurane in air (1.3% isoflurane at 1 dm^3/min air) through a mask placed over the mouth and nose. Tumors were shaved to improve optical contact for transmitting light. Body temperature was maintained by a warm water blanket and was monitored by a rectally inserted thermal probe connected to a digital thermometer (Digi-Sense, model 91100-50, Cole-Parmer Instrument Company, Vernon Hills, IL). A pulse oximeter (model 8600, Nonin, Inc., Plymouth, MN) was placed on the hind foot to monitor arterial oxygenation (S_aO_2). Tumor volume V (in cubic centimeters) was estimated as $V=(4\pi/3)\,[(L+W+H)/6]^3$, where L, W, and H are the three respective orthogonal dimensions.

In general, the source-detector fiber separation was about 1 to 1.5 cm in transmittance geometry, and thus the maximal tumor volume interrogated by NIR light can be estimated as follows. By the diffusion approximation, the optical penetration depth from the central line between the source and detector is about one half of the separation (source-detector separation$=d$). The total tumor volume interrogated by NIR light can be estimated as the spherical volume with a radius of one half of d, i.e., $(\pi/6)d^3$. In this way, the estimated tumor volume interrogated by NIR light is in the range of 0.5 to 2.0 cm^3, depending on the actual source-detector separation.

3.2 NIRS and pO_2 Needle Electrode Measurements

Figure 1 shows the schematic setup for animal experiments using both NIRS and a pO_2 needle electrode. A needle type oxygen electrode was placed in the tumor, and the reference electrode was placed rectally. The electrodes were connected to a picoammeter (Chemical Microsensor, Diamond Electro-Tech Inc., Ann Arbor, MI) and polarized at −0.75 V. Linear two-point calibrations were performed with air (21% O_2) and pure nitrogen (0% O_2) saturated saline buffer solutions before the electrode was inserted into the tumor, and we estimated an instrumental precision of 2 to 3 mm Hg. Measurement points of pO_2 were manually recorded, while the NIRS data were acquired automatically. Measurements of pO_2 and NIRS were initiated, while the rats breathed air for ~10 min to demonstrate a stable baseline. The inhaled gas was then switched to carbogen for 15 min and switched back to air.

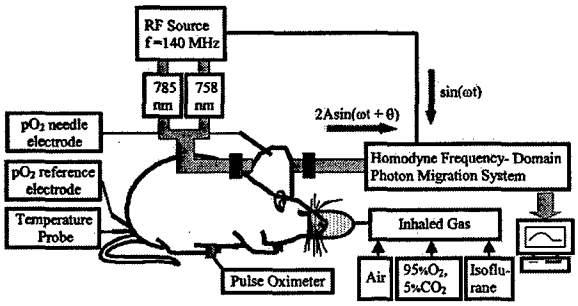

Fig. 1 Schematic experimental setup of one-channel, near-infrared, frequency-domain IQ instrument for tumor investigation *in vivo*. The 5-mm-diameter fiber bundles deliver the laser light, comprising two wavelengths (758 and 785 nm), and detect the laser light transmitted through the implanted tumor. The pO_2 needle electrode measures tumor tissue pO_2.

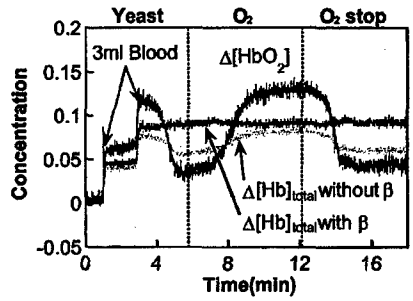

Fig. 2 Simultaneous dynamic changes of $\Delta[HbO_2]$, $\Delta[Hb]$, and $\Delta[Hb]_{total}$ in the phantom solution measured using NIRS. The gray solid curve is for $\Delta[Hb]_{total}$ without using β_{HbO_2} and β_{Hb} values. Oxygen consumption by yeast produced deoxygenated blood and blowing oxygen restored oxygenation. During the oxy- and deoxygenation process, $\Delta[Hb]_{total}$ is supposed to be a constant. However, as we can see here, $\Delta[Hb]_{total}$ calculated without β_{HbO2} and β_{Hb} values shows the fluctuation during the oxy- and deoxygenation while $\Delta[Hb]_{total}$ calculated using β_{HbO2} and β_{Hb} values shows the veracity of these modified algorithms.

Our NIR system as shown in Figure 1 (Refs. 11 and 22) is a homodyne frequency-domain photon migration system (NIM, Inc., Philadelphia, PA) and uses commercially available in-phase and quadrature (IQ) demodulator chips to demodulate the detected, amplitude-modulated optical signal.

3.3 Experimental Validation for β_{HbO2} and β_{Hb} Values

In order to validate β_{HbO2} and β_{Hb} values, we conducted phantom calibration measurements. We used 2 l of 0.01 M phosphate buffered saline (P-3813, Sigma, St Louis, MO) and 1% Intralipid (Intralipid® 20%, Baxter Healthcare Corp., Deerfield, IL) with pH=7.4 at 25 °C. To deoxygenate the solution, 14 g of baking yeast was dissolved in the phantom solution, and pure oxygen gas was used to oxygenate the solution. After the yeast was well mixed in the solution, 3 ml of human blood was added twice. When the blood was fully deoxygenated, pure oxygen was introduced in the solution to oxygenate the blood. After the blood was fully oxygenated, oxygen blowing was stopped in order to deoxygenate the solution with yeast again.

Equations (4) and (5) were applied to the raw amplitude data to calculate $\Delta[HbO_2]$ and $\Delta[Hb]$. Large unexpected and erroneous fluctuation of $\Delta[Hb_{total}]$ $(=\Delta[HbO_2]+\Delta[Hb])$ were seen during the oxygenation and deoxygenation cycles (Figure 2). However, when we applied Eqs. (13) to (15) to calculate $\Delta[HbO_2]$, $\Delta[Hb]$, and $\Delta[Hb_{total}]$, $\Delta[Hb_{total}]$ remained constant during the oxygenation and deoxygenation cycles as expected. This demonstrates that the values of $\beta_{HbO2}=1.103$ and $\beta_{Hb}=0.9035$ are correct and necessary to compensate the differences in DPFs caused by the two different wavelengths.

3.4 Tissue Phantom Solution Model

In order to study the relationship between pO_2 and $\Delta[HbO_2]$ in regular tissues, we conducted a tissue-simulating phantom study by using the liquid solution similar to that mentioned above. In normal tissues, there are several steps of oxygen transport from the blood to tissue cells.[23] In the tissue-simulating phantom, blowing oxygen gas represents oxygenation process of blood in the lungs, and blowing nitrogen gas simulates deoxygenation process of blood in the tissues. The differences between the tissue-simulating phantom and real tissues are that there is no capillary membrane in the phantom, and that the phantom is more homogeneous than real tissues. Capillary membranes have high permeability of oxygen, so oxygen transport from blood to tissues crossing the capillary membranes occurs straightforwardly. Furthermore, normal tissues are well vascularized, and the NIR techniques are more sensitive toward measuring small vessels and vascular bed of the tissue.[24] Therefore, vasculature of normal tissues has been simulated by a turbid solution mixed with blood as a simplified laboratory model in NIRS measurements for oxygen transport from blood to normal tissues.[10,18,22]

The experimental setup shown in Figure 3 was made to simulate tumor oxygenation/deoxygenation. Oxygen needle electrodes, a pH electrode, and a thermocouple probe (model 2001, Sentron, Inc., Gig Harbor, WA) were placed in the solution, and the gas tube for delivery of N_2 or air was placed opposite the NIRS probes to minimize any liquid movement effects. Source and detector probes for the NIRS were placed in reflection geometry with a direct separation of 3 cm. The

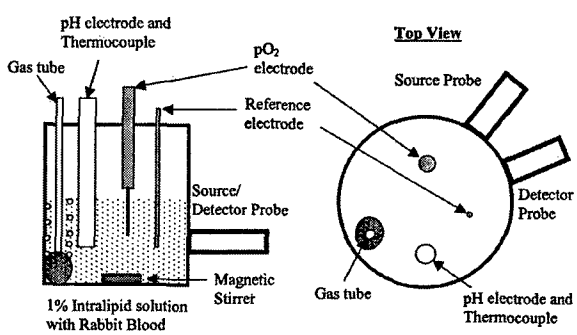

Fig. 3 Experimental setup for phantom study using 1% Intralipid in saline buffer. NIRS probes were placed in reflectance mode, while the gas bubbler was placed opposite to minimize liquid movement effects. After adding 2 ml of rabbit blood to a 200 ml solution, nitrogen gas and air were introduced to deoxygenate and oxygenate the solution, respectively.

solution was stirred constantly to maintain homogeneity by a magnetic stirrer at ~37 °C. Fresh whole rabbit blood (2 mL) was added to the 200 mL solution before baseline measurement. Nitrogen gas and air were used to deoxygenate and oxygenate the solution, respectively.

3.5 MRI Instrumentation and Procedure

To support the findings obtained from the pO_2 electrode measurements and NIRS, we conducted MRI experiments using an Omega CSI 4.7 T 40 cm system with actively shielded gradients. A homebuilt tunable $^1H/^{19}F$ single turn solenoid coil was placed around the tumor. 45 μL hexafluorobenzene (HFB; Lancaster, Gainesville, FL) was administered directly into the tumor using a Hamilton syringe (Reno, NV) with a custom-made fine sharp (32 gauge) needle and HFB was deliberated dispersal along several tracks to interrogate both central and peripheral tumor regions, as described in detail previously.[5] HFB is ideal for imaging pO_2 because it has a single resonance and its relaxation rate varies linearly with oxygen concentration. ^1H images were acquired for anatomical reference using a traditional 3-D spin-echo pulse sequence. Conventional ^{19}F MR images were taken to show the 3-D distribution of the HFB in the tumor. ^{19}F MR images were directly overlaid over ^1H images to show the position of the HFB in that slice.

Tumor oxygenation was assessed using fluorocarbon relaxometry using echo planar imaging for dynamic oxygen mapping (FREDOM) based on ^{19}F pulse burst saturation recovery (PBSR) echo planar imaging (EPI) of HFB.[25] The PBSR preparation pulse sequence consists of a series of 20 nonspatially selective saturating 90 deg pulses with 20 ms spacing to saturate the ^{19}F nuclei. Following a variable delay time τ, a single spin-echo EPI sequence with blipped phase encoding was applied.[26] Fourteen 32×32 PBSR-EPI images, with τ ranging from 200 ms to 90 sec and a field of view (FOV) of 40×40 mm, were acquired in 8 min using the alternated relaxation delays with variable acquisitions to reduce clearance effects (ARDVARC) acquisition protocol.[25] An $R1(=1/T1)$ map was obtained by fitting the signal intensity of each voxel of the 14 images to a three-parameter relaxation model by the Levenberg-Marquardt least-squares algorithm:

$$y_n(i,j)=A(i,j)\cdot[1-(1+W)\exp(-R1(i,j)\cdot\tau_n)] \tag{24}$$

$$(n=1,2,\cdots\cdots,14)$$

$$(i,j=1,2,\cdots\cdots,32),$$

where $y_n(i,j)$ is the measured signal intensity corresponding to delay time τ_n (the n'th images) for voxel (i,j), $A(i,j)$ is the fully relaxed signal intensity amplitude of voxel (i,j), W is a dimensionless scaling factor allowing for imperfect signal conversion, $R1(i,j)$ is the relaxation rate of voxel (i,j) in units of sec^{-1}, and A, W, and $R1$ are the three fit parameters for each of the 32×32 voxels. Finally, the pO_2 maps were generated by applying the calibration curve, pO_2 (mm Hg) $=[R1(s^{-1})-0.0835]/0.001876$ at 37 °C, to the $R1$ maps.[25]

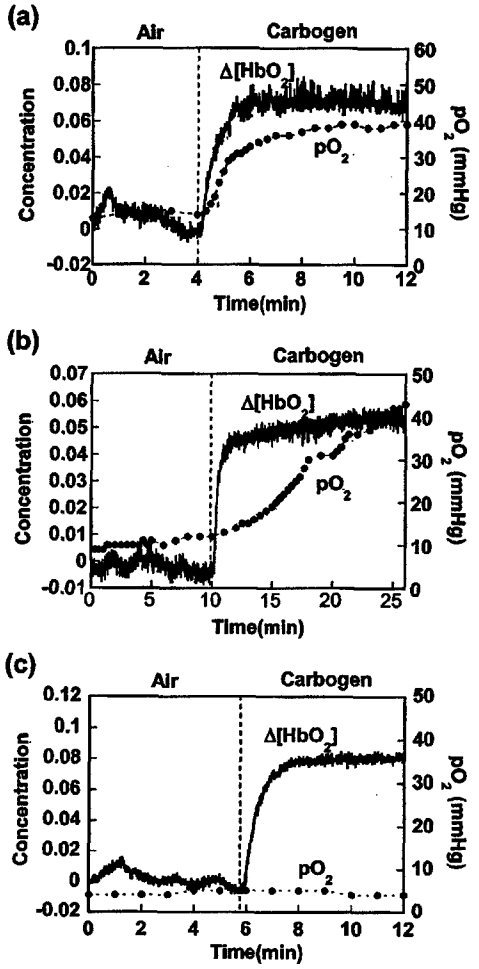

Fig. 4 Simultaneous dynamic changes of $\Delta[HbO_2]$ and pO_2 in R3327-HI rat prostate tumors using NIRS and pO_2 needle electrode. (a) A small tumor (1.5 cm^3) showed a rapid pO_2 response (case 1), whereas (b) a bigger tumor (3.1 cm^3) showed a slower pO_2 response (case 2). (c) In a third tumor (1.6 cm^3) where regional baseline pO_2 was <5 mm Hg, there was no pO_2 response (case 3). The unit of $\Delta[HbO_2]$ is mM/DPF, where DPF is equal to the optical path length divided by the source-detector separation. Dotted vertical line marks the time when the gas was changed.

4 Results

4.1 Tumor Study Results

We have measured relative changes of $[HbO_2]$, $[Hb]$, $[Hb_{total}]$, and tumor tissue pO_2 (electrode) from eight Dunning prostate R3327-HI tumors, and Figure 4 shows three representative data sets. Figure 4(a) shows the temporal profiles of $\Delta[HbO_2]$ and pO_2 in a small Dunning prostate R3327-HI tumor (1.5 cm^3) measured simultaneously with NIRS and the pO_2 needle electrode during respiratory challenge. After a switch from air to carbogen, $\Delta[HbO_2]$ increased rapidly, along with tumor tissue pO_2. Figure 4(b) was obtained from a large tumor (3.1 cm^3): the electrode readings showed a slower pO_2 response, whereas the NIRS response was biphasic, which has been a commonly observed dynamic feature.[11] In a third tumor (1.6 cm^3), NIRS behaved as before, but pO_2 did not change [Figure 4(c)].

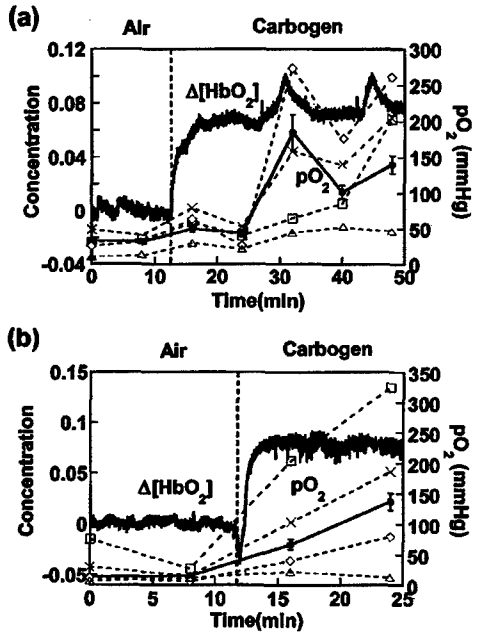

Fig. 5 Dynamic changes of $\Delta[HbO_2]$ and pO_2 in two R3327-AT1 rat prostate tumors measured sequentially using NIRS and ^{19}F MR pO_2 mapping. The solid curves represent $\Delta[HbO_2]$, and the solid lines with solid circles represent mean $pO_2 \pm SE$ (standard error) of 21 (a) and 45 (b) voxels of the respective tumor. Dashed lines with open symbols are 4 representative voxels for each case. After a gas switched from air to carbogen, the mean pO_2 values of both tumors increased, but individual voxels showed quite different responses, indicating high heterogeneity in the tumors. The tumor sizes were 3.2 cm^3 and 2.7 cm^3 for (a) and (b), respectively.

In four tumors from a separate subline (Dunning prostate R3327-AT1), NIRS and ^{19}F MRI were taken sequentially with carbogen challenge, and two representative data sets are shown in Figure 5. NIRS response showed vascular oxygenation changes as before, and FREDOM revealed the distinct heterogeneity of the tumor tissue response. Initial pO_2 was in the range of 1 to 75 mm Hg, and carbogen challenge produced pO_2 values in the range of 6 to 350 mm Hg. Representative voxels are shown in each figure by dashed lines with open symbols. In addition, mean pO_2 values were calculated by averaging all available pO_2 readings over 21 and 45 voxels for the two respective tumors. We usually obtain pO_2 temporal profiles from individual voxels among 200 to 400 voxels in a tumor during the entire intervention period. The pO_2 readings presented here were picked to show heterogeneity of the tumor. In Figure 5(a), the closest distance between the two voxels is 1.25 mm (between ◇ and □), and the furthest distance is 7.6 mm (between × and △). In Figure 5(b), the closest distance is 3.6 mm (between × and △) and the furthest distance is 16 mm (between × and □). These indeed showed that tumor pO_2 responses to carbogen intervention could be quite different at different locations. Notice that Figure 5(a) showed spikes of $\Delta[HbO_2]$ during the measurement. We expect this to be caused by sudden changes in rat respiratory circulation or motion, rather than resulting from simple instrumental noise. It is also seen that mean pO_2 values have displayed a consistent increase when $\Delta[HbO_2]$ showed

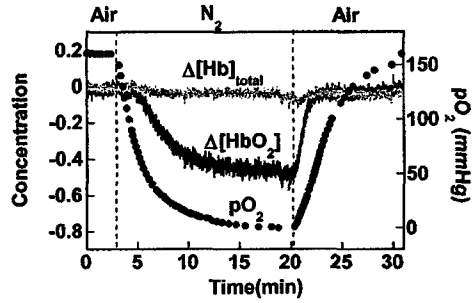

Fig. 6 Simultaneous dynamic changes of $\Delta[HbO_2]$, $\Delta[Hb]_{total}$, and pO_2 in the phantom solution measured using NIRS and pO_2 needle electrode. The dark solid curve is for $\Delta[HbO_2]$, the lighter solid line is for $\Delta[Hb]_{total}$, and the solid circles show pO_2 values in the phantom solution. After ~3 min baseline, the bubbling gas was changed from air to nitrogen to deoxygenate the solution and then switched back to air to reoxygenate the solution. The unit of $\Delta[HbO_2]$ is mM/DPF.

spikes, suggesting that such spikes may result from changes in rat physiological conditions.

4.2 Tissue Phantom Study Results

Figure 6 shows a temporal profile for $\Delta[HbO_2]$ and pO_2 measured from the tissue phantom during a cycle of gas change from air to nitrogen and back. The first three minutes were measured as a baseline after adding 2 ml blood. Bubbling nitrogen deoxygenated the solution and caused the pO_2 values to fall; $\Delta[HbO_2]$ declined accordingly with a small time lag. After the bubbling gas was switched from nitrogen to air, both $\Delta[HbO_2]$ and pO_2 started to increase simultaneously, but the recovery time of $\Delta[HbO_2]$ to the baseline was faster than that of pO_2. The small time lag between the changes of $\Delta[HbO_2]$ and pO_2 is probably due to the allosteric interactions between hemoglobin and oxygen molecules. According to the hemoglobin oxygen-dissociation curve,[19,27] oxyhemoglobin starts to lose oxygen significantly when pO_2 falls below 70 mm Hg at standard conditions (pH=7.4, pCO_2=40 mm Hg, and temperature=37 °C). The same principle can explain why $\Delta[HbO_2]$ has a faster recovery than that of pO_2. Figure 6 shows that $\Delta[HbO_2]$ is already saturated when pO_2 is at 50 mm Hg, while the solution was still being oxygenated. This may be due to low pCO_2 in the solution where this can shift the oxyhemoglobin dissociation curve to the left, causing oxyhemoglobin to be saturated at lower pO_2. Importantly, $\Delta[Hb]_{total}$ remained unchanged, as expected, during a cycle of deoxygenation and oxygenation.

4.3 Correlation between pO_2 and Normalized $\Delta[HbO_2]$

For Tissue Phantoms. Figure 7(a) replots the data given in Figure 6, showing the relationship between normalized $\Delta[HbO_2]$ and pO_2 measured from the tissue phantom during the oxygenation (air blowing) period after the nitrogen blowing. Open circles are the measured data, and the solid line is the fitted curve using Eq. (23). The error bars for the data were not shown here since they are smaller than the symbols of the data points. For the curve fitting procedure, we used a nonlinear curve-fitting routine provided through KaleidaGraph (Synergy software, Reading, PA). The fitted parameters

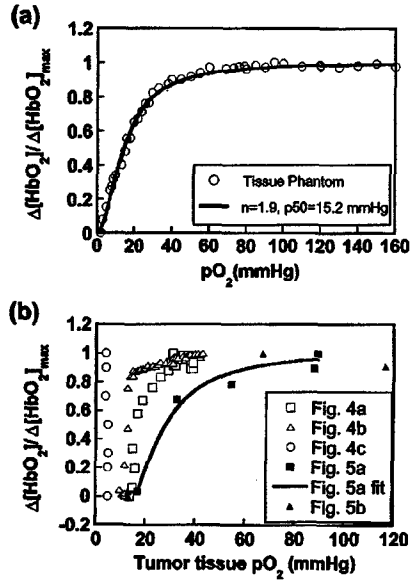

Fig. 7 Changes of tissue pO_2 with normalized changes of oxygenated hemoglobin (a) in the phantom solution using the NIRS and pO_2 needle electrode and (b) in tumors measured with NIRS, pO_2 needle electrode, and ^{19}F MR pO_2 mapping. In (a), the open circles are measured data and the solid line is the fitted curve using Eq. (21). This shows that Eq. (21) works well in a homogeneous system. In (b), all the tumor data are shown indicating that tumors are highly heterogeneous for pO_2 response to carbogen inhalation. Open symbols show local pO_2 changes (from Figure 4) and solid symbols show the mean pO_2 changes (from Figure 5) during gas intervention. To estimate global sO_2 in tumors during respiratory challenges, we applied Eq. (23) to Figure 5(a), indicating sO_2 changes during carbogen inhalation when compared via tumor pO_2.

are $n=1.9$, $P_{50}=15.2$ mm Hg, $[sO_2]_{base}=0\%$, and $[sO_2]_{max}=99\%$ with $R=0.997$ and minimized chi-square. The fitted values of $[sO_2]_{base}$ and $[sO_2]_{max}$ are in good agreement with the expected values, since the corresponding pO_2 values are 0 and 160 mm Hg, respectively. This agreement validates Eq. (23) and further indicates that we can measure approximate sO_2 values during the gas interventions in a homogeneous system by fitting the experimental data using Eq. (23) even though we do not measure absolute $[HbO_2]$. The Hill coefficient (n) and pO_2 value at 50% of sO_2 (P_{50}) are smaller than the values from a standard oxyhemoglobin saturation curve, probably due to the shift of the oxyhemoglobin dissociation curve.

For Tumor Study. Figure 7(b) replots the data given in Figures 4 and 5, showing a direct relationship between the normalized $\Delta[HbO_2]$ and tissue pO_2 in the tumors. NIRS results tended to be similar for several tumors, and pO_2 electrode measurements showed considerable variation even in the same tumor type, suggesting distinct tumor heterogeneity. This was substantiated by the ^{19}F MR pO_2 mappings (Figure 5): indeed, in some cases, pO_2 values did not change with respiratory challenge, especially when baseline pO_2 values were lower than 10 mm Hg.

Equation (23) can be used to estimate values of $[sO_2]_{base}$ and $[sO_2]_{max}$ for the tissue-simulating phantom (a homogeneous system). However, the relationship fails for heterogeneous systems such as tumors. The NIRS measurements interrogate a large volume of tumor tissue, giving a global value of normalized $\Delta[HbO_2]$, whereas the pO_2 readings are local near the tip of the needle electrode. However, to estimate mean values of $[sO_2]_{base}$ and $[sO_2]_{max}$, it is reasonable to compare the global normalized $\Delta[HbO_2]$ with global tissue pO_2, which can be obtained by summing up all local pO_2 readings at different pixels measured from the ^{19}F MRI mapping, as done in Sec. 4.1 and shown by solid lines in Figure 5. The data shown in Figure 7(b) with solid symbols are the global mean pO_2 values calculated from the corresponding MRI data. The solid fitting curve shown in Figure 7(a) is obtained from the mean pO_2 data given in Figure 5(a). In this case, the fitting parameters are P_{50}, $[sO_2]_{base}$, and $[sO_2]_{max}$ with a fixed Hill coefficient n to be the same as that under standard conditions. The best fitting curve of Eq. (23) is shown in Figure 7(b), having $P_{50}=20.6\pm4.1$ mm Hg, $[sO_2]_{base}=37\pm13\%$, and $[sO_2]_{max}=100\%$ with $R=0.985$ and goodness-of-fit $\chi^2=0.031$. Estimated errors for P_{50} and $[sO_2]_{base}$ are not insignificant and a better fit could be found by measuring pO_2 with better temporal resolution.

5 Discussion and Conclusion

Tumor oxygenation involves a complex interplay of multiple compartments and parameters: blood flow, blood volume, blood vessel structure, and oxygen consumption. NIRS provides a global noninvasive estimate of average vascular oxygenation encompassing arterial, venous, and capillary compartments. In agreement with our previous observations,[11] the $\Delta[HbO_2]$ response is often biphasic, which we believe represents rapid elevation of arterial oxygenation, followed by more sluggish capillary components.

Comparison with simultaneous electrode measurements indeed revealed that tumors are heterogeneous. Like NIRS measurements, pO_2 electrodes provide rapid assessment of pO_2 facilitating real-time observation of dynamic changes. In Figure 4(a), pO_2 starts at a baseline value ~15 mm Hg and increases rapidly in response to respiratory challenge with carbogen. Indeed, the rate approaches that of the vascular compartments. In a second tumor [Figure 4(b)], where the interrogated location showed a slightly lower pO_2, the tissue response was more sluggish. For a third HI tumor, local baseline pO_2 was found to be <5 mm Hg, and this did not change with carbogen inhalation despite the response observed by NIRS. This suggests a danger of comparing a global vascular measurement with regional tumor pO_2, since tumors are known to be highly heterogeneous. This also demonstrates an essential need for NIR imaging of tumors to provide regional tumor vascular oxygenation details.

FREDOM measurements in Figure 5 revealed the heterogeneity in baseline oxygenation within individual tumors of this second tumor subline as also reported previously.[25] Baseline pO_2 ranged from 1 to 75 mm Hg, and response to carbogen was variable in terms of rate and extent, as also seen for the HI subline using electrodes (Figure 4). As with the electrodes, the better oxygenated tumor regions showed a faster and greater response to carbogen inhalation. The oxygen electrode measurements in Figure 4 showed a maximum pO_2 of around 45 mm Hg, though we have observed values as high as 95 mm Hg using oxygen needle electrode. Observations using

the fluorescence-based OxyLite™ fiber-optic devices for measuring HI tumor reached the maximum detectable pO_2 of 100 mm Hg during carbogen inhalation.[5] FREDOM has shown values of less than 5 mm Hg and greater than 160 mm Hg under air breathing conditions, and reaching 350 mm Hg in HI tumors while breathing carbogen.[5] Each method indicates that tumors are highly heterogeneous, but it has been shown that there can be a positive linear relationship between baseline pO_2 and maximum pO_2 during carbogen inhalation in the Dunning prostate AT1 tumor line.[8]

The phantom measurements indicate and validate the reliability of the NIRS technique and also prove that normalized $\Delta[HbO_2]$ is closely related to the normalized hemoglobin-oxygen dissociation curve. The phantom data confirmed that we can obtain absolute sO_2 values in a homogeneous system by measuring both $\Delta[HbO_2]$ and pO_2. We could estimate mean sO_2 values of the tumor under intervention using global $\Delta[HbO_2]$ and averaged pO_2 readings, and the fitting errors are expected to be improved by having more data points. Measuring regional tumor vascular oxygenation by NIR imaging of tumors should allow us to correlate local $\Delta[HbO_2]$ and pO_2 and to understand the oxygen transport process from tumor vasculature to tumor tissue, and this is the direction of our future work.

Both NIRS and electrodes offer essentially real-time measurement of changes in oxygenation, which can be rapid (Figure 4). Indeed, the inflow kinetics of vascular O_2 detected by NIRS are similar to those previously reported in the HI tumor line following a bolus of the paramagnetic contrast agents Gd-DTPA.[28] FREDOM has lower temporal resolution, but reveals the tumor heterogeneity and differential response of regions exhibiting diverse baseline pO_2. The results here correspond closely with more extensive observation.[5,8,25] While FREDOM currently requires 6.5 min per pO_2 map, we have previously demonstrated an alternative data acquisition protocol achieving 1 s time resolution in a perfused heart, albeit providing less precision in measurements and only a global determination.[29] Such an approach could allow us to measure global $\Delta[HbO_2]$ and global pO_2 simultaneously with a high temporal resolution, understand the relationship between global $\Delta[HbO_2]$ and global pO_2, and obtain absolute values of sO_2 of the tumors as tumors grow.

In conclusion, we have refined the algorithms for calculating [Hb], $[HbO_2]$, and $[Hb_{total}]$ and measured relative $[HbO_2]$ changes in tumor vasculature and tumor tissue pO_2 under carbogen intervention using NIRS and a needle type pO_2 electrode. The pO_2 data were also supported by the ^{19}F MR pO_2 mapping. We have also developed an algorithm to estimate sO_2 values in the tumor during respiratory interventions. The NIRS data showed significant changes in vascular oxygenation accompanying respiratory interventions, and changes in tumor vascular oxygenation preceded tumor tissue pO_2. Oxygen electrode measurements and ^{19}F MR pO_2 mapping results proved that tumors are highly heterogeneous. The phantom data confirmed that normalized $[HbO_2]$ data together with pO_2 measurements can be used to estimate absolute sO_2 values in a homogeneous system. For a highly heterogeneous medium, such as tumors, local comparison between the $[HbO_2]$ and pO_2 value is desired and required in order to reveal the process of oxygen delivery from the tumor vascular bed to the tumor tissues. Therefore, this study not only demonstrates that the NIRS technology can provide an efficient, real-time, noninvasive approach to monitoring tumor physiology and is complementary to other techniques, but also emphasizes the need to develop an imaging technique to study spatial heterogeneity of tumor vasculature under oxygen or other therapeutic interventions.

Acknowledgments

This work was supported in part by the Department of Defense Breast Cancer Initiative grant BC990287 (HL) and NIH RO1 CA79515 (RPM). NMR experiments were conducted at the Mary Nell & and Ralph B. Rogers MR Center, an NIH BRTP Facility no. 5-P41-RR02584. We are grateful to Dr. Britton Chance from the University of Pennsylvania for assistance with tissue phantom study and to Dr. Peter Peschke for providing the original tumor cells.

References

1. L. Gray, A. Conger, M. Ebert, S. Hornsey, and O. Scott, "The concentration of oxygen dissolved in tissues at time of irradiation as a factor in radio-therapy," *Br. J. Radiol.* **26**, 638–648 (1953).
2. J. H. Kaanders, L. A. Pop, H. A. Marres, J. Liefers, F. J. van den Hoogen, W. A. van Daal, and A. J. van der Kogel, "Accelerated radiotherapy with carbogen and nicotinamide (ARCON) for laryngeal cancer," *Radiother. Oncol.* **48**, 115–122 (1998).
3. J. Overgaard and M. R. Horsman, "Modification of hypoxia-induced radioresistance in tumors by the use of oxygen and sensitizers," *Semin. Radiat. Oncol.* **6**, 10–21 (1996).
4. H. B. Stone, J. M. Brown, and T. Phillips, "Oxygen in human tumors: correlations between methods of measurement and response to therapy," *Radiat. Res.* **136**, 422–434 (1993).
5. D. Zhao, A. Constantinescu, E. W. Hahn, and R. P. Mason, "Tumor oxygenation dynamics with respect to growth and respiratory challenge: investigation of the Dunning prostate R3327-HI tumor," *Radiat. Res.* **156**(5), 510–520 (2001).
6. D. Cater and I. Silver, "Quantitative measurements of oxygen tension in normal tissues and in the tumors of patients before and after radiotherapy," *Acta Radiol. (1921-1962)* **53**, 233–256 (1960).
7. J. A. O'Hara, F. Goda, E. Demidenko, and H. M. Swartz, "Effect on regrowth delay in a murine tumor of scheduling split-dose irradiation based on direct pO_2 measurements by electron paramagnetic resonance oximetry," *Radiat. Res.* **150**, 549–556 (1998).
8. R. P. Mason, A. Constantinescu, S. Hunjan, D. Le, E. W. Hahn, P. P. Antich, C. Blum, and P. Peschke, "Regional tumor oxygenation and measurement of dynamic changes," *Radiat. Res.* **152**, 239–249 (1999).
9. M. S. Patterson, B. Chance, and B. C. Wilson, "Time resolved reflectance and transmittance for the non-invasive measurement of tissue optical properties," *Appl. Opt.* **28**, 2331–2336 (1986).
10. E. M. Sevick, B. Chance, J. Leigh, S. Nokia, and M. Maris, "Quantitation of time- and frequency-resolved optical spectra for the determination of tissue oxygenation," *Anal. Biochem.* **195**, 330–351 (1991).
11. H. Liu, Y. Song, K. L. Worden, X. Jiang, A. Constantinescu, and R. P. Mason, "Noninvasive investigation of blood oxygenation dynamics of tumors by near-infrared spectroscopy," *Appl. Opt.* **39**, 5231–5243 (2000).
12. W. G. Zijlstra, A. Buursma, and W. P. Meeuwsen-van der Roest, "Absorption spectra of human fetal and adult oxyhemoglobin, deoxyhemoglobin, carboxyhemoglobin, and methemoglobin," *Clin. Chem.* **37**, 1633–1638 (1991).
13. D. T. Delpy, M. Cope, P. van der Zee, S. Arridge, S. Wray, and J. Wyatt, "Estimation of optical pathlength through tissue from direct time of flight measurement," *Phys. Med. Biol.* **33**(12), 1433–1442 (1988).
14. M. Ferrari, Q. Wei, L. Carraresi, R. A. De Blasi, and G. Zaccanti, "Time-resolved spectroscopy of human forearm," *J. Photochem. Photobiol.* **16**, 141–153 (1992).
15. P. van der Zee, M. Cope, S. R. Arridge, M. Essenpreis, L. A. Potter,

A. D. Edwards, J. S. Wyatt, D. C. McCormick, S. C. Roth, E. O. R. Reynolds, and D. T. Delpy, "Experimentally measured optical pathlengths for the adult head, calf and forearm and the head of the newborn infants as a function of inter optode spacing," *Adv. Exp. Med. Biol.* **316**, 143–153 (1992).

16. R. G. Steen, K. Kitagishi, and K. Morgan, "*In vivo* measurement of tumor blood oxygenation by near-infrared spectroscopy: immediate effects of pentobarbital overdose or carmustine treatment," *J. Neuro-Oncol.* **22**, 209–220 (1994).
17. H. Liu, "Unified analysis of the sensitivities of reflectance and path length to scattering variations in a diffusive medium," *Appl. Opt.* **40**(10), 1742–1746 (2001).
18. E. L. Hull, D. L. Conover, and T. H. Foster, "Carbogen-induced changes in rat mammary tumour oxygenation reported by near infrared spectroscopy," *British J. Cancer* **79**(11/12), 1709–1716 (1999).
19. R. L. Fournier, "Oxygen transport in biological systems," Chap. 4 in *Basic Transport Phenomena in Biomedical Engineering*, pp. 87–94, Taylor & Francis, Lillington (1999).
20. P. Peschke, E. W. Hahn, F. Lohr, F. Brauschweig, G. Wolber, I. Zuna, and M. Wannenmacher, "Differential sensitivity of three sublines of the rat Dunning prostate tumor system R3327 to radiation and/or local tumor hyperthermia," *Radiat. Res.* **150**, 423–430 (1998).
21. E. W. Hahn, P. Peschke, R. P. Mason, E. E. Babcock, and P. P. Antich, "Isolated tumor growth in a surgically formed skin pedicle in the rat: a new tumor model for NMR studies," *Magn. Reson. Imaging* **11**, 1007–1017 (1993).
22. Y. Yang, H. Liu, X. Li, and B. Chance, "Low-cost frequency-domain photon migration instrument for tissue spectroscopy, oximetry, and imaging," *Opt. Eng.* **36**, 1562–1569 (1997).
23. M. H. Friedman, "Gas transport," Chap. 9 in *Principles and Models of Biological Transport*, pp. 240–242, Springer, Berlin Heidelberg (1986).
24. H. Liu, A. H. Hielscher, F. K. Tittel, S. L. Jacques, and B. Chance, "Influence of blood vessels on the measurement of hemoglobin oxygenation as determined by time-resolved reflectance spectroscopy," *Med. Physics* **22**, 1209–1217 (1995).
25. S. Hunjan, D. Zhao, A. Constantinescu, E. W. Hahn, P. Antich, and R. P. Mason, "Tumor oximetry: demonstration of an enhanced dynamic mapping procedure using fluorine-19 echo planar magnetic resonance imaging in the dunning prostate R3327-AT1 rat tumor," *Int. J. Radiat. Oncol., Biol., Phys.* **49**, 1097–1108 (2001).
26. B. R. Barker, R. P. Mason, N. Bansal, and R. M. Peshock, "Oxygen tension mapping by ^{19}F echo planar NMR imaging of sequestered perfluorocarbon," *JMRI* **4**, 595–602 (1994).
27. S. I. Fox, "Respiratory physiology," Chap. 16 in *Human Physiology*, pp. 508–513, McGraw-Hill, Boston (1999).
28. G. Brix, J. Debus, M. Mueller-Schimpfle, P. Peschke, P. Huber, H. J. Zabel, and W. Lorenz, "MR-tomographische Quantifizierung struktureller und funktioneller Gewebeveraenderungen an stosswellentherapierten Dunning-Prostata-Tumoren," *Z. Med. Phys.* **3**, 76–82 (1993).
29. R. P. Mason, F. M. H. Jeffrey, C. R. Malloy, E. E. Babcock, and P. P. Antich, "A noninvasive assessment of myocardial oxygen tension: ^{19}F NMR spectroscopy of sequestered perfluorocarbon emulsion," *Magn. Reson. Med.* **27**, 310–317 (1992).

Dynamic response of breast tumor oxygenation to hyperoxic respiratory challenge monitored with three oxygen-sensitive parameters

Yueqing Gu, Vincent A. Bourke, Jae G. Kim, Anca Constantinescu, Ralph P. Mason, and Hanli Liu

The simultaneous measurement of three oxygen-sensitive parameters [arterial hemoglobin oxygen saturation (SaO_2), tumor vascular-oxygenated hemoglobin concentration ([HbO_2]), and tumor oxygen tension (pO_2)] in response to hyperoxic respiratory challenge is demonstrated in rat breast tumors. The effects of two hyperoxic gases [oxygen and carbogen (5% CO_2 and 95% O_2)] were compared, by use of two groups of Fisher rats with subcutaneous 13762NF breast tumors implanted in pedicles on the foreback. Two different gas-inhalation sequences were compared, i.e., air–carbogen–air–oxygen–air and air–oxygen–air–carbogen–air. The results demonstrate that both of the inhaled, hyperoxic gases significantly improved the tumor oxygen status. All three parameters displayed similar dynamic response to hyperoxic gas interventions, but with different response times: the fastest for arterial SaO_2, followed by biphasic changes in tumor vascular [HbO_2], and then delayed responses for pO_2. Both of the gases induced similar changes in vascular oxygenation and regional tissue pO_2 in the rat tumors, and changes in [HbO_2] and mean pO_2 showed a linear correlation with large standard deviations, which presumably results from global versus local measurements. Indeed, the pO_2 data revealed heterogeneous regional response to hyperoxic interventions. Although preliminary near-infrared measurements had been demonstrated previously in this model, the addition of the pO_2 optical fiber probes provides a link between the noninvasive relative measurements of vascular phenomena based on endogenous reporter molecules, with the quantitative, albeit, invasive pO_2 determinations. © 2003 Optical Society of America

OCIS codes: 170.1470, 170.3660, 170.4580, 120.3890, 120.1880, 230.2090.

1. Introduction

It is widely recognized that hypoxic regions in solid tumors may limit the efficacy of nonsurgical therapy, including radiotherapy, photodynamic therapy, and chemotherapy.[1–4] Many adjuvant interventions have been tested, including simple strategies such as breathing hyperoxic gases.[5–7] However, a meta-analysis of some 10,000 patients showed only a modest benefit, and this benefit was restricted to specific tumor types.[8] It is thought that the failure of such interventions was largely due to the inability to identify those patients who would benefit. Indeed, there is growing emphasis on tailoring therapy to the individual characteristics of each patient's tumor. Furthermore, carbogen (5% CO_2 and 95% O_2) and oxygen have been used on experimental tumors in animals as well as on clinical trials in patients for many years.[9,10] But the therapeutic benefits of the two kinds of respiratory hyperoxic gases are diverse, depending on the tumor types and individuals.[11–13] Accordingly, accurate assessment of tumor oxygenation at various stages of tumor growth and in response to interventions may provide a better understanding of tumor development and may serve as a prognostic indicator for treatment outcome, potentially allowing therapy to be tailored to individual characteristics.

Various techniques have been developed to measure oxygen tension (pO_2) or vascular oxygenation of tumors.[14] Many methods are invasive, and those requiring biopsy preclude dynamic investigations. Optical techniques based on light absorption of endogenous chromophores, e.g., near-infrared (NIR)

Y. Gu, J. G. Kim, and H. Liu (Hanli@uta.edu) are with the Biomedical Engineering Program, The University of Texas at Arlington, Arlington, Texas 76019. V. A. Bourke, A. Constantinescu, and R. P. Mason are with the Department of Radiology, University of Texas Southwestern Medical Center, Dallas, Texas 75390.

Received 8 September 2002; revised manuscript received 15 January 2003.
0003-6935/03/162960-08$15.00/0
© 2003 Optical Society of America

spectroscopy of oxygenated and deoxygenated hemoglobin, are entirely noninvasive and allow real-time monitoring of tumor vascular oxygenation.[15–17] However, NIR has limited spatial resolution, and it remains to be determined whether vascular oxygenation is related to therapeutic outcome. Hitherto, quantitative pO_2 has been shown to have prognostic value,[18–21] but pO_2 represents a balance between oxygen delivery and consumption. Thus, we seek to explore the interplay of vascular and tissue oxygenation. Electrodes have been used widely to study tumor oxygen dynamics with respect to interventions,[22–24] but they are generally limited to a single location and small probes can be fragile. We have ourselves recently shown a correlation between pO_2 and ΔHbO_2 in some tumors, but we noted distinct heterogeneity, and thus, the global NIR measurements were not always related to local pO_2.[25] Multiple fiber-optic probes may be inserted into a tumor,[26–28] and we have now investigated correlation between NIR measurements and multiple (three) simultaneous pO_2 measurements.

We now report simultaneous measurements of three oxygen-related parameters, i.e., arterial hemoglobin oxygen saturation, SaO_2; tumor oxygenated hemoglobin concentration, $[HbO_2]$; and tumor oxygen tension, pO_2, to assess dynamic responses of rat breast tumors to hyperoxic gases. Changes in tumor vascular $[HbO_2]$ were measured by NIR spectroscopy (NIRS) using a photon-migration, frequency-domain device; changes in regional pO_2 were monitored by a fluorescence-quenched, oxygen-sensing, fiber-optic system (FOXY); the arterial SaO_2 values were recorded with a fiber-based, pulse oximeter.

2. Materials and Methods

A. Near-Infrared Spectroscopy System for Measurement of Changes in $[HbO_2]$

NIR light (700 to 900 nm) has considerable tissue penetration depth (several centimeters) and permits *in vivo* sampling of large tissue volumes (e.g., human breast, brain, skeletal muscle, or tumors), since photon transport in tissue is dominated by scattering rather than by absorption. Absorption of NIR light by the oxygenated and the deoxygenated hemoglobin chromophores may be used to determine hemoglobin oxygenation and blood concentration changes. As described in detail previously,[16,25] a homodyne frequency-domain system (NIM, Philadelphia, Pennsylvania) was used to monitor the global changes in oxygenated and deoxygenated hemoglobin concentrations, $\Delta[HbO_2]$ and $\Delta[Hb]$, respectively, in rat breast tumors in response to variations in inhaled gas. Briefly, the light from two NIR laser diodes (758 nm and 785 nm) was coupled into a bifurcated fiber bundle and illuminated on the tumor, and the transmitted light was collected and propagated to a photomultiplier tube (Fig. 1). The fiber bundles were placed on the surface of the tumors in a transmittance mode parallel to the body of the rat. The fiber tips touched firmly on the skin (without compression) in the middle parts of the tumors, providing optimal geometry to interrogate deep tumor tissue.

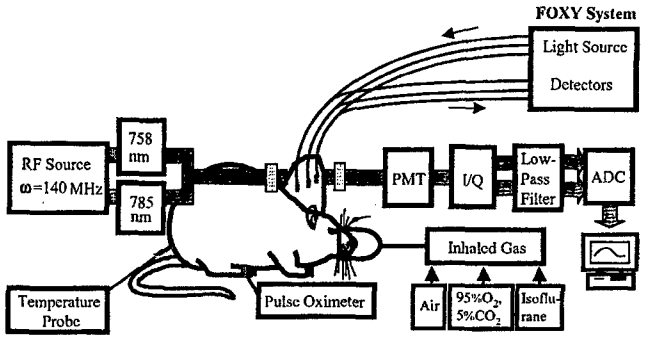

Fig. 1. Experimental setup for simultaneous oximetry. The 3-mm-diameter fiber bundles of the NIRS system deliver and detect the laser light through the tumor in transmittance geometry. PMT represents a photomultiplier tube. I/Q is an in-phase and quadrature phase demodulator for retrieving amplitude and phase information. The FOXY system comprises three fiber-optic oxygen-sensing probes that are inserted into different regions of the tumor. The pulse oximeter probe is placed on the hind foot of the rat.

Based on modified Beer–Lambert's law,[29] changes in oxygenated and deoxygenated hemoglobin concentrations, $\Delta[HbO_2]$ and $\Delta[Hb]$, due to respiratory intervention were derived from the measured amplitudes at the two wavelengths and calculated with the following equations[25]:

$$\Delta[HbO_2] = \frac{-10.63 \log\left(\frac{A_B}{A_T}\right)^{758} + 14.97 \log\left(\frac{A_B}{A_T}\right)^{785}}{d}, \quad (1)$$

$$\Delta[Hb] = \frac{8.95 \log\left(\frac{A_B}{A_T}\right)^{758} - 6.73 \log\left(\frac{A_B}{A_T}\right)^{785}}{d}, \quad (2)$$

where A_B and A_T are the baseline and transient amplitudes measured from the NIR system, respectively; d is the source–detector separation; the unit for both $\Delta[HbO_2]$ and $\Delta[Hb]$ is millimolar per differential path-length factor (DPF); and the DPF is for tumor tissues. As demonstrated in our previous study, normalization of $\Delta[HbO_2]$ and $\Delta[Hb]$ to their maximal values can eliminate the effects of d and DPF on the results.[25]

B. Fiber-Optic Oxygen-Sensing System for Measurement of Changes in pO_2

Regional pO_2 in tumors was monitored with a multichannel, fiber-optic, oxygen-sensing system (FOXY, Ocean Optics, Inc., Dunedin, Florida).[30] Three fluorescence-quenched, optical fiber probes (AL300, tip diameter 410 μm) were inserted into different regions of the tumors (Fig. 1). Probes were positioned so that at least one was in a poorly oxygenated region (low baseline pO_2) and at least one in a well-oxygenated region (high baseline pO_2). If necessary,

the probes were gently moved through the tumor until such diverse regions were located. In some cases, the mean pO_2 derived from the three individual measurements is presented. Although this is a commercial system, few details have been published previously,[31] and no applications to *in vivo* tumor oximetry have been published to our knowledge. Light from a pulsed blue LED (475 nm) was coupled into one branch of a bifurcated optical fiber bundle and propagated to the probe tip. The distal end of the probe is coated with a thin layer of a hydrophobic solgel material, where an oxygen-sensing ruthenium complex is effectively trapped. Illumination of the ruthenium complex causes fluorescence at ~600 nm. If the excited ruthenium complex encounters an oxygen molecule, the excess energy is transferred to the oxygen molecule in a nonradiative transition, decreasing or quenching the fluorescence signal. The degree of quenching correlates with the oxygen concentration, and hence, pO_2.

The fluorescence response of the ruthenium crystal complex is highly temperature dependent, so to accomplish probe calibration it was necessary to stream gases of known oxygen concentrations (100%, 20.9%, 10%, 2%, and 0%) through a cylindrical water jacket heated to 37 °C. Calibration curves were automatically calculated by means of the vendor-supplied software, with the second-order, polynomial calibration:

$$\frac{I_0}{I} = 1 + K_1[O] + K_2[O]^2 \tag{3}$$

where, I_0 is the fluorescence intensity at zero oxygen concentration (nitrogen), I is the measured intensity of fluorescence at a pressure of oxygen, $[O]$ represents the oxygen concentration (related to pO_2), K_1 and K_2 are the first- and the second-order coefficients and are automatically supplied by the curve-fitting routine from the calibration measurements.

C. Pulse Oximeter for Measurement of Arterial S_aO_2

Arterial SaO_2 of the breast-tumor-bearing rats was also monitored with a fiber-optic pulse oximeter (Nonin Medical, Inc., Plymouth, Minnesota) placed on the hind foot of the rats. The system consisted of two optical fibers used for delivering and receiving the light. The tips were placed on either side of the foot in transmission mode.

D. Animal Model

Mammary adenocarcinomas 13762NF (originally obtained from the Division of Cancer Therapeutics, NIH, Bethesda, Maryland) were implanted in skin pedicles[32] on the foreback of adult female Fisher 344 rats (~150 g). Once the tumors reached 1–2 cm diameter, rats were anesthetized with 150-μl ketamine hydrochloride (100 mg/ml, i.p.) and maintained under general gaseous anesthesia with 1.3% isoflurane in air (1 dm^3/min). Body temperature was maintained at 37 °C by a warm water blanket. Tumors were shaved to improve optical contact for transmitting NIR light. The tumor diameters along the three major orthogonal axes (a, b, c) were measured with calipers and volume estimated with an ellipsoid approximation with the formula: $V = (\pi/6)(abc)$.

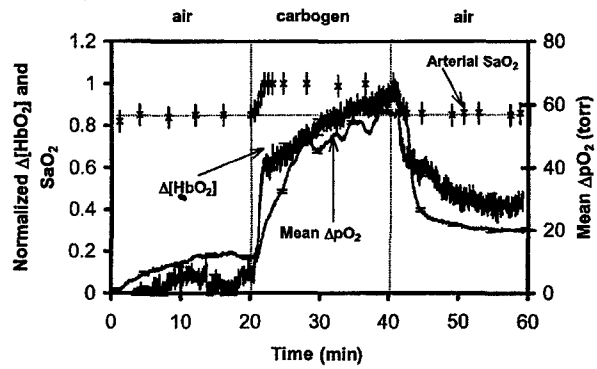

Fig. 2. Time profile of the three oxygen-sensitive parameters, i.e., the normalized changes of tumor $\Delta[HbO_2]$, the mean changes of tumor ΔpO_2, and the arterial SaO_2 with respect to carbogen breathing in a representative 13762NF rat breast tumor (No. 1, 3.2 cm^3).

Two groups of rats ($n = 7$ in each group) were used to compare the effects of carbogen and oxygen on vascular oxygenation of breast tumors. Group 1 experienced the gas-inhalation sequence of air–carbogen–air–oxygen–air. Group 2 was exposed to the reverse sequence of air–oxygen–air–carbogen–air. Each gas was maintained for 20 min. In addition, the FOXY pO_2 probes were applied to five rats from Group 1, and the dynamics of the three oxygen-related parameters were measured simultaneously.

3. Results

A. Dynamic Responses of Three Oxygen-Related Parameters to Carbogen Intervention

Typical time profiles of the normalized $\Delta[HbO_2]$, mean ΔpO_2, and SaO_2 in response to carbogen intervention are shown for a representative 13762NF breast tumor (No. 1, 3.2 cm^3) in Fig. 2. When the inspired gas was switched from air to carbogen, the SaO_2 readings increased rapidly and significantly from the baseline value of 85% to the maximum of 100% within 2.5 minutes ($p < 0.0001$). The normalized $\Delta[HbO_2]$ showed a sharp initial rise in the first minute ($p < 0.0001$) followed by a slower, gradual, but further significant increase over the next 19 min ($p < 0.001$). Mean ΔpO_2 increased rapidly by approximately 50 Torr within 8 min ($p < 0.0005$) and also continued a slower and gradual increase over the next 12 min ($p < 0.005$). Return to breathing air produced a significant decline for all three signals ($p < 0.0001$).

SaO_2 and pO_2 displayed a single-phase dynamic behavior in response to carbogen intervention, whereas $\Delta[HbO_2]$ showed an apparent biphasic response. These dynamics may be characterized by time constants of a single-exponential response. For the tumor in Fig. 3, SaO_2 had the fastest response, with a time constant of $\tau(SaO_2) = 1.1 \pm 0.2$ min ($R =$

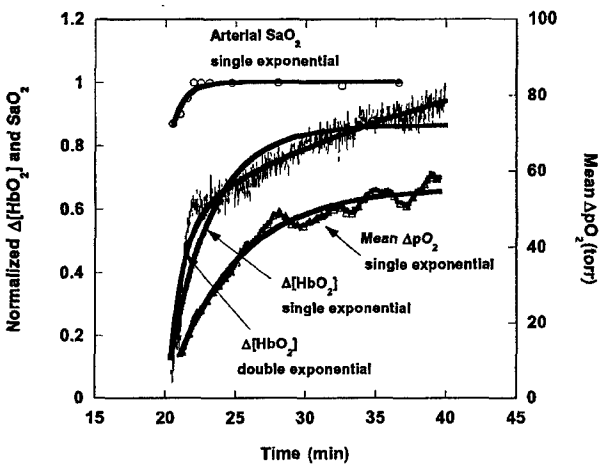

Fig. 3. Dynamic responses of the three oxygen-sensitive parameters to carbogen intervention in a rat breast tumor (No. 1, 3.2 cm^3). Single-exponential curve fitting yielded $SaO_2 = 0.204\{1 - \exp[-(t - 20.02)/1.1]\} + 0.85$ ($R = 0.93$), $\Delta[HbO_2] = 0.655\{1 - \exp[-(t - 20.36)/2.59]\} + 0.125$ ($R = 0.89$), and $\Delta pO_2 = 42.68\{1 - \exp[-(t - 21.01)/4.56]\} + 16.66$ ($R = 0.98$); biexponential fitting resulted in $\Delta[HbO_2] = 0.373\{1 - \exp[-(t - 20.36)/0.61]\} + 0.648\{1 - \exp[-(t - 20.36)/21]\}$ ($R = 0.97$).

0.93), followed by $[HbO_2]$ with $\tau(\Delta[HbO_2]) = 2.59 \pm 0.06$ min ($R = 0.89$), whereas ΔpO_2 yielded the slowest response $\tau(\Delta pO_2) = 4.56 \pm 0.06$ min ($R = 0.98$). Time constants for Group 1 are listed in Table 1. In every case $\tau(SaO_2) < \tau(\Delta[HbO_2]) < \tau(\Delta pO_2)$, based on the single-exponential fitting. No apparent relation between the time constant and the tumor volume was observed.

It is clear that the response of ΔHbO_2 is not well represented by a single exponential, and thus, a double-exponential expression with two time constants, τ_1 and τ_2, was also used (Fig. 3). Comparison between the biexponential fitting for $\Delta[HbO_2]$ and the single-exponential results for both SaO_2 and ΔpO_2 in the first five rat tumors (Table 1) shows that the time constants of SaO_2 (~1.2 ± 0.4 min) are similar to those of the first phase of $\Delta[HbO_2]$ (~0.5 ± 0.2 min), whereas the second phase is longer and highly variable (~14 ± 11 min). No significant correlations were found between any of the time constants in Table 1.

Time delay, t_d, between the time when the gas intervention was initiated and the time when the changes in signals were detected, reveals another difference among the three oxygen-sensitive parameters. For tumor 1 (Fig. 2), the SaO_2 signal was the first to respond to the intervention. Change in $\Delta[HbO_2]$ was observed 30 s later with $t_d = 30$ s, followed by changes in ΔpO_2 another 30 s later ($t_d = 60$ s). Similarly, when the gas was returned from carbogen to air, the SaO_2 signal decreased immediately, followed by declines in $\Delta[HbO_2]$ and in ΔpO_2 with t_d of 30 and 120 s later, respectively. As expected, changes in SaO_2 always preceded ΔHbO_2, and ΔpO_2 occurred last for all tumors.

B. Comparison of the Effects of Carbogen and Oxygen Intervention on Tumor Oxygenation

Switching from air breathing to carbogen or oxygen produced similar changes in ΔHbO_2 [Fig. 4(a)]. However, the time course was substantially different, requiring a biphasic exponential fit for carbogen, but a single exponential for oxygen [Fig. 4(b)]. For the seven tumors in Group 1, there was no significant difference ($p > 0.3$) in the maximum magnitude of $\Delta[HbO_2]$ caused by carbogen or oxygen interventions [Fig. 4(c)].

To examine the possible effect of preconditioning required that Group 2 experience a reversed gas intervention, with exposure to oxygen prior to carbogen [Fig. 5(a)]. In this case, the time constants of the normalized tumor vascular $\Delta[HbO_2]$ were now similar for both gas challenges: indeed, for six of seven tumors, carbogen no longer induced the biphasic behavior. Figure 5(b) shows that changes in $(\Delta HbO_2)_{max}$ were similar to those in Group 1, and again, the two gases did not produce significantly different response in $(\Delta HbO_2)_{max}$. This is emphasized for both Groups 1 and 2 by a strong linear correlation (slope ≅ 1.16) between the $\Delta[HbO_2]_{max}$ values observed in response to each of the two con-

Table 1. Time Constants of SaO_2, $\Delta[HbO_2]$, and ΔpO_2 Response to Carbogen and Oxygen Intervention in the Breast Tumors[a]

Breast Tumors	Single-Exponential Fitting of SaO_2, $\Delta[HbO_2]$ and ΔpO_2 (Carbogen Intervention)						Double-Exponential Fitting for $\Delta[HbO_2]$ (Carbogen Intervention)			Single-Exponential Fitting of $\Delta[HbO_2]$ (O_2 Intervention)	
	SaO_2		$\Delta[HbO_2]$		ΔpO_2						
Volume (cm^3)	τ (min)	R	τ (min)	R	τ (min)	R	$\tau 1$ (min)	$\tau 2$ (min)	R	τ (min)	R
No. 1 (3.2)	1.1 ± 0.2	0.93	2.59 ± 0.06	0.89	4.56 ± 0.04	0.98	0.61 ± 0.03	21 ± 3	0.97	0.35 ± 0.01	0.92
No. 2 (3.0)	1.6 ± 0.2	0.98	3.40 ± 0.07	0.91	4.6 ± 0.1	0.82	0.62 ± 0.06	11 ± 1	0.96	0.51 ± 0.01	0.91
No. 3 (4.6)	1.2 ± 0.2	0.97	2.12 ± 0.06	0.76	2.26 ± 0.02	0.98	0.6 ± 0.1	37 ± 3	0.96	1.52 ± 0.02	0.89
No. 4 (2.6)	1.9 ± 0.3	0.98	2.68 ± 0.05	0.93	3.5 ± 0.1	0.86	0.12 ± 0.02	5.2 ± 0.1	0.98	1.71 ± 0.03	0.94
No. 5 (5.6)	0.8 ± 0.2	0.91	2.68 ± 0.05	0.74	4.51 ± 0.02	0.99	0.17 ± 0.03	12.5 ± 0.6	0.99	5.49 ± 0.03	0.98
No. 6 (1.9)	0.9 ± 0.2	0.81	1.62 ± 0.01	0.95	nd	/	0.63 ± 0.08	2.3 ± 0.1	0.96	5.16 ± 0.06	0.93
No. 7 (0.72)	1.0 ± 0.5	0.95	3.60 ± 0.03	0.93	nd	/	0.61 ± 0.02	10.5 ± 0.3	0.98	3.54 ± 0.03	0.95
Mean	1.2 ± 0.4		2.7 ± 0.6		4 ± 1		0.5 ± 0.2	14 ± 11		2.5 ± 2	

[a]Under the inhalation sequence of air–carbogen–air–oxygen–air.
[b]nd, not determined.

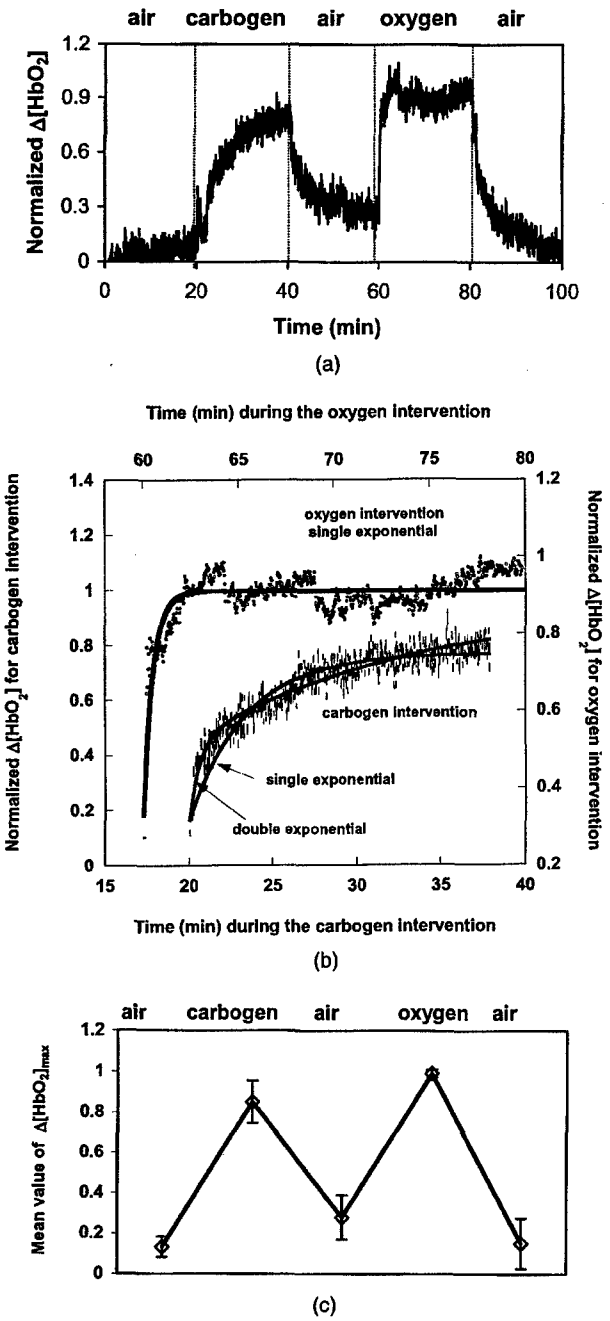

Fig. 4. (a) Time course of changes in tumor vascular $\Delta[HbO_2]$ for a representative 13762NF breast tumor from Group 1 (No. 2, 3.0 cm^3) with respect to altering inhaled gas. (b) Respective curve fits for the carbogen and oxygen interventions. (c) Average maximum values of normalized $\Delta[HbO_2]$ for the seven breast tumors in Group 1.

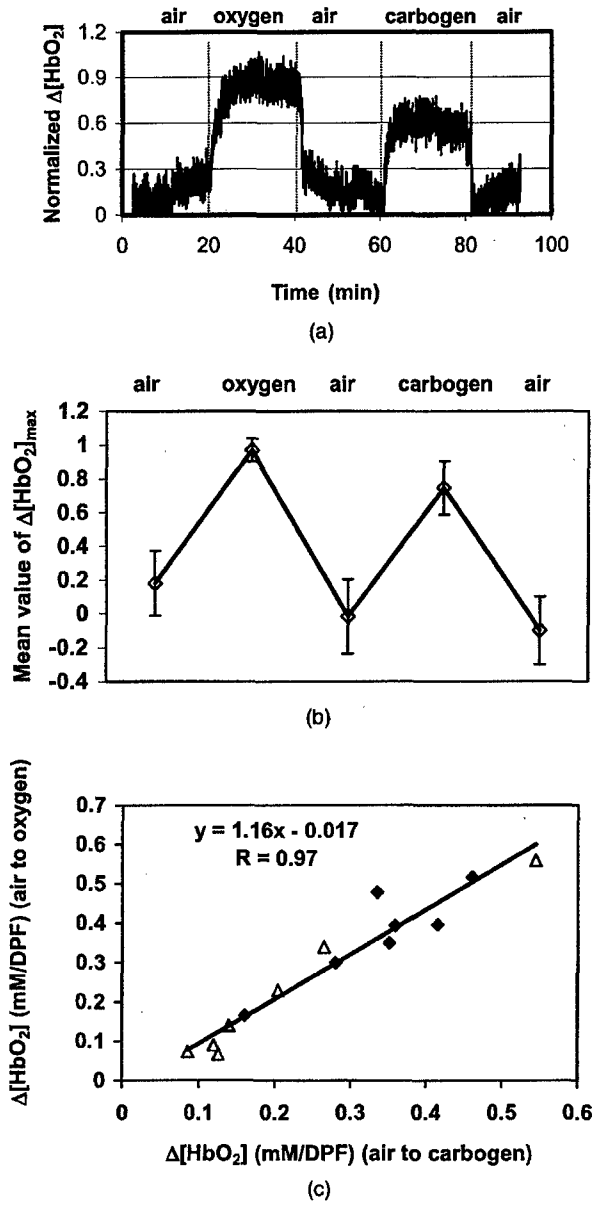

Fig. 5. (a) Dynamic changes in tumor vascular $\Delta[HbO_2]$ for a representative 13762NF breast tumor from Group 2 (No. 9, 2.6 cm^3) with gas-inhalation sequence reversed compared with Group 1. (b) Average maximum values of normalized $\Delta[HbO_2]$ for Group 2. Gas-inhalation sequence reversed compared with Group 1. (c) Correlation between maximum $\Delta[HbO_2]$ achieved with carbogen inhalation versus that with oxygen ($R = 0.97$): ◆, carbogen first; △, oxygen first.

secutive interventions [Fig. 5(c)]. In this case, nonnormalized data are shown for specific comparison of the absolute $\Delta[HbO_2]_{max}$ produced by oxygen and carbogen for each of the tumors.

C. Tumor pO_2

The FOXY pO_2 probes generally indicated distinct heterogeneity in pO_2. Moreover, response to the hyperoxic gas was diverse: those probes that indicated apparently well-oxygenated regions usually showed a large and rapid response, whereas those with lower baseline pO_2 often showed little change [Fig. 6(a)]. The pO_2 responses to the two interventions showed a highly consistent behavior at each individual location [Fig. 6(b)]. There was also a distinct correlation between the global NIR measurements and the mean ΔpO_2 (Fig. 7). Because of heterogeneity in regional pO_2, the standard deviations of the mean pO_2 values were large.

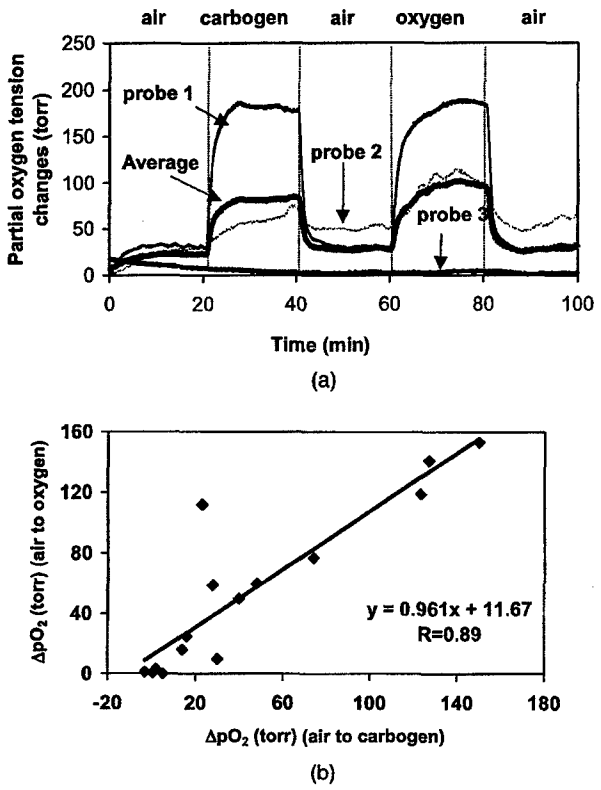

Fig. 6. (a) Time profiles of tumor ΔpO_2, measured with the three channels of the FOXY fiber-optic, oxygen-sensing system with respect to different gas inhalations for breast tumor No. 3 (4.6 cm^3). The mean signal for the three channels was calculated and is plotted by the thicker trace. (b) Correlation between ΔpO_2 at individual locations in the tumors in response to carbogen or oxygen for the five tumors in Group 1 ($R > 0.8$).

4. Discussion

In this study, we have simultaneously measured the arterial SaO_2, the global changes in the $\Delta[HbO_2]$ of tumor vasculature, and the regional changes in the ΔpO_2 of tumor tissue, in response to hyperoxic (i.e., carbogen and oxygen) gas interventions with a pulse oximeter, an NIRS system and a multichannel, fiber-optic, oxygen-sensing system, respectively. All three oxygen-sensitive indicators displayed similar dynamic tendency in response to carbogen intervention (Fig. 2).

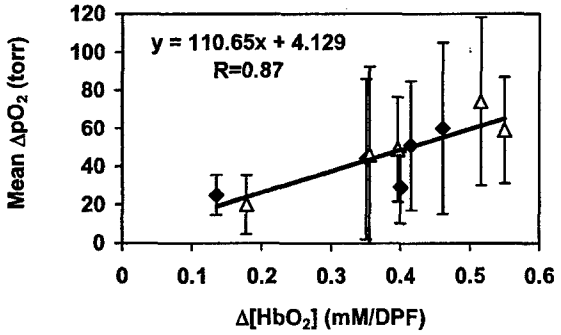

Fig. 7. Correlation between mean ΔpO_2 and $\Delta[HbO_2]$ for the five breast tumors ($R > 0.86$): ◆, transition from air to carbogen; △, transition from air to oxygen.

The simultaneous measurements demonstrate the compatibility of the NIRS system with the FOXY fiber-optic oxygen-sensing system, without interference. Both systems are relatively inexpensive and provide real-time measurements, but the multichannel FOXY fiber-optic system monitors ΔpO_2 in specific locations, whereas the NIRS system provides global measurements. Whether ΔHbO_2 determined with this methodology will be a clinically useful predictor for tumor response to oxygen-dependent interventions and therapies remains to be determined. However, it is established that measurements of pO_2 have prognostic value in the clinic[18,20] so that correlations between pO_2 and NIR measurements would be very important.

We have previously applied a polarographic oxygen electrode simultaneously with NIR.[25] However, that study provided only a single local pO_2 value, and in some cases correlations with global NIR measurements were very poor. The optical fiber system used here allows multiple locations to be interrogated simultaneously. The device can be expanded to many channels, but our system uses four channels. Unfortunately, probes are fragile, and the oxygen-sensitive coating on the tips is readily damaged. Thus, we only had three probes available for this study. Indeed, fiber-optic probe fragility is a well-recognized problem, and our previous experience with the more expensive OxyLite system was also restricted to three channels owing to probe damage.[26]

The FOXY system (~$13k) is much less expensive than the OxyLite (~$48k), and its mode of action is also simpler, detecting fluorescent signal intensity rather than fluorescence lifetime. It seems capable of measuring pO_2 across the whole range of atmospheric oxygen tensions (0–760 Torr), whereas the OxyLite is restricted and becomes very insensitive above approximately 100 Torr. However, our experience shows that although the FOXY system provides precise measurements of ΔpO_2, absolute values of pO_2 may not be reliable. We continue to perform validation experiments. By contrast, the OxyLite system seems to give very accurate pO_2 values.

Our experience shows that the FOXY probes are much easier to use than electrodes, particularly, in terms of calibration and stability. Since the probes are fragile, we insert them into tumors through a fine needle (25 gauge), which readily punctures the surrounding skin and penetrates tough fibrous tissues. The needle is then backed up from the tip to facilitate measurements. The probes often require a few minutes to settle at a stable baseline value, but then show good baseline stability and rapid response to interventions [Figs. 2 and 6(a)]. They are easily moved within the tumor to locate regions, presenting a particular pO_2 of interest, e.g. hypoxic or well oxygenated. In the search for appropriate locations, probes are moved forward to interrogate fresh tissues rather than in reverse, since blood may pool in the tracks owing to vascular damage. However, we observe

minimal bleeding on removal of the probes from the tumors.

We have found no interference between the NIR and FOXY instruments, although any tumor motion associated with moving the fiber probes can alter the optical contact of the NIR optrodes, and thus, alter apparent ΔHbO_2. Thus, baseline ΔHbO_2 is determined once the fiber probes are situated. New fiber-optic probes of the FOXY system have a thick coating of fluorescent gel and a black covering, but this wears with use and gradually allows reception of the NIR light. Since the LEDs of the two systems operate at very different wavelengths, viz. 475 versus 760 nm, there is no interference for detection. The detection of local NIR light by the FOXY probe opens the exciting possibility of detecting regional hemoglobin oxygen saturation. We believe the FOXY optical probes could be moved within the tumor to map the distribution and path of the transmitted NIR light, helping to explore and validate the optical characteristics of the tumor. This can simultaneously provide a correlation between local ΔHbO_2 and ΔpO_2.

In this study, we have examined a much larger group of rats than previously.[16,25] We have now shown rigorously that the two hyperoxic gases induce similar changes in vascular oxygenation (NIR) and regional tissue pO_2 (FOXY) in this type of rat breast tumor. These data are consistent with our previous observations using ^{19}F NMR imaging (FREDOM)[33] in this tumor type and also in rat prostate tumors.[34,35] If the two gases are indeed equivalent in terms of manipulation of tumor oxygenation, it could have great therapeutic benefit since the popular carbogen, which is in use in clinical trials,[36] can cause respiratory discomfort.

The current data show that ΔHbO_2 and ΔpO_2 are correlated (Fig. 7), and thus, such noninvasive observations could have value in the clinic. The major deficiency in our current NIR approach is lack of spatial discrimination, and thus efforts to implement NIR imaging will be of great value. It will also be interesting to correlate other measurements, such as blood-oxygen-level-dependent (BOLD) proton magnetic resonance imaging, which provide high spatial resolution, but which are sensitive to vascular flow and volume as well as oxygenation.[37]

The biphasic response of ΔHbO_2 to carbogen is intriguing, and we believe it represents the distinct vascular compartments of arterioles (high flow) and capillaries. However, the change to monophasic behavior, when carbogen is administered second, requires further exploration; in the future, we propose to test various concentrations of oxygen and carbon dioxide and air to separate the components of the response. The carbogen dioxide component of carbogen is known to be vasoactive; however, the specific effects may depend on tumor type, site of growth, and other factors.[9,38]

In terms of vascular oxygen delivery, the data in Table 1 reveal the progressive movement of oxygen: t_d (SaO_2) < t_d ($\Delta[HbO_2]$) < t_d (ΔpO_2). As expected, switching to hyperoxic gas caused the systemic arterial SaO_2 to increase, as a result of the immediate combination of deoxyhemoglobin with oxygen. The highly oxygenated blood circulated in the systemic vasculature of the rats (including the capillary bed of the tumor tissue), resulting in a delayed increase in $[HbO_2]$ in the tumor vasculature, and led to an unloading of oxygen to the tumor tissue. For the biexponential model of $\Delta[HbO_2]$, the fast component has a similar time constant to the SaO_2 measured with the pulse oximeter on the hind leg, strongly suggesting that it represents arteriolar oxygenation in the tumor. In this study, tumor volumes do not show any direct relation with time constants or changes of amplitude in response to hyperoxic gas interventions.

It is increasingly evident that oxygen and hypoxia play important roles in tumor development and response to therapy.[18] NIR offers an attractive noninvasive means of investigating tumor oxygenation, particularly in terms of dynamic response to interventions, but we had previously shown a potential mismatch between global ΔHbO_2 and local ΔpO_2.[25] The data presented here indicate a correlation between the global NIR measurements and mean pO_2 values with even as few as three representative locations per tumor. This does suggest that it will be important to develop regional NIR measurements and that even relatively crude mapping could reveal heterogeneity. In the meantime, we believe these studies provide further evidence for the value of NIRS to explore tumor physiology.

This study was supported in part by the Department of Defense Breast Cancer Research grants BC000833 (YG) and BC990287 (HL), and NIH RO1 CA79515 (RPM) and RO1 supplement CA79515-S (VB). We are grateful to Mengna Xia and Dawen Zhao for their assistance with data processing. We gratefully acknowledge Weina Cui for helpful discussions.

References

1. R. S. Bush, R. D. T. Jenkin, W. E. C. Allt, F. A. Beale, A. J. Dembo, and J. F. Pringle, "Definitive evidence for hypoxic cells influencing cure in cancer therapy," Br. J Cancer **37**(suppl 3), 302–306 (1978).
2. E. J. Hall, *Radiobiology for the Radiologist*, 4th ed. (Lippincott, Philadelphia, Pa., 1994).
3. M. Nordsmark and J. Overgaard, "A confirmatory prognostic study on oxygenation status and loco-regional control in advanced head and neck squamous cell carcinoma treated by radiation therapy," Radiother. Oncol. **57**, 39–43 (2000).
4. O. Thews, D. K. Kelleher, and P. Vaupel, "Erythropoietin restores the anemia-induced reduction in cyclophosphamide cytotoxicity in rat tumors," Cancer Res. **61**, 1358–1361 (2001).
5. J. H. A. M. Kaanders, L. A. M. Pop, H. A. M. Marres, R. W. M. van der Maazen, A. J. van der Kogel, and W. A. J. van Daal, "Radiotherapy with carbogen breathing and nicotinamide in head and neck cancer: feasibility and toxicity," Radiother. Oncol. **37**, 190–198 (1995).
6. M. I. Saunders, P. J. Hoskin, and K. Pigott, "Accelerated radiotherapy, carbogen and nicotinamide (ARCON) in locally advanced head and neck cancer: a feasibility study," Radiother. Oncol. **45**, 159–166 (1997).
7. J. A. Kruuv, W. R. Inch, and J. A. McCredie, "Blood flow and

oxygenation of tumors in mice. I. Effects of breathing gases containing carbon dioxide at atmospheric pressure," Cancer. **20,** 51–59 (1967).
8. J. Overgaard and M. R. Horsman, "Modification of hypoxia-induced radioresistance in tumors by the use of oxygen and sensitizers," Semin. Radiat. Oncol. **6,** 10–21 (1996).
9. P. Vaupel, D. K. Kelleher, and O. Thews, "Modulation of tumor oxygenation," Int. J. Radiat. Oncol. Bio. Phys. **42,** 843–848 (1998).
10. S. Dische, "What we learnt from hyperbaric oxygen?" Radiother. Oncol. **20**(Suppl.), 71–74 (1991).
11. S. Dische, M. I. Saunders, and R. Sealy, "Carcinoma of the cervix and the use of hyperbaric oxygen with radiotherapy: a report of a randomized controlled trial," Radiother. Oncol. **53,** 93–98 (1999).
12. V. M. Laurence, R. Ward, I. F. Dennis, and N. M. Bleehen, "Carbogen breathing with nicotinamide improves the oxygen status of tumors in patients," Br. J Cancer **72,** 198–205 (1995).
13. L. Martin, E. Lartigau, and P. Weeger, "Changes in the oxygenation of head and neck tumors during carbogen breathing," Radiother. Oncol. **27,** 123–130 (1993).
14. H. B. Stone, J. M. Brown, T. Phillips, and R. M. Sutherland, "Oxygen in human tumors: correlations between methods of measurement and response to therapy," Radiat. Res. **136,** 422–434 (1993).
15. E. L. Hull, D. L. Conover, and T. H. Foster, "Carbogen induced changes in rat mammary tumor oxygenation reported by near infrared spectroscopy," Br. J. Cancer **79,** 1709–1716 (1999).
16. H. Liu, Y. Song, K. L. Worden, X. Jiang, A. Constantinescu, and R. P. Mason, "Noninvasive investigation of blood oxygenation dynamics of tumors by near-infrared spectroscopy," Appl. Opt. **39,** 5231–5243 (2000).
17. R. G. Steen, K. Kitagishi, and K. Morgan, "*In vivo* measurement of tumor blood oxygenation by near-infrared spectroscopy: immediate effects of pentobarbital overdose or carmustine treatment," J. Neuro-Oncol. **22,** 209–220 (1994).
18. M. Höckel and P. Vaupel, "Tumor hypoxia: definitions and current clinical, biologic, and molecular aspects," J. Natl. Cancer Inst. **93,** 266–276 (2001).
19. L. Gray, A. Conger, M. Ebert, S. Hornsey, and O. Scott, "The concentration of oxygen dissolved in tissues at time of irradiation as a factor in radio-therapy," Br. J. Radiol. **26,** 638–648 (1953).
20. A. W. Fyles, M. Milosevic, R. Wong, M. C. Kavanagh, M. Pintile, A. Sun, W. Chapman, W. Levin, L. Manchul, T. J. Keane, and R. P. Hill, "Oxygenation predicts radiation response and survival in patients with cervix cancer," Radiother. Oncol. **48,** 149–156 (1998).
21. D. Zhao, A. Constantinescu, E. W. Hahn, and R. P. Mason, "Measurement of tumor oxygen dynamics predicts beneficial adjuvant intervention for radiotherapy in Dunning prostate R3327-HI tumors," Radiat. Res. (to be published) (2003).
22. C. Song, I. Lee, T. Hasegawa, J. Rhee, and S. Levitt, "Increase in pO_2 and radiosensitivity of tumors by Fluosol and carbogen," Cancer Res. **47,** 442–446 (1987).
23. D. Cater and I. Silver, "Quantitative measurements of oxygen tension in normal tissues and in the tumors of patients before and after radiotherapy," Acta Radiol. **53,** 233–256 (1960).
24. D. Zhao, A. Constantinescu, E. W. Hahn, and R. P. Mason, "Differential oxygen dynamics in two diverse Dunning prostate R3327 rat tumor sublines (MAT-Lu and HI) with respect to growth and respiratory challenge," Int. J. Radiat. Oncol. Biol. Phys. **53,** 744–756 (2002).
25. J. G. Kim, Y. Song, D. Zhao, A. Constantinescu, R. P. Mason, and H. Liu, "Interplay of tumor vascular oxygenation and pO_2 in tumors using NIRS, ^{19}F MR pO_2 mapping, and pO_2 needle electrode," J. Biomed. Optics **8,** 53–62 (2003).
26. D. Zhao, A. Constantinescu, E. W. Hahn, and R. P. Mason, "Tumor oxygen dynamics with respect to growth and respiratory challenge: investigation of the Dunning prostate R3327-HI tumor," Radiat. Res. **156,** 510–520 (2001).
27. J. Bussink, J. H. A. M. Kaanders, A. M. Strik, B. Vojnovic, and A. J. van der Kogel, "Optical sensor-based oxygen tension measurements correspond with hypoxia marker binding in three human tumor xenograft lines," Radiat. Res. **154,** 547–555 (2000).
28. J. R. Griffiths, "The OxyLite: a fibre-optic oxygen sensor," Br. J. Radiol. **72,** 627–630 (1999).
29. Y. Gu, Z. Qian, J. Chen, D. Blessington, N. Ramanujam, and B. Chance, "High resolution three dimensional scanning optical image system for intrinsic and extrinsic contrast agents in tissue," Rev. Sci. Instrum. **73,** 172–178 (2002).
30. Ocean Optics Inc., Dunedin, Fla., March 2003. http://www.oceanoptics.com/products/foxysystem.asp
31. C. B. Allen, B. K. Schneider, and C. J. White, "Limitations to oxygen diffusion in *in vitro* cell exposure systems in hyperoxia and hypoxia," Am. J. Physiol. Lung Cell Molec. Physiol. **281,** L1021–L1027 (2001).
32. E. W. Hahn, P. Peschke, R. P. Mason, E. E. Babcock, and P. P. Antich, "Isolated tumor growth in a surgically formed skin pedicle in the rat: a new tumor model for NMR studies," Magn. Reson. Imaging **11,** 1007–1017 (1993).
33. Y. Song, A. Constantinescu, and R. P. Mason, "Dynamic breast tumor oximetry: the development of prognostic radiology," Technol. Cancer Res. Treat. **1,** 1–8 (2002).
34. S. Hunjan, D. Zhao, A. Constantinescu, E. W. Hahn, P. P. Antich, and R. P. Mason, "Tumor oximetry: demonstration of an enhanced dynamic mapping procedure using Fluorine-19 echo planar magnetic resonance imaging in the Dunning prostate R3327-AT1 rat tumor," Int. J. Radiat. Oncol. Biol. Phys. **49,** 1097–1108 (2001).
35. D. Zhao, A. Constantinescu, L. Jiang, E. W. Hahn, and R. P. Mason, "Prognostic radiology: quantitative assessment of tumor oxygen dynamics by MRI," Am. J. Clin. Oncol. **24,** 462–466 (2001).
36. J. H. Kaanders, J. Bussink, and van der A. J. Kogel, "ARCON: a novel biology-based approach in radiotherapy," Lancet Oncol. **3,** 728–737 (2002).
37. F. A. Howe, S. P. Robinson, L. M. Rodrigues, and J. R. Griffiths, "Flow and oxygenation dependent (FLOOD) contrast MR imaging to monitor the response of rat tumors to carbogen breathing," Magn. Reson. Imaging. **17,** 1307–1318 (1999).
38. T. J. Dunn, R. D. Braun, W. E. Rhemus, G. L. Rosner, T. W. Secomb, G. M. Tozer, D. J. Chaplin, and M. W. Dewhirst, "The effects of hyperoxic and hypercarbic gases on tumour blood flow," Br. J. Cancer **80,** 117–126 (1999).

METHODS IN ENZYMOLOGY

EDITORS-IN-CHIEF

John N. Abelson Melvin I. Simon

DIVISION OF BIOLOGY
CALIFORNIA INSTITUTE OF TECHNOLOGY
PASADENA, CALIFORNIA

FOUNDING EDITORS

Sidney P. Colowick and Nathan O. Kaplan

Methods in Enzymology

Volume 386

Imaging in Biological Research

Part B

EDITED BY

P. Michael Conn

OREGON NATIONAL PRIMATE RESEARCH CENTER
OREGON HEALTH AND SCIENCE UNIVERSITY
BEAVERTON, OREGON

ELSEVIER
ACADEMIC
PRESS

AMSTERDAM • BOSTON • HEIDELBERG • LONDON
NEW YORK • OXFORD • PARIS • SAN DIEGO
SAN FRANCISCO • SINGAPORE • SYDNEY • TOKYO

Academic Press is an imprint of Elsevier

Appendix 3

Elsevier Academic Press
525 B Street, Suite 1900, San Diego, California 92101-4495, USA
84 Theobald's Road, London WC1X 8RR, UK

This book is printed on acid-free paper. ♾

Copyright © 2004, Elsevier Inc. All Rights Reserved.

No part of this publication may be reproduced or transmitted in any form or by any means, electronic or mechanical, including photocopy, recording, or any information storage and retrieval system, without permission in writing from the Publisher.

The appearance of the code at the bottom of the first page of a chapter in this book indicates the Publisher's consent that copies of the chapter may be made for personal or internal use of specific clients. This consent is given on the condition, however, that the copier pay the stated per copy fee through the Copyright Clearance Center, Inc. (www.copyright.com), for copying beyond that permitted by Sections 107 or 108 of the U.S. Copyright Law. This consent does not extend to other kinds of copying, such as copying for general distribution, for advertising or promotional purposes, for creating new collective works, or for resale. Copy fees for pre-2004 chapters are as shown on the title pages. If no fee code appears on the title page, the copy fee is the same as for current chapters. 0076-6879/2004 $35.00

Permissions may be sought directly from Elsevier's Science & Technology Right Department in Oxford, UK: phone: (+44) 1865 843830, fax: (+44) 1865 853333, E-mail: permissions@elsevier.com.uk. You may also complete your request on-line via the Elsevier homepage (http://elsevier.com), by selecting "Customer Support" and then "Obtaining Permissions."

For all information on all Academic Press publications visit our Web site at www.academicpress.com

ISBN: 0-12-182791-7

PRINTED IN THE UNITED STATES OF AMERICA
04 05 06 07 08 9 8 7 6 5 4 3 2 1

ICP. Such processes include hydrocephalus, pseudotumor cerebri, intracranial mass lesions, and toxic–metabolic encephalopathy (where a depressed level of consciousness may or may not correspond to an increased ICP). MR–ICP measurement may prevent unnecessary invasive monitoring in an increased risk setting. Single time measurement of ICP may also be helpful in the evaluation of patients with possible ventriculoperitoneal shunt malfunction—particularly young children who present with nonspecific complaints and/or who are unable to communicate their symptoms. The MRI-based technique would limit exposure to harmful radiation from repeated CT scans. Also, a finding of normal ICP by the MRI-based method might prevent unnecessary shunt exploration.

If proven accurate and reliable, noninvasive, MRI-based measurement of intracranial compliance and pressure and TCBF may provide a valuable adjunct to the evaluation of patients with various neurologic problems. In the setting of TBI, a finding of increased ICP may provide an early warning signal for a physician to adjust therapy. This tool also may prove valuable in situations where external factors confound clinical evaluation (i.e., drug intoxication), where "coma" does not necessarily reflect an increased pressure state (i.e., diffuse axonal injury), or where coexisting medical problems make placement of an invasive monitor too dangerous (i.e., bleeding disorders). In each case, noninvasive MR–ICP measurement would enhance the array of currently available evaluation modalities, providing a novel adjunct to patient diagnosis and serial monitoring with limited expense and morbidity.

[17] Near-Infrared Spectroscopy and Imaging of Tumor Vascular Oxygenation

By Hanli Liu, Yueqing Gu, Jae G. Kim, and Ralph P. Mason

Introduction

Current Development in Optical Methods for Vascular Hemoglobin Oxygenation

In recent years, a large number of investigations have been conducted in both laboratory and clinical settings to noninvasively monitor tissue vascular oxygenation using near-infrared (NIR) spectroscopy (NIRS) and imaging. Although the NIR imaging techniques are limited by their spatial resolutions, they have a great potential to be developed as a new imaging

Copyright 2004, Elsevier Inc.
All rights reserved.
0076-6879/04 $35.00

modality because of their capabilities to provide functional images. NIR spectroscopy and imaging research has been mainly focused on two organs: (1) the brain and (2) the breast.

The NIR studies of the brain include detection of brain injury or trauma,[1] determination of cerebrovascular hemodynamics and oxygenation,[2,3] and functional brain imaging in response to a variety of neurologic activations.[4–7] NIR functional brain imaging increasingly has become of great interest in studying hemodynamic response to brain activation.[8] This is mainly because the optical signals of the NIR techniques are able to noninvasively penetrate through the scalp and skull of an adult human and are sensitive to changes in the concentration of oxygenated (HbO) and deoxygenated hemoglobin (Hb). Although it is difficult to obtain very accurate quantification of cerebral HbO and Hb concentrations from the NIR imaging techniques due to rigorous requirements of theory and boundary conditions,[9] the techniques can offer relatively accurate measurements of changes of HbO and Hb, thus providing quantitative changes in total cerebral blood volume (CBV, which is assumed to be proportional to total hemoglobin concentration, HbT, where HbT = HbO + Hb).

The objective of NIR breast imaging is to develop a novel functional imaging modality for early breast cancer detection and diagnosis beyond currently available techniques. Various efforts by several research groups[10–15] have been made in either laboratory or clinical studies. For example, the research groups of Paulsen and colleagues[12] and of Jiang[15]

[1] S. Gopinath, C. S. Robertson, R. G. Grossman, and B. Chance, *J. Neurosurg.* **79,** 43 (1993).
[2] C. Cheung, J. P. Culver, K. Takahashi, J. H. Greenberg, and A. G. Yodh, *Phys. Med. Biol.* **46,** 2053 (2001).
[3] G. Zhang, A. Katz, R. R. Alfano, A. D. Kofinas, P. G. Stubblefield, W. Rosenfeld, D. Beyer, D. Maulik, and M. R. Stankovic, *Phys. Med. Biol.* **45,** 3143 (2000).
[4] M. Fabiani, G. Gratton, and P. M. Corballis, *J. Biomedi. Opti.* **1,** 387 (1996).
[5] R. Wenzel, H. Obrig, J. Ruben, K. Villringer, A. Thiel, J. Bernarding, U. Dirnagl, and A. Villringer, *J. Biomed. Opt.* **1,** 399 (1996).
[6] B. Chance, E. Anday, S. Nioka, S. Zhou, L. Hong, K. Worden, C. Li, T. Murray, Y. Ovetsky, D. Pidikiti, and R. Thomas, *Opt. Express.* **2,** 411 (1998).
[7] D. A. Boas, T. Gaudette, G. Strangman, X. Cheng, J. J. A. Marota, and J. B. Mandeville, *Neuroimage* **13,** 76 (2001).
[8] D. A. Boas, G. Jasdzewski, G. Strangman, J. P. Culver, and R. Poldrack, "OSA Biomedical Topical Meetings, Technical Digest," p. 307. Miami, FL, April 7–10, 2002.
[9] J. C. Hebden, E. M. C. Hillman, A. Gibson, N. Everdell, R. M. D. Yusof, D. T. Delpy, S. R. Arridge, T. Austin, and J. H. Meek, "OSA Biomedical Topical Meetings, Technical Digest," p. 587. Miami, FL, April 7–10, 2002.
[10] B. Tromberg, N. Shah, R. Lanning, A. Cerussi, J. Espinoza, T. Pham, L. Svaasand, and J. Butler, *Neoplasia* **2,** 26 (2000).
[11] S. Fantini, S. A. Walker, M. A. Franceschini, M. Kaschke, P. M. Schlag, and K. T. Moesta, *Appl. Opt.* **37,** 1982 (1998).

have developed a frequency-domain (FD) 16-source, 16-detector breast imager and have reported their *in vivo* results of optical properties of abnormalities from female volunteers and patients. The research group led by Chance has employed a time-domain (TD) 32-channel imaging system in conjunction with magnetic resonance imaging (MRI) to increase specificity and sensitivity of breast cancer detection.[13] Because of simplicity and low cost in comparison to the FD and TD imaging systems, continuous-wave (CW) NIR breast imaging systems also have been developed by the groups of Barbour *et al.*[14] and Chance.[16] These systems are currently under clinical tests for better breast cancer detection and diagnosis.

Although Hb, HbO, and HbT concentrations and light-scattering properties of tumors may be different from those of surrounding tissues, the optical contrast between tumor and surrounding tissue is about 2–3-fold at most in absorption, and much less in light scattering.[17] Thus much effort on increasing the optical contrast between tumor and healthy surrounding tissues also has been made using fluorescence imaging[18] or molecular beacons[16] to detect and diagnose cancer or tumor with improved sensitivity and specificity.

However, efforts in using NIR techniques to monitor tumor responses to therapeutic interventions[19–21] and therapy, such as to chemotherapy[22] or photodynamic therapy,[23] are very limited and preliminary. Moreover,

[12] T. O. McBride, B. W. Pogue, S. Jiang, U. L. Österberg, and K. D. Paulsen, *Opt. Lett.* **26,** 822 (2001).
[13] V. Ntziachristos and B. Chance, "SPIE Proceedings of Optical Tomography and Spectroscopy of Tissue III," Vol. 3597, p. 565, 1999.
[14] R. L. Barbour, C. H. Schmitz, H. L. Graber, and Y. Pei, "OSA Biomedical Topical Meetings, Technical Digest," p. 456. Miami, FL, April 7–10, 2002.
[15] X. Gu, N. Iftimia, Y. Xu, H. Jiang, and L. L. Fajardo, "OSA Biomedical Topical Meetings, Technical Digest," p. 468. Miami, FL, April 7–10, 2002.
[16] B. Chance, "OSA Biomedical Topical Meetings, Technical Digest" p. 450. Miami, FL, April 7–10, 2002.
[17] J. B. Fishkin, O. Coquoz, E. R. Anderson, M. Brenner, and B. J. Tromberg, *Appl. Opt.* **36,** 10 (1997).
[18] R. H. Mayer, J. S. Reynolds, and E. M. Sevick-Muraca, *Appl. Opt.* **38,** 4930 (1999).
[19] H. Liu, Y. Song, K. L. Worden, X. Jiang, A. Constantinescu, and R. P. Mason, *Appl. Opt.* **39,** 5231 (2000).
[20] J. G. Kim, Y. Song, D. Zhao, A. Constantinescu, R. P. Mason, and H. Liu, *J. Biomed. Opt.* **8,** 53 (2003).
[21] E. L. Hull, D. L. Conover, and T. Foster, *Br. J. Cancer* **79,** 1709 (1999).
[22] D. B. Jakubowski, A. E. Cerussi, F. Bevilacqua, N. Shah, and B. J. Tromberg, "OSA Biomedical Topical Meetings, Technical Digest," p. 456. Miami, FL, April 7–10, 2002.
[23] H. Wang, T. C. Zhu, M. Solonenko, S. M. Hahn, J. Metz, A. Dimofte, J. Mile, and A. G. Yodh, "OSA Biomedical Topical Meetings, Technical Digest." Miami, FL, April 7–10, 2002.

few reports have been found on using NIR spectroscopy and imaging as a prognostic tool for therapy planning and optimization, or for tumor prognosis. Based on the existing knowledge and development of NIR spectroscopy and imaging for the brain and breast, we were motivated a few years ago by the possibility of using NIRS as an efficient, real-time, noninvasive means to monitor tumor vascular oxygenation during respiratory interventions. The recent results in our study were obtained from animal breast and prostate tumors *in vivo* with a one-channel NIR spectrometer. The data have demonstrated that the NIR techniques could have applications as a prognostic means accompanying cancer therapy.[19,20,24]

Tumor Oxygenation as an Indicator for Tumor Response to Interventions

The presence and significance of tumor hypoxia has been recognized since the 1950s. Hypoxic cells *in vitro* and in animal tumors *in vivo* are documented to be three times more resistant to radiation-induced killing compared with aerobic cells.[25] Recent studies have shown that tumor hypoxia is a possible prognostic indicator and is related to the aggressiveness of a tumor, the clinical stage, and poor clinical outcome.[26–30] To improve the efficacy of oxygen-dependent treatment modalities, one possible strategy is the reduction of tumor hypoxia by raising the arterial oxygen partial pressure, P_aO_2 to overcome diffusion-limited hypoxia. Raising the arterial pO_2 by breathing hyperoxic or hyperbaric gas mixtures could be effective.[31,32] However, attempts to apply increased oxygen breathing in the clinic have not always been successful, and this may be attributed to the inability to identify those patients with hypoxic tumors.[33] More specifically, it may be

[24] Y. Gu, V. Bourke, J. G. Kim, A. Constantinescu, R. P. Mason, and H. Liu, *Appl. Opt.* **42**, 2960 (2003).
[25] S. M. Evans, W. T. Jenkins, M. Shapiro, and C. J. Koch, *Adv. Exp. Med. Biol.* **411**, 215 (1997).
[26] M. Höckel, K. Schlenger, B. Aral, M. Mitze, U. Schäffer, and P. Vaupel, *Cancer Res.* **56**, 4509 (1996).
[27] E. K. Rofstad and T. Danielsen, *Br. J. Cancer* **80**, 1697 (1999).
[28] A. W. Fyles, M. Milosevic, R. Wong, M. C. Kavanagh, M. Pintile, A. Sun, W. Chapman, W. Levin, L. Manchul, T. J. Keane, and R. P. Hill, *Radiother. Oncol.* **48**, 149 (1998).
[29] D. M. Brizel, S. P. Scully, J. M. Harrelson, L. J. Layfield, J. M. Bean, L. R. Prosnitz, and M. W. Dewhirst, *Cancer Res.* **56**, 941 (1996).
[30] J. H. A. M. Kaanders, K. I. E. M. Wijffels, H. A. M. Marres, A. S. E. Ljungkvist, L. A. M. Pop, F. J. A. van den Hoogen, P. C. M. de Wilde, J. Bussink, J. A. Raleigh, and A. J. van der Kogel, *Cancer Res.* **62**, 7066 (2002).
[31] S. Dische, *Br. J. Radiol.* **51**, 888 (1979).
[32] O. Thews, D. K. Kelleher, and P. Vaupel, *Radiother. Oncol.* **62**, 77 (2002).

attributed to the inability to identify those patients who would benefit from such interventions. Therefore evaluation of tumor oxygenation distributions and their changes during various stages of tumor growth, during therapeutic interventions, and during therapy is needed. Such evaluation can provide a better understanding of tumor development and tumor response to therapy, potentially allowing therapy to be planned to individual characteristics.

Numerous studies on tumor oxygen tension (pO_2) measurements have been conducted in recent years using a variety of methods,[34–36] such as microelectrodes,[37] optical reflectance,[38] electron spin resonance (EPR),[39,40] or MRI.[36,41–45] The latter two methods have advantages of making repeated measurements of pO_2 noninvasively, and MRI has the further advantage of providing dynamic maps of pO_2, which can reveal tumor heterogeneity.[46] Although NIRS does not quantify pO_2, it can indicate dynamic changes in vascular oxygenation and has the advantage of being entirely noninvasive, providing real-time measurements, and being cost-effective and portable. Our recent studies have revealed the need for NIR imaging of tumor vasculatures to study tumor heterogeneous response to therapeutic interventions and therapy. In the following sections, we briefly introduce basic algorithms used to quantify tumor hemoglobin oxygenation, followed by the NIR instrument description, system calibration, and experimental methods. Then, we provide several representative results taken

[33] J. Overgaard, *in* "Progress in Radio-Oncology V" (H. D. Kogelnik, ed.), p. 469. Monduzzi Editore, Bologna, Italy, 1995.
[34] H. B. Stone, J. M. Brown, T. Phillips, and R. M. Sutherland, *Radiat. Res.* **136**, 422 (1993).
[35] R. P. Mason, S. Ran, and P. E. Thorpe, *J. Cell. Biochem.* **87**, 45 (2002).
[36] D. Zhao, L. Jiang, and R. P. Mason, *Methods Enzymol.* **386**, 378 (2004).
[37] O. Thews, D. K. Kelleher, B. Lecher, and P. Vaupel, *Adv. Exp. Med. Biol.* **428**, 123 (1996).
[38] F. Steinberg, H. J. Röhrborn, K. M. Scheufler, S. Asgari, H. A. Trost, V. Seifert, D. Stolke, and C. Streffer, *Adv. Exp. Med. Biol.* **428**, 553 (1996).
[39] P. E. James, J. A. O'Hara, O. Y. Grinberg, T. Panz, and H. M. Swartz, *Adv. Exp. Med. Biol.* **428**, 97 (1996).
[40] J. A. O'Hara, F. Goda, J. F. Dunn, and H. M. Swartz, *Adv. Exp. Med. Biol.* **411**, 233 (1996).
[41] D. Le, R. P. Mason, S. Hunjan, A. Constantinescu, B. R. Barker, and P. P. Antich, *Magn. Reson. Imaging* **15**, 971 (1997).
[42] S. Hunjan, R. P. Mason, A. Constantinescu, P. Peschke, E. W. Hahn, and P. P. Antich, *Int. J. Radiat. Oncol. Biol. Phys.* **41**, 161 (1998).
[43] D. Zhao, A. Constantinescu, L. Jiang, E. W. Hahn, and R. P. Mason, *Am. J. Clin. Oncol.* **24**, 462 (2001).
[44] D. Zhao, A. Constantinescu, C.-H. Chang, E. W. Hahn, and R. P. Mason, *Radiat. Res.* **159**, 621 (2003).
[45] D. Zhao, S. Ran, A. Constantinescu, E. W. Hahn, and R. P. Mason, *Neoplasia* **5**, 308 (2003).
[46] R. P. Mason, A. Constantinescu, S. Hunjan, D. Le, E. W. Hahn, P. P. Antich, C. Blum, and P. Peschke, *Radiat. Res.* **152**, 239 (1999).

from both prostate and breast tumors under hyperoxic respiratory interventions, using both one-channel and multichannel NIR systems, as well as one-channel and three-channel pO_2 fiber optic needle probes. At the end, we wish to demonstrate that the NIR techniques are complementary with tumor pO_2 readings and can be used as a new prognostic means for cancer therapy prognosis and therapy planning.

Theory and Algorithms

It is well known that hemoglobin concentrations and oxygen saturation in tissue vasculature can be determined using NIRS, since light absorptions of HbO and Hb in the NIR range are distinct. As with our previous work,[19,20] we assumed that HbO and Hb are the major significant absorbing species in tissue vasculature, including tumors, within the selected NIR range of 700–900 nm. Although diffusion theory has been a well-accepted theoretical approach to mathematically quantify light–tissue interaction,[6,7,10,47] no analytical solution has been available for solid tumors because of their finite size and high heterogeneity. While our future work will use the finite element method to obtain numerical solutions for the diffusion equation, our current approach is based on modified Beer–Lambert's law to account for light scattering in tumor tissue.

For a nonscattering medium, Beer–Lambert's law gives rise to the following expressions for the relationships between the absorption coefficient, μ_a, and the extinction coefficient for deoxyhemoglobin (ε_{Hb}) and oxyhemoglobin (ε_{HbO}):

$$\mu_a^{758} = 2.3\{\varepsilon_{Hb}^{758}[Hb] + \varepsilon_{HbO}^{758}[HbO]\} \quad (1)$$

$$\mu_a^{785} = 2.3\{\varepsilon_{Hb}^{785}[Hb] + \varepsilon_{HbO}^{785}[HbO]\} \quad (2)$$

where [HbO] and [Hb] are concentrations of HbO and Hb, respectively, the factor of 2.3 results from the different definitions of μ_a and ε in relation to the incident and detected optical intensities. The conventional definitions for μ_a and ε are $I = I_0 e^{-\mu_a L}$ and $I = I_0 10^{-\varepsilon CL}$, respectively, where I_0 and I are the incident and detected optical intensities in transmission measurement from a nonscattering medium, C is the concentration of hemoglobin measured in m*M*/L, and L is the optical pathlength through the medium in cm. By eliminating I and I_0 in these two expressions, we arrived at a relationship of $\mu_a = 2.3\,\varepsilon C$.

[47] M. S. Patterson, B. Chance, and B. C. Wilson, *Appl. Opt.* **28,** 2331 (1989).

Because of light scattering in tissue, Beer–Lambert's law cannot be applied directly to biologic tissue, such as tumors. By taking an empiric approach to modify Beer–Lambert's law, we arrived at $\mu_a = 2.3\,\varepsilon C = 2.3/L_S \log(I_0/I)$, where L_S represents the optical pathlength in a scattering medium and is no longer equal to the physical distance between the source and detector, d. In a highly light-scattering medium, L_S is much longer than d. Specifically, in the tumor study, we use I_0 and I to represent the incident and detected light intensities, when the tissue sample is without and with light absorption from [HbO] and/or [Hb]. Then, changes in absorption coefficient of the tumor, $\Delta\mu_a$, between baseline and transient conditions under respiratory intervention can be expressed as

$$\Delta\mu_a = \mu_{aT} - \mu_{aB} = 2.3\log(I_B/I_T)/L_S \quad (3)$$

where I_B and I_T are baseline and transient light intensities of the measured optical signals, respectively.

Using the transmitted light intensities at $\lambda_1 = 758$ nm and $\lambda_2 = 785$ nm and manipulating Eqs. (1)–(3), we can quantify the changes of tumor [HbO] and [Hb] due to an intervention as follows:

$$\Delta[HbO] = -11.73 \times \frac{\log(I_B/I_T)^{\lambda 1}}{L_S^{\lambda 1}} + 14.97 \times \frac{\log(I_B/I_T)^{\lambda 2}}{L_S^{\lambda 2}} \quad (4)$$

$$\Delta[Hb] = 8.09 \times \frac{\log(I_B/L_T)^{\lambda 1}}{L_S^{\lambda 1}} - 6.73 \times \frac{\log(I_B/I_T)^{\lambda 2}}{L_S^{\lambda 2}} \quad (5)$$

where $L_S^{\lambda 1}$ and $L_S^{\lambda 2}$ are optical path lengths between the source and detector at the respective wavelengths. The units of Δ[HbO] and Δ[Hb] in Eqs. (4) and (5) are m*M*. The constants given in the equations were computed with the extinction coefficients for oxygenated and deoxygenated hemoglobin at the two wavelengths used.[48]

In principle, $L_S^{\lambda 1}$ and $L_S^{\lambda 2}$ in Eqs. (4) and (5) are variables, depending on the actual separation of source and detector, as well as the optical properties of tumor. Previously, a differential pathlength factor (DPF), (i.e., $L_S = d \times DPF$) has been introduced to associate L_S with d.[49] The DPF values of blood-perfused tissues have been studied intensively for muscles[50] and

[48] W. G. Zijlstra, A. Buursma, and W. P. Meeuwsen-van der Roest, *Clin. Chem.* **37,** 1633 (1991).

[49] D. T. Delpy, M. Cope, P. van der Zee, S. Arridge, S. Wray, and J. Wyatt, *Phys. Med. Biol.* **33,** 1433 (1988).

[50] M. Ferrari, Q. Wei, L. Carraresi, R. A. De Blasi, and G. Zaccanti, *J. Photochem. Photobiol.* **16,** 141 (1992).

brains[51] with approximate values of 4–6 and 5–6, respectively. However, little is known about DPF for tumors, although a DPF value of 2.5 has been used by others.[52] In our approach, we made two assumptions: (1) DPF is the same for both Δ[HbO] and Δ[Hb] at 785 nm (i.e., $DPF = DPF^{785}_{\mathrm{HbO}} = DPF^{785}_{\mathrm{Hb}}$). This assumption was based on the fact that the absorption difference between oxygenated and deoxygenated blood at 785 nm is much smaller than that at 758 nm. The maximal relative error caused by this assumption in tumor oxygen interventions was estimated to be less than 12%, and detailed justification and discussion were given by Liu *et al.*[19] Furthermore, we associated L_S to μ_a by $L = \sqrt{3}/2d\sqrt{\mu_s'/\mu_a}$, where μ_s' is the reduced scattering coefficient, according to Sevick-Muraca *et al.*[53] and Liu.[54] The second assumption was $\mu_s'(758\ \mathrm{nm}) \cong \mu_s'(785\ \mathrm{nm})$ because of weak wavelength dependence of light scattering from tissue. With all the conditions mentioned and further derivation, as given in details by Kim *et al.*[20] we arrived at the final expressions for Δ[HbO] and Δ[Hb]:

$$\Delta[\mathrm{HbO}] = \frac{-10.63 \cdot \log\left(\frac{A_B}{A_T}\right)^{758} + 14.97 \cdot \log\left(\frac{A_B}{A_T}\right)^{785}}{d} \tag{6}$$

$$\Delta[\mathrm{Hb}] = \frac{8.95 \cdot \log\left(\frac{A_B}{A_T}\right)^{758} - 6.73 \cdot \log\left(\frac{A_B}{A_T}\right)^{785}}{d} \tag{7}$$

where d is the direct physical distance between source and detector. $\Delta[\mathrm{Hb}]_{\mathrm{total}}$ is followed by adding Eqs. (6) and (7), as

$$\Delta[\mathrm{Hb}]_{\mathrm{total}} = \Delta[\mathrm{HbO}] + \Delta[\mathrm{Hb}] \tag{8}$$

Equations (6) to (8) will be used in calculating Δ[HbO], Δ[Hb], and $\Delta[\mathrm{Hb}]_{\mathrm{total}}$ in tissue phantoms and tumors during gas interventions in later sections.

The units for Δ[HbO], Δ[Hb], and $\Delta[\mathrm{Hb}]_{\mathrm{total}}$ in Eqs. (6) to (8) are mM/DPF, which still depends on the optical properties of tumor at a particular wavelength. Because our focus is on dynamic changes in [HbO] due to respiratory challenges, in some cases, we normalize Δ[HbO] at its maximal value (i.e., $\Delta[\mathrm{HbO}]/\Delta[\mathrm{HbO}]_{\max}$) to eliminate the effect of DPF on our results.

[51] P. van der Zee, M. Cope, S. R. Arridge, M. Essenpreis, L. A. Potter, A. D. Edwards, J. S. Wyatt, D. C. McCormick, S. C. Roth, E. O. R. Reynolds, and D. T. Delpy, *Adv. Exp. Med. Biol.* **316**, 143 (1992).

[52] R. G. Steen, K. Kitagishi, and K. Morgan, *J. Neurooncol.* **22**, 209 (1994).

[53] E. M. Sevick-Muraca, B. Chance, J. Leigh, S. Nokia, and M. Maris, *Anal. Biochem.* **195**, 330 (1991).

[54] H. Liu, *Appl. Opt.* **40**, 1742 (2001).

Experimental Methods

One-Channel and Multichannel NIR System

A dual-wavelength (at 758 and 785 nm), one-channel NIR system (NIM, Inc., Philadelphia, PA) uses an in-phase and quadrature-phase chip (IQ chip). As shown in Fig. 1, the NIR system starts with a radiofrequency (RF) source to modulate the light intensities of two laser diodes (LD_1 and LD_2) at 140 MHz through a time-sharing system. The light passes through a bifurcated fiber optic probe, is transmitted through the tumor tissue, and is collected by a second fiber bundle. The light is then amplified by a photomultiplier tube (PMT), demodulated by the IQ circuit, and filtered by a lowpass filter (LPF) for passing only the direct current (DC) components. The signals are digitized by an analog-to-digital converter (ADC) and stored in a laptop computer. The measured DC signals at the IQ branches

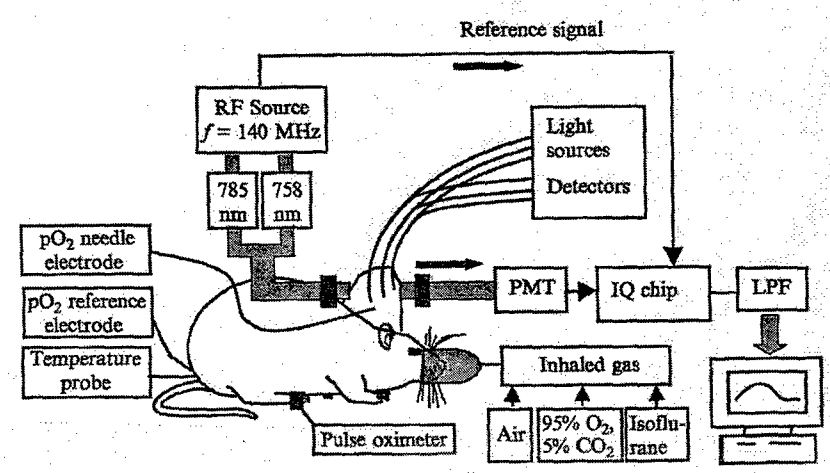

FIG. 1. Experimental setup for simultaneous tumor oximetry, using an NIRS system with either a needle electrode or a three-channel fiber-optic FOXY system. The NIR system consists of two laser diodes modulated at 140 MHz, two fiber bundles for light delivery and collection, a photomultiplier tube (PMT), an in-phase and quadrature-phase demodulator (IQ chip), and lowpass filter (LPF) for retrieving amplitude and phase information. The FOXY system comprises three fiber-optic, oxygen-sensing probes that are inserted into different regions of the tumor. Alternatively, a needle electrode probe can be inserted into the tumor for single-channel pO_2 reading.

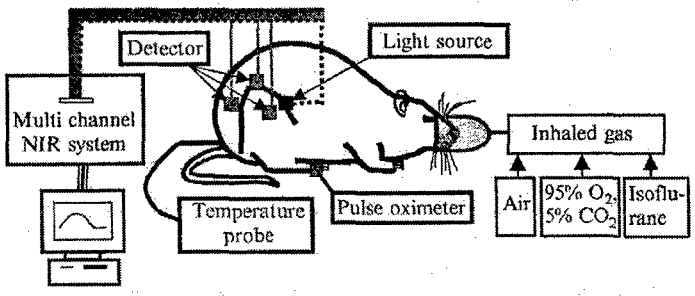

FIG. 2. Schematic experimental setup for three-channel NIRS experiments. One of the three detectors was placed opposite to the light source in order to detect light in transmission mode, and the other two detectors were set in the semireflection mode on the tumor surface.

at the measured wavelengths, $I_{bc}(\lambda)$ and $Q_{bc}(\lambda)$, lead to the quantification of optical amplitudes, $A(\lambda)$, and phase, $\theta(\lambda)$, that have passed through the tumor tissues[55]:

$$A(\lambda) = \sqrt{I(\lambda)_{DC}^2 + Q(\lambda)_{DC}^2} \tag{9}$$

$$\theta(\lambda) = \arctan\left(\frac{Q(\lambda)_{DC}^2}{I(\lambda)_{DC}^2}\right) \tag{10}$$

where λ represents the respective wavelengths used in the NIR system. Then, changes in light intensity through the tumor caused by hyperoxic interventions are used to compute changes in tumor vascular [HbO] and [Hb]. Whether the readings of $\theta(\lambda)$ can be linked to tumor physiology remains to be further explored.

Besides a one-channel NIR system, we have also used a multichannel NIR system (Fig. 2) to explore and reveal intratumoral vascular heterogeneity by having simultaneous readings at several separations of the source and detectors. Unlike the single-channel system, the multichannel system uses two laser diodes at 730 and 850 nm with constant light intensities (i.e., DC light) and three photo detectors. These detectors are placed along the circumference together with the light source, with three different source–detector separations in order to detect different depths within the tumor volume, as demonstrated in Fig. 3.

Following the same procedures as those described in the previous section, we arrived at the expression of Δ[HbO] for the multichannel system with the two wavelengths of 730 and 830 nm, as follows:

[55] Y. Yang, H. Liu, X. Li, and B. Chance, *Opt. Eng.* **36**, 1562 (1997).

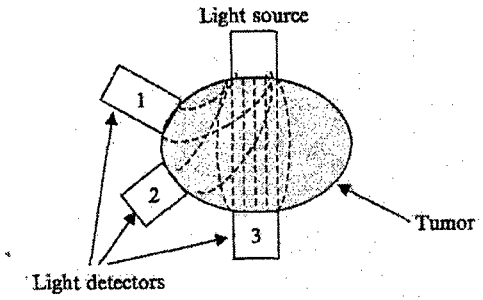

FIG. 3. A schematic diagram showing the locations of the three detectors and possible internal tumor volumes interrogated by the different detectors.

$$\Delta[\text{HbO}] = \frac{-0.674 \cdot \log\left(\frac{A_B}{A_T}\right)^{730} + 1.117 \cdot \log\left(\frac{A_B}{A_T}\right)^{830}}{d} \tag{11}$$

where d is the direct source–detector separation in cm, and the unit of Δ[HbO] is m*M*/DPF.

System Testing and Calibration

It is important to characterize and verify linearity of the NIRS system before any animal experiment starts. We have performed two critical system tests: (1) to quantify the output voltage range, within which the NIR system has a linear response, and (2) to perform liquid phantom measurements to confirm the physiologic readings derived from the optical NIRS system.

Linearity Testing Associated with Crosstalk Between the Amplitude and Phase. In principle, changes in amplitude of an FD photon migration system should be independent of its changes in phase (i.e., the crosstalk between amplitude and phase should be minimal for an ideal NIR system): However, in reality, it is difficult to have such a perfect condition for an actual instrument, so it is necessary to conduct the crosstalk test. We altered the optical densities (O.D.) of optical filters in front of the two light sources (758 and 785 nm) to attenuate the detected amplitude, so we could see whether changes in amplitude and phase were correlated. The test showed that phase–amplitude crosstalk exists, if the measured output intensity is either too small (<50 mV) or too large (>380 mV), as shown in Fig. 4A and 4B for 758 nm and 785 nm, respectively. We also plotted O.D. values of the filters versus log (amplitude of the output signal) to see the electrical attenuation of the system output in response to the optical

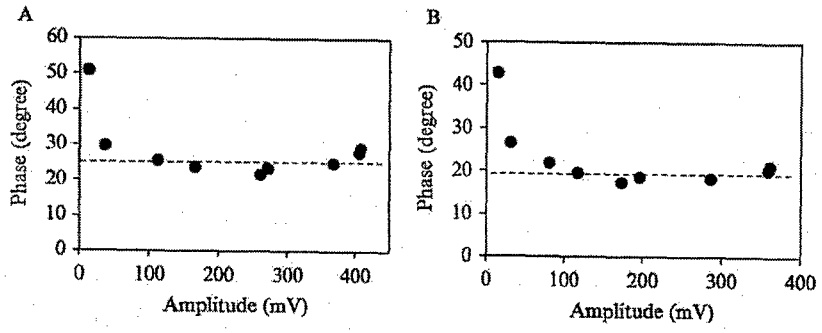

FIG. 4. Relationships between the output amplitude (mV) and phase (in degree) of the NIR single-channel system at (A) 758 nm and (B) 785 nm.

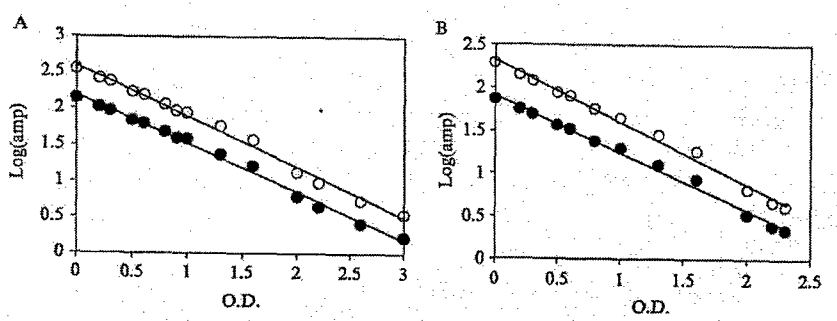

FIG. 5. Linearity tests for the NIR system between the optical input attenuation and electrical output signals at 758 nm (open circles) and 785 nm (solid circles). The X variable is the optical density (O.D. = $\log[I_0/I]$) of the filters, which were inserted before the detector to attenuate the light intensity. Cases (A) and (B) correspond to a higher (350 mV for 758 nm) and lower (193 mV for 758 nm) output voltage, respectively. Both 350 and 193 mV were obtained when the measurement was performed without any optical attenuation.

attenuation. It was found that as long as the output is in the range 100–350 mV, good linearity is achieved for the system response, as shown in Fig. 5A and 5B.

Blood Phantom Study. To calibrate the NIRS system for quantifying hemoglobin concentrations, we used human blood for tissue phantom experiments. Two packets of Sigma (St. Louis, MO) P-3813 phosphate buffered saline (PBS) (pH 7.4) powder was used to make a 2-liter buffer, and 100 ml of 20% intralipid was added into the buffer for a 1% intralipid solution, as shown in Fig. 6A. Then 14 g of baking yeast was mixed with tap

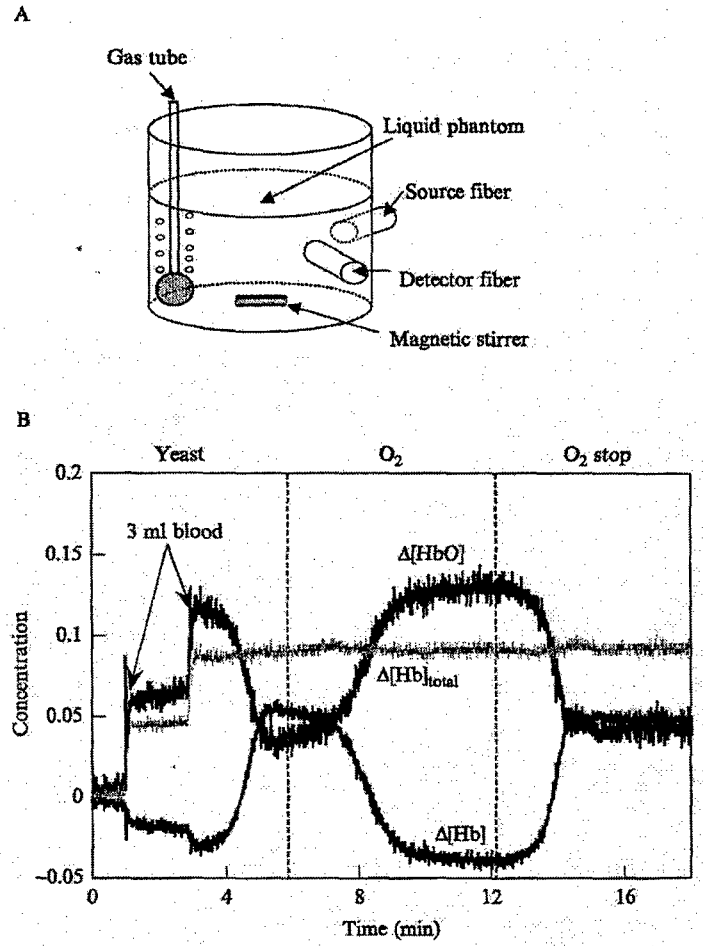

FIG. 6. (A) Experimental setup for system calibration using a liquid phantom with 1% Intralipid and baker's yeast in saline buffer. The NIRS probes were placed in reflectance geometry, while the gas bubbler was placed opposite to minimize liquid movement effects. (B) Simultaneous dynamic changes of Δ[HbO], Δ[Hb], and $\Delta[Hb]_{total}$ in the phantom solution measured using the NIR single-channel system. The dark solid curve is for Δ[HbO], the lighter solid line is for $\Delta[Hb]_{total}$, and the gray solid line shows Δ[Hb] in the phantom solution. Blood was deoxygenated by the yeast's oxygen consumption and oxygenated by bubbling O_2. During the oxygenation and deoxygenation process, $\Delta[Hb]_{total}$ was maintained as a constant.[20]

water before being added into the 2-liter buffer solution to deoxygenate the tissue phantom solution. Amount of blood for each addition to the solution was 3 ml for two additions after the yeast was well mixed in the solution.

When the blood was fully deoxygenated by yeast, pure oxygen was introduced in the solution to oxygenate the blood. After the blood was fully oxygenated, oxygen blowing was stopped in order to re-deoxygenate the solution by yeast again. The gas tube for oxygen delivery was placed far from the NIRS probes to minimize any liquid movement effects, as shown in Fig. 6A. Source and detector probes for the NIRS system were placed in reflection geometry with a direct separation of ~3 cm. The solution was stirred constantly with a magnetic stirrer to maintain homogeneity.

After getting the raw amplitude data from the experiment, we used Eqs. (6) to (8) to calculate Δ[HbO], Δ[Hb], and $\Delta[\mathrm{Hb}]_{\mathrm{total}}$. As shown in Fig. 6B, $\Delta[\mathrm{Hb}]_{\mathrm{total}}$ remained constant, as expected, whereas Δ[HbO] and Δ[Hb] altered in opposite directions during the oxygenation and deoxygenation cycle. This demonstrates that the two assumptions used to derive Eqs. (6) and (8) are correct and necessary to compensate the differences in DPF caused by two different wavelengths.[20] Notice that there appears to be a delay between the gas switch and responses of Δ[HbO] and Δ[Hb] as shown in Fig. 6B. This delay is possibly caused by the entire process of transporting oxygen gas from the tube to the solution, oxygenating/deoxygenating the solution, and reaching a homogeneous state near the detectors.

Animal Models

In the prostate tumor study, Dunning prostate R3327-HI rat tumors (originally obtained from Dr. Peter Peschke, DKFZ Heidelberg) were implanted in pedicles on the foreback of adult male Copenhagen rats.[56] In the breast tumor study, rat mammary adenocarcinomas 13762NF (originally obtained from the Division of Cancer Therapeutics, National Cancer Institute [DCT NCI]) grown in the hindlimb of adult female Fisher 344 rats (~200 g) were used. Once the tumors reached approximately 1–2 cm in diameter, the rats were anesthetized with 0.2 ml ketamine hydrochloride (100 mg/ml; Aveco, Fort Dodge, IA) and maintained under general gaseous anesthesia with isoflurane in air (1.3% isoflurane at 1 dm^3/min air) through a mask placed over the mouth and nose. Tumors were shaved to improve optical contact for transmitting light. Body temperature was maintained by a warm water blanket and was monitored by a rectally

[56] E. W. Hahn, P. Peschke, R. P. Mason, E. E. Babcock, and P. P. Antich, *Magn. Reson. Imaging* **11**, 1007 (1993).

inserted thermal probe (see Fig. 1) connected to a digital thermometer (Digi-Sense, Model 91100–50; Cole-Parmer Instrument Company, Vernon Hills, IL). A pulse oximeter (Model 8600; Nonin, Inc., Plymouth, MN) was placed on the hindfoot to monitor arterial oxygenation (S_aO_2). Tumor volume V (in cm^3) was estimated as $V = 4\pi/3(L + W + H/6)^3$, where L, W, and H are the three respective orthogonal dimensions.

In general, the source–detector fiber separation was about 1–1.5 cm in transmittance geometry, and thus the tumor volume interrogated by NIR light can be estimated as follows. The radius of probe is 0.4 cm, which makes the volume of the cylinder 0.5–0.75 cm^3. By diffusion approximation, the optical penetration depth is about one third of the direct distance between the source and detector, which makes an additional spherical volume with a radius from 0.5–0.75 cm. Therefore the total tumor volume interrogated by NIR light can be estimated in the range of 1.0–2.5 cm^3, depending on the actual source–detector separation.[20]

Measurements of pO_2 Using Oxygen Needle Electrode and Fiber-Optic Fluorescence-Quenched Probe

Needle Electrode. We used a needle-type oxygen electrode for local pO_2 readings in several tumors. Linear two-point calibrations were performed with air (21% O_2) and pure nitrogen (0% O_2) saturated saline buffer solutions before the animal experiments, and we estimated an instrumental precision of 2–3 mmHg. After calibration, the needle electrode was inserted carefully into the tumor with the reference electrode being placed rectally, as described in detail previously.[20] Both the sample and reference electrodes were connected to a picoammeter (Chemical Microsensor; Diamond Electro-Tech, Inc., Ann Arbor, MI) and polarized at −0.75 V. Measurement points of pO_2 were manually recorded, whereas the NIRS data were acquired automatically. Measurements of pO_2 and NIRS were initiated, while rats breathed air for ~10 min to demonstrate a stable baseline. The inhaled gas was then switched to carbogen (5% CO_2 and 95% O_2) or oxygen for 15 min and switched back to air.

Fiber-Optic Fluorescence-Quenched Probe. For multiple pO_2 readings, we used a multichannel, fiber-optic, oxygen-sensing system (FOXY; Ocean Optics, Inc.). We calibrated the three fluorescence-quenched, optical fiber probes initially and then inserted them into different regions of the tumors to monitor the changes of oxygen tension (ΔpO_2) in response to the respiratory challenges as described previously.[24] The probes were placed in such a way that at least one was in a relatively poorly oxygenated region (low baseline pO_2) and at least one was in a relatively well-oxygenated region (high baseline pO_2). A mean ΔpO_2 of the tumor was obtained by

averaging the three readings. A typical FOXY channel used a pulsed blue light-emitting diode (LED) at ~475 nm and was coupled into one branch of a bifurcated optical fiber bundle. Then, the fluorescent light was propagated to the FOXY probe tip. Each probe had two 300-μm-diameter optical fibers with an aluminum jacket. The distal end of the probes was coated with a thin layer of a hydrophobic sol-gel material, so that an oxygen-sensing ruthenium complex was effectively trapped and protected from water. The ruthenium complex at the probe tips was excited by the blue LED and emitted fluorescence at ~600 nm. If the excited ruthenium complex encountered an oxygen molecule, the excess energy would be transferred to the oxygen molecule in a nonradiative transition, decreasing or quenching the fluorescence signal.

The fluorescence response of the ruthenium complex was highly temperature dependent, so the probe calibration was accomplished by streaming gases of known oxygen concentrations (100, 20.9, 10, 2, and 0%) through a cylindrical water jacket heated to 37°. Calibration curves were calculated by the vendor-supplied software, using the second-order, polynomial calibration:

$$\frac{I_0}{I} = 1 + K_1[O] + K_2[O]^2 \tag{12}$$

where I_0 is the fluorescence intensity at zero concentration (nitrogen), I is the measured intensity of fluorescence at a pressure p of oxygen, $[O]$ represents the oxygen concentration (related to pO_2), and K_1 and K_2 are the first- and second-order coefficients and are automatically supplied by the curve-fitting routine from the calibration measurements. After the system calibration, the oxygen concentration in tumor–tissue sample measurements was deduced using Eq. (12).

NIR Measurements of Breast–Prostate Tumors Under Interventions

We conducted all animal experiments in a darkened room, and the measurements were initiated while the rats breathed air for 10 min to get a stable baseline. The inhaled gas was switched to carbogen (5% CO_2 and 95% O_2) or pure oxygen for 15–20 min, and then back to air for 15 min. Sometimes, repeated cycles were taken either to check the reproducibility or to minimize preconditioning effects. Raw amplitude data from either the one-channel or three-channel detectors were recorded simultaneously during the experiments, processed, and displayed through the computer to obtain tumor Δ[HbO] and $\Delta[Hb]_{total}$. The dynamic data were fitted with a single-exponential and/or double-exponential expression, using Kaleidagraph software (Synergy Software, Reading, PA), to obtain time constants

and amplitudes. Those fitted parameters allowed us to further develop a two-region tumor model, which will be discussed in a later section.

In many cases, we performed simultaneous measurements of changes in tumor HbO and in tumor pO_2, using either the needle electrode or the fiber-optic FOXY system along with the NIRS readings, as shown in Fig. 1, for both breast and prostate tumors.

Results and Model Development

HbO and pO_2 Changes in Prostate Tumors Under Carbogen Intervention

We have measured relative changes of [HbO], $[Hb]_{total}$, and tumor tissue pO_2 from several Dunning prostate R3327-HI tumors, and Fig. 7 shows two representative data sets. Figure 7A shows the temporal profiles of Δ[HbO] and pO_2 in a Dunning prostate R3327-HI tumor (3.6 cm^3) measured simultaneously with the NIRS and pO_2 needle electrode during carbogen respiratory challenge. After the breathing gas was switched from air to carbogen, Δ[HbO] increased rapidly, whereas $\Delta[Hb]_{total}$ seemed to have much smaller responses. In this case, tumor tissue pO_2 increased at a much slower rate, from a baseline of 60 mmHg to ~80 mmHg during the entire carbogen intervention. Figure 7B is obtained from another prostate tumor (3.1 cm^3); the electrode readings showed a slower pO_2 response from ~15 to 40 mmHg, whereas the NIRS response was biphasic, a sharp rise in Δ[HbO] followed by a further slow, gradual significant increase over the next ~15 min. In this case, $\Delta[Hb]_{total}$ showed little change, ~2% of the maximum in Δ[HbO]. The biphasic feature of Δ[HbO] has been a commonly observed dynamic characteristic under tumor vascular oxygenation, as reported previously.[19,20,24]

HbO and pO_2 Changes in Breast Tumors Under Carbogen and Oxygen Intervention

For a representative 13762NF breast tumor (3.2 cm^3), typical time profiles of the normalized Δ[HbO] and mean ΔpO_2 in response to carbogen and then oxygen intervention are shown in Fig. 8. When the inspired gas was switched from air to carbogen, the normalized Δ[HbO] showed a sharp initial rise in the first minute ($p < 0.0001$), followed by a slower, gradual, but further significant increase over the next 19 min ($p < 0.001$). The mean ΔpO_2 profile was averaged over the three individual ΔpO_2 readings (FOXY), and it increased rapidly by about 50 torr (= mmHg) within 8 min ($p < 0.0005$) and also continued a slower and gradual increase over the next 12 min ($p < 0.005$). Return to breathing air produced a significant

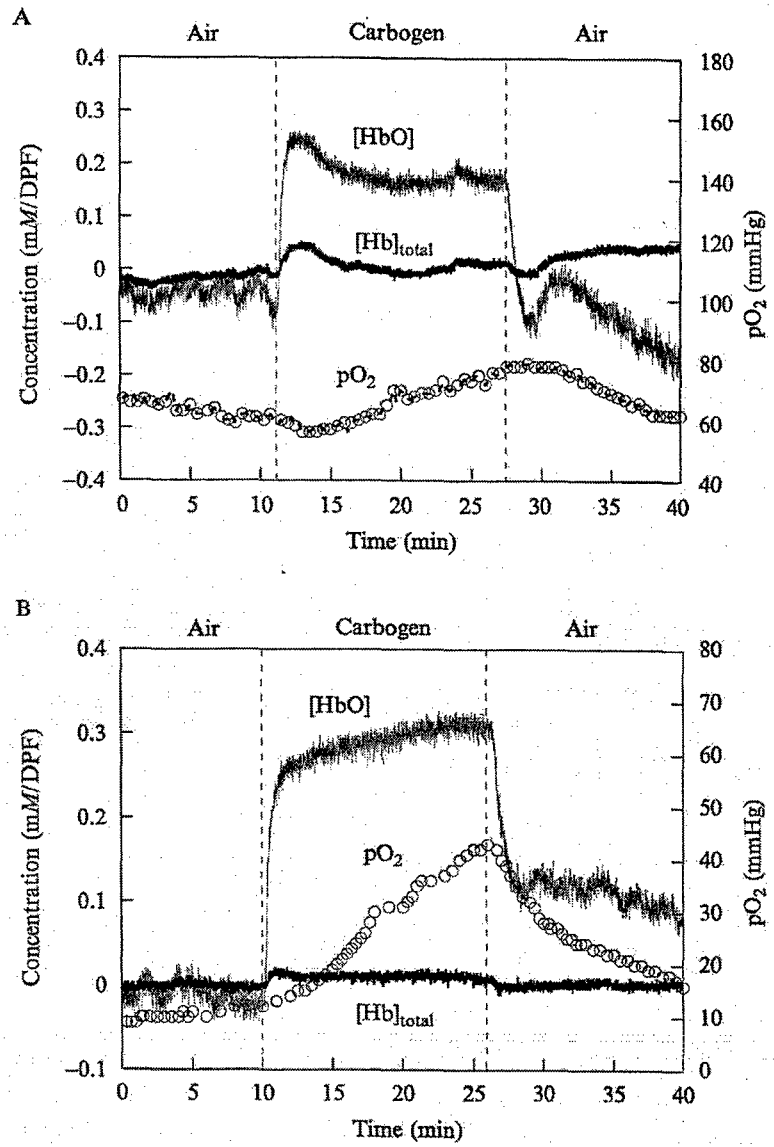

FIG. 7. Simultaneous dynamic changes of Δ[HbO] and pO_2 in R3327-HI rat prostate tumors using NIRS and pO_2 needle electrode. (A) A representative tumor (3.6 cm^3) showed a rapid NIR response, whereas (B) another tumor (3.1 cm^3) showed a clear biphasic feature in Δ[HbO] with a slow pO_2 response. The unit of Δ[HbO] is m*M*/DPF, where DPF is equal to the optical pathlength divided by the source–detector separation. Dotted vertical line marks the time when the gas was changed.

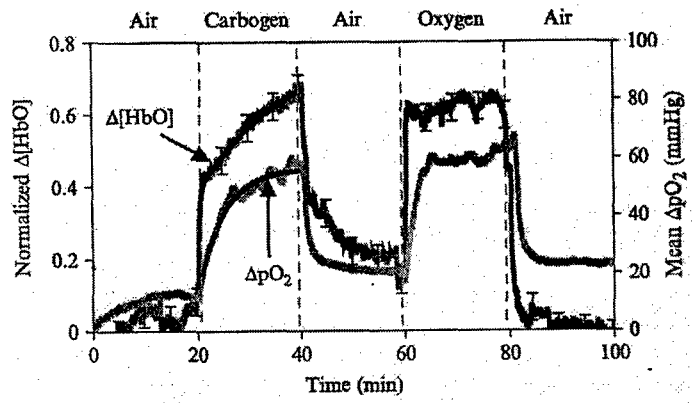

FIG. 8. Dynamic responses of Δ[HbO] and mean ΔpO_2 to hyperoxic gas intervention in a rat breast tumor (3.2 cm^3). In response to carbogen breathing, single-exponential curve fitting yielded $\Delta pO_2 = 42.68\,\{1 - \exp[-(t-21.01)/4.56]\} + 16.66$ ($r = 0.98$), and biexponential fitting resulted in $\Delta[\mathrm{HbO}] = 0.373\,\{1 - \exp[-(t-20.36)/0.61]\} + 0.648\,\{1-\exp[-(t-20.36)/21]\}$ ($r = 0.97$). The smooth black curves plotted along with the data are obtained according to the previous exponential expressions, respectively.

decline for both signals ($p < 0.0001$). When the hyperoxic intervention was repeated with pure oxygen, the dynamic features of Δ[HbO] and ΔpO_2 remained consistent, except that the biphasic behavior of Δ[HbO] was less apparent. A detailed investigation on Δ[HbO] differences in response to carbogen and oxygen interventions has been given in our earlier study.[24]

In response to carbogen intervention, the pO_2 profile displayed a single-phase dynamic behavior, whereas Δ[HbO] showed an apparent biphasic response. These dynamics may be characterized by time constants of single- and double-exponential responses, respectively. A single exponential fitting gives rise to a slow ΔpO_2 response of $\tau(\Delta pO_2) = 4.56 \pm 0.06$ min ($r = 0.98$). A double-exponential expression with two time constants, τ_1 and τ_2, was used to fit the normalized Δ[HbO], yielding fast and slow time constants of 0.61 min and 21 min, respectively. Figure 8 plots the fitted curves along with the experimental data. During the course of our study, we have often observed biphasic characteristic of Δ[HbO], which motivated us to develop a model to interpret the experimental finding, to be described in a later section.

The advantage of using FOXY pO_2 probes is to detect distinct heterogeneity in tumor pO_2. The individual responses at different locations within the tumor to the hyperoxic gas were diverse: those probes that indicated

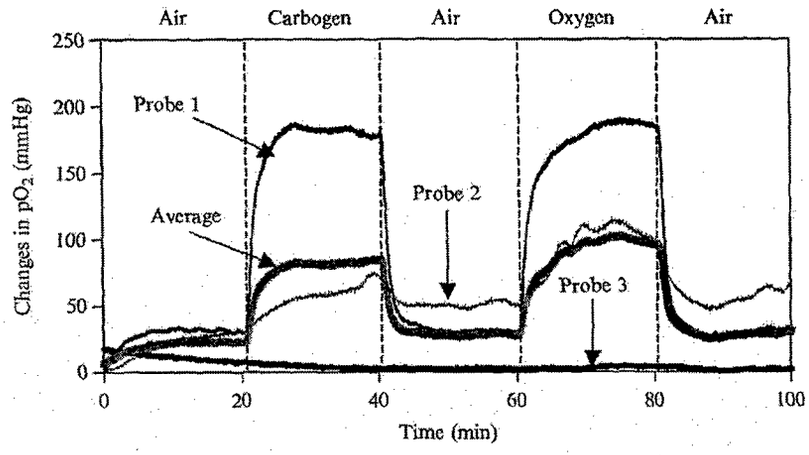

FIG. 9. Time profiles of tumor oxygen tension changes, ΔpO_2, measured with three channels of a FOXY fiber-optic, oxygen-sensing system with respect to different gas inhalations for a breast tumor (4.6 cm^3). The mean signal for the three channels was calculated and plotted by the thicker trace. Modified from Gu *et al.*[24]

apparently well-oxygenated regions usually showed a large and rapid response, whereas those with lower baseline pO_2 often showed little change (Fig. 9). By studying a group of five rats with both carbogen and oxygen interventions, we obtained a distinct correlation between the maximal values of global Δ[HbO] and the mean ΔpO_2, as shown in Fig. 10. Because of heterogeneity in regional pO_2, the standard deviations of the mean pO_2 values were quite large.

Tumor Heterogeneity Observed by a Multichannel NIRS System

To study tumor heterogeneity, the multichannel NIRS system also has been used to detect changes in [HbO] with different source-detector separations. Fig. 11A shows three temporal profiles of Δ[HbO] obtained from three detectors in a breast tumor (16.6 cm^3), with a source–detector separation of 1.5 cm for detector 1, 2.5 cm for detector 2, and 2.8 cm for detector 3, respectively (Fig. 3). The measurement uncertainties are plotted at discrete times in Fig. 11A. After 10 min of air breathing measurement as the baseline, the inhaled gas was switched from air to carbogen, causing a sharp increase in Δ[HbO] ($p < 0.0001$ after 1 min from gas switch), followed by a further gradual, but significant, increase over the next 15 min ($p < 0.0001$).

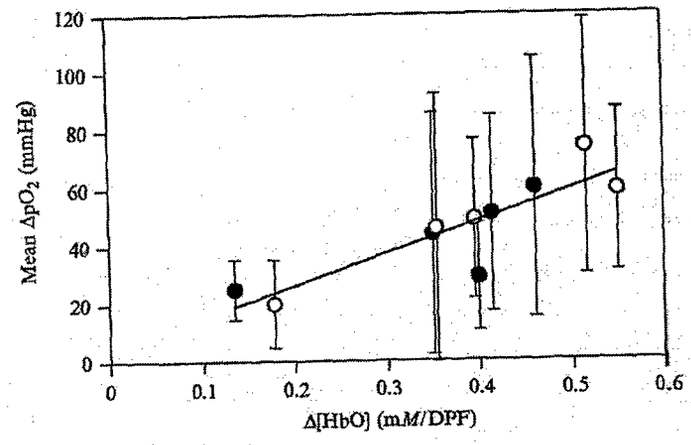

FIG. 10. Correlation between mean ΔpO_2 and ΔHbO for five breast tumors ($r > 0.86$) with a linear relationship of $\Delta pO_2 = 110.65\ \Delta HbO + 4.1285$. Solid circles are for transition air to carbogen, whereas open circles are for transition air to oxygen.[24]

As with the single-channel NIRS measurement, the biphasic features appear clearly in the multichannel results. The rising parts of Δ[HbO] from detectors 1, 2, and 3 after gas switch to carbogen are shown in Fig. 11B–11D, respectively, along with the fitted curves. The two equations used for the curve fitting are

$$\Delta[HbO]_{single} = A\{1 - \exp[-(t - t_0)/\tau]\} \tag{13}$$

$$\Delta[HbO]_{double} = A_1\{1 - \exp[-(t - t_0)/\tau_1]\} + A_2\{1 - \exp[-(t - t_0)/\tau_2]\} \tag{14}$$

respectively, for the single-exponential and double-exponential expressions. It is clear that the double-exponential expression gives a much better fit, as confirmed by the respective chi squared (χ^2) and R^2 values. Table I summarizes all the fitted parameters for the respective detectors.

Mathematical Model Development to Interpret Data

As shown in the last section, the temporal profiles of tumor Δ[HbO] caused by respiratory challenge can be well fitted with a double-exponential equation, represented by two time constants (fast and slow). To understand these time constants and to interpret the experimental findings, we further developed a hemoperfusion model,[19] briefly described as follows.

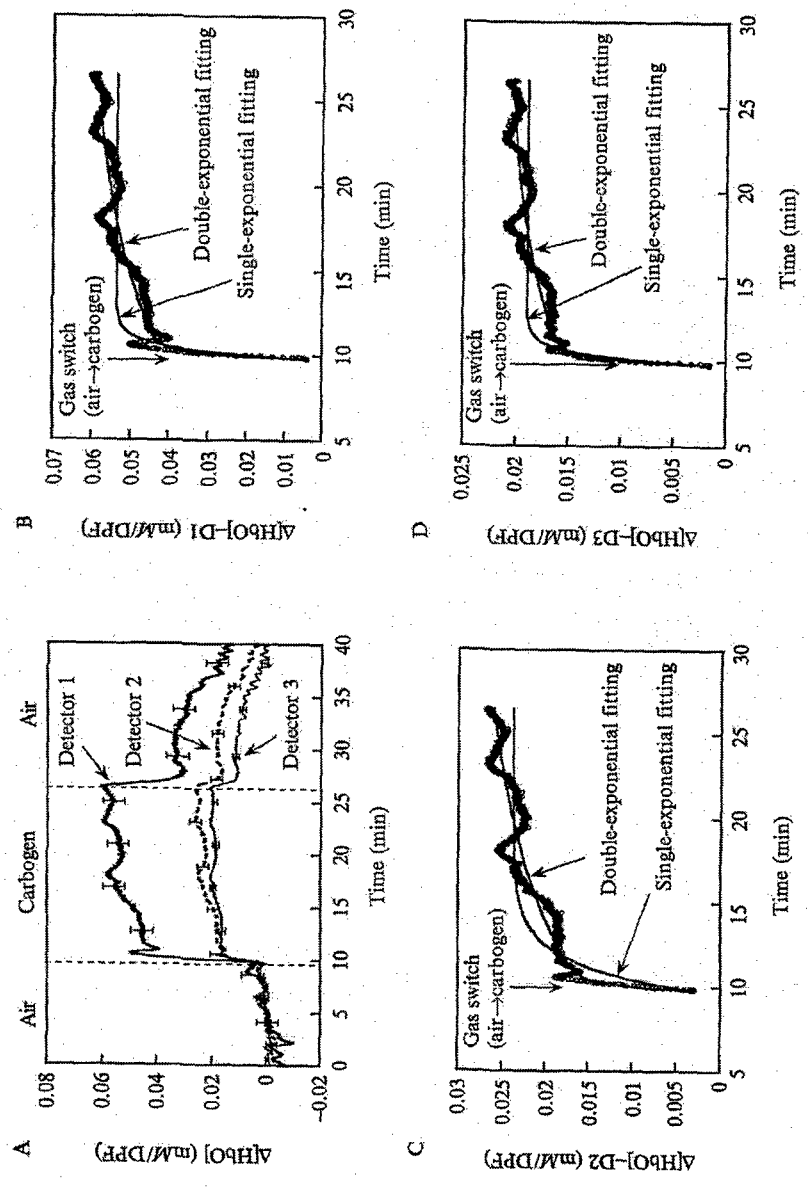

TABLE I
SUMMARY OF VASCULAR OXYGEN DYNAMICS FROM THREE DETECTORS FROM FIG. 11

Double-exponential fitting $\Delta HbO_2 = A_1[1 - \exp(-t/\tau_1)] + A_2[1 - \exp(-t/\tau_2)]$

Parameters	Detector 1	Detector 2	Detector 3
Separation: d (cm)	1.5	2.5	2.8
A_1 (mM/DPF)	0.037 ± 0.001	0.0125 ± 0.0002	0.0134 ± 0.0002
τ_1 (min)	0.24 ± 0.01	0.30 ± 0.02	0.27 ± 0.01
A_2 (mM/DPF)	0.020 ± 0.001	0.0130 ± 0.0004	0.0060 ± 0.0002
τ_2 (min)	8.27 ± 0.72	9.87 ± 0.84	7.00 ± 0.58
χ^2	0.005	0.001	0.0005
R^2	0.95	0.96	0.95
$\tau_1/\tau_2 = A_1/A_2$	1.85 ± 0.07	0.96 ± 0.05	2.23 ± 0.08
τ_1/τ_2	0.029 ± 0.004	0.030 ± 0.004	0.039 ± 0.005
$f_1/f_2 = (A_1/A_2)/(\tau_1/\tau_2)$	64 ± 9	32 ± 5	58 ± 9

Following an approach used to measure regional cerebral blood flow (rCBF) with diffusible radiotracers,[57–59] we made an analogy to evaluate tumor hemodynamics, using the respiratory intervention gas as a tracer.

In response to respiratory intervention, a sudden small change introduced in arterial O_2 saturation (S_aO_2) results in an increase in arterial HbO concentration (ΔHbO^{artery}). This increase in HbO^{artery} can be considered as an intravascular tracer.[60] Following Kety's method and assuming that changes in dissolved O_2 are negligible,[60] we have

$$\frac{d}{dt}(\Delta HbO^{vasculature}) = f\left(\Delta HbO^{artery} - \frac{\Delta HbO^{vasculature}}{\gamma}\right) \quad (15)$$

[57] S. S. Kety, *Pharmacol. Rev.* **3**, 1 (1951).
[58] S. S. Kety, *Israel J. Med. Sci.* **23**, 3 (1987).
[59] H. Watabe, M. Itoh, V. Cunningham, A. A. Lammertsma, P. Bloomfield, M. Mejia, T. Fujiwara, A. K. P. Johes, T. Johes, and T. Nakamura, *J. Cerebr. Blood Flow Metab.* **16**, 311 (1996).
[60] A. D. Edwards, C. Richardson, P. van der Zee, C. Elwell, J. S. Wyatt, M. Cope, D. T. Delpy, and E. O. R. Reynolds, *J. Appl. Physiol.* **75**, 1884 (1993).

FIG. 11. (A) Dynamic changes of [HbO] measured at three detectors from a rat breast tumor (volume: 16.6 cm^3). Dotted vertical lines mark the points when the gas was changed. The rising parts of Δ[HbO] obtained from three detectors were fitted using both single-exponential and double-exponential expressions, and (B) to (D) are from detectors 1 to 3, respectively.

where f represents blood perfusion rate, and γ is defined as a vasculature coefficient of the tumor. The coefficient, γ, is the ratio of HbO concentration change in the vascular bed to that in veins and equals $(\Delta\mathrm{HbO}^{\mathrm{vasculature}})/(\Delta\mathrm{HbO}^{\mathrm{vein}})$.

In Eq. (15), whereas f and γ are constants, $\Delta\mathrm{HbO}^{\mathrm{vasculature}}$ is a time-dependent variable. In principle, $\Delta\mathrm{HbO}^{\mathrm{vasculature}}$ can be solved rigorously given a constant input, H_0, for $\Delta\mathrm{HbO}^{\mathrm{artery}}$ after time 0. Our previous study demonstrates that changes in arterial HbO ($\mathrm{S_aO_2}$) are much faster than that in the vascular bed.[19] Then we arrive at Eq. (16):

$$\Delta\mathrm{HbO}^{\mathrm{vasculature}}(t) = \gamma \times \mathrm{H}_0 \times \left(1 - e^{-ft/\gamma}\right) \tag{16}$$

Equation (16) indicates that the change in oxygenated hemoglobin concentration in tumor vasculature, $\Delta\mathrm{HbO}^{\mathrm{vasculature}}(t)$, depends on the blood perfusion rate, f, the arterial oxygenation input, H_0, and the vasculature coefficient of the tumor, γ.

Our NIR instrument indeed measures changes in vascular HbO concentration (i.e., $\Delta[\mathrm{HbO}]^{\mathrm{vasculature}}$). Then, Eq. (16) can be used to interpret the NIR measurements, since it gives the same exponential form as Eqs. (13) and (14), used to fit the experimental data. The comparison between Eqs. (13) and (16) reveals that the measured time constant is closely associated with the blood perfusion rate, f, and the vasculature coefficient of the tumor, γ in the measured volume. Furthermore, if the measured volume involves two distinct regions, then the detected signal will involve two different blood perfusion rates, f_1 and f_2, and/or two different vasculature coefficients, γ_1 and γ_2. In this case, it is reasonable to assume that the measured signal results from both of the regions, as illustrated in Fig. 12A. Consequently, Eq. (16) can be modified with a two-exponential expression and two time constants:

$$\begin{aligned}\Delta\mathrm{HbO}^{\mathrm{vasculature}}(t) &= \gamma_1 \times \mathrm{H}_0 \times \left(1 - e^{-f_1 t/\gamma_1}\right) + \gamma_2 \times \mathrm{H}_0 \times \left(1 - e^{-f_2 t/\gamma_2}\right) \\ &= \mathrm{A}_1 \times \left(1 - e^{-f_1 t/\gamma_1}\right) + \mathrm{A}_2 \times \left(1 - e^{-f_2 t/\gamma_2}\right)\end{aligned} \tag{17}$$

where f_1 and γ_1 are the blood perfusion rate and vasculature coefficient from region 1, respectively, f_2 and γ_2 are from region 2, and $\mathrm{A}_1 = \gamma_1 \times \mathrm{H}_0$ and $\mathrm{A}_2 = \gamma_2 \times \mathrm{H}_0$. The two time constants are equal to $\tau_1 = \gamma_1/f_1$ and $\tau_1 = \gamma_2/f_2$, respectively. When A_1, A_2, and the two time constants are determined from our NIR measurements, we arrive at the ratios for the two vasculature coefficients and the two blood perfusion rates:

$$\frac{\gamma_1}{\gamma_2} = \frac{\mathrm{A}_1}{\mathrm{A}_2}; \qquad \frac{f_1}{f_2} = \frac{\mathrm{A}_1/\mathrm{A}_2}{\tau_1/\tau_2} \tag{18}$$

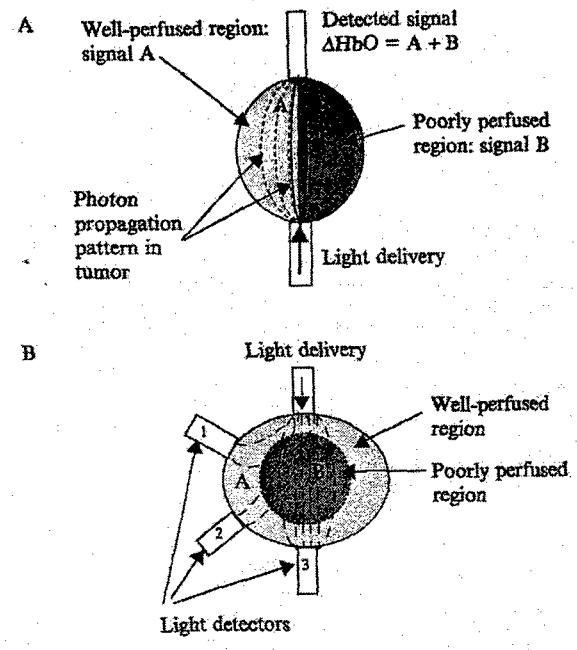

FIG. 12. (A) Schematic diagram to show a tumor model with two vascular perfusion regions, along with the light patterns propagating within the tumor tissue. "A" represents a portion of the detected signal interrogating the well-perfused region, and "B" represents another portion of the detected signal, mainly passing through the poorly perfused region. Our assumption is that the total detected signal is a sum of A and B. (B) A more realistic tumor tissue model with the center poorly perfused (leading to signal A) and the periphery well perfused (leading to signal B). It demonstrates possible tumor volumes interrogated by the multichannel detectors. The total detected signal is still a sum of A plus B.

In this way, by quantifying these two ratios, we are able to obtain insight into the tumor vasculature and blood perfusion. For example, a rather uniform vascular structure will result in a ratio of γ_1/γ_2 near 1, whereas the coexistence of two time constants possibly reveals two mechanisms of regional blood perfusion in the tumor. A large time constant implies a slow perfusion through a poorly perfused area, whereas a small time constant indicates a fast perfusion through a well-perfused area. In the meantime, we can determine the ratio of the perfusion rates in these two areas after obtaining the ratios of amplitudes and time constants from the two-exponential curve fitting. In this way, we have developed a hemodynamic model for the NIR data interpretation, which allows us to associate tumor

blood oxygenation dynamics with regional blood perfusion and vascular structures of the tumor within the measured volume.

Discussions

NIRS is noninvasive and provides a real-time assessment of changes in tumor vascular hemoglobin oxygenation. In this chapter, we basically provide demonstration of the ease and utility of NIRS studies of tumors. By switching the inhaled gas from air to carbogen, the NIRS measurement produces a rapid biphasic elevation in Δ[HbO]. The rapid time constant is in the range of seconds to a minute, whereas the slow component (10 to 50 times slower) continues for many minutes (see Figs. 7B and 8). The elevated oxygenation process is completely reversible upon returning air breathing, but still present 10 to 20 min after the baseline inhalation in many cases (see Figs. 7B and 8). The high reproducibility of results suggests that one can apply repeated interventions to explore the efficacy of interventions designed to alter tumor vascular oxygenation (e.g., vascular targeting agents). Our recent study has also shown that tumor response to oxygen was much more rapid and fit well to a monoexponential curve. For almost every tumor in a group of seven breast tumors, the time to reach 80% of maximum elevation in Δ[HbO] was longer with carbogen intervention than with oxygen breathing.[24]

With single-channel and multichannel NIRS, we have measured relative changes in $[Hb]_{total}$ and [HbO] in breast and prostate rat tumors in response to hyperoxic respiratory intervention. We observed that respiratory challenge caused Δ[HbO] to rise promptly and significantly in both breast and prostate tumors. However, the total concentration of hemoglobin did not always behave consistently. The dynamic changes of tumor oxygenation can be modeled by a two-exponential expression with a fast and slow time constant. Based on the model, we suggest that the NIRS measurement can "see" two vascular mechanisms during tumor oxygenation under hyperoxic gas intervention. By fitting the two-exponential model with the NIR experimental data, we can determine the two time constants and their corresponding amplitudes, leading to the relationships between the two perfusion rates and between the vascular structures, as expressed in Eq. (18).

With this tumor model, we are able to obtain information on the blood perfusion of tumor: a large time constant usually represents a slow blood perfusion, whereas a small time constant indicates a fast blood perfusion. A combination of well-perfused and poorly perfused mechanisms in tumor vasculature will result in coexistence of two time constants. Indeed, some tumor lines have been reported with only 20–85% of vessels

perfused,[61] and it is known that tumor structures and oxygen distribution are highly heterogeneous.[46,62] Therefore it is highly possible that our NIRS readings often detect a mixture of both well-perfused and poorly perfused regions in the tumor, depending on the locations of sources and detectors of the NIR system.

In the process of developing the model, we introduced a vasculature coefficient, γ. We expect that γ depends on (1) oxygen consumption and (2) capillary density of the tumor. Further studies are underway to quantify more about this coefficient and to confirm our speculations.

As an example to demonstrate the direct use of the newly developed model, the multichannel NIR results are fitted with the model, and the corresponding fitted parameters are listed in Table I. It is reasonable to expect that the central region of a solid tumor is close to necrosis (i.e., a poorly perfused region), whereas the tumor peripheral region is highly vascularized. Then, Fig. 12B can be used to schematically illustrate possible tumor volumes interrogated by the multichannel detectors. Close inspection of Table I reveals that the tumor structure ratios of γ_1/γ_2 from the three respective detectors are significantly different, whereas the perfusion ratios of f_1/f_2 from detectors 1 and 3 are almost doubled with respect to that from detector 2. Besides the results presented here, we have observed similar ΔHbO profiles and fitted parameters from other breast tumors. In such a way, we can obtain more details of tumor heterogeneity by having more source–detector pairs in the measurements. Indeed, we are now in the process of developing a multichannel NIR imaging system, along with the imaging reconstruction algorithm, so that tumor heterogeneity can be studied with better spatial resolution.

The time constants are not source–detector separation-sensitive. Equations (6), (7), and (11) demonstrate that ΔHbO and ΔHb are proportional to $1/d$, where d is the source–detector separation. This indicates that a different d value will only stretch or compress an entire temporal profile of ΔHbO, but it does not change the transient behavior of time response. The same argument can apply to DPF. Currently we have grouped DPF into the unit of [HbO] for simplicity. If the DPF value is larger than 1, the values of Δ[HbO] and $\Delta[Hb]_{total}$ will decrease by a factor of DPF. However, this decrease does not affect the time constants, τ_1 and τ_2 the dynamic responses of tumor Δ[HbO] to respiratory intervention.

[61] H. J. J. A. Bernsen, P. F. J. W. Rijken, T. Oostendorp, and A. J. van der Kogel, *Br. J. Cancer* **71**, 721 (1995).

[62] R. P. Mason, P. P. Antich, E. E. Babcock, A. Constantinescu, P. Peschke, and E. W. Hahn, *Int. J. Radiat. Oncol. Biol. Phys.* **29**, 95 (1994).

The simultaneous measurements of Δ[HbO] and ΔpO_2, shown in this chapter, demonstrate the compatibility of the NIRS system with the needle electrode and the FOXY fiber-optic oxygen-sensing system, without interference. All three systems are relatively inexpensive and provide real-time measurements, but the needle electrode and the three-channel FOXY system monitor pO_2 (viz., ΔpO_2) in specific locations, whereas the NIRS system provides global measurements. There are a few advantages of the FOXY system over the needle electrode: (1) it allows multiple locations to be interrogated simultaneously and (2) it is much easier to use than electrodes, particularly in calibration and stability. However, the FOXY probes may not provide accurate absolute pO_2 readings.

It is well known that measurements of tumor pO_2 have prognostic value in the clinic.[28,63] In this chapter, we have shown a linear correlation between tumor ΔHbO and mean ΔpO_2 (Fig. 10) when a tumor undergoes a hyperoxic respiratory intervention, and thus the noninvasive NIRS monitoring could have a potential value for clinical practice. The major deficiency in our current approach is lack of spatial resolution, so implementation of an NIR imaging system for tumor monitoring is our current effort.

NIRS provides a global assessment, in contrast to blood oxygenation level dependent (BOLD)-MRI, which can provide high-resolution images.[64,65] Although the latter approach can show heterogeneity in both temporal and spatial response, the results are often summarized to show mean values only. As such, an a priori global measurement can provide similar insight into dynamic tumor physiology or drug pharmacodynamics, while being more cost-effective, portable, and easier to implement and operate. For example, several groups of researchers have previously used NIR studies of tumors to observe the influence of chemotherapy,[52] pentobarbital overdose,[52] ischemic clamping,[66] and infusion of perfluorocarbon blood substitute.[67] All of these investigations demonstrate potential versatility of the NIRS application for diverse future studies.

Furthermore, the setup in our NIRS uses transmission mode between the source and detector, which we believe probes large and deep portions of the tumor, including the periphery on each side, as well as the center (see Fig. 3). This is in contrast to the setups used by most other investigators,

[63] M. Höckel and P. Vaupel, *J. Natl. Cancer Inst.* **93**, 266 (2001).
[64] S. P. Robinson, D. R. Collingridge, F. A. Howe *et al.*, *NMR Biomed.* **12**, 98 (1999).
[65] X. Fan, J. N. River, M. Zamora *et al.*, *Int. J. Radiat. Oncol. Biol. Phys.* **54**, 1202 (2002).
[66] F. Steinberg, H. J. Röhrborn, K. M. Scheufler, T. Otto, and C. Streffer, *Adv. Exp. Med. Biol.* **428**, 69 (1996).
[67] H. D. Sostman, S. Rockwell, A. L. Sylva, D. Madwed, G. Cofer, H. C. Charles, R. Negro-Villar, and D. Moore, *Magn. Reson. Med.* **20**, 253 (1991).

who apply reflectance mode,[21,66,68] which predominately detects the behavior of the peripheral vasculature. Indeed, the dynamic results measured from breast tumors reported by Hull *et al.*[21] are consistent with the fast component that we have observed and attributed to the well-perfused regions of our tumors.

Given the evidence for intratumoral heterogeneity from MRI[46,69] and histology,[70] it will be important to advance the NIRS system to an NIR imaging system so as to study not only dynamic, but also spatial aspects of blood oxygenation in tumor vasculature. In the meantime, we believe the preliminary results reported here are proof of principle for NIR imaging of tumor vascular oxygenation, laying a foundation for more extensive studies to correlate NIR imaging measurements with tumor heterogeneity and heterogeneous responses to various tumor therapeutic interventions and treatments.

Conclusions

In conclusion, we believe that NIRS presents a new potential imaging modality to examine tumor vasculature rapidly, noninvasively, and cost-effectively. Ease of implementation and operation permit rapid application to accessible tumors in cancer patients. The inherent compatibility of fiber-optics technology and light with other modalities, such as electrodes[20,24] and MRI,[71] will facilitate multiparametric multimodality investigations of tumor heterogeneity and vasculature in the near future.

In summary, we have demonstrated in this chapter that the NIR technology can provide an efficient, real-time, noninvasive means for monitoring vascular oxygenation dynamics in tumors during hyperoxic respiratory challenge. Concentration changes in HbO measured from both breast and prostate tumors often display a very prompt rise, followed by a gradual persistence throughout the intervention. By developing a hemoperfusion model with two exponential terms and fitting the model to the ΔHbO data, we have recognized two perfusion mechanisms in tumor vasculature and quantified the ratios of the two perfusion rates.

Furthermore, we have also obtained tumor pO_2 measurements using a needle electrode or multichannel, fiber-optic, FOXY probe in simultaneous conjunction with the noninvasive NIRS measurement. The comparative

[68] M. Kragh, B. Quistorff, and P. E. Kristjansen, *Eur. J. Cancer* **37**, 924 (2001).
[69] S. P. Robinson, F. A. Howe, L. M. Rodrigues, M. Stubbs, and J. R. Griffiths, *Semin. Radiat. Oncol.* **8**, 198 (1998).
[70] B. M. Fenton, *Radiother. Oncol.* **44**, 183 (1997).
[71] G. Gulsen, H. Yu, J. Wang, O. Nalcioglu, S. Merritt, F. Bevilacqua, A. J. Durkin, D. J. Cuccia, R. Lanning, and B. J. Tromberg, *Technol. Cancer Res. Treatment* **1**, 497 (2002).

results exhibit a linear correlation between ΔHbO and ΔpO_2 of the tumors under hyperoxic gas intervention, suggesting that the NIRS approach could have a good potential value in the clinic. Finally, the newly developed tumor hemodynamic model allows us to reveal tumor heterogeneities at different tumor locations based on the multichannel NIRS results. Through this chapter, we lay a foundation for an NIR imaging technique to be further developed to facilitate investigations of tumor heterogeneity and vascular perfusion. Such a noninvasive imaging approach can enhance our understanding of the dynamics of tumor oxygenation and the mechanism of tumor physiology under baseline and perturbed conditions.

Acknowledgments

This work was supported in part by the Department of Defense Breast Cancer Research grants BC990287 (HL) and BC000833 (YG), and NIH R01 CA79515 (NCI)/EB002762 (NIBIB) (RPM). We are grateful to Vincent Bourke for his collaborative work on multichannel pO_2 measurements and Dr. Anca Constantinescu for her assistance with all the tumor investigations. We also gratefully acknowledge Dr. Britton Chance for his technical support on the multichannel NIR system.

[18] Measuring Changes in Tumor Oxygenation

By Dawen Zhao, Lan Jiang, and Ralph P. Mason

Introduction

Significance of pO_2 in Oncology

It has long been appreciated that hypoxic tumor cells are more resistant to radiotherapy.[1] Indeed, a 3-fold increase in radio resistance may occur when cells are irradiated under hypoxic conditions compared with oxygen pressure $pO_2 > 15$ torr for a given single radiation dose. However, recent modeling has indicated that the proportion of cells in the range 0–20 torr may be most significant in terms of surviving a course of fractionated radiotherapy.[2] Certain chemotherapeutic drugs also present differential efficacy, depending on hypoxia.[3,4] Increasingly, there is evidence that hypoxia also

[1] L. Gray, A. Conger *et al.*, *Br. J. Radiol.* **26,** 638 (1953).
[2] B. G. Wouters and J. M. Brown, *Radiat. Res.* **147,** 514 (1997).
[3] B. Teicher, J. Lazo *et al.*, *Cancer Res.* **41,** 73 (1981).
[4] A. C. Sartorelli, *Cancer Res.* **48,** 775 (1988).

Copyright 2004, Elsevier Inc.
All rights reserved.
0076-6879/04 $35.00

influences such critical characteristics as angiogenesis, tumor invasion, and metastasis.[5–8] Moreover, repeated bouts of intermittent hypoxic stress may be important in stimulating tumor progression.[9] Thus the ability to measure pO_2 noninvasively and repeatedly, with respect to acute or chronic interventions, becomes increasingly important.

Early work examined cells *in vitro*, where ambient oxygen concentrations are readily controlled. *In vivo*, hypoxia may be achieved by clamping the blood supply to a tumor,[10] but other levels of oxygenation reflect the interplay of supply and consumption.[11,12] Robust fine-needle polarographic electrodes opened the possibility of measuring pO_2 in tumors *in situ* and *in vivo* to define local pO_2 under baseline conditions or with respect to interventions. In early work, Cater and Silver[13] showed the ability to monitor pO_2 at individual locations in patients' tumors with respect to breathing oxygen. Later, Gatenby *et al.*[14] showed that pO_2 in a tumor was correlated with clinical outcome. Tumor oximetry received its greatest boost with the development of the Eppendorf Histograph polarographic needle electrode system.[15] This computer-controlled device equipped with a stepper motor can reveal distributions of tumor oxygenation and has been applied extensively to clinical trials. Many reports have now shown that tumors are highly heterogeneous and have extensive hypoxia; furthermore, strong correlations have been shown in cervix and head and neck tumors between median pO_2 or hypoxic fraction and survival or disease-free survival.[5,16–20] Extensive hypoxia also has been found in tumors of the prostate and breast.[21–23] Thus tumor oxygenation is now recognized as a strong

[5] E. K. Rofstad, K. Sundfor *et al.*, *Br. J. Cancer* **83,** 354 (2000).
[6] K. De Jaeger, M. C. Kavanagh *et al.*, *Br. J. Cancer* **84,** 1280 (2001).
[7] M. Höckel and P. Vaupel, *J. Natl. Cancer Inst.* **93,** 266 (2001).
[8] H. J. Knowles and A. L. Harris, *Breast Cancer Res.* **3,** 318 (2001).
[9] R. A. Cairns, T. Kalliomaki *et al.*, *Cancer Res.* **61,** 8903 (2001).
[10] J. Moulder and S. Rockwell, *Int. J. Radiat. Oncol. Biol. Phys.* **10,** 695 (1984).
[11] T. W. Secomb, R. Hsu *et al.*, *Adv. Exp. Med. Biol.* **454,** 629 (1998).
[12] M. W. Dewhirst, B. Klitzman *et al.*, *Int. J. Cancer* **90,** 237 (2000).
[13] D. Cater and I. Silver, *Acta Radiol.* **53,** 233 (1960).
[14] R. A. Gatenby, H. B. Kessler *et al.*, *Int. J. Radiat. Oncol. Biol. Phys.* **14,** 831 (1988).
[15] M. Nozue, I. Lee *et al.*, *J. Surg. Oncol.* **66,** 30 (1997).
[16] D. M. Brizel, S. P. Scully *et al.*, *Cancer Res.* **56,** 941 (1996).
[17] M. Höckel, K. Schlenger *et al.*, *Cancer Res.* **56,** 4509 (1996).
[18] M. Nordsmark, M. Overgaard *et al.*, *Radiother. Oncol.* **41,** 31 (1996).
[19] A. W. Fyles, M. Milosevic *et al.*, *Radiother. Oncol.* **48,** 149 (1998).
[20] T. H. Knocke, H. D. Weitmann *et al.*, *Radiother. Oncol.* **53,** 99 (1999).
[21] P. W. Vaupel, K. Schlenger *et al.*, *Cancer Res.* **51,** 3316 (1991).
[22] P. Hohenberger, C. Felger *et al.*, *Breast Cancer Res. Treat.* **48,** 97 (1998).
[23] B. Movsas, J. D. Chapman *et al.*, *Urology* **53,** 11 (1999).

EFFECT OF PHOTOTHERMAL THERAPY ON BREAST TUMOR VASCULAR CONTENTS: *NON-INVASIVE MONITORING BY NEAR INFRARED SPECTROSCOPY*

Yueqing Gu[1,3], Wei R. Chen[2], Mengna Xia[1], Sang W. Jeong[2], and Hanli Liu[1]*

[1] Biomedical Engineering Program

University of Texas at Arlington, Arlington, TX 76019

[2] Biomedical Engineering Program, Department of Physics and Engineering,

University of Central Oklahoma, Edmond, OK 73034

[3]Biomedical Engineering Laboratory, China Pharmaceutical University,

Nanjing, Jiangsu Province, P.R. China

Key words: Vascular Oxygenation, Breast Tumors, Photothermal Therapy, Non-invasive Monitoring, Near Infrared Spectroscopy, 805-nm Laser

Footnotes page

To whom correspondence should be addressed at:

Hanli Liu

Biomedical Engineering graduate program,

University of Texas at Arlington, TX76019

501 west first, ELB-220, P.O.Box 19138

Email: Hanli@uta.edu

Tel: 817-272-2054 Fax: 817-272-2251

Abbreviations: NIR , near infrared ; NIRS, near infrared spectroscopy; I&Q, In-phase and Quadrature-phase ; [HbO_2], oxygenated hemoglobin concentration; [Hb], deoxygenated hemoglobin concentration; $[Hb]_{total}$, total hemoglobin concentration;

ABSTRACT

The goal of this study was to investigate the effect of photothermal laser irradiation on rat breast tumor (DMBA-4) vascular contents. An 805-nm diode laser was used in our experiment with a power density ranging from 0.32 to 1.27 W/cm^2. The dynamic changes of oxygenated hemoglobin and total hemoglobin concentrations, $\Delta[HbO_2]$ and $\Delta[Hb]_{total}$, in rat tumors during photothermal irradiation were *non-invasively* monitored by a near infrared spectroscopy system (NIRS). A multi-channel thermal detection system was also used simultaneously to record temperatures at different locations within the tumors. Our experimental results showed that: 1) Photo irradiation did have the ability to induce hyperthermic effect inside the rat breast tumors in a single exponential trend; 2) The significant changes ($p<0.005$) of $\Delta[HbO_2]$ and $\Delta[Hb]_{total}$ in response to a low dosage of laser irradiation (0.32 W/cm^2) have a single exponential increasing trend, similar to that seen in the tumor interior temperature. This increase in vascular content may be attributed to vessel dilation under both thermal and photo effect. 3) The increase in magnitude of $\Delta[HbO_2]$ is nearly 2 times greater than that of $\Delta[Hb]_{total}$, suggesting that photo irradiation may enhance tumor vascular oxygenation. The last observation may be important to reveal the hidden mechanism of photo irradiation on tumors, leading to improvement of tumor treatment efficiency.

INTRODUCTION

Laser phototherapy, a non-surgical modality for cancer treatment, is gaining widespread acceptance because of precise energy delivery into the tumor tissue (1-3). The laser energy delivered to the targeted tumors can induce localized photomechanical, photochemical and photothermal reactions, thus killing tumor cells. In general, photochemical reactions may cause the change of chemical bonds and form toxic radicals, such as release of singlet oxygen, leading to the death of organized tissues. Photomechanical reactions may induce tissue stress, resulting in tissue cells broken up and ejection. Photothermal reactions may induce hyperthermia and coagulation, causing cell destruction (4). In particular, thermal cytotoxicity effects are found to be more profound under acidotic (low pH) conditions, which are often present in poorly oxygenated tissues (5-7), such as in tumors. Many research studies have reported the existence of acute/chronic hypoxic regions within the majority of solid tumors (8-10). As a result, cytotoxicity induced by selective photothermal irradiation can be more effective in tumor tissue than normal tissue. To further enhance the desirable photothermal effects, photosensitizers are often used in the targeted tumor tissue along with laser irradiation to cause selective and localized photon-tissue interactions (11-12). In addition, administration of an immunoadjuvant has been proved to increase systemic cancer cure and long-term resistance to cancer of the same origin, when combined with the selective thermal treatment (13-14). Chen et al have developed a laser immunotherapy by combining laser irradiation, a laser-absorbing dye and an immunoadjuvant to improve cancer therapy efficiency (15-18). The previous experimental results have demonstrated that this unique approach has positive effects on both primary and metastatic tumors.

However, the hemodynamic and physiological properties inside the tumors during photothermal therapy are poorly understood, although the underlying mechanism of the laser irradiation has been intensively studied (19-22). Measuring the reduction of tumor size and survival rates is the current practice to evaluate the therapeutic outcome of therapy. Obviously, non-invasive, real time monitoring of tumor hemodynamic characteristics before, during, and after therapy is highly desirable. Such a technique may help reveal the tumor physiology and therapeutic process caused by the therapy, providing treatment prognoses and guidance to optimize the light dosimetry so as to improve the therapeutic outcome. Near infrared spectroscopy (NIRS) has been demonstrated in our recent studies to be such a non-invasive means in monitoring tumor vascular oxygenation during therapeutic interventions (23-25).

In this study, we investigated the effects of photothermal therapy on tumor vascular contents and tumor temperature. An 805-nm diode laser was used for photothermal irradiation of mammary tumors in rats. The dynamic changes caused by the laser irradiation in oxygenated, deoxygenated and total hemoglobin concentrations, $\Delta[HbO_2]$, $\Delta[Hb]$, and $\Delta[Hb]_{total}$, in the tumor vasculature were monitored by an NIRS system. A multi-channel, thermal monitor was also used simultaneously to record the temperatures at three different locations inside the breast tumors. The correlations between the optical irradiation dosages, tumor temperatures, and tumor vascular contents were studied. The dynamic features of tumor temperature and vascular oxygenation were quantified to reveal the dynamic effects within the tumors under the laser irradiation.

MATERIALS AND METHODS

Near infrared spectroscopy The changes of oxygenated, deoxygenated, and total hemoglobin concentrations, $\Delta[HbO_2]$, $\Delta[Hb]$, and $\Delta[Hb]_{total}$, in tumor tissue caused by laser

irradiation were determined by a near-infrared, homodyne, frequency-domain, spectroscopy system (NIM, Philadelphia, PA), which has been described in detail elsewhere(23-25). Briefly, the amplitude-modulated light at 140 MHz at wavelengths of 758 nm and 785 nm illuminated the tumor surface through a light-delivery fiber bundle with output powers of 9 mW and 11 mW at 785 nm and 758 nm wavelengths, respectively, measured at the tip of the bundle by an optical power meter. The experimental setup is shown in Figure 1. The 805-nm laser light was vertically applied on the tumor surface. The delivering and detecting fiber bundles of the NIRS system were placed horizontally and in good contact with the surface of the tumors in a transmittance mode, without compressing the tumors. The diffused light through the tumor tissue was collected and filtered by a sharp low-pass optical filter, which cut off the optical signal above 805 nm from the laser irradiation, and then propagated into a photo multiplier tube (PMT) through the detecting fiber bundle. The signal detected by the PMT was demodulated through an In-phase and Quadrature-phase (I&Q) circuit, and the amplitude and phase of the signal were recorded.

Algorithms for calculations of $\Delta[HbO_2]$, $\Delta[Hb]$, and $\Delta[Hb]_{total}$ Historically, biological chemists and biochemists have utilized Beer-Lambert's law and developed the notation of optical density to express light absorption as a function of hemoglobin concentration (26-30),

$$\text{Optical Density (OD)} = Log(A_0/A) = \varepsilon c l \qquad (1)$$

where A_0 and A are light intensities of the incident and transmitted light, respectively, ε is the extinction coefficient of hemoglobin, c is the concentration of hemoglobin, and l is the length of light path through the measured sample. When the measured sample has a mixture of oxygenated and deoxygenated hemoglobin, Equation (1) can be further evolved to (28-30),

$$OD(\lambda) = \{\varepsilon_{Hb}(\lambda)\,[Hb] + \varepsilon_{HbO2}(\lambda)\,[HbO_2]\}\,l \qquad (2)$$

where $OD(\lambda)$ is the optical density at wavelength λ, $\varepsilon_{Hb}(\lambda)$ and $\varepsilon_{HbO2}(\lambda)$ are the extinction coefficients at wavelength λ for molar concentrations of deoxygenated hemoglobin, $[Hb]$, and oxygenated hemoglobin, $[HbO_2]$, respectively, assuming ferrihemoglobin is minimal. By employing two wavelengths, both $[HbO_2]$ and $[Hb]$ can be determined by measuring the OD values at the two specific wavelengths, provided that the values for $\varepsilon_{Hb}(\lambda)$ and $\varepsilon_{HbO2}(\lambda)$ are known:

$$[HbO_2] = \frac{\varepsilon_{Hb}(\lambda_2)OD(\lambda_1) - \varepsilon_{Hb}(\lambda_1)OD(\lambda_2)}{l[\varepsilon_{Hb}(\lambda_2)\varepsilon_{HbO2}(\lambda_1) - \varepsilon_{Hb}(\lambda_1)\varepsilon_{HbO2}(\lambda_2)]}, \tag{3}$$

$$[Hb] = \frac{\varepsilon_{HbO2}(\lambda_2)OD(\lambda_1) - \varepsilon_{HbO2}(\lambda_1)OD)(\lambda_2)}{l[\varepsilon_{Hb}(\lambda_1)\varepsilon_{HbO2}(\lambda_2) - \varepsilon_{Hb}(\lambda_2)\varepsilon_{HbO2}(\lambda_1)]}. \tag{4}$$

It follows that changes in [Hb] and [HbO_2] can be consequently given as:

$$\Delta[HbO_2] = \frac{\varepsilon_{Hb}(\lambda_2)\Delta OD(\lambda_1) - \varepsilon_{Hb}(\lambda_1)\Delta OD(\lambda 2)}{l[\varepsilon_{Hb}(\lambda_2)\varepsilon_{HbO2}(\lambda_1) - \varepsilon_{Hb}(\lambda_1)\varepsilon_{HbO2}(\lambda_2)]}, \tag{5}$$

$$\Delta[Hb] = \frac{\varepsilon_{HbO2}(\lambda_2)\Delta OD(\lambda_1) - \varepsilon_{HbO2}(\lambda_1)\Delta OD(\lambda_2)}{l[\varepsilon_{Hb}(\lambda_1)\varepsilon_{HbO2}(\lambda_2) - \varepsilon_{Hb}(\lambda_2)\varepsilon_{HbO2}(\lambda_2)]}, \tag{6}$$

where $\Delta OD(\lambda)$ represents a change in optical density at the specific wavelength, λ, and equals to $log(A_B/A_T)$. A_B and A_T correspond to light intensities measured under the baseline and transient conditions.

Note that in principle, l represents the optical path length between the source and detector. While l is simply the physical separation, d, between the source and detector through a non-scattering medium, exact quantification of l for an intact tissue or organ is complex because of light scattering in tissue. Since l is in proportion to the separation, d, we can associate l to d as $l=DPF*d$, where DPF is a differential path length factor to account for light scattering. It has been well accepted that together with DPF, Equation (2) can be treated as modified Beer-Lambert's law; and consequently, Equations (5) and (6) can be correctly used to quantify

changes in *[Hb]* and *[HbO₂]* in highly scattering media (31-32), such as in intact tissue or organs.

To be consistent with our previous work, we adopt in this paper the ε values published by Zijlstra et al (33). We had to interpolate the ε values at the two wavelengths employed in our study, followed by certain corrections due to the interpolation errors by phantom calibration measurements (24). Specifically, we included two factors, β_1 and β_2, for the calibrated algorithm, as given below:

$$\Delta[HbO_2] = \frac{\frac{\varepsilon_{Hb}(785\,nm)}{\beta_1} \times OD(758\,nm) - \varepsilon_{Hb}(758\,nm) \times OD(785\,nm)}{l\left[\varepsilon_{Hb}(785\,nm)\varepsilon_{HbO2}(758\,nm) - \varepsilon_{Hb}(758\,nm)\varepsilon_{HbO2}(785\,nm)\right]}, \tag{7}$$

$$\Delta[Hb] = \frac{\frac{\varepsilon_{HbO2}(785\,nm)}{\beta_2} \times OD(758\,nm) - \varepsilon_{HbO2}(758\,nm) \times OD(785\,nm)}{l\left[\varepsilon_{Hb}(785\,nm)\varepsilon_{HbO2}(758\,nm) - \varepsilon_{Hb}(758\,nm)\varepsilon_{HbO2}(785\,nm)\right]}, \tag{8}$$

where ε_{Hb}(758 nm) = 1.418, ε_{HbO2}(758 nm) = 0.6372, ε_{Hb}(785 nm) = 1.111, and ε_{HbO2}(785 nm) = 0.766, all in $mM^{-1}cm^{-1}$. Note that a factor of 4 has been multiplied for each of the ε's at the respective wavelengths to account for light absorption from 4 hemes per hemoglobin molecule (34) since the extinction coefficients published in the field of biochemistry were expressed on a heme basis (26-30). Furthermore, we have used β_1=1.103 and β_2=0.9035 according to our phantom study (24). After substituting all of the parameters into Equations (7) and (8), we have arrived at the final equations to quantify changes in hemoglobin concentration:

$$\Delta[HbO_2] = \frac{-2.658 \cdot OD(758\,nm) + 3.743 \cdot OD(785\,nm)}{d}, \tag{9}$$

$$\Delta[Hb] = \frac{2.238 \cdot OD(758\,nm) - 1.683 \cdot OD(785\,nm)}{d}. \tag{10}$$

$\Delta[Hb]_{total}$ can also be obtained by adding Equations (9) and (10),

$$\Delta[Hb]_{total} = \Delta[HbO_2] + \Delta[Hb] = \frac{-0.42 \cdot OD(758\,nm) + 2.06 \cdot OD(785\,nm)}{d}. \quad (11)$$

Notice that the units for $\Delta[HbO_2]$, $\Delta[Hb]$, and $\Delta[Hb]_{total}$ are mM; however, the values obtained from Equations (9) to (11) are scaled by a factor of DPF. Since DPF is so far an unknown parameter for tumors, we include it within the unit as mM/DPF.

Laser photothermal irradiation system The system used for the photothermal therapy consisted of an NIR diode laser, DIOMED 25 (DIOMEDICS, The Woodlands, TX), with an emitting peak wavelength at 805 nm and a maximum power output of 25 W. The laser light was coupled into an optical fiber, fitted with a microlens at the tip (Pioneer Optics, Windsor Locks, CT) to ensure a uniform beam density, and delivered onto the tumor surface. The laser beam diameter projected on the tumor surface was set as 2 cm in all the measurements by using the visible aiming light in the laser system. After the beam diameter was adjusted, the aiming light was turned off during NIR measurements.

Multi-channel thermal monitor A multi-channel thermal monitor (Omega, Stamford, CT), incorporating an OM-700 Omega Engineering Data Acquisition and Control Unit, was used simultaneously with the NIRS observation to monitor the internal temperatures at several locations within the tumors. Specifically, three thermal probes were inserted at the top (immediately below the overlaying skin), middle and bottom positions of the tumors, and one probe was located outside the tumor for room temperature recording. The data of each probe were recorded continuously, and the middle thermal probe recorded the internal tumor temperature near the center of the optical field of NIRS.

Animal model The transplantable, metastatic mammary tumor cells (DMBA-4)(35-37) were implanted in one of the inguinal fat pads of female Wistar Furth rats (Harlan Sprague Dawley Co. Indianapolis, IN). Once the tumors reached 0.5 to 0.8 cm in diameter, the rats were

anesthetized for the experiments. Hairs around tumors were removed for better probe contact in the NIRS measurement and for more efficient tumor exposure to the laser irradiation. The tumor diameters along the three major orthogonal axes (a,b,c) were measured to determine the volume of the tumors by using an ellipsoid approximation with the formula of $V=(\pi/6)abc$.

In this study, sixteen rat breast tumors were used in two different treatment protocols. Ten of the 16 rat tumors were first exposed to a single laser irradiation with a laser power of 0.32 W/cm^2 (1 W laser power in a 2-cm diameter beam) for 10 minutes. Three or four days later, 4 of the treated tumors, along with other six untreated tumors, were exposed to repeated laser irradiations with a power density of 0.32, 0.64, 0.96 and 1.28 W/cm^2 (1 W, 2 W, 3 W, and 4 W in 2 cm diameter beam), for 10 minutes with a recovery period of 10 minutes between two adjacent irradiations. Tumor temperatures, tumor vascular $\Delta[HbO_2]$, and $\Delta[Hb]_{total}$ were measured simultaneously in all the experiments.

RESULTS

Dynamic responses of $\Delta[HbO_2]$, $\Delta[Hb]_{total}$ and temperature to photothermal treatment

Using the experimental setup shown in Figure 1 and Equations (9) and (11), tumor vascular $\Delta[HbO_2]$, $\Delta[Hb]_{total}$ and internal temperatures were quantified simultaneously. Figure 2 shows the temporal profiles of $\Delta[HbO_2]$, $\Delta[Hb]_{total}$ and the internal temperatures of a rat tumor under photothermal irradiation with a laser power density of 0.32 W/cm^2. The experimental data consisted of 4 temporal periods, as labeled in the figure. In period 1, without irradiation, the thermal probes recorded the baseline temperatures at three different locations inside the tumor for about 6 minutes. In period 2, the NIRS system was turned on while the thermal recording continued, and the recorded thermal readings showed no obvious perturbation from the NIRS.

After the NIRS signals were stabilized, a 10-minute laser irradiation started. During the laser treatment, the tumor temperatures, $\Delta[HbO_2]$, and $\Delta[Hb]_{total}$ showed significant elevation (period 3 in Figure 2). Tumor temperatures increased significantly ($p<0.0001$) with the irradiation. The tumor volumes near the tumor surface had more significant thermal effects: the temperature at the top (T-top) varied from $25.3 \pm 0.1\ ^0C$ to $30.3 \pm 0.1\ ^0C$ (mean ± standard deviation), while the temperatures at the middle and bottom (T-middle and T-bottom) of the tumor were elevated from 26.1 ± 0.1 to $29.8 \pm 0.1\ ^0C$ and from $27.5 \pm 0.1\ ^0C$ to $28.9 \pm 0.1\ ^0C$, respectively. The maximal changes in T-top, T-middle and T-bottom caused by the laser irradiation were 5.0 ± 0.1^0C, 3.7 ± 0.1^0C and 1.4 ± 0.1^0C, respectively. Similarly, both $\Delta[HbO_2]$ and $\Delta[Hb]_{total}$ displayed significant increasing over the entire irradiation period ($p<0.005$), with the elevations of 0.37 ± 0.01 mM/DPF and 0.20 ± 0.01 mM/DPF, respectively. When the laser beam was turned off in period 4, $\Delta[HbO_2]$, $\Delta[Hb]_{total}$ and temperatures all decreased: with the temperatures reaching quickly the baselines, while $\Delta[HbO_2]$, $\Delta[Hb]_{total}$ declining more gradually and not quite reaching the baselines within the 10-minute recovery period.

In order to quantify the dynamic behaviors observed in Figure 2(a), single-exponential fittings were applied to T-top, T-middle, $\Delta[HbO_2]$, and $\Delta[Hb]_{total}$, on both rising and falling periods, as shown in Figures 2(b) and 2(c). The time constants obtained from such fittings reveal the dynamic responses of signals to the initiation and termination of photothermal irradiation. As shown in Figure 2(b), T-top (time constant of 4.5 ± 0.5 min) has a faster response to laser irradiation than T-middle (time constant as 14.4 ± 0.6 min). The time constants for $\Delta[HbO_2]$ and $\Delta[Hb]_{total}$ are 3.85 ± 0.03 min and 3.95 ± 0.06 min, respectively. In response to the termination of laser irradiation, T-top and T-middle have a time constant of 3.9 ± 0.5 min and 12.3 ± 0.6 min, respectively (Figure 2(c)). It is clearly seen that the dynamic thermal responses of the tumor to

laser irradiation and to the termination of laser irradiation are well matched both at the tumor surface and within the tumor. However, the time constants for $\Delta[HbO_2]$ and $\Delta[Hb]_{total}$ to return to the baseline are much longer in the falling period, with 18.5 ± 0.5 min and 24.3 ± 0.8 min, respectively, also shown in Figure 2(c).

Similar protocols and measurements were performed on the other 9 tumors. Figure 3 shows the average increases of the temperature at different locations. Temperatures near the tumor surface have maximal increases, while local temperatures near the bottom of the tumors have minimal increases observed from all the ten tumors. The average elevations for T-top and T-bottom are $7 \pm 3\ ^0C$ and $3 \pm 2\ ^0C$, respectively. The thermal readings from the middle position (T-middle) represent the average temperatures in the tumor volumes probed by the NIRS beams, and the average increase in T-middle for the 10 rats is $5 \pm 2\ ^0C$. The statistical analysis indicates significant differences between T-top, T-middle, and T-bottom ($p<0.05$).

To investigate dynamic behaviors of the tumors in response to the initiation and termination of laser irradiation, the time constants of T-top, T-middle, $\Delta[HbO_2]$, and $\Delta[Hb]_{total}$ obtained from the rising and falling periods are summarized in Table 1. The results demonstrate several points: 1) An average dynamic change in T-top is significantly ($p<0.05$) faster than that in T-middle in the rising period, with a time constant of 3.7 ± 1.1 min for T-top and 6.4 ± 3.2 min for T-middle. A similar significant difference ($p<0.01$) also holds in the falling period with a time constant of 3.8 ± 1.2 min for T-top and 6.6 ± 2.7 min for T-middle, respectively. 2) The dynamic responses of $\Delta[HbO_2]$, $\Delta[Hb]_{total}$, and T-middle have no significant differences during the initiation of photo irradiation ($p > 0.4$). 3) The average time constant of T-top in the rising period is similar ($p >0.9$) with that in the falling period, and so does that of T-middle ($p > 0.7$). However, 4) the dynamic response of $\Delta[HbO_2]$ in the falling period (a time constant of 28 ± 22 min) is

significantly slower ($p<0.01$) than that in the rising period (a time constant of 5.3 ± 2.8 min), and so does $\Delta[Hb]_{total}$ response with a time constant of 6.2 ± 3.7 min and 41 ± 32 min for the rising and falling periods, respectively ($p < 0.01$).

Furthermore, while $\Delta[HbO_2]$ and $\Delta[Hb]_{total}$ have similar dynamic trends in response to photo irradiation, the difference between their magnitudes exists. A strong correlation ($R^2= 0.95$) between $\Delta[HbO_2]$ and $\Delta[Hb]_{total}$ has been observed, as shown in Figure 4, where the amplitude in $\Delta[HbO_2]$ is nearly twice of that of $\Delta[Hb]_{total}$ for all of the 10 tumors (with a slop of the fitted curve being 0.54).

Effect of the optical power density on tumor $\Delta[HbO_2]$, $\Delta[Hb]_{total}$ and temperatures

Repeated laser irradiation was applied to the 10 tumors, 4 of which were used in the previous single-irradiation treatment. Figure 5(a) shows the profiles of the tumor vascular $\Delta[HbO_2]$, $\Delta[Hb]_{total}$ and tumor temperatures in response to irradiations under power densities of 0.32, 0.64, 0.96 and 1.27 W/cm^2, with an irradiation period of 10 minutes and a 10-minute recovery period between each treatment. Tumor temperatures (T-top, T-middle and T-bottom) increased significantly ($p<0.0001$) from the baseline to different maximum values according to the different laser powers. The maximal changes in temperature in the middle of the tumor (T-middle) due to consecutive irradiation displayed a strong linear dependence on the laser power density, as shown in Figure 5(b). However, $\Delta[HbO_2]$ and $\Delta[Hb]_{total}$ showed interesting behaviors in response to the thermal irradiations of different light dosages. Under relatively low laser power irradiations (0.32, 0.64, 0.96 W/cm^2), both $\Delta[HbO_2]$ and $\Delta[Hb]_{total}$ increased significantly ($p<0.0001$) with respect to the baselines, and they both declined significantly under a high laser power irradiation (1.27 W/cm^2), as shown in Figure 5(b). Similar to the feature observed in

single irradiation, $\Delta[HbO_2]$ values had greater magnitude than $\Delta[Hb]_{total}$, while their dynamic trends were consistent.

Temperature data for all of the 10 tumors under different power irradiations are plotted in Figure 6. The maximum changes in T-middle increase linearly with the optical radiation dosages, with a correlation of $R^2>0.91$ for all the cases and having an average slop of 4 ± 1.

DISCUSSION

In this study, we have investigated vascular $\Delta[HbO_2]$, $\Delta[Hb]_{total}$ and internal temperature simultaneously in rat breast tumors using an NIRS system and a thermal monitor, respectively, in response to photothermal therapy. The results obtained in this study clearly demonstrate the compatibility of the NIRS system with the temperature monitoring system, without noticeable interference between the two systems (Figure 2). The NIRS system offers a real-time measurement of $\Delta[HbO_2]$ and $\Delta[Hb]_{total}$ in tumor vasculature within the optical field of the NIR probes, while the multi-channel thermal monitor records the temperatures at specific locations within the tumors in real time. The compatibility of the two systems permits simultaneous determinations of thermal and vascular characteristics of treated tumors under photothermal therapy, providing valuable insight into the dynamic relationship between the tumor vascular contents and the thermal effect in treated tumor tissues.

As known, the hyperthermic treatment of tumors has been well established (38-40), and the cellular cytotoxicity caused by hyperthermic treatment has been proven to destruct the tumor cells. Laser irradiation applied in this study demonstrates its ability to induce hyperthermic effect inside the rat breast tumors. The single exponential increase in tumor temperature obtained in our results indicates that an extended exposure period to the laser beam may gradually stabilize the

tumor temperature at a certain level, depending on both the laser power density and the individual tumors (as seen in Figures 2(a) and 5(a)). Manipulation of the laser power may help adjust the internal tumor temperature, resulting in optimal hyperthermic tissue destruction. While a strong linear relationship between the maximum temperature increase within the tumors and the irradiation power density has been observed for all the tumors, the actual dependence of tumor temperature on the laser power density does vary from tumor to tumor (Figure 6). Such inter-tumor variability demonstrates the necessity of real time monitoring for tumor temperature under photothermal therapy. Moreover, the tumor temperatures near the surface (T-top) response to the photo irradiation more rapid and more significant than those within deeper tumor tissues (T-middle) (as seen in Figures 2, 3, 5(a), and Table 1). Such large thermal effect can cause tissue burning at the tumor surface. To avoid such thermal damage, intratumoral injection of a photosensitizer has been used by Chen et al to selectively manipulate the temperature within the tumor without severe damage at the tumor surface (15-17,41).

It is seen clearly in this study that tumor vascular contents, i.e., oxygenated and deoxygenated hemoglobin, are greatly affected by photothermal therapy. When the photothermal irradiation with a low power density (0.32 W/cm^2) was applied to the breast tumors, both $\Delta[HbO_2]$ and $\Delta[Hb]_{total}$ increased significantly ($p<0.005$) in all the tumors (Figs. 2(a), 4 and 5(a)). The dynamic behaviors of $\Delta[HbO_2]$ and $\Delta[Hb]_{total}$ in response to photo irradiation, quantified by the time constants, are in the same order as those of tumor interior temperature, T-middle (Table 1). This consistency suggests that the changes in tumor vascular contents result from the changes in internal tumor temperature. We expect that an increase in tumor temperature may lead to vessel dilation within tumor vasculature, further resulting in an increase in blood

volume. Such an increase in blood volume will give rise to an increase in $\Delta[Hb]_{total}$ as well as $\Delta[HbO_2]$.

Besides thermal effects, it is reasonable to expect other photo-activation processes involved in the laser irradiation. It is known that direct exposure of vascular tissue to visible light causes vasodilation (42), while the thermal effect from visible light is minor. Photoactivation has also been reported to cause upregulation of nitric oxide, and thus, producing vasodilation (43-45). The increase of tumor blood volume demonstrated in our study due to laser irradiation may be attributed to the vessel dilation under both thermal and photo effect. Consistently, the single-exponential trend of $\Delta[Hb]_{total}$, as well as of $\Delta[HbO_2]$, in response to laser irradiation indicated the existence of the limitation in vessel dilation. Furthermore, the dynamic response of $\Delta[HbO_2]$ and $\Delta[Hb]_{total}$ to the termination of photo irradiation is much slower than that of T-middle (Figure 2(b) and Table 1), implying a slower recovery of vasculature from its dilation.

Intriguingly, while $\Delta[HbO_2]$ has the same dynamic trend as $\Delta[Hb]_{total}$ in response to photo irradiation, the magnitude of $\Delta[HbO_2]$ are more profound than that of $\Delta[Hb]_{total}$ (Figure 4). This phenomenon let us speculate that the increase in $\Delta[HbO_2]$ comes from two parts: one part is from the increase of $\Delta[Hb]_{total}$, and another is from the conversion of deoxygenated hemoglobin to oxygenated hemoglobin. The correlation of magnitude between $\Delta[HbO_2]$ and $\Delta[Hb]_{total}$ unambiguously demonstrates that the increased total hemoglobin concentration, due to blood vessel dilation, is fully oxygenated immediately after the irradiation starts. It is also imply that photo irradiation may increase the tumor oxygenation, which will be beneficial to some non-surgical treatments, such as chemotherapy and radiotherapy (39). Also, this is perhaps the

reason that low-intensity near infrared irradiation has documented benefits for promoting wound healing in humans and animals (46-48).

However, when the laser irradiation power increased, $\Delta[HbO_2]$, as well as $\Delta[Hb]_{total}$, showed interesting responses. In some tumors, both increased with laser power while in some tumors both decreased, as shown in Figure 5(b). This may be due partly to the different tumor conditions. One reason for the decrease of $\Delta[HbO_2]$ and $\Delta[Hb]_{total}$ might be that higher level irradiations may destroy the vasculature in tumor, resulting in shut-down of blood supply to the tumors. Further experiments will help better determine and understand the changes of $\Delta[HbO_2]$ and $\Delta[Hb]_{total}$ under higher power levels of laser irradiations.

In summary, changes in breast tumor temperature and vascular oxygenation have been simultaneously measured using a multi-channel thermal monitor and an NIRS system, while the tumors were under photothermal irradiation. The results have demonstrated that: 1) the compatibility of thermal monitoring system and the NIR system permits simultaneous determinations of thermal and vascular characteristics of the treated tumors; 2) photo irradiation did have the ability to induce hyperthermic effect inside the rat breast tumors in a single exponential trend, thus, leading to destruction of the tumor cells; 3) the response of $\Delta[HbO_2]$ and $\Delta[Hb]_{total}$ to photo irradiation may be attributed to vessel dilation under both thermal and photo effect; 4) the fact that the change in the magnitude of $\Delta[HbO_2]$ is two times greater than that of $\Delta[Hb]_{total}$ suggests that photo irradiation may enhance tumor vascular oxygenation. The primary results from this study clearly suggest that besides a considerable thermal effect, low power density irradiation could also result in a significant enhancement of tumor vascular oxygenation. This enhancement may lead to improvement of treatment efficiency.

Acknowledgements: The authors acknowledge the support from the Department of Defense Breast Cancer Research Programs DAMD17-01-1-0423 (Y. Gu) and DAMD17-00-1-0459 (H. Liu), from the Oklahoma Center for Advancement of Science and Technology (OCAST) AP01-016 (W.R. Chen) and from the University of Central Oklahoma (W.R. Chen).

REFERENCE

1. Jacques, S. L. (1992) Laser-tissue interactions. Photochemical, photothermal, and photomechanical. *Surg.Clin. North Am.* **72**, 531-558.

2. Thomsen, S. L. (1991) Pathologic analysis of photothermal and photomechanical effects of laser-tissue interactions. *Photochem. Photobiol.* **53**, 825-835.

3. Chen, W. R., R. L. Adams, S. Heaton , D.T. Dickey, K. E. Bartels and R. E. Nordquist (1995) Chromophore-enhanced laser-tumor tissue photo-thermal interaction using an 808-nm diode laser. *Cancer Lett.* **88**, 15-19.

4. Chen, W. R., R. L. Adams, K. E. Bartels, and R. E. Nordquist (1995) Chromophore enhanced in vivo tumor cell destruction using an 808-nm diode laser. *Cancer Lett.* **94**, 125-131.

5. Thistlethwaite, A. J., D. B. Leeper, D. J. Moylan, R. E. Nerlinger (1986). pH distribution in human tumors. *Int J.Radiat Oncol Biol Phys* **11**,1647-1652.

6. Reinhold, H. S., B. Endrich (1986) Tumor microcirculation as a target for hyperthermia: a review. *Int. J. Hyperthermia*, **2**, 111-137.

7. Anghileri, L. J., J. Robert (1986) *Hyperthermia in Cancer Treatment*, Boca Raton, FL: CRC Press.

8. Thews, O., D. K. Kelleher, P. Vaupel (2002) Dynamics of tumor oxygenation and red blood cell flux in response to inspiratory hyperoxia combined with different levels of inspiratory hypercapnia. *Radiotherapy and Oncology*, **62**: 77-85.

9. Hockel, M., P. Vaupel (2001) Biological consequences of tumor hypoxia. *Semin Oncol.* **28** (2 Suppl 8), 36-41.

10. Wouters, B. G., S. A. Weppler, M. Koritzinsky, W. Landuyt, S. Nuyts, J. Theys, P. K. Chiu, P. Lambin (2002) Hypoxia as a target for combined modality treatments. *Eur J Cancer*. **38**(2), 240-57.

11. Henderson, B. W., T. J. Dougherty (1992) How does photodynamic therapy work? *Photochem. Photobiol.* **55**,145-157.

12. Ochsner, M. (1997) Photophysical and photobiological processes in the photodynamic therapy of tumors. *J. Photochem. Photobiol. B Biol.,* **39**, 1-18.

13. Korbelik, M., V.R. Naraparaju, N. Yamamoto (1997) Macrophage-directed immunotherapy as adjuvant to photodynamic therapy of cancer. *Br. J. Cancer*. **75**, 202-207

14. Curry, P. M., A. J. Steward., L. Hardwicke, C. Smith, J.R. North (2001) Augmentation of tumor immunity with ENHANZYN adjuvant following verteporfin PDT: photodynamic vaccination (PDV). *Proc. SPIE*, **4257**: 9-18.

15. Chen, W. R., R. L Adams, R. Carubelli, R. E. Nordquist (1997) Laser-photosensitizer assisted immunotherapy: A novel modality for cancer treatment. *Cancer Lett.*, **115**, 25-30.

16. Chen,W. R., A. K. Singhal, H. Liu, R. E. Nordquist (2001) Antitumor Immunity induced by laser immunotherapy and its adoptive transfer *Cancer Res.*,**61**,459-461.

17. Chen, W. R., W. G. Zhu, J. R. Dynlacht, H. Liu, R.E. Nordquist (1999) long-term tumor resistance induced by laser photo-immunotherapy. *Int. J. Cancer*, **81**, 808-812.

18. Chen, W.R., H. Liu, J.W. Ritchey, K.E Bartels, M.D. Lucroy, R.E. Nordquist (2002) Effect of different components of laser immunotherapy in treatment of metastatic tumors in rats. *Cancer Res.* **62**, 4295-4299.

19. Fingar, V. H., T. J. Wieman, K. W. Doak (1991) Mechanistic studies of PDT-induced vascular damage: evidence that eicosanoids mediate this process. *Int. J. Radiat. Biol.*, **60**, 303-309.

20. Yu, W., J. Naim, R. Lanzafame (1994) The effect of laser irradiation on the release of bFGF from 3T3 Fibroblasts, *Photochem. & Photobiol.* **59**,167-170.

21. Karu, T. (1988) Molecular mechanism of the therapeutic effect of low intensity laser radiation. *Lasers in the life sciences* **2(1),** 53-74.

22. Margaret, T. T., W. Riley, X. Bai, E. Buchmann, H. T. Whelan (2001) Light-emitting diode treatment reverses the effect of TTX on cytochrome oxidase in neurons. *Neurochemistry.* **12,** 3033-3037.

23. Liu, H., Y. Song, K. L. Worden, X. Jiang, A. Constantinescu, and R. P. Mason (2000) Noninvasive Investigation of Blood Oxygenation Dynamics of Tumors by Near Infrared Spectroscopy. *Applied Optics* **39**(28), 5231-5243.

24. Kim, J. G., Y. Song, D. Zhao, A. Constantinescu, R. P. Mason, and Hanli Liu (2003) Interplay of Tumor Vascular Oxygenation and pO_2 in Tumors Using NIRS, ^{19}F MR pO_2 Mapping, and pO_2 Needle Electrode. *J. of Biomedical Optics* **8** (1), 53-62.

25. Gu, Y., V. Bourke, J. G. Kim, A. Constantinescu, R. P. Mason, H. Liu (2003) Dynamic response of breast tumor oxygenation to hyperoxic respiratory challenge monitored with three oxygen-sensitive parameters. *Applied Optics* **42**(16), 2960-2967.

26. Horecker, B. L. (1943) The absorption spectra of hemoglobin and its derivatives in the visible and near infrared regions. *J. of Biol. Chem.* **148**, 173-183.

27. Van Kampen, E. J. and W. G. Zijlstra (1965) Determination of hemoglobin and its derivatives. *Adv. Clin. Chem.*, **8**, 141-187.

28. Benesch, R., G. Macduff, and R. E. Benesch (1965) Determination of oxygen equilibria with a versatile new tonometer. *Anal. Biochem.*, **11**, 81-87.

29. Benesch, R. E., R. Benesch, and S. Yung (1973) Equations for the spectrophotometric analysis of hemoglobin mixtures. *Anal. Biochem.*, **55**, 245-248.

30. Van Assendelft, O. W. and W. G. Zijlstra (1975) Extinction coefficients for use in equations for the spectrophotometric analysis of haemoglobin mixtures. *Anal. Biochem.*, **69**, 43-48.

31.Sevick, E. M., B. Chance, J. Leigh, S. Nioka, and M. Maris (1991) Quantitation of time- and frequency-resolved optical spectra for the determination of tissue oxygenation. *Anal. Biochem.* **195,** 330-351.

32. Gu, Y., Z. Qian, J. Chen, D. Blessington, N. Ramanujam, and B. Chance (2002) High resolution three dimensional scanning optical image system for intrinsic and extrinsic contrast agents in tissue. *Rev. Sci. Instrum.***73**, 172-178.

33. Zijlstra, W. G., A. Buursma, H. E. Falke and J. F. Catsburg (1994) Spectrophotometry of hemoglobin: absorption spectra of rat oxyhemoglobin, deoxyhemoglobin, carboxyhemoglobin, and methemoglobin. *Comp. Biochem. Physiol.* **107B**(1),161-166.

34. Cope, M. (1991) The application of near infrared spectroscopy to non invasive monitoring of cerebral oxygenation in the newborn infant. Ph.D. thesis, Appendix B, 316-323, University College London.

35. Chatterjee, S. K., and U. Kim (1978) Fucosyltransferase activity in metastasizing and nonmetastasizing rat mammary carcinomas. *J. National Cancer Institute*, **61**, 151-162.

36. Chatterjee, S. K., and U. Kim (1977) Galactosyltransferase activity in metastasizing and nonmetastasizing rat mammary carcinomas and its possible relationship with tumor cell surface antigen shedding. *J. National Cancer Institute*, ***58***, 273-280.

37. Chatterjee, S. K. and U. Kim (1976) Biochemical properties of cyclic nucleotide phosphodiesterase in metastasizing and nonmetastasizing rat mammary carcinomas. *J. National Cancer Institute*, ***56***, 105-110.

38. Song, C. W., A. lokshina, J. G. Rhee, M. Patten, S. H. Levitt (1984) Implication of blood flow in hyperthermic treatment of tumors. *IEEE Trans Biomed Eng* **31**, 9-16.

39. Dewey, E. C., L. E. Hopwood, S. A. Sapareto, L. E Gerweck (1977) Cellular responses to combination of hyperthermia and radiation *Radiology* **123**, 463-474.

40. Sapareto, S. A., W. C. Dewey (1984) Thermal dose determination in cancer therapy. *Int. J. Radiat Oncol Biol Phys.***10**, 787-800.

41. Liu, V. G. , T. M. Cowan, S. W. Jeong, S. L. Jacques, E. C. Lemley, W. R. Chen (2002) Selective photothermal interaction using an 805nm diode laser and indocyanine green in gel phantom and chicken breast tissue. *Lasers Med Sci.* **17**,272-279.

42. Furchgott, R. F., S. J. Ehrreich, E. Greenblatt (1961) The photoactivated relaxation of smooth muscle of rabbit aorta. *J. General Phusiology*, **44**, 499-518.

43.Lee, K. C., Y. J. Kang, H. Y. Lee (1998) Comparison of relaxations evoked by photoactivation of NO-Containing compounds and nitrergic nerve stimulation in 5-Hydroxytryptamine and potassium contracted rat gastric fundus. *General Pharmac.* **30**(4), 585-591.

44. Venturini, C. M., R. M. J. Palmer, and S. Moncada (1993) Vascular smooth muscle contains a depletable store of a vasodilator which is light-activated and restored by donors of Nitric Oxide. *J. Pharmacol. Exp. Therap.* **266(3)**, 1497-1500.

45. Matsunaga, K. R., F. Furchgott (1991) Response of rabbit aorta to nitric oxide and superoxide generated by ultraviolet irradiation of solutions containing inorganic nitrite. *J. Pharmacol. Exp. Ter.* **259**,1140-1146.

46. Whelan, H., R. Smits, E. Buchman, N. Whelan, S. Turner, D. Margolis (2001) Effect of NASA light-emitting diode irradiation on wound healing. *J. Clinical Laser Medicine & Surgery.* **19**, 305-314.

47. Noble, J. G., A. S. Lowe, G. D. Baxter (2001) Monochromatic infrared irradiation (890nm): Effect of a multisource array upon conduction in the human median nerve. *J. Clinical Laser Medicine & Surgery*, **19**(6), 291-295 .

48. Schindl, A., M. Schindl, H. Pernerstorfer-Schon, L. Schindl (2000) Low-intensity laser therapy: A review," *J. Investigative Medicine* **48**, 313-326.

Figure Legends

Figure 1. Experimental setup for the simultaneous NIRS and thermal measurements of breast tumors under photothermal therapy. PMT represents a photo multiplier tube; I/Q is an in-phase and quadrature-phase demodulator for retrieving amplitude and phase information. The thermal detection system comprises multiple thermal sensing probes, three of which are inserted into different regions of the tumor, and one probe was used to measure room temperature. The power- adjustable laser light (805 nm) is vertically delivered to tumor surface with a 2-cm beam diameter for photo irradiation.

Figure 2. (a) Temporal profiles of the changes in tumor oxygenation and total hemoglobin concentrations, $\Delta[HbO_2]$ and $\Delta[Hb]_{total}$, and three intra-tumor temperatures during photothermal intervention in a representative DMBA-4 rat breast tumor (2.4 cm^3). The profile is divided into 4 periods, and the laser irradiation was applied only in Period 3. (b) Respective single-exponential curve fittings for the rising period of T-top, T-middle, $\Delta[HbO_2]$ and $\Delta[Hb]_{total}$ displayed in (a). Single exponential fitting yields: T-top=5.76*(1-exp(-(t-14)/4.49)+ 24.95 with R=0.99; T-middle =7.28*(1-exp(-(t-14)/14.3)+25.98 with R=0.99; $\Delta[HbO_2]$=0.093*(1-exp(-(t-14)/3.85)+ 0.013 with R=0.98; $\Delta[Hb]_{total}$ =0.044*(1-exp(-(t-14)/3.95)+0.012 with R=0.98; (c) Respective single-exponential curve fittings for the falling period of T-top, T-middle, $\Delta[HbO_2]$ and $\Delta[Hb]_{total}$ displayed in (a). Single exponential fitting yields: T-top = -4.48*(1-exp(-(t-25)/3.86)+29.23 with R=0.98; T-middle = -3.83*(1-exp(-(t-25)/12.29)+30.42 with R=0.99; $\Delta[HbO_2]$=-0.163*(1-exp(-(t-25)/18.5)+ 0.10 with R=0.94; $\Delta[Hb]_{total}$]= -0.114*(1-exp(-(t-25)/24.3)+ 0.06 with R=0.92.

Figure 3. Average changes in temperature from the 10 rats for T-top, T-middle and T-bottom.

Figure 4. Relationship between $\Delta[HbO_2]$ and $\Delta[Hb]_{total}$ for the 10 rat tumors under single laser irradiation treatment (0.32 W/cm^2 for 10 minutes) with a linear fit of $\Delta[Hb]_{total} = 0.54*\Delta[HbO_2] - 0.0039$ (the solid curve) and a correlation of $R^2=0.96$. The dashed line represents the situation of $\Delta[HbO_2] = \Delta[Hb]_{total}$.

Figure 5. (a) The temporal profiles of vascular $\Delta[HbO_2]$, $\Delta[Hb]_{total}$ and temperatures of a tumor (#6, 3.0 cm^3), in response to repeated laser irradiations with different laser power densities (0.32, 0.64, 0.96 and 1.27 W/cm^2) for a 10-minute treatment cycle with a 10-minute recovery period between each treatment. (b). The correlations between the changes in $\Delta[HbO_2]$ (solid triangles), $\Delta[Hb]_{total}$ (squares), T-middle (open triangles), and laser irradiation power densities in the tumors.

Figure 6. (a) Correlations between the maximum changes in T-middle reached at the end of each photothermal treatment cycle and the optical irradiation power density from the 10 treated rats.

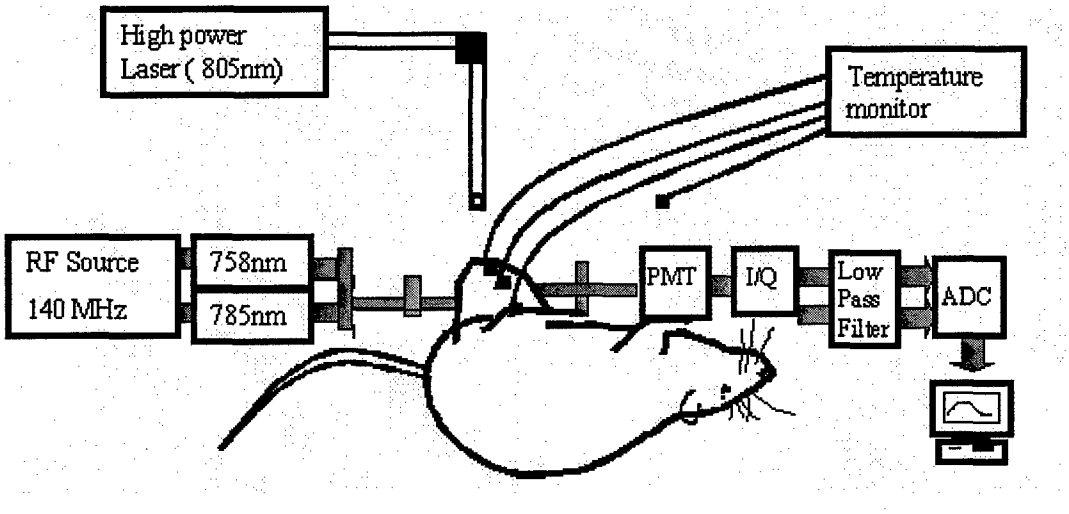
High power
Laser (805nm)
Temperature
monitor
RF Source
140 MHz
758nm
785nm
PMT
I/Q
Low
Pass
Filter
ADC

Figure 1

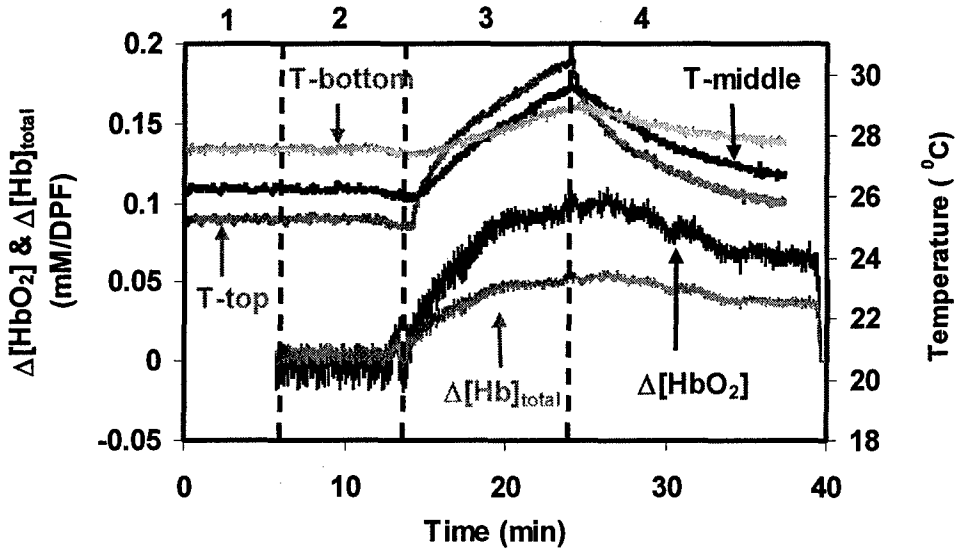

Figure 2(a)

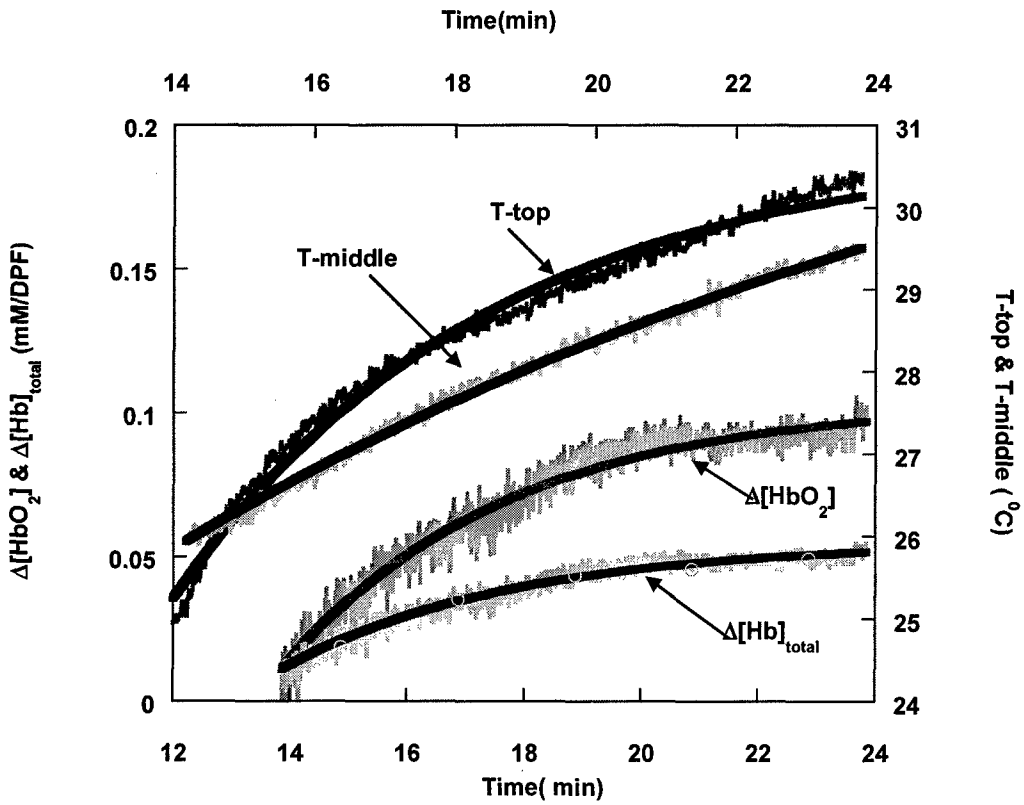

Figure 2(b)

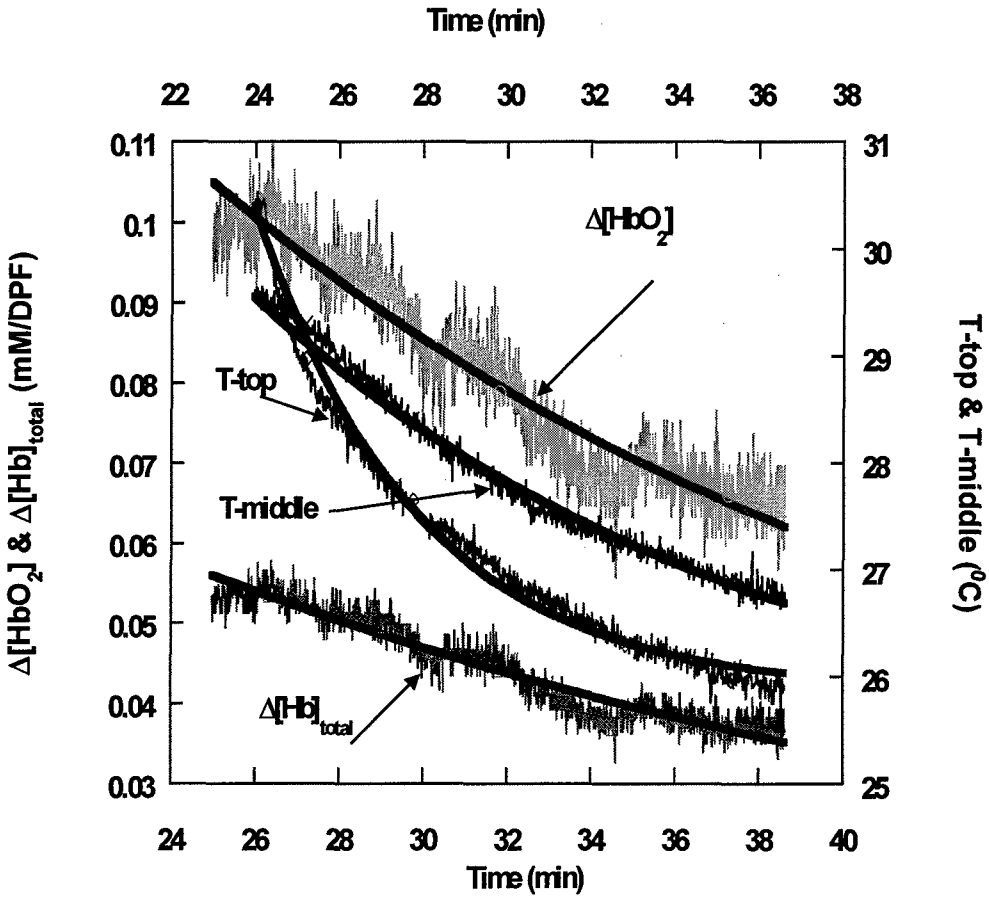
Time (min)
22
24
26
28
30
32
34
36
38
0.11
0.1
0.09
0.08
0.07
0.06
0.05
0.04
0.03
31
30
29
28
27
26
25
Δ[HbO2]
T-top
T-middle
Δ[Hb]total
Δ[HbO2] & Δ[Hb]total (mM/DPF)
T-top & T-middle (°C)
24
26
28
30
32
34
36
38
40
Time (min)

Figure 2(c)

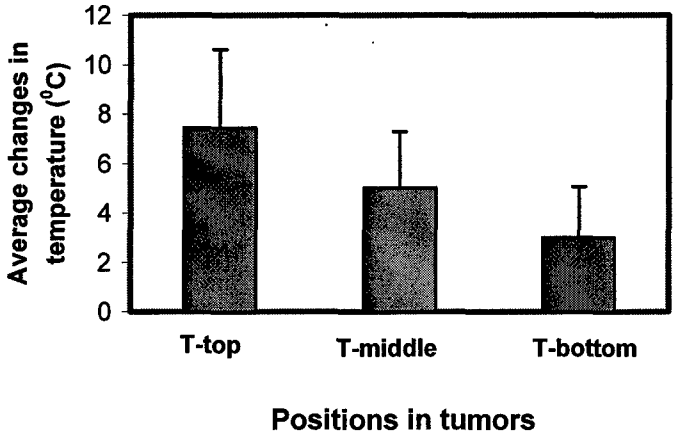

Figure 3

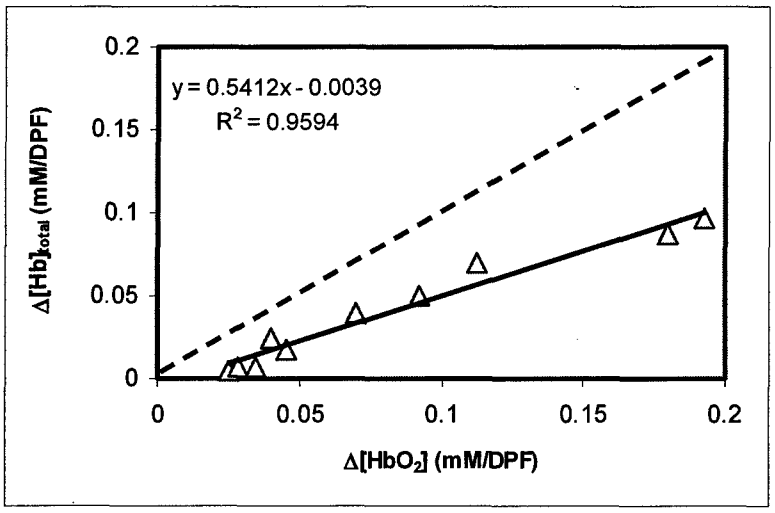

Figure 4

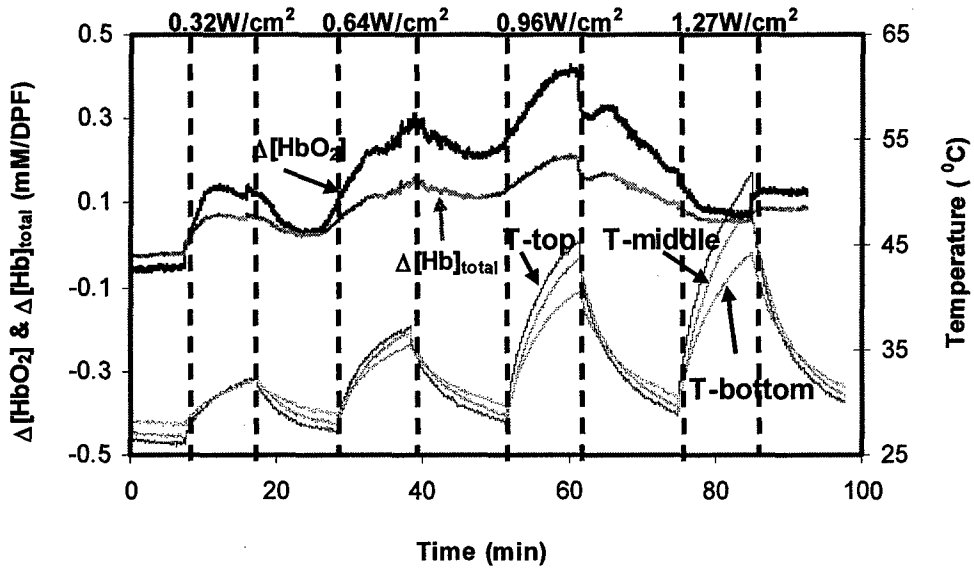

Fig.5 (a)

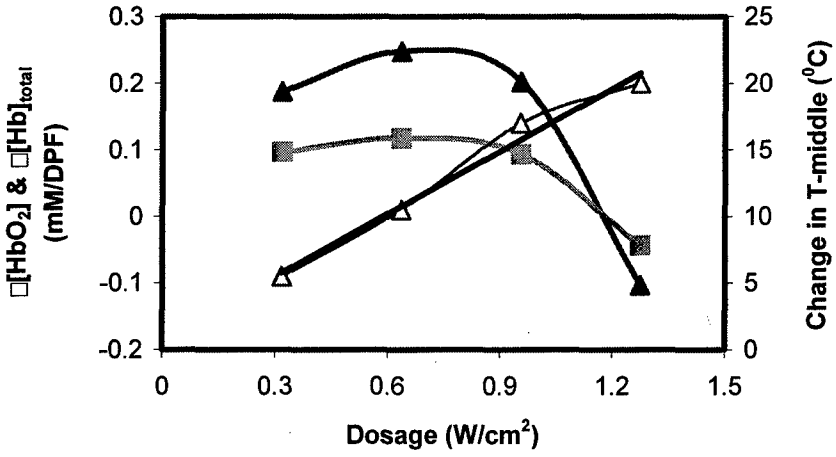

Figure 5(b)

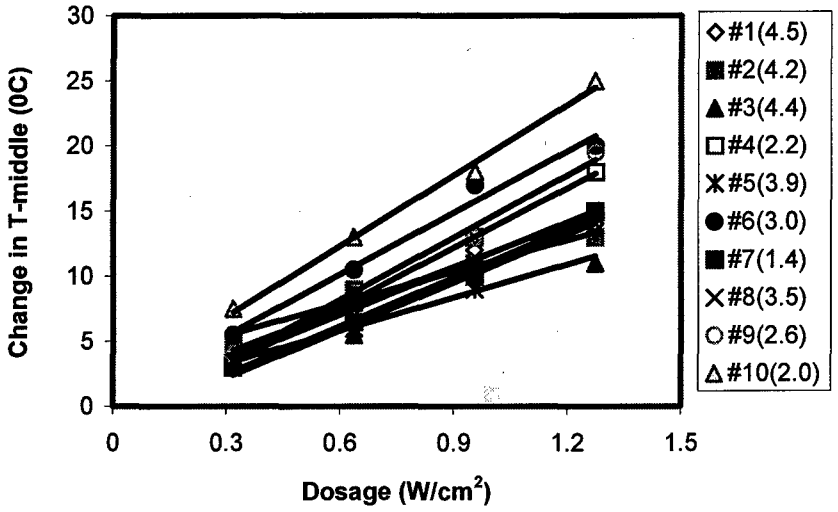
30
25
20
15
10
5
0
Change in T-middle (0C)
0
0.3
0.6
0.9
1.2
1.5
Dosage (W/cm2)
#1(4.5)
#2(4.2)
#3(4.4)
#4(2.2)
#5(3.9)
#6(3.0)
#7(1.4)
#8(3.5)
#9(2.6)
#10(2.0)

Figure 6

Table1. Time constants of T-top, T-middle, $\Delta[HbO_2]$, and $\Delta[Hb]_{total}$ with respect to photo irradiation and termination

tumor size (cm^3)	Rising part (in response to irradiation)				Falling part (in response to termination)			
	T-top	T-middle	$[HbO_2]$	$[Hb]_{total}$	T-top	T-middle	$[HbO_2]$	$[Hb]_{total}$
2.4	4.49	14.3	3.85	3.95	3.86	12.29	18.5	24.3
2.5	2.47	6.77	1.99	1.53	3.17	8.27	50	74
0.68	4.83	4.83	1.76	1.66	3.87	4.45	20	25
0.53	4.61	7.62	1.84	1.91	4.56	8.37	3.63	2.75
1.2	3.28	5.17	6.9	9.8	4.20	6.30	80	120
3.3	4.70	6.65	7.34	7.83	3.58	4.45	11.3	29.9
1.9	1.89	3.85	10.0	12.0	1.30	3.43	28	37
3.4	2.69	3.13	6.76	7.81	2.96	4.58	35	45
2.1	3.25	4.31	7.32	7.58	4.52	5.65	23.5	30
3.0	4.50	7.80	5.60	8.40	5.50	8.30	15.5	23.4
Average	3.7	6.4	5.3	6.2	3.8	6.6	28.	41
S.D.	1.1	3.2	2.8	3.7	1.2	2.7	22.	33

Estimation of blood volume fraction sampled by near infrared spectroscopy and ^{19}F magnetic resonance spectroscopy

Yueqing Gu[1,3], Ralph Mason[2], and Hanli Liu[1]

[1]*Joint Program of Biomedical Engineering, University of Texas at Arlington, Arlington, TX 76019*
[2]*Dept.of Radiology, University of Texas Southwestern Medical Center, Dallas, TX 75390*
[3]*School of Life Science and Technology, China Pharmaceutical University, Nanjing, PR.China 21009*
yueqing@uta.edu, Ralph.mason@utswmed.edu, hanli@uta.edu

Abstract: The purpose of this study is to introduce an experimental approach to estimate the percentage of blood volume sampled by near infrared (NIR) system. Carbogen (5% CO_2, 95% O_2) respiratory intervention was used to induce physiological changes in a group of Fisher rat breast tumors. The change of total hemoglobin concentration, $\Delta[Hb]_{total}$, and of tumor blood volume, $\Delta V_{T\text{-}blood}$, in 6 breast tumors were measured by near infrared spectroscopy and ^{19}F magnetic resonance spectroscopy of perflubron, respectively. The ratio of $\Delta[Hb]_{total}/\Delta V_{T\text{-}blood}$ was used to calculate the blood vascular percentage sampled by NIR spectroscopy. The overall results showed that the mean value of the vascular blood volume fraction interrogated by the NIR measurement is within the range of 15~30% of total blood volume in tumor tissues. Such information is useful in understanding the sampling area most sensitive by the NIR techniques, practically valuable in assessing absolute changes in vascular hemoglobin concentrations and oxygenation in solid tumors under therapeutic interventions.

©2003 Optical Society of America

OCIS codes: (000.0000) optical path length, Near infrared spectroscopy, MRS, breast tumor.

References and links

1. W. Cheong, S. A. Prahl, and A. J. Welch,."A review of the optical properties of biological tissue," IEEE J. Quantum Electron. **26** (12), 2166-2183 (1990).
2. N. Ramanujam, "Fluorescence spectroscopy of Neoplastic and non-Neoplastics tissue," Neoplasia. **2**(1), 89-117 (2000).
3. A. M. Siege, J. J. A. Marota, and D. A. Boas. "Design and evaluation of a continuous wave diffuse optical tomography system," Opt. Express. **4**(8), 287-298 (1999).
4. B. Chance, E. Anday, S. Nioka, S. Zhou, L. Hong, K. Worden, C. Li, T. Murray, Y. Ovetsky, D. Pidikiti, and R. Thomas, "A novel method for fast imaging of brain function, non-invasively, with light," Opt. Express. **2**(10), 411-423 (1998).
5. V. Ntaiachristors, H. Ma, and B. Chance, "Multichannel photon counting instrument for spatially resolved near infrared spectroscopy," Rev. Sci. Instrum. **70**(1), 1444-1451 (1999).
6. B. W. Pogue, M. Testorf, and T. Mcbride, "Instrumentation and design of a frequency domain diffuse optical tomography imager for breast cancer detection," Opt. Express. **1**(13), 391-403 (1999).
7. K. Sokolov, R. Drezek, and K. Gossage, "Reflectance spectroscopy with polarized light: is it sensitive to cellular and nuclear morpology," Opt. Express. **5**(13), 302-317 (1999).
8. A. Mayevsky, S. Lebourdais, and B. Chance, "The interrelation between brain PO_2 and NADH oxidation-reduction state in the Gerbil," J. Neuroscience Res. **5**, 173-182 (1980).
9. E. M. Sevick, B. Chance, J. Leigh, and M. Maris "Quantitation of time- and frequency- resolved optical spectra for the determination of tissue oxygenation," Anal. Biochem. **195**, 330-351 (1991).
10. H. Liu, Y. Song, K. L. Worden, X. Jiang, A. Constantinescu, and R. P. Mason, "Noninvasive investigation of blood oxygenation dynamics of tumors by near-infrared spectroscopy," Appl. Opt. **39**, 5231-5243 (2000).
11. J. G. Kim, Y. Song, D. Zhao, A. Constantinescu, R. P. Mason, and H. Liu, "Interplay of Tumor Vascular Oxygenation and pO_2 in Tumors Using NIRS, ^{19}F MR pO_2 Mapping, and pO_2 Needle Electrode," J. Biomed. Optics. **8**, 53-62 (2003).

12. Y. Gu, V. Bourke, J. Kim, A. Constantinescu, R. P. Mason, and H. Liu, "Dynamic response of breast tumor oxygenation to hyperoxic respiratory challenge monitored with three oxygen-sensitive parameters," Applied Optics, **42**(16), 2960-67 (2003)
13. H. Liu, B. Chance, "Influence of blood vessels on the measurement of hemoglobin ocygenation as determined by time-resolved reflectance spectroscopy", Med.Phys. **22**(8), 1209-1216 (1995).
14. M. Firbank, E. Okada, D. T. Delpy, "Investigation of the effect of discrete absorbers upon the measurement of blood volume with near-infrared spectroscopy", Phys. Med. Biol. **42**, 465-477(1997).
15. B. W. Pogue, E. A. White, U. L. Osterberg, K. D. Paulsen, "Absorbance of opaque microstructures in optically diffuse media", Applied. Optics, **40**, 4616-4621(2001).
16. M. C. Van Beekvelt, W. N. Colier, R. A. Wevers and B. G. Van Engelen, "Performance of near infrared spectroscopy in measuring local O2 comsumption and blood flow in skeletal muscle", J. Apple Physiol. **90**(2), 511-519(2001).
17. R. A. De Blasi, M. Ferrari, A. Natali, G. Conti, A. Mega, A. Gasparetto, "Noninvasive measurement of forearm blood flow and oxygen comsumption by near infrared spectroscopy", J. Appl Physiol. **76**(3), 1388-1393(1994).
18. C. Thomas, C. Counsell, P. Wood, G.E. Adams, "Use of F-19 NMR spectroscopy and hydralazine for measuring dynamic changes in blood perfusion volume in tumors in mice," JNCI; **84**,174-80(1992).
19. N. J. Baldwin, Y. Wang, and T. C. Ng, "In situ ^{19}F MRS measurement of RIF-1 tumor blood volume: Corroboration by radioisotope-labeled [^{125}I]-albumin and correlation to tumor size," Magn. Reson. Imaging, **14**(3),275-280 (1996).
20. M. Cope, D. T. Delpy, E. O. R.Reynolds, S. Wray, J. S. Wyatt, and P. van der Zee, "Methods of quantitating cerebral near infrared spectroscopy data," Adv. Exp. Med. Biol., **222**, 183-190 (1988).
21. Y. Gu, Z. Qian, J. Chen, D. Blessington, N. Ramanujam, and B. Chance, "High resolution three dimensional scanning optical image system for intrinsic and extrinsic contrast agents in tissue," Rev. Sci. Instrum. **73**, 172-178 (2002).
22. H. P. Shukla, R. P. Mason, D. E. Woessner, and P. P. Antich, "A comparison of three commercial perfluorocarbon emulsions as high field NMR probes of oxygen tension and temperature," J. Magn. Reson. B, **106**, 131-141 (1995).
23. E. W. Hahn, P. Peschke, R. P. Mason, E. E. Babcock,, and P.P.Antich, "Isolated tumor growth in a surgically formed skin pedicle in the rat: A new tumor model for NMR studies," Magn.Reson. Imaging **11**, 1007-1017 (1993).
24. B. L. Horecker, "The absorption spectra of hemoglobin and its derivatives in the visible and near infrared regions", *J. of Biol. Chem.* **148**, 173-183 (1943).
25. E. J. Van Kampen, and W. G. Zijlstra, " Determination of hemoglobin and its derivatives", *Adv. Clin. Chem.*, **8**, 141-187 (1965).
26. R. Benesch, G. Macduff, and R. E. Benesch, " Determination of oxygen equilibria with a versatile new tonometer", *Anal. Biochem.*, **11**, 81-87 (1965).
27. R. E. Benesch, R. Benesch, and S. Yung, " Equations for the spectrophotometric analysis of hemoglobin mixtures", *Anal. Biochem.*, **55**, 245-248(1973).
28. O. W. Van Assendelft, and W. G. Zijlstra, "Extinction coefficients for use in equations for the spectrophotometric analysis of haemoglobin mixtures", *Anal. Biochem.*, **69**, 43-48 (1975).
29. W. G. Zijlstra, A. Buursma, H. E. Falke and J. F. Catsburg, "Spectrophotometry of hemoglobin: absorption spectra of rat oxyhemoglobin, deoxyhemoglobin, carboxyhemoglobin, and methemoglobin", *Comp. Biochem. Physiol.* **107B**(1),161-166 (1994).
30. M. Cope, "The application of near infrared spectroscopy to non invasive monitoring of cerebral oxygenation in the newborn infant", Ph.D. thesis, Appendix B, 316-323, University College London(1991)
31. S. I. Fox, *Human Physiology*, 6th edition, McGraw-Hill Companies, Inc. Chapter 13, Heart and Circulation, 388-391(1999).
32. L. A. Paunescu, "Tissue blood flow and oxygen consumption measured with near infrared frequency-domain spectroscopy," Degree of Doctor of Philosophy (University of Illinois, Urbana,2001)
33. S. R. Arridge, M. Cope, and D. T. Delpy, "The theroretical basis for the determination of optical pathlengths in tissue: temporal and frequency analysis," Phys. Med. Biol., **37**(7), 1531-1560 (1992).
34. M. Ferrari, Q. Wei, L. Carraresi, R. A. de Blasi, and G. Zaccanti, "Time-resolved spectroscopy of the human forearm," J. Photochem. Photobiol. B:Biol., **16**, 141-153 (1992).
35. P. van der Zee, M. Cope, S. R. Arridge, M. Essenpreis, L. A. Potter, A. D. Edwards, J. S. Wyatt, D. C. McCormick, S. C. Roth, E. O. R. Reynolds, and D. T. Delpy, "Experimentally measured optical pathlengths for the adult head, calf and forearm and the head of the newborn infants as a function of inter optode spacing," Adv. Exp. Med. Biol., **316**, 143-153 (1992).
36. D. T. Delpy, M. Cope, P. van der Zee, S. Arridge, S. Wray, and J. Wyatt, "Estimation of optical pathlength through tissue from direct time of flight measurement," Phys. Med. Biol. **33**(12), 1433-1442 (1988).
37. M. Kohl, C. Nolte, H. R. Heekeren, S. Horst, U. Scholz, H. Obrig, and A. Villringer, "Determination of the wavelength dependence of the differential pathlength factor from near-infrared pulse signals," Phys. Med. Biol., **43**, 1771-1782 (1998).
38. J. S. Ultman, and C. A. Piantadosi, " Differential pathlength factor for diffuse photon scattering through tissue by a pulse-response method," Math. Biosci. **107**, 73-82 (1991).

39. P. van der Zee, S. R. Arridge, M. Cope, and D. T. Delpy, "The effect of optode positioning on optical pathlength in near infrared spectroscopy of brain," Adv. Exp. Med. Biol., **277**, 79-84 (1990).
40. H. Liu, M. Miwa, B. Beauvoit, N.G. Wang, and B. Chance, "Characterization of absorption and scattering properties of small-volume biological samples using time-resolved spectroscopy," *Anal. Biochem.* **213**, 378-385 (1993).
41. R. G. Steen, K. Kitagishi, and K. Morgan, "In vivo measurement of tumor blood oxygenation by near-infrared spectroscopy: Immediate effects of pentobarbital overdose or carmustine treatment," J. Neuro-Oncol., **22**, 209-220 (1994).
42. R. P. Choudhury, V. Fuster; J. J. Badimon, E. A. Fisher; Z. A. Fayad, "MRI and Characterization of Atherosclerotic Plaque," *Arteriosclerosis, Thrombosis, and Vascular Biology*.**22**,1065-1072 (2002).
43. J. R. Forder and G. M. Pohost, "Cardiovascular nuclear magnetic resonance: basic and clinical applications" J Clin Invest. **111** (11), 1630–1639 (2003).
44. Y. Gu, H. Liu, Y. Song, W. Cui, A. Constantinescu, and R. P. Mason, "Tumor vascular hemodynamic contents: assessed by NIR spectroscopy and ^{19}F MRS of PFOB," to be submitted to Int. J.Radiat.Oncol.Bio.Phys..

1. Introduction

In biomedical research, optical spectroscopy and imaging can potentially provide rapid, economical, and non-invasive diagnostic links between crucial tissue characteristics and cancer detection or diagnosis [1-7]. Near infrared (NIR) light in the range of 700 nm to 900 nm has an optimal penetrating depth in tissue (up to 15 centimeters), since photon transport in tissue is dominated by light scattering rather than absorption. Therefore, the use of NIR light enables sampling of large tissue volumes, such as the breast, brain, and skeletal muscles as well as tumors deep in the tissue. In the NIR spectral range, two important endogenous tissue chromospheres, i.e., oxygenated and deoxygenated hemoglobin (HbO_2 and Hb, respectively), display oxygen-dependent absorption features [8,9].Experimental determination of absorption quantities of tissue can provide an indication of several physiological parameters, such as hemoglobin /myoglobin concentrations, vascular oxygenation, and blood volume changes. Such quantification could be important in cancer investigations with a potential for impact in cancer research, as we have demonstrated in our previous reports [10-12].

However, although the measurement of absorption by the endogenous tissue chromosphere can be quantified accurately, it is not known as how much the total blood volume within the tissue is sampled by NIR system. It has been reported that NIR system is most sensitive to microvessel density (i.e., arterioles, capillaries, venules)[13-14]. The opaque microstructures in tissue have also contribution to the absorption [15]. The measured absorption is actually a volume-weighted average absorption of the sampled vessels and the surrounding tissue. Thus, the measured chromosphere concentration is usually less than the actual value. Meanwhile, the blood flow measured by NIRS was reported 2~3 times lower than the plethysmographic flow[16-17]. These reports motivated us to investigate what the percentage of blood volume in tissue is sampled by NIR system. In particular, tumor tissue is recognized as high heterogeneous and angiogenous. Accurate determination of tumor vascular blood by NIRS may provide crucial information for assessing tumor progress and guiding tumor treatment.

Several investigators have shown that vascular blood volume can be estimated by ^{19}F NMR (Nucleus Magnetic Resonance) spectroscopy following infusion of a perfluorocarbon blood substitute emulsion [18-19]. And our previous reports indicated the ability of NIR spectroscopy as a monitoring tool for the changes in tumor total hemoglobin concentration. Correlating NMR and NIR measurements could then provide an experimental approach to estimate the percentage of blood volume sampled by NIR spectroscopy in solid tumors. Specifically, we performed measurements of changes in total hemoglobin concentration, $\Delta[Hb]_{total}$, and changes in tumor blood volume, $\Delta V_{T\text{-}blood}$, in breast tumors using near infrared spectroscopy (NIRS) and ^{19}F magnetic resonance spectroscopy (MRS) of perflubron (formerly called perfluorooctyl bromide or PFOB), respectively. The ratio of $\Delta[Hb]_{total}/\Delta V_{T\text{-}blood}$ was used to calculate the fractions of blood volume sampled by NIRS and MRS in tumors.

2. Materials and Methods

2.1 Near Infrared spectroscopy for the measurement of $\Delta[Hb]_{total}$

A homodyne, frequency-domain NIRS system (NIM, Philadelphia, PA) was used in our experiments, as described in detail previously [10-12]. Briefly, the amplitude-modulated light at 140 MHz from two NIR laser diodes at 758 nm and 785 nm was projected on one side of the tumor through a delivery fiber bundle. The diffused light through the tumor was collected and propagated to a photomultiplier tube (PMT) by a second fiber bundle. The signal from the PMT was demodulated through an In-phase and Quadrature-phase circuit, and the amplitude and phase were recorded. Figure 1 shows the schematic diagram. Based on modified Beer-Lambert's law [10,20-21] and the recorded amplitude, the changes in oxy-, deoxygenated hemoglobin and total hemoglobin concentrations, $\Delta[HbO_2]$, $\Delta[Hb]$ and $\Delta[Hb]_{total}$ due to respiratory intervention were estimated as described below. In this NIRS system, phase signal possess high noise, only amplitude signal was used for the calculation.

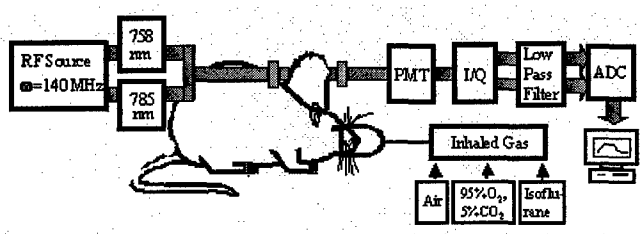

Fig. 1. Schematic diagram of experimental setup for the NIR spectroscopy system. A 3 mm-diameter fiber bundles deliver and detect the laser light through the tumor in transmittance geometry. PMT represents a photomultiplier tube. I/Q is an in-phase and quadrature phase demodulator for retrieving amplitude and phase information.

2.2 ^{19}F MRS of perflubron for the measurement of tumor blood volume $V_{T\text{-}blood}$

An Omega CSI 4.7 T superconducting magnet system (Acustar™, Bruker Instrument, Inc., Fremont, CA) was used for the measurement of tumor blood volume. The artificial blood substitutes [18-19], An emulsion of perflubron (Oxygent™,Alliance Pharmaceutical Corp., San Diego, CA) (2ml) was infused into a tumor breathing rat i.v. as a blood volume indicator. The tumors were placed within a frequency-tunable ($^1H/^{19}F$), single-turn, solenoid coil, together with a sealed capillary containing sodium trifluoroacetate (TFA), which was used as an external standard for quantifying/calibrating tumor blood volume.

Under fully relaxed conditions, integration of ^{19}F signal from the tumor was linearly proportional to the total number of ^{19}F nuclear spins of perflubron in the tumor, which, in turn, was linearly proportional to the total blood volume in the tumor, assuming that the perflubron emulsion had reached an equilibrium state with the blood throughout the tumor [22]. To ensure full relaxation a repetition time (TR) of 30 seconds was used. The spectral peaks of perflubron were integrated in the data post-processing. Following the tumor measurement, the rat was removed leaving the reference TFA capillary in the original position in the RF coil. 0.5 ml blood was drawn from the rat tail vein and placed in the RF coil without disturbing the reference TFA capillary. Another quantitative ^{19}F spectrum was acquired. Thus, the tumor blood volume can be calculated based on the following equation:

$$V_{T_blood} = V_{S_blood} \cdot \left(\frac{I_{T_blood}}{I_{S_blood}}\right) \cdot \left(\frac{I_{S_TFA}}{I_{T_TFA}}\right) \qquad (1)$$

where, V_{T_blood} and V_{S_blood} were the tumor blood volume and blood sample volume (ml), I_{T_blood} and I_{S_blood} were the integrated NMR signal from ^{19}F of perflubron in the rat tumor and in the blood sample, respectively and I_{blood_TFA} and I_{Tumor_TFA} were the integrals of the ^{19}F NMR signal from the TFA capillary.

2.3 Animal model and protocols

Mammary adenocarcinomas 13762NF were implanted in skin pedicles [23] on the forebacks of female Fisher 344 rats (~150 g). Once the tumors reached 1~2 cm diameter, rats were anesthetized with ketamine hydrochloride (100 mg/ml, i.p.) and maintained under general gaseous anesthesia with 1.3% isoflurane in air (1 dm^3/min). Tumors were shaved to improve optical contact for NIR light transmission. Tumor volume was estimated using an ellipsoid approximation ($V=(\pi/6).a.b.c$) from the three orthogonal diameters (a,b,c) measured with calipers.

In this study, breast tumor bearing Fisher rats were challenged with carbogen (95% O_2 + 5% CO_2) in the sequence air-carbogen–air. The $\Delta[Hb]_{total}$ values with respect to the carbogen inhalations were monitored by NIRS. For rats exhibiting a significant $\Delta[Hb]_{total}$ in response to hyperoxic gas, the same rat was re-anesthetized in the next day and infused with 2 ml of perflubron emulsion. ^{19}F MRS measurement of tumor blood volume was performed 30 min later allowing sufficient time for the perflubron emulsion to reach an equilibrium state within the blood. The inhaled gas sequence was repeated. Six breast tumor rats exhibited significant responses in $\Delta[Hb]_{total}$ to hyperoxic gas intervention and were studied here.

3. Algorithm for calculations of $\Delta[Hb]_{total}$ and fraction of sampled blood volume

Based on Beer-Lambert's law, optical attenuation, presented by Optical Density (OD), can be expressed as a function of concentration of chromospheres (24-28),

$$\text{Optical Density (OD)} = Log(A_0/A) = \varepsilon c l \quad (1)$$

where A_0 and A are light intensities of the incident and transmitted light, respectively, ε is the extinction coefficient of chromospheres, c is the concentration of chromosphere, and l is the optical path-length through the measured sample. When the measured sample has a mixture of chromosphere, i.e., oxygenated and deoxygenated hemoglobin in tumor tissue, the changes in oxygenated and deoxygenated hemoglobin concentrations ($\Delta[HbO_2]$, $\Delta[Hb]$) can cause a change in optical density, which can be evolved as (26-28) the following:

$$\Delta OD(\lambda) = log(A_B/A_T) = \{\varepsilon_{Hb}(\lambda)\Delta[Hb] + \varepsilon_{HbO2}(\lambda)\Delta[HbO_2]\}\, l \quad (2)$$

where $\Delta OD(\lambda)$ represents a change in optical density at the specific wavelength, λ. A_B and A_T correspond to light intensities measured under the baseline and transient conditions. $\varepsilon_{Hb}(\lambda)$ and $\varepsilon_{HbO2}(\lambda)$ are the extinction coefficients at wavelength λ for molar concentrations of deoxygenated hemoglobin, $[Hb]$, and oxygenated hemoglobin, $[HbO_2]$, respectively, assuming ferrihemoglobin is minimal. By employing two wavelengths in Equation (2), both $\Delta[HbO_2]$ and $\Delta[Hb]$ can be determined by measuring the ΔOD values at the two specific wavelengths, provided that the values for $\varepsilon_{Hb}(\lambda)$ and $\varepsilon_{HbO2}(\lambda)$ are known:

$$\Delta[HbO_2] = \frac{\varepsilon_{Hb}(\lambda_2)\Delta OD(\lambda_1) - \varepsilon_{Hb}(\lambda_1)\Delta OD(\lambda_2)}{l\left[\varepsilon_{Hb}(\lambda_2)\varepsilon_{HbO2}(\lambda_1) - \varepsilon_{Hb}(\lambda_1)\varepsilon_{HbO2}(\lambda_2)\right]}, \quad (3)$$

$$\Delta[Hb] = \frac{\varepsilon_{HbO2}(\lambda_2)\Delta OD(\lambda_1) - \varepsilon_{HbO2}(\lambda_1)\Delta OD(\lambda_2)}{l\left[\varepsilon_{Hb}(\lambda_1)\varepsilon_{HbO2}(\lambda_2) - \varepsilon_{Hb}(\lambda_2)\varepsilon_{HbO2}(\lambda_2)\right]}. \quad (4)$$

Note that in principle, l represents the optical path length between the source and detector. While l is simply the physical separation, d, between the source and detector through a non-scattering medium, exact quantification of l for an intact tissue or organ is complex because of light scattering in tissue. Since l is in proportion to the separation, d, we can associate l to d as $l=DPF*d$, where DPF is a differential path length factor to account for light scattering. It has been well accepted that together with DPF, Equation (2) can be treated

as modified Beer-Lambert's law; and consequently, Equations (5) and (6) can be correctly used to quantify changes in *[Hb]* and *[HbO_2]* in highly scattering media, such as in intact tissue or organs.

To be consistent with our previous work, we adopt in this paper the ε values published by Zijlstra et al (29). We had to interpolate the ε values at the two wavelengths employed in our study, i.e., ε_{Hb}(758 nm) = 1.418, ε_{HbO2}(758 nm) = 0.6372, ε_{Hb}(785 nm) = 1.111, and ε_{HbO2}(785 nm) = 0.766, all in $mM^{-1}cm^{-1}$. Note that a factor of 4 has been multiplied for each of the ε's at the respective wavelengths to account for light absorption from 4 hemes per hemoglobin molecule (30) since the extinction coefficients published in the field of biochemistry were expressed on a heme basis (26-30).

To further calibrate the calculation of $\Delta[HbO_2]$, $\Delta[Hb]$, and $\Delta[Hb]_{total}$ derived in Equation (5)-(6) with the interpolated extinction coefficient, we conducted a serial of phantom experiments, which was previously described in detail (11). The calibration performance gave rise to two empiric factors β_1 and β_2, where β_1=1.103 and β_2=0.9035, as given below:

$$\Delta[HbO_2] = \frac{\frac{\varepsilon_{Hb}(785\,nm)}{\beta_1} \times OD(758\,nm) - \varepsilon_{Hb}(758\,nm) \times OD(785\,nm)}{l\left[\varepsilon_{Hb}(785\,nm)\varepsilon_{HbO2}(758\,nm) - \varepsilon_{Hb}(758\,nm)\varepsilon_{HbO2}(785\,nm)\right]}, \quad (7)$$

$$\Delta[Hb] = \frac{\frac{\varepsilon_{HbO2}(785\,nm)}{\beta_2} \times OD(758\,nm) - \varepsilon_{HbO2}(758\,nm) \times OD(785\,nm)}{l\left[\varepsilon_{Hb}(785\,nm)\varepsilon_{HbO2}(758\,nm) - \varepsilon_{Hb}(758\,nm)\varepsilon_{HbO2}(785\,nm)\right]}. \quad (8)$$

After substituting all of the parameters into Equations (7) and (8), we have arrived at the final equations to quantify changes in hemoglobin concentration:

$$\Delta[HbO_2] = \frac{-2.658 \cdot OD(758\,nm) + 3.743 \cdot OD(785\,nm)}{d * DPF}, \quad (9)$$

$$\Delta[Hb] = \frac{2.238 \cdot OD(758\,nm) - 1.683 \cdot OD(785\,nm)}{d * DPF}. \quad (10)$$

$\Delta[Hb]_{total}$ can also be obtained by adding Equations (9) and (10),

$$\Delta[Hb]_{total} = \Delta[HbO_2] + \Delta[Hb] = \frac{-0.42 \cdot OD(758\,nm) + 2.06 \cdot OD(785\,nm)}{d * DPF} \quad (11)$$

The units of $\Delta[HbO_2]$, $\Delta[Hb]$, and $\Delta[Hb]_{total}$ are mM; Since DPF is so far an unknown parameter for tumors, we include it within the unite as mM/DPF in the relative measurements. Here, a reasonable range of 2~4 was assigned in this study (reference). Based on the amplitude measured from NIR spectroscopy and Equation (11), we can get the changes of total hemoglobin concentration, $\Delta[Hb]_{total}$, in breast tumors under carbogen intervention.

On the other hand, the changes of tumor blood volume, $\Delta V_{T\text{-}blood}$, with respect to carbogen inhalation can be obtained from MRS measurement. Assuming K is hemoglobin concentration in gram/liter in blood, M is hemoglobin molecular weight in gram/mole, $V_{T\text{-}physical}$ represents tumor physical volume in cm^3, the average changes of tumor hemoglobin concentration, ΔC, sampled by MRS can be expressed as

$$\Delta C = \frac{\Delta V_{T-blood} * K}{M * V_{T-physical}} \tag{12}$$

The unit for ΔC is mole/liter $=10^3$ mM. The percentage of tumor vascular blood volume sampled by NIRS and by MRS can be expressed as:

$$\frac{\Delta[Hb]_{total}}{\Delta C} * 100\% = \frac{\Delta[Hb]_{total} * M * V_{T-physical}}{\Delta V_{T-blood} * K} * 100\% \tag{13}$$

Taking K=150 g/l [30] and M=68000 g/mol [31], the percentage can be deduced from Eq.(13) based on the measurements of $\Delta[Hb]_{total}$ and $\Delta V_{T\text{-}blood}$ from NIRS and MRS, respectively.

4. Results

The changes of total hemoglobin concentration, $\Delta[Hb]_{total}$, and blood volume, $V_{T\text{-}blood}$, were monitored by NIR spectroscopy and ^{19}F MRS of perflubron on consecutive days, respectively. Figure 2 shows the time course profiles of $\Delta[Hb]_{total}$ and $V_{T\text{-}blood}$ on a representative breast tumor (2.6 cm^3) with respect to carbogen intervention. When the inhaled gas was switched from air to carbogen, $\Delta[Hb]_{total}$ increased significantly ($p<0.0001$) from a baseline value of 0.0005 ± 0.0015 mM/DPF to a maximal value of 0.0199 ± 0.001 mM/DPF over the period of carbogen intervention, with a maximal increasing of 0.0194 mM/DPF. After the gas was switched back to air, a significant drop ($p< 0.0001$) of $\Delta[Hb]_{total}$ occurred, and followed by a plateau at 0.009 ± 0.001 mM/DPF.

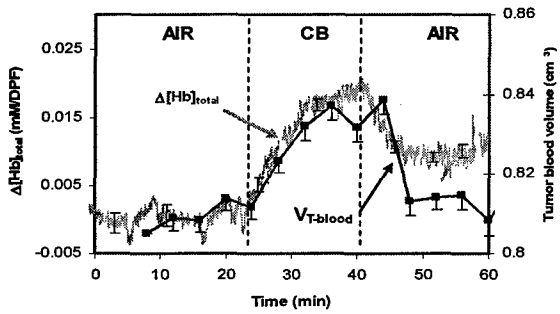

Fig. 2. Time course profile of $\Delta[Hb]'_{Total}$ and $V_{T\text{-}blood}$ for a representative breast tumor (2.6 cm^3) with respect to carbogen (CB) intervention, monitored by NIRS and ^{19}F MRS of perflubron, respectively. Error bars indicated the standard deviation

A similar time course pattern in response to carbogen intervention was displayed for $V_{T\text{-}blood}$. Specifically, $V_{T\text{-}blood}$ increased significantly ($p<0.0001$) from a baseline of 0.809 ± 0.004 cm^3 to the maximum of 0.837 ± 0.004 cm^3 during carbogen intervention, having a maximal change of 0.028 cm^3 in tumor blood volume. The average changes of tumor hemoglobin concentration, ΔC, obtained from MRS can be calculated as

$$\Delta C = \frac{\Delta V_{T-blood} * K}{M * V_{T-physical}} = \frac{0.028 * 150}{68000 * 2.6} = 0.0237(mM)$$

From NIRS measurement, we get $\Delta[Hb]_{total}$ =0.0194 mM/DPF. If considering DPF = 2~4, $\Delta[Hb]_{total}$ = 0.0097 ~ 0.0049 mM. Thus, the percentage of tumor vascular blood volume sampled by NIRS over the tumor blood volume measured by ^{19}F MRS is within the range of 20.4%~40.8%.

Data for all the breast tumors are shown in *Table 1.* The tumor vascular blood percentage sampled by NIRS is within the range of 16.7~47.2% (considering DPF=2) and 8.4~23.6 % (considering DPF=4).The mean value of the percentage is about 15± 6 % ~ 30± 12 %. No obvious correlation between percentage values and tumor volume was found (Figure 3).

Table 1 Percentage of tumor vascular blood volume sampled by NIRS over that by ^{19}F MRS

Tumor physical volume (cm^3	$\Delta[Hb]_{total}$ (mM/DPF)	$\Delta V_{T\text{-}blood}$ (cm^3)	$\Delta[Hb]_{total}/\Delta C$ (%) DPF=2	$\Delta[Hb]_{total}/\Delta C$ (%) DPF=4
1.6	0.0258	0.056	16.7	8.4
1.2	0.0616	0.067	25.0	12.5
1.9	0.0525	0.081	27.9	13.9
2.5	0.0375	0.045	47.2	23.6
2.6	0.0194	0.028	40.8	20.4
2.2	0.0219	0.056	18.7	9.4
Mean ± S.D.	0.0365 ± 0.017	0.056 ± 0.018	30 ± 12	15 ± 6

† S.D. indicates standard deviation

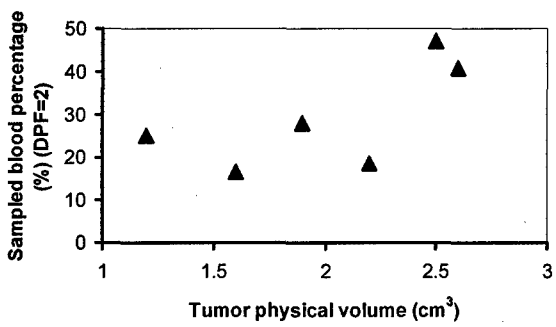

Fig. 3 Percentage of tumor vascular blood sampled by NIRS vurse tumor physical volume

5. Discussion

In this study, we introduced an experimental approach to estimate the percentage of tumor vascular blood volume sampled by NIR system. Changes in breast tumor total hemoglobin concentration, $\Delta[Hb]_{total}$, and in tumor vascular blood volume, $\Delta V_{T\text{-}blood}$, with respect to carbogen intervention were monitored by NIR spectroscopy and ^{19}F MRS of perflubron, respectively. The ratio of $\Delta[Hb]_{total}/\Delta V_{T\text{-}blood}$ was used to calculate the fraction of blood volume sampled by NIRS and MRS. Since the modality of ^{19}F MRS of perflubron can sample all blood volume in the tumor within the RF coil of the magnetic machine[18-19], the fraction calculated from our experiments can be considered as the percentage of tumor vascular blood volume sampled by NIR system. With the available MRS facility and the simple NIR DC signal, this experimental approach first provides the estimated percentage of blood volume sampled by NIR system, with a average range of 15~30% (Table 1). This range gives investigators in NIR field an important reference for quantifying their measurements. In other hand, the consistent response trends between $\Delta[Hb]_{total}$ and $\Delta V_{T\text{-}blood}$ during hyperoxic gas interventions (Fig.2) convinced the investigators in the NMR field that

low cost, portable NIR system can be a reliable non-invasive real time monitoring tool for changes in tumor blood contents.

As known, the NIR light propagated in tissue is dominated by scattering rather than absorption, although the quantification of vascular blood contents is based on the absorption of oxygenated and deoxygenated hemoglobin. Due to the fact that the size of microscopic blood vessel (arterioles, capillaries, venules) is in the same order of magnitude as the average scattering length in tissue(~100μm) [15, 31], NIR light was multiple scattered by the small blood vessel. This multiple scattering allows the blood in small vessel to be sampled several times, causing the high sensitive of NIR signal to small vessel and enhancing the blood absorptions. However, despite the large number of small vessels, only 250 ml out of 5000 ml blood volume (5%) is in capillaries. A large amount of blood is in big vessel, which is less sensitive to NIR signal. Moreover, small vessels have lower hematocrit compared to big vessel because of the reducing of hematocrit with the decreasing of vessel diameter [32]. Thus, the NIR system only samples a small portion of blood hemoglobin. 15~30% estimated from our experiments may have included the factor of multiple scattering in tissue.

As seen in Equation (9)~(11), DPF is a very important parameter for quantifying NIR measurements. Many investigators [33-37] have conducted research on the estimation of optical path length of the brain and muscle of both human subjects and animal models. Typical DPF factor was estimated within the range of 5~6 for human brain and 3~4 for muscle, independent of the source-detector separation when d>2.5cm [38-39]. However, the NIR light propagated in tumor tissue is different from that in brain and muscle. Due to tumor angiogenesis, tumor tissues possess more blood vessels and have higher light absorption than the normal brain and muscle. Furthermore, the solid tumors in the study have finite size, where "photon escape" from the measured volume can take place [40]. The term of "photon escape" has been used to refer to the situation where the sample size under study is finite, and a large amount of light may escape from the sample and never be detected, leading to a shorter path length in comparison with the path length in other large volumes of tissues. Steen et. al took DPF = 2.5 for their tumor study [41]. Therefore, DPF=2~4 is a reasonable maximal range for breast tumors.

Indeed, the accurate DPF for breast tumors could be derived from time-resolved and intensity-modulated spectroscopy, which determines the photon mean time-of-flight and the phase shift of an intensity-modulated light wave, respectively. Meanwhile, the errors in the percentage measurement can be potentially reduced by conducting measurements of NIRS and ^{19}F MRS simultaneously, thus, to eliminate experimental variations between the two kinds of measurements. One might also apply ^{1}H MRI of vascular volume markers such as the super paramagnetic iron oxide particles (SPIOs) [42-43] in place of the ^{19}F NMR approach used here. Since agents such as Combidex are in clinical use, correlated studies with NIR could allow examination of percentage of blood sampled by NIR system in human tumors. The uncertainty in both the size measurement and volume calculation will contribute to the error critically in the estimated percentage.

Also, no obvious correlation between the percentage of blood volume sampled by NIRS and tumor size has been observed (Fig. 3), which is possiblely due to fact that the tumor size(<2.6 cm^3) is not big enough to induce necrosis in the central of the tumors, and thus, no structure changes occurred. In our study, not all tumors showed a change accompanying challenge with hyperoxic gas, and thus many additional tumors were tested by NIRS, but deemed unsuitable for this study due to lack of response[44]. In other contexts, response versus lack of response may be significant observation for tumor biology.

In conclusion, we have introduced a new experimental approach to estimate the percentage of tumor blood volume sampled by NIR system by combining the measurements of NIRS with ^{19}F MRS. The results gave rise to a percentage range of 15~30%. The practical importance and usefulness of this study is the potential capability for investigators to quantify absolute changes in vascular hemoglobin concentrations and oxygenation in solid tumors under therapeutic interventions, which could be important for cancer prognosis and therapy planning.

Acknowledgements

This work was supported in part by the Department of Defense Breast Cancer Research grants BC000833 (YG) and BC990287 (HL), and in part by NIH RO1 CA79515/EB2762 (RPM), Tumor cells were provided by the Division of Cancer Therapeutics, NIH, and perflubron emulsion (Oxygent™) was kindly provided by Alliance Pharmaceuticals.

Vascular oxygen dynamics of breast tumors in response to physiological interventions monitored by Near Infrared Spectroscopy

Yueqing Gu, Ph. D.[+], Yulin Song, Ph. D.[+*], Anca Constantinescu, Ph. D. *, Hanli Liu, Ph.D. and Ralph P. Mason, Ph. D. *[a],

Biomedical Engineering Graduate Program, The University of Texas at Arlington and

*Department of Radiology, The University of Texas Southwestern Medical Center, Dallas, Texas

[+] Contributed equally to this work

This work was supported in part by the Department of Defense Breast Cancer Research Initiative: pre-doctoral grant DAMD17-97-1-7261 (YS), post doctoral grant BC000833 (YG) and IDEA award BC990287 (HL), together with NIH RO1 CA79515 (EB002762) (RPM) and in conjunction with the Cancer Imaging Program P20 CA086354.

[a] Address correspondence to:
Ralph P. Mason, Ph.D., C. Chem.,
Department of Radiology,
U.T. Southwestern Medical Center,
5323 Harry Hines Blvd.,
Dallas, TX 75390-9058
Tel: (214) 648-8926; Fax: (214) 648-2991;
E. mail: Ralph.Mason@UTSouthwestern.edu

ABSTRACT

Purpose: The goal of this investigation was to demonstrate the feasibility of applying Near Infrared Spectroscopy (NIRS) to examine tumor vascular dynamics. Various interventions expected to modulate the concentration of oxygenated hemoglobin, $\Delta[HbO_2]$, and total hemoglobin, $\Delta[Hb]_{total}$, were evaluated in rat breast tumors.

Methods and Materials: Transmission mode NIRS was applied to 13762 breast adenocarcinomas, while the Fisher rats were exposed to respiratory challenge with the hyperoxic gases carbogen (5% CO_2 and 95% O_2), oxygen, a hypercarbic mixture of 5% CO_2 in air and with respect to infusion of the vasoactive agent hydralazine.

Results: Repeated carbogen breathing yielded increases in vascular oxygenation with highly reproducible modulation both in magnitude and response time. Carbogen and oxygen breathing each significantly elevated oxygenation of the tumor vasculature, however, the rate and pattern of response differed and depended on the sequence of gas breathing. Addition of CO_2 to air generated a small, but significant elevation of $\Delta[HbO_2]$. Hydralazine administration during carbogen or air breathing decreased both the vascular oxygenation and total vascular hemoglobin (vascular volume) significantly.

Conclusions: These results demonstrate NIRS as a non-invasive, real-time means for monitoring tumor vascular oxygen dynamics in response to acute interventions, indicating potential utility for evaluating novel therapies and possibly treatment planning.

Keywords: Near infrared spectroscopy, breast tumor, oxyhemoglobin, carbogen, hydralazine.

1. Introduction

There is increasing evidence that tumor oxygenation plays a critical role in disease progression and response to therapy. In particular, modulation of tumor oxygenation may improve therapeutic outcome, since hypoxic cells resist radiotherapy and certain drugs exhibit selective cytotoxicity. Several recent studies have shown poor prognosis for patients with relatively hypoxic tumors of the cervix and head and neck (1-4) and extensive hypoxia has been found in tumors of the prostate and breast (5, 6). While many attempts to improve therapeutic outcome by manipulation of tumor oxygenation have shown only modest success (7), recent work by Kaanders *et al.* (8) has shown dramatic improvement for patients with hypoxic head and neck tumors, when treated with the ARCON protocol. Thus, there is a developing interest in measuring tumor oxygenation, and many techniques have been developed for quantitative measurement of pO_2 (9, 10), *e.g.*, electrodes (11), optical probes (12-14), EPR (15-17), and ^{19}F MRI (18-21). The Eppendorf Histograph has provided extensive clinical data showing correlation between tumor oxygenation (either median pO_2 or hypoxic fraction) and therapeutic outcome and is considered by some to be a "gold standard". Other techniques detect hypoxia itself using labels such as pimonidazole or EF5 (8, 22) in biopsy specimens, though imaging approaches are being developed (23).

Near-infrared spectroscopy (NIRS) offers an alternative approach based on the differential light absorption of the strong chromophores oxy- and deoxy hemoglobin (Fig 1a). NIRS provides a non-invasive means to monitor global tumor vascular oxygenation in real time based on endogenous molecules. While many investigations have been conducted in the brain and breast in both laboratory and clinical settings over the last

decade, there have been relatively few reports of NIRS studies of solid tumors (12, 24-34). Most studies to date have used reflectance mode. By contrast, we have favored transmission mode, so as to interrogate deep tumor regions, and we have presented preliminary studies in rat breast and prostate tumors with respect to various interventions (12, 25, 26). In this study, we have extended our investigations to larger cohorts of animals and more diverse interventions to investigate vascular oxygenation. Specifically, altering inhaled gas from air to oxygen, carbogen (95% O_2 and 5% CO_2) and a hypercarbic air mixture (5% CO_2 in air), as well as administration of the vasoactive agent hydralazine (HDZ).

2. Methods and Materials

2.1 NIRS for measurement of changes in $[HbO_2]$ and $[Hb]_{total}$

The homodyne frequency-domain NIRS system (NIM, Philadelphia, PA) used in this study has been described in detail previously (25). Briefly, as shown in Fig. 1(b), the amplitude-modulated light (140 MHz) from two NIR laser diodes at 758 nm and 785 nm was coupled into a bifurcated fiber bundle and illuminated on one side of the tumor. The light diffusing through the tumor was collected by a second fiber bundle and propagated to a photomultiplier tube (PMT). The signal from the PMT was demodulated through an In-phase and Quadrature-phase circuit, and the amplitude variations recorded. Absorption of the NIR light by the two major absorbers within the tumor tissue, oxygenated and deoxygenated hemoglobin, can be quantified by modifying Beer-Lambert's law (25). Changes in oxygenated, deoxygenated, and total hemoglobin

concentrations, *i.e.*, $\Delta[HbO_2]$, $\Delta[Hb]$ and $\Delta[Hb]_{total}$ are calculated using equations, which have been derived previously (12, 26):

$$\Delta[HbO_2] = \frac{-10.63 \cdot \log(\frac{A_B}{A_T})^{758} + 14.97 \cdot \log(\frac{A_B}{A_T})^{785}}{d}, \qquad (1)$$

$$\Delta[Hb] = \frac{8.95 \cdot \log(\frac{A_B}{A_T})^{758} - 6.73 \cdot \log(\frac{A_B}{A_T})^{785}}{d}, \qquad (2)$$

$$\Delta[Hb]_{total} = \Delta[HbO_2] + \Delta[Hb], \qquad (3)$$

where A_B and A_T are the baseline and transient amplitudes measured from the NIR system, respectively, and "d" is the source-detector separation, subject to the differential path-length factor (DPF) for tumor tissues. Thus, $\Delta[HbO_2]$, $\Delta[Hb]$ and $\Delta[Hb]_{total}$ all have relative units of mM/DPF. The four coefficients in the equations were derived using the extinction coefficients of Hb and HbO_2 at corresponding wavelengths and have been corrected for the pathlength differences at the two wavelengths (26).

2.2 Animal model and protocols

The Institutional Animal Care and Use Committee approved these investigations. Rat mammary adenocarcinomas 13762NF (35) (originally obtained from DCT, NCI) were implanted in skin pedicles (36) on the foreback of adult female Fisher 344 rats (~150 g). Once the tumors reached 1~3 cm diameter, rats were anesthetized with 150-

μl ketamine hydrochloride (100 mg/ml, i.p.) and maintained under general gaseous anesthesia with 1.3% isoflurane in air (1 dm^3/min). For gas interventions, the anesthetic and gas flow were maintained at a constant level. Tumors were shaved to improve optical contact for NIR light transmission, and the body temperature was maintained at 37 ^{0}C using a warm water blanket. Tumor volume was estimated using an ellipsoid approximation ($V=(\pi/6).a.b.c$) from the three orthogonal diameters (a,b,c). In some cases a pulse oximeter (Nonin Medical Inc., Plymouth, MN) was applied to the hind foot to assess dynamic response of arterial oxygenation.

In this study, four groups of rats were used to investigate the dynamic response of breast tumor oxygenation to interventions. Group 1 (n=8) experienced repeated carbogen breathing using the sequence air-carbogen-air-carbogen-air to demonstrate reproducible effects of carbogen on tumor oxygenation. Group 2 (n=7) breathed the sequence air-carbogen–air–oxygen–air, while Group 3 (n=7) experienced the reverse sequence (air-oxygen-air-carbogen-air), so as to compare the two hyperoxic gas interventions and allow for any preconditioning. A subgroup (3A) also received an i.v. infusion of hydralazine (HDZ; 5 mg/kg in 0.5 ml saline, Sigma) as a bolus by hand (< 1 min) in the tail vein during the carbogen breathing (air-oxygen-air-carbogen-carbogen+HDZ–air; n= 5). Group 4 (n=5) experienced air-hypercarbic air (5% CO_2 in air)–carbogen–air–oxygen–air-air+HDZ, to investigate the effect of CO_2 on the tumor vascular bed. Each gas was applied for 20-24 minutes in all the breathing sequences.

3. Results

Figure 2a shows the typical time course for response of $\Delta[HbO_2]$ to successive carbogen interventions for a representative Group 1 tumor (No. 2, 9.9 cm^3). When the inhaled gas was switched from air to carbogen, $\Delta[HbO_2]$ increased rapidly and significantly ($p < 0.0001$) from the baseline to about 0.87± 0.03 within the first two minutes, followed by a slower, but further significant increase ($p<0.001$) over the next 21 minutes. Returning to air breathing produced a significant drop ($p < 0.0001$) of $\Delta[HbO_2]$ with asymptotic tendency towards the baseline value. A very similar temporal response was observed during the second cycle of carbogen intervention. The magnitude of response was highly consistent, as shown for the eight individual tumors in Fig. 2b (R^2 >0.92). In addition to magnitude of response, the dynamic behavior of $\Delta[HbO_2]$ with respect to carbogen intervention may be characterized by time constants for exponential curves (25). We have previously found that a bi-exponential fit is required to represent the biphasic nature of the response to carbogen breathing, and fitted curves are overlaid on Fig. 2a. We believe the fast component represents rapid arteriolar inflow with a typical time constant < 1 minute, whereas the 2nd component is more sluggish. The ratio $\tau 1/\tau 2$ reveals the relative efficiency of these components, which was highly reproducible for the successive interventions (Fig. 2c).

To assess the relative ability of oxygen versus carbogen to modulate tumor vascular oxygenation, response to the two gases was compared. Separate groups of rats received the gases in reversed sequence in order to reveal any preconditioning effects. Figure 3 shows the time course of $\Delta[HbO_2]$ for a representative 13762NF breast tumor (3.2 cm^3) in Group 2. The carbogen intervention produced a similar biphasic

response of $\Delta[HbO_2]$ to that seen for Group 1. Following the initial exposure to carbogen and 20 minutes of air breathing for re-equilibration, the rat was exposed to oxygen. As with carbogen, there was a rapid increase in $\Delta[HbO_2]$ within the first 2 minutes, but this was followed by a plateau and curve fitting required a single exponential only. The maximal response of $\Delta[HbO_2]$ to carbogen and oxygen interventions was similar, as shown in Fig. 3b. While each gas produced a significant elevation in $\Delta[HbO_2]$, there was no significant difference in magnitude for these two hyperoxic gas interventions ($p>0.3$). However, we note that 20 mins was sometimes insufficient time for $\Delta[HbO_2]$ to return to baseline after carbogen breathing. Thus, the apparent increase is based on an elevated starting point. To address this potential anomaly, we considered both the ascending response with each hyperoxic gas and the ascending response to carbogen versus the decrease following oxygen inhalation, which occurred more rapidly (Fig. 3a). Indeed, both the increase and the decline in $\Delta[HbO_2]$ were significantly faster with respect to oxygen breathing than carbogen (Fig. 3c, d).

In order to examine the possible effect of preconditioning, tumors in Group 3 experienced the "reversed" gas intervention, with exposure to oxygen prior to carbogen (Fig. 4a). As for Group 2, the maximal changes of $\Delta[HbO_2]$ due to oxygen or carbogen intervention for each of these 7 tumors were found to be similar (Fig. 4b). However, both interventions now produced a monophasic response: in 6 of the 7 tumors the biphasic response to carbogen was no longer seen.

To further explore the vasoactive contribution of the CO_2 component, rats in Group 4 inhaled a hypercarbic air mixture (air + 5% CO_2), followed by carbogen (95% O_2 +5% CO_2). Fig. 5a shows the time course of $\Delta[HbO_2]$ for a representative tumor (1.9

cm^3). When CO_2 was added to the inhaled air $\Delta[HbO_2]$ increased immediately, and significantly, to a plateau 0.15 ± 0.01 (normalized to the maximum value achieved with hyperoxic gas; $p<0.05$). Response to carbogen was as before. Typically, addition of the CO_2 component to air caused $\Delta[HbO_2]$ to increase by about 10-20% of that due to carbogen (Fig. 5b).

Several rats were also infused with HDZ during carbogen (subgroup 3A) or air breathing (Group 4), and the response of $\Delta[HbO_2]$ is shown for representative tumors in Figs. 4a and 5a. For Group 3a, the mean decrease in $\Delta[HbO_2]$ was 0.8 ± 0.2 for the transition oxygen to air, 1.2 ± 0.4 following HDZ administration during carbogen breathing, and a further 0.5 ± 0.3 for the final switch back to air. The decrease in oxygenation due to hydralazine was generally greater than the change accompanying oxygen to air breathing. However, the change attributable to HDZ was not significantly different during carbogen (Group 3a) or air (Group 4) breathing.

In addition to $\Delta[HbO_2]$, dual wavelength NIRS can also show changes in total hemoglobin ($\Delta[Hb]_{total}$), as shown by equation 3. Fig. 2a indicates that $\Delta[Hb]_{total}$ increased in response to breathing carbogen with a response about 20% of that for $\Delta[HbO_2]$. This was typical of many tumors, though some showed minimal response and often there was a continual drift throughout the variation in inhaled gases (Figs. 4a and 5a). Return to air breathing rarely reversed the $\Delta[Hb]_{total}$ and minimal change accompanied initial oxygen or secondary carbogen challenges (Fig. 2a, 4a, 5a). In some cases, $\Delta[Hb]_{total}$ increased with addition of CO_2 to air, but the pattern was highly variable. Infusion of HDZ always caused a significant decline in $\Delta[Hb]_{total}$, and during air

breathing the magnitude of the changes approached or exceeded the change in $\Delta[HbO_2]$.

4. Discussion

These studies reveal the vascular response to breathing hyperoxic and hypercarbic gases and the vasoactive pharmacological agent hydralazine. NIRS is non-invasive and provides a real time assessment of changes in tumor vascular hemoglobin saturation. These investigations provide a considerable extension of our previous NIR studies of tumors (12, 25, 26), in terms of numbers of animals, range of interventions, and extent of analysis. Most importantly, the results provide further demonstration of the ease and utility of NIRS studies of tumors.

As we have previously observed in various rat tumors (12, 25), switching the inhaled gas from air to carbogen produced a rapid biphasic elevation in hemoglobin oxygenation. The rapid component has a time constant in the range of seconds to a minute, and approaches that observed for arterial oxygen saturation detected in the hind foot with a pulse oximeter (Fig. 3a). The slow component (10 to 50 times slower) continues for many minutes, and generally represents 10-20% of the total change. Oxygenation was reversible upon returning to air inhalation. The decrease in $\Delta[HbO_2]$ was also biphasic, and elevated oxyhemoglobin was still present after ten to twenty minutes in many cases (Fig. 2a, 3a). The response was found to be highly consistent for repeat carbogen interventions (Fig. 2), as emphasized both in terms of magnitude (Fig. 2b) and rate (Fig. 2c). The high reproducibility of results suggests that repeat

interventions could be a valuable method for exploring the efficacy of interventions designed to modulate tumor vascular oxygenation (*e.g.*, vascular targeting agents).

Response to oxygen was much more rapid and fit well to a mono exponential curve. For almost every tumor, the time to reach 80% of maximum elevation in $\Delta[HbO_2]$ was longer for carbogen and for the group of seven tumors the difference was significant. Likewise, the decline in $\Delta[HbO_2]$ was more rapid following exposure to oxygen (Fig. 3d). Further examination of Fig. 3a indicates that the maximum $\Delta[HbO_2]$ reached with either hyperoxic gas was similar, but required longer with carbogen. Given that tumors had often not returned to baseline between hyperoxic gases, there could be a question of pre-conditioning or residual oxygenation. The decline in $\Delta[HbO_2]$ following oxygen breathing was faster than following carbogen, prompting a comparison of the increase on the rising part of carbogen (Fig. 3b) with the decrease following oxygen. Both analyses showed a strong correlation demonstrating that the ultimate increase in $\Delta[HbO_2]$ is similar for either hyperoxic gas.

Intriguingly, the biphasic response (slow component) for carbogen was usually eliminated, when the order of breathing hyperoxic gases was reversed (Fig. 4), yet the ultimate response was equivalent (Fig. 4b), whichever gas was breathed first. These data may be important in the context of the existing literature. Many investigators have compared the relative merits of oxygen or carbogen for improving tumor oxygenation. Overall carbogen is favored, and is being applied in clinical trials such as ARCON (3, 37). Our own previous investigations in the subcutaneous (pedicle) syngeneic breast tumor model showed that each gas appeared equally effective at improving tumor oxygenation (38). In practice oxygen might be favored since the response is more rapid,

suggesting that an effective pre-irradiation breathing time could be shorter. Given the reported respiratory distress induced by 5%CO_2, oxygen appears advantageous. However, as a corollary, the elevated oxygenation is more persistent following carbogen breathing, as also reported previously by Thews *et al.* (39). This could be important in circumstances where hyperoxic gas may be administered prior to, but not during irradiation. Indeed, others found evidence for persistence of improved oxygenation following exposure to hyperbaric oxygen (40, 41).

While improvement of tumor oxygenation has been a primary goal of much research and many clinical trials, an alternative paradigm is induction of hypoxia to enhance the efficacy of hypoxia selective cytotoxins, *e.g.*, tirapazamine (42). Our results show that while either gas is being breathed (air or carbogen) IV infusion of HDZ caused a rapid decline in $\Delta[HbO_2]$ to a level below baseline (Figs. 4a , 5a). The overall change in $\Delta[HbO_2]$ due to HDZ infusion was similar, whether the rats were breathing air or carbogen. The decline in $\Delta[HbO_2]$ could be caused by decreased hemoglobin oxygen saturation or reduced blood volume (*viz*. hematocrit). NIRS can provide measurements of both $\Delta[Hb]_{total}$ and $\Delta[HbO_2]$, simultaneously, as we have demonstrated in preliminary data in the past (25). Our current data indicate substantial changes in $\Delta[Hb]_{total}$ revealing reduced vascular volume in response to HDZ infusion coinciding with previous reports for implanted tumors (43-45).

Insight into tumor vascular volume is also pertinent to the hyperoxic gases, where there has been much debate concerning the relative vasoconstriction versus vasodilatory effects of CO_2 (46). Here, the addition of CO_2 to air caused a significant increase in $\Delta[HbO_2]$, but results for $\Delta[Hb]_{total}$ were less distinct. Likewise, the hyperoxic

gases were accompanied by a variable response in $\Delta[Hb]_{total}$. Our previous work in phantoms has rigorously validated the stability of the instrument and veracity of the algorithms used here (26), leading us to believe that our observations represent physiological phenomena. The results for $\Delta[HbO_2]$ with the hyperoxic gases are both consistent and intuitive. The results for $\Delta[Hb]_{total}$ are as expected for HDZ. The observations for response of $\Delta[Hb]_{total}$ to gas challenge indicate highly variable behavior. However, it must be noted that changes in $\Delta[Hb]_{total}$ are relatively smaller than $\Delta[HbO_2]$, so that errors in calculation become more significant.

Others have suggested that the carbon dioxide component of carbogen is critical to improving tumor oxygenation. Some tumors appear to respond only in the presence of CO_2 (33), which has variously been described as a vasoconstrictor or vasodilator (46). BOLD (or FLOOD - Flow and Oxygen Dependant contrast) MRI of G3H prolactinomas, a highly vascularized and perfused tumor type, showed some response to the addition CO_2 to air and much greater response to carbogen (47). However, oxygen produced a smaller effect than either hypercarbic gas. Here, carbogen and oxygen both induced significant increases in vascular hemoglobin oxygenation, which were essentially equal, though changes accompanying carbogen were slower. To probe the importance of the CO_2 component further, we tested the addition of 5% CO_2 to air. In all five tumors of Group 4, the addition of 5% CO_2 produced a rapid increase in $\Delta[HbO_2]$ with a stable plateau. Further switch to carbogen produced the usual response, which was five to six times greater than that due to the addition of CO_2 to air alone (Fig. 5b). The importance of the CO_2 component remains intriguing, since it generates rapid

response, when added to air, but appears to be responsible for the biphasic response of carbogen.

NIRS provides a global assessment, in contrast to BOLD MRI, which can provide high resolution images (20, 47). Imaging can show heterogeneity in temporal and spatial response, but results are often summarized using data reduction to show mean values only. As such, an *a priori* global measurement can provide similar insight into dynamic tumor physiology or drug pharmacodynamics, while being cheaper and easier to implement. Our approach to NIRS uses transmission mode, which we believe probes large and deep portions of the tumor, including the periphery on each side, as well as the center. This is in contrast to the methodology used by most other investigators, who apply reflectance mode (24, 28-30), which predominately indicates the behavior of the peripheral vasculature. Indeed, results from Hull *et al.* (24) are consistent with the fast component that we attribute to the well-perfused regions of our tumors.

Likely, the response to interventions depends on tumor type, site of implantation, and anesthetic. To place our current work in context, the 13762NF tumor type was originally developed by Bogden *et al.* (35) and has been used in investigations of tumor oxygenation in the past. In particular, Teicher *et al.* (48, 49) examined the effects of various cytotoxic drugs and blood substitutes on pO_2 using the Eppendorf Histograph. When tumors were implanted subcutaneously in the hind limb of Fisher rats there was extensive base line hypoxia with HF_5 greater than 60% (48).

We have previously investigated dynamic oxygenation in the 13762 NF adenocarcinoma using *FREDOM* (Fluorocarbon Relaxometry using Echo planar imaging for Dynamic Oxygen Mapping) (38). It should be noted that this particular tumor

develops extensive central necrosis and exhibits great heterogeneity in terms of tissue appearance and tumor oxygenation. The baseline hypoxic faction, in our hands, ranged from five to sixty percent with increasing hypoxic fraction and decreasing mean pO_2 as the tumors grew. Interestingly, the response to oxygen or carbogen was very similar, and on a voxel by voxel basis, the maximum pO_2 achieved was proportional to the initial baseline pO_2. It was also noteworthy that after forty minutes exposure to oxygen or carbogen, the mean tumor pO_2 continued to rise and had not reached a plateau. Not surprisingly, this indicates that the diffusion of oxygen into the tumor tissue is considerably slower than changes in vascular oxygenation, and continues beyond the time when the vascular oxygenation has reached a plateau. Investigations with oxygen electrodes (26) or FOXY™ fiber optic probes (12) in these breast tumors showed heterogeneity within the tumors with baseline pO_2 ranging from hypoxia to greater than 50 torr. These other techniques also indicated heterogeneity in response. Generally, those regions that had an initially low pO_2 showed minimal response to oxygenation, while those with higher pO_2 showed a rapid response. Thus, while we believe NIRS can provide important insight into the pharmacodynamics of interventions on tumors, it must be noted that responsive regions may mask the tumor heterogeneity, and in particular, fail to show those regions that do not respond (26). This emphasizes the need for NIR imaging, and indeed, we have obtained preliminary data in this tumor type using a single transmitter and three receivers placed at various regions across the tumor, indicating that while each region of the tumor responded to hyperoxic gas, the extent and rate were different, showing the heterogeneity of tumor vasculature (50).

In conclusion, we believe that NIRS presents a new opportunity to examine tumor vasculature rapidly, non-invasively, and cheaply. Ease of implementation will allow rapid application to accessible tumors in patients. The inherent compatibility of fiber optics technology and light with other modalities, such as electrodes (26) and MRI (28), will facilitate multiparametric multimodality investigations in the future.

ACKNOWLEDGEMENT

We are grateful to Jae G. Kim, Vincent Bourke, and Mengna Xia for assistance.

Figure Legends

Figure 1

a) Relative absorption characteristics for oxy and deoxy-hemoglobin (based on (51))

b) Schematic experimental setup for the NIR spectroscopy system. NIR light is delivered and detected using two 3 mm-diameter fiber bundles placed in transmittance geometry around the tumor. PMT represents a photomultiplier tube. I/Q is an in-phase and quadrature phase demodulator for retrieving amplitude and phase information.

Figure 2

a) Time course of tumor vascular $\Delta[HbO_2]$ and $\Delta[Hb]_{total}$ with respect to altering inhaled gas in the sequence carbogen-air-carbogen-air for a representative 13762NF breast tumor in Group 1. Bi-exponential curve fitting to the dynamic responses of $\Delta[HbO_2]$ gave time constants τ_1=0.854 ±0.008 min and τ_2=7.56 ±0.09 min for the first intervention, and τ_1 = 0.653 ±0.004 min and τ_2 = 6.01 ±0.08 min for the second intervention with R^2>0.94 and χ^2<1.2 in both cases.

b) Comparison of $\Delta[HbO_2]$ produced by carbogen breathing for each tumor in Group 1 in the two cycles (R^2>0.92).

c) Comparison of the ratios of the time constants, τ_1 and τ_2, for the two interventions. There was strong linear correlation (R^2>0.9).

Figure 3

a. Time course of tumor vascular $\Delta[HbO_2]$ for a representative 13762NF breast tumor in Group 2. Curve fitting required a bi-exponential application for the carbogen intervention, but mono exponential for oxygen. Two-exponential fitting for the carbogen intervention yielded: $0.318\{1-\exp[-(t-19.656)/0.59]\}+0.394\{1-\exp[-(t-19.656)/21]\}$ with $R^2>0.96$, and mono exponential fitting for the oxygen intervention yielded: $0.484\{1-\exp[-(t-59.893)/0.397]\}+0.138$ with $R^2>0.8$. Variation in arterial oxygen saturation is also shown.

b. Comparison of maximal changes of $\Delta[HbO_2]$, caused by carbogen and oxygen interventions for tumors in Group 2. □ Comparison of the rising parts for each intervention; □ Comparison of the rising part for carbogen versus the falling part for oxygen. In both cases $R^2>0.8$.

c. Comparison of response times to each gas intervention. Here, the time to 80% maximum response to each intervention is compared for carbogen versus oxygen: Δ rising parts (onset of hyperoxia), □ falling parts (return to normoxic gas breathing). The line of unity shows that the time for carbogen was almost always longer than for oxygen, but the correlation between the times was very weak for either rising or falling components ($R^2<0.25$).

d. The average time for the 7 rats in Group 2 for signals to increase or decrease to 80% of the maximal $\Delta[HbO_2]$ in the rising part or falling part for carbogen (open bars) and oxygen interventions (shaded bars), respectively.

Figure 4

a. Time course of tumor vascular $\Delta[HbO_2]$ and $\Delta[Hb]_{total}$ for a representative tumor in Group 3a.

b. Correlation between maximum $\Delta[HbO_2]$ achieved with carbogen inhalation versus that with oxygen (R^2 >0.94): □ carbogen prior to oxygen (Group 2), ▲ oxygen prior to carbogen (Group 3).

Figure 5

a Time course of tumor vascular $\Delta[HbO_2]$ and $\Delta[Hb]_{total}$ for a representative tumor in Group 4.

b Comparison of maximal changes of tumor vascular oxygen hemoglobin concentration, $\Delta[HbO_2]$, caused by hypercarbic gas. Open bars from air to air+CO_2, hatched bars from air+CO_2, to oxygen + CO_2 (carbogen).

References

1. Fyles AW, Milosevic M, Wong R, *et al.* Oxygenation predicts radiation response and survival in patients with cervix cancer. *Radiother. Oncol.* 1998;48:149-56.
2. Brizel DM, Sibly GS, Prosmitz LR, *et al.* Tumor hypoxia adversely affects the prognosis of carcinoma of the head and neck. *Int. J. Radiat. Oncol. Biol. Phys.* 1997;38:285-289.
3. Kaanders JAHM, Pop LAM, Marres HAM, et al. Experience in 215 patients with advanced head and neck cancer. *Int. J. Radiat. Oncol. Biol. Phys.* 2002;52:769-778.
4. Nordsmark M, Overgaard M, Overgaard J. Pretreatment oxygenation predicts radiation response in advanced squamous cell carcinoma of head and neck. *Radiother. Oncol.* 1996;41:31-39.
5. Hohenberger P, Felger C, Haensch W, *et al.* Tumor oxygenation correlates with molecular growth determinants in breast cancer. *Breast Cancer Res. Treatment* 1998;48:97-106.
6. Movsas B, Chapman JD, Horwitz EM, *et al.* Hypoxic regions exist in human prostate carcinoma. *Urology* 1999;53:11-18.
7. Overgaard J, Horsman MR. Modification of hypoxia-induced radioresistance in tumors by the use of oxygen and sensitizers. *Semin. Radiat. Oncol.* 1996;6:10-21.

8. Kaanders JHAM, Wijffels KIEM, Marres HAM, *et al.* Pimonidazole binding and tumor vascularity predict for treatment outcome in head and neck cancer. *Cancer Res* 2002;62:7066-7074.

9. Stone HB, Brown JM, Phillips T, *et al.* Oxygen in human tumors: correlations between methods of measurement and response to therapy. *Radiat. Res.* 1993;136:422-434.

10. Mason RP, Ran S, Thorpe PE. Quantitative assessment of tumor oxygen dynamics: Molecular Imaging for Prognostic Radiology. *J. Cell. Biochem.* 2002;87S:45-53.

11. Höckel M, Schlenger K, Knoop C, *et al.* Oxygenation of carcinomas of the uterine cervix: evaluation by computerized O_2 tension measurements. *Cancer Res.* 1991;51:6098-6102.

12. Gu Y, Bourke V, Kim JG, *et al.* Dynamic Response of Breast Tumor Oxygenation to Hyperoxic Respiratory Challenge Monitored with Three Oxygen-Sensitive Parameters. *Applied Optics* 2003;42:1-8.

13. Braun RD, Lanzen JL, Snyder SA, *et al.* Comparison of tumor and normal tissue oxygen tension measurements using OxyLite or microelectrodes in rodents. *AJP - Heart & Circulatory Physiology* 2001;280:H2533-44.

14. Wilson DF, Vinogradov SA, Dugan BW, *et al.* Measurement of tumor oxygenation using new frequency domain phosphorometers. *Comp. Biochem. Physiol. Part A, Molecul. Integrat. Physiol.* 2002;132:153-9.

15. O'Hara JA, Blumenthal RD, Grinberg OY, *et al.* Response to radioimmunotherapy correlates with tumor pO2 measured by EPR oximetry in human tumor xenografts. *Radiat. Res.* 2001;155:466-73.

16. Elas M, Williams BB, Parasca A, *et al.* Quantitative tumor oxymetric images from 4D electron paramagnetic resonance imaging (EPRI): Methodology and comparison with blood oxygen level-dependent (BOLD) MRI. *Magn. Reson. Med.* 2003;49:682-91.

17. Krishna MC, English S, Yamada K, *et al.* Overhauser enhanced magnetic resonance imaging for tumor oximetry: coregistration of tumor anatomy and tissue oxygen concentration. *PNAS (USA)* 2002;99:2216-21.

18. Zhao D, Constantinescu A, Jiang L, *et al.* Prognostic Radiology: quantitative assessment of tumor oxygen dynamics by MRI. *Am. J. Clin. Oncol* 2001;24:462-466.

19. Zhao D, Constantinescu A, Chang C-H, *et al.* Measurement of tumor oxygen dynamics predicts beneficial adjuvant intervention for radiotherapy in Dunning prostate R3327-HI tumors. *Radiat. Res.* 2003;159:621-631.

20. Fan X, River JN, Zamora M, *et al.* Effect of carbogen on tumor oxygenation: combined fluorine-19 and proton MRI measurements. *Int. J. Radiat. Oncol. Biol. Phys.* 2002;54:1202-9.

21. Wang Z, Su M-Y, Nalcioglu O. Applications of Dynamic Contrast Enhanced MRI in Oncology: Measurement of Tumor Oxygen Tension. *Technol. Cancer Res. Treat.* 2002;1:29-38.

22. Evans SM, Hahn S, Pook DR, *et al.* Detection of hypoxia in human squamous cell carcinoma by EF5 binding. *Cancer Res.* 2000;60:2018-2024.

23. Dehdashti F, Grigsby PW, Mintun MA, *et al.* Assessing tumor hypoxia in cervical cancer by positron emission tomography with 60Cu-ATSM: relationship to therapeutic response-a preliminary report. *Int. J. Radia. Oncol. Biol., Phys.* 2003;55:1233-8.

24. Hull EL, Conover DL, Foster TH. Carbogen-induced changes in rat mammary tumour oxygenation reported by near infrared spectroscopy. *Br. J. Cancer* 1999;79:1709-1716.

25. Liu H, Song Y, Worden KL, *et al.* Noninvasive Investigation of Blood Oxygenation Dynamics of Tumors by Near-Infrared Spectroscopy. *Appl. Optic* 2000;39:5231-43.

26. Kim JG, Zhao D, Constantinescu A, *et al.* Interplay of Tumor Vascular Oxygenation and Tumor pO_2 Observed Using NIRS, Oxygen Needle Electrode, and ^{19}F MR pO_2 Mapping. *J. Biomed. Optics* 2003;8:53-62.

27. Sostman HD, Rockwell S, Sylva AL, *et al.* Evaluation of BA 1112 rhabdomyosarcoma oxygenation with microelectrodes, optical spectrometry, radiosensitivity, and MRS. *Magn. Reson. Med* 1991;20:253-267.

28. Gulsen G, Yu H, Wang J, *et al.* Congruent MRI and near-infrared spectroscopy for functional and structural imaging of tumors. *Technol. Cancer Res. Treat.* 2002; 1:497-505.

29. Kragh M, Quistorff B, Kristjansen PE. Quantitative estimates of angiogenic and anti-angiogenic activity by laser Doppler flowmetry (LDF) and near infra-red spectroscopy (NIRS). *Eur. J. Cancer* 2001;37:924-9.

30. Steinberg F, Rohrborn HJ, Scheufler KM, *et al.* NIR reflection spectroscopy based oxygen measurements and therapy monitoring in brain tissue and intracranial neoplasms. Correlation to MRI and angiography. *Adv. Exp. Med. Biol.* 1997;428:553-60.

31. Heffer EL, Fantini S. Quantitative oximetry of breast tumors: a near-infrared method that identifies two optimal wavelengths for each tumor. *Applied Optics* 2002;41:3827-39.

32. McBride TO, Pogue BW, Poplack S, *et al.* Multispectral near-infrared tomography: a case study in compensating for water and lipid content in hemoglobin imaging of the breast. *J. Biomed. Optics* 2002;7:72-9.

33. van der Sanden BJP, Heerschap A, Hoofd L, *et al.* Effect of carbogen breathing on the physiological profile of human glioma xenografts. *Magn. Reson. Med.* 1999;*42*:490-9.

34. Steen RG, Kitagishi K, Morgan K. In vivo measurement of tumor blood oxygenation by near-infrared spectroscopy: immediate effects of pentobarbital overdose or carmustine treatment. *J. Neuro-Oncol.* 1994;22:209-20.

35. Bogden AE, Kelton DE, Cobb WR, *et al.* Effect of serial passage in nude athymic mice on the growth characteristics and chemotherapy responsiveness of 13762 and R3230AC mammary tumor xenografts. *Cancer Res.* 1978;38:59-63.

36. Hahn EW, Peschke P, Mason RP, *et al.* Isolated tumor growth in a surgically formed skin pedicle in the rat: A new tumor model for NMR studies. *Magn. Reson. Imaging* 1993;11:1007-1017.

37. Denekamp J, Fowler JF. ARCON-current status: summary of a workshop on preclinical and clinical studies. *Acta Oncol.* 1997;36:517-525.

38. Song Y, Constantinescu A, Mason RP. Dynamic Breast tumor oximetry: the development of Prognostic Radiology. *Technol. Cancer Res. Treat.* 2002;1:471-478.

39. Thews O, Kelleher DK, Vaupel P. Tumor oxygenation under normobaric and hyperbaric hyperoxia: impact of various inspiratory CO2 concentration. *Adv. Exp. Med. Biol.* 1997;428:79-87.

40. Kunugita N, Kohshi K, Kinoshita Y, *et al.* Radiotherapy after hyperbaric oxygenation improves radioresponse in experimental tumor models. *Cancer Letters* 2001;164:149-54.

41. Becker A, Kuhnt T, Liedtke H, *et al.* Oxygenation measurements in head and neck cancers during hyperbaric oxygenation. *Strahlenther. Onkol.* 2002;178:105-8.

42. Brown JM. Exploiting the hypoxic cancer cell: mechanisms and therapeutic strategies. *Molecular Medicine Today* 2000;6:157-162.

43. Fenton BM. Influence of hydralazine administration on oxygenation in spontaneous and transplanted tumor models. *Int. J. Radiat. Oncol. Biol. Phys.* 2001;49:799-808.

44. Horsman MR, Nordsmark M, Hoyer M, *et al.* Direct evidence that hydralazine can induce hypoxia in both transplanted and spontaneous murine tumours. *Br. J. Cancer* 1995;72:1474-8.

45. Wood PJ, Stratford IJ, Sansom JM, *et al.* The response of spontaneous and transplantable murine tumors to vasoactive agents measured by ^{31}P magnetic resonance spectroscopy. *Int J. Radiat. Oncol. Biol. Phys.* 1992;22:473-6.

46. Dunn TJ, Braun RD, Rhemus WE, *et al.* The effects of hyperoxic and hypercarbic gases on tumour blood flow. *Br. J. Cancer* 1999;80:117-26.

47. Robinson SP, Collingridge DR, Howe FA, *et al.* Tumor response to hypercapnia and hyperoxia monitored by FLOOD magnetic resonance imaging. *NMR Biomed* 1999;12:98-106.

48. Dupuis NP, Kusumoto T, Robinson MF, *et al.* Restoration of tumor oxygenation after cytotoxic therapy by a perflubron emulsion/carbogen breathing. *Art. Cells. Blood Subs. Immob. Biotech.* 1995;23:423-429.

49. Teicher BA, Ara G, Herbst R, *et al.* PEG-hemoglobin: effects on tumor oxygenation and response to chemotherapy. *In Vivo* 1997;11:301-11.

50. Kim JG, Gu Y, Constantinescu A, *et al.* Non-Uniform Tumor Vascular Oxygen Dynamics Monitored By Three-Channel Near-Infrared Spectroscopy. *Proc. SPIE-Int. Soc. Opt. Eng* 2003;4955:388-396.

51. http://omlc.ogi.edu/spectra/hemoglobin/index.html

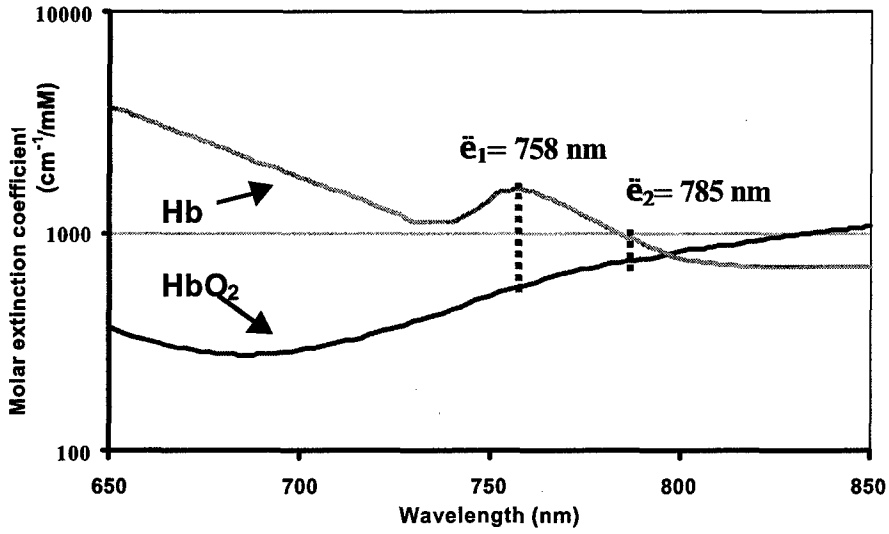

Figure 1a

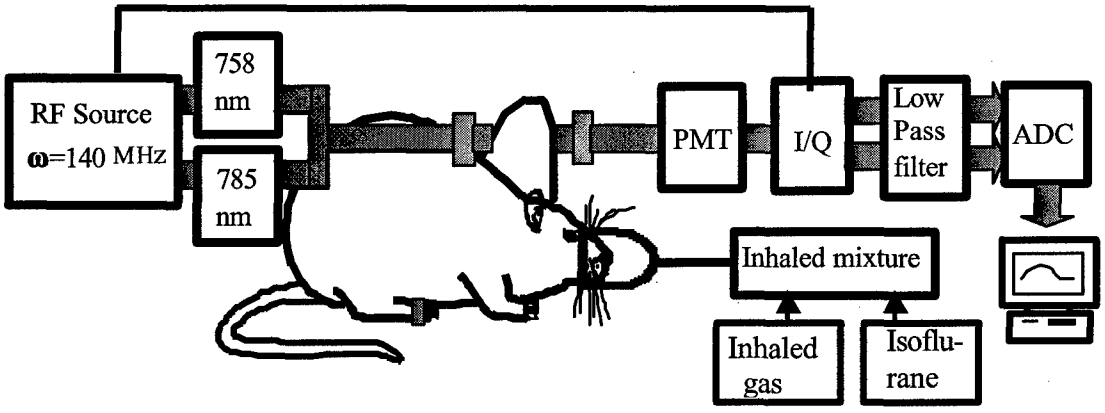

Figure 1b

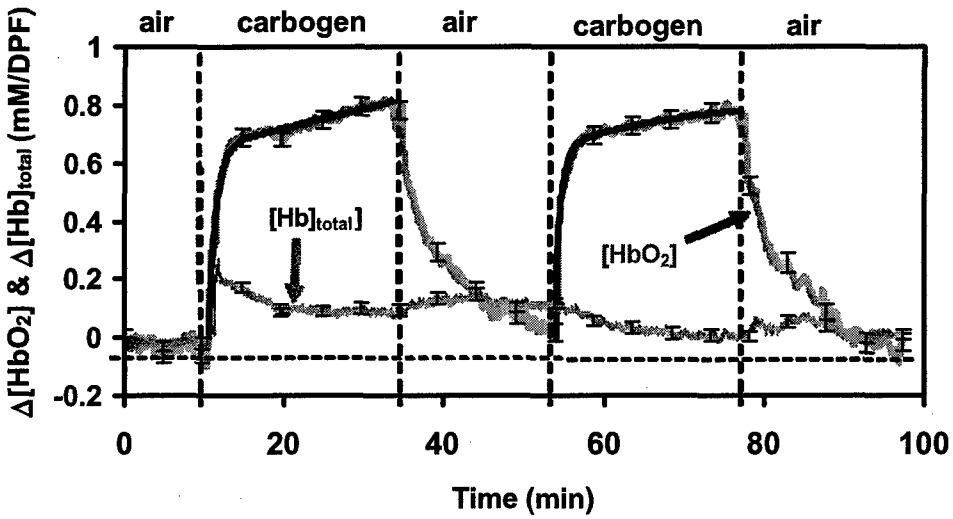

Figure 2a

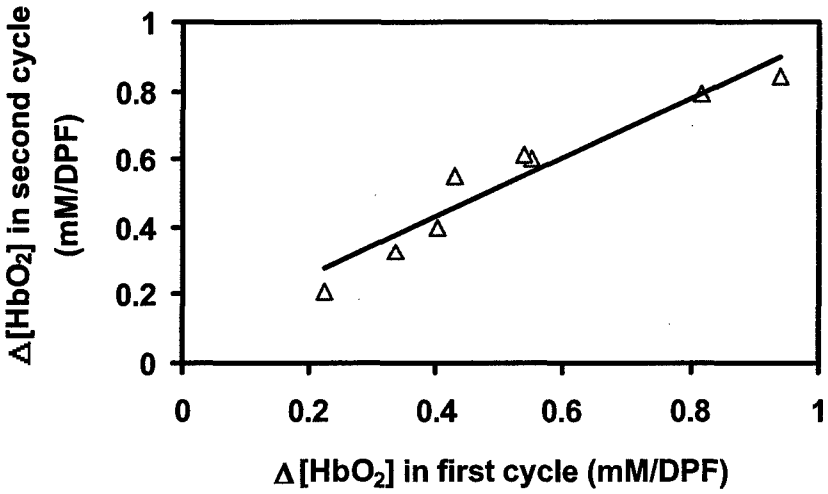

Figure 2b

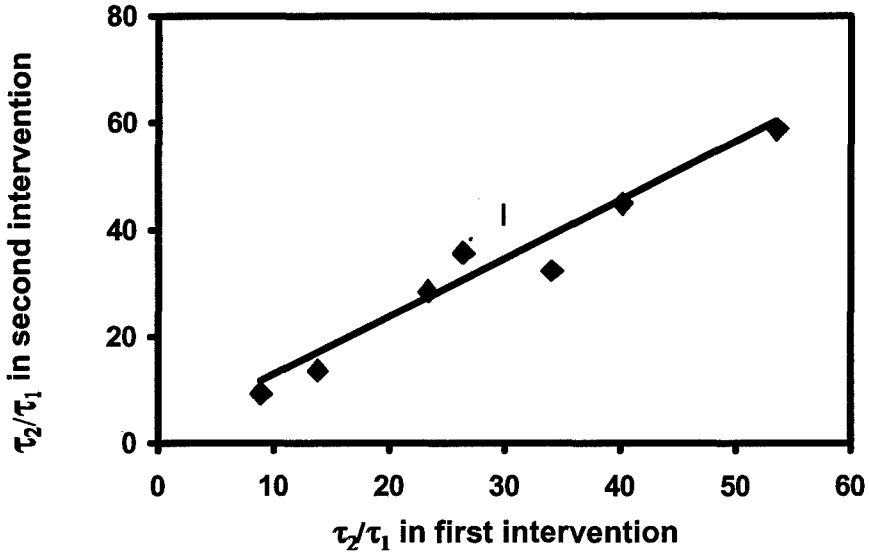
80
60
40
20
0
0
10
20
30
40
50
60
τ_2/τ_1 in second intervention
τ_2/τ_1 in first intervention

Figure 2c

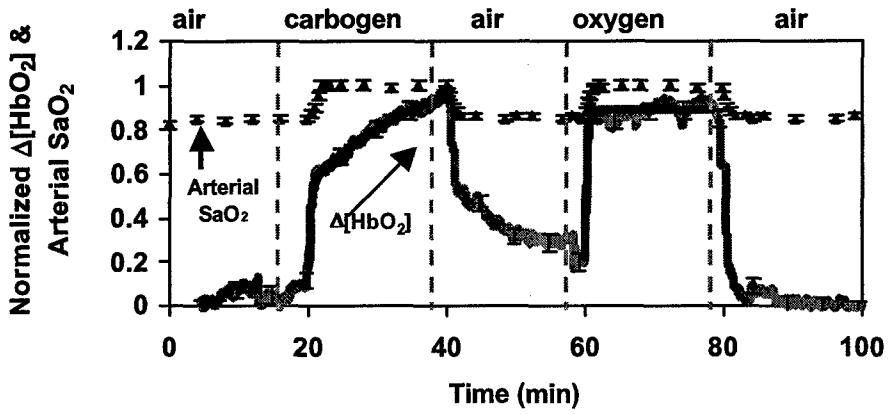

Figure 3a

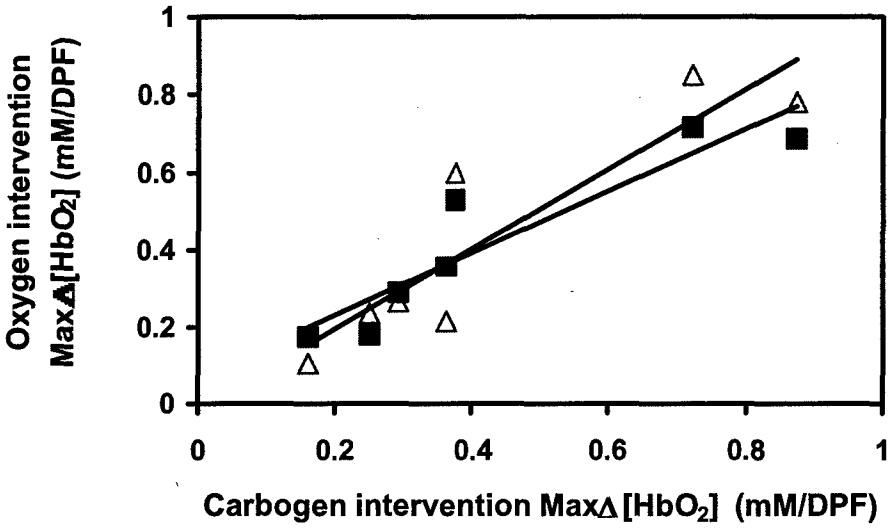

Figure 3b

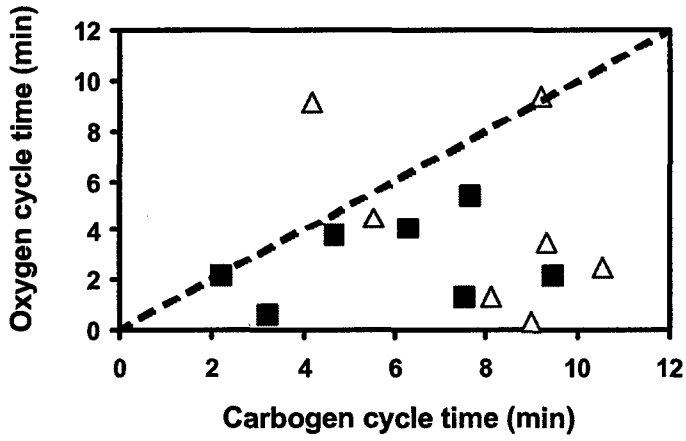

Figure 3c

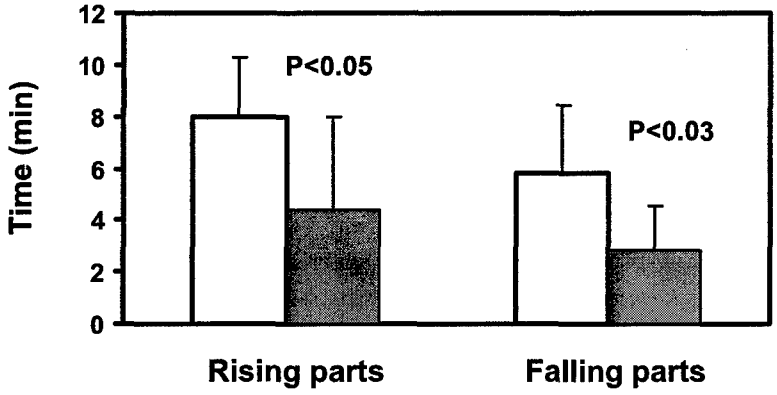

Figure 3d

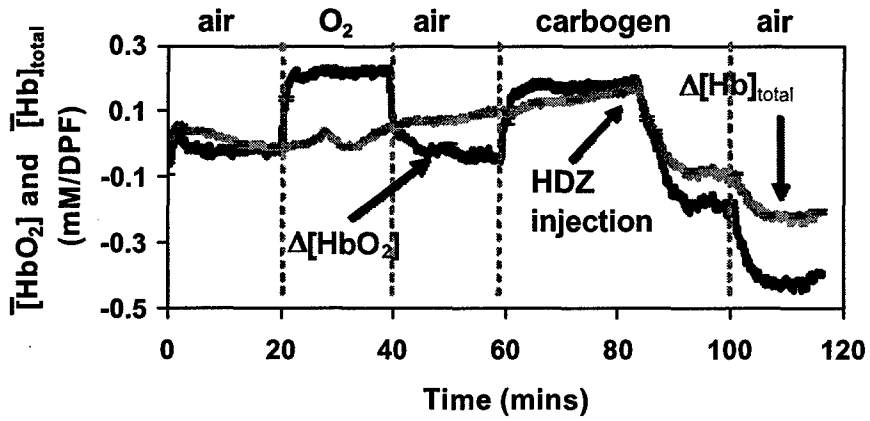

Figure 4a

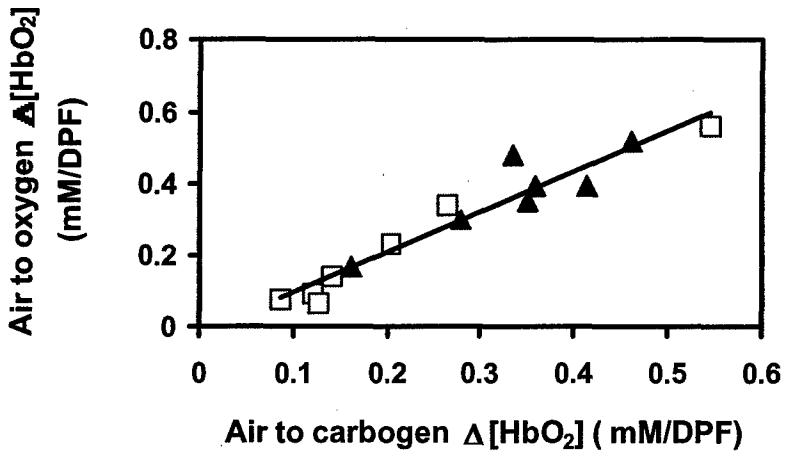

Figure 4b

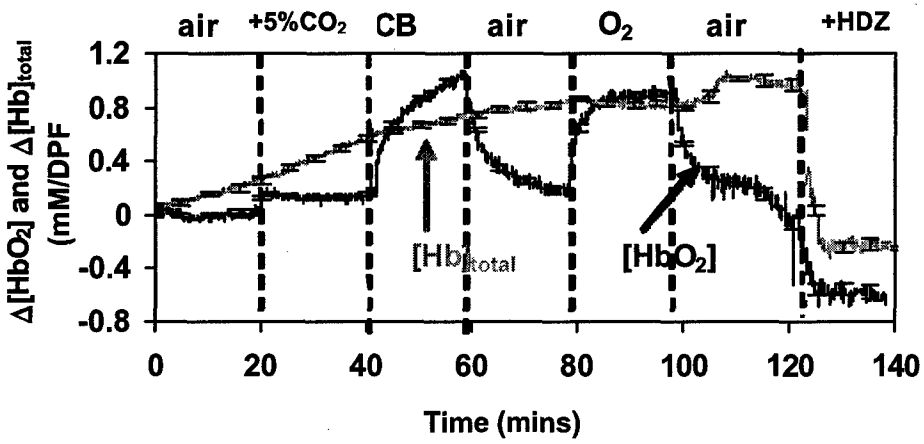

Figure 5a

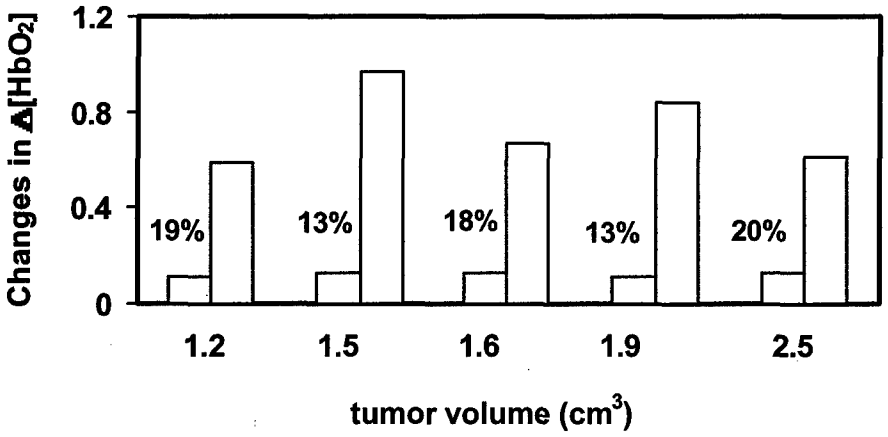

Figure 5b

Tumour oxygen dynamics measured simultaneously by near infrared spectroscopy and ^{19}F magnetic resonance imaging in rats[+]

Mengna Xia [1], Vikram Kodibagkar [2], Hanli Liu [1] and Ralph P. Mason [1,2]

[1]Joint Biomedical Engineering Graduate Program,

University of Texas at Arlington/University of Texas Southwestern Medical Center at Dallas, TX 76013

[2]Cancer Imaging Program, Department of Radiology,

University of Texas Southwestern Medical Center at Dallas,

TX 75390

Corresponding author:
Ralph P. Mason, PhD, C. Chem,
Department of Radiology,
University of Texas Southwestern Medical Center at Dallas,
5323 Harry Hines Boulevard,
Dallas, TX 75390-9058, USA;
Email: ralph.mason@utsouthwestern.edu

Running title: Tumour oxygen dynamics in vasculature and tissue

Keywords: Near infrared spectroscopy, Magnetic resonance imaging, Breast tumour, Oxygenation, Haemoglobin, Hexafluorobenzene.

[+]Presented in part at the 12th annual meeting of the International Society of Magnetic Resonance in Medicine, Kyoto, 2003

ABSTRACT

Simultaneous near-infrared spectroscopy (NIRS) and magnetic resonance imaging (MRI) were used to investigate the correlation between tumour vascular oxygenation and tissue oxygen tension dynamics in rat breast 13762NF tumours with respect to hyperoxic gas breathing. NIRS directly detected global variations in the oxygenated haemoglobin concentration ($\Delta[HbO_2]$) within tumours and oxygen tension (pO_2) maps were achieved using ^{19}F MRI of the reporter molecule hexafluorobenzene. Multiple correlations were examined between rates and magnitudes of vascular ($\Delta[HbO_2]$) and tissue (pO_2) responses. Significant correlations were found between response to oxygen and carbogen breathing using either modality. Comparison of results for the two methods showed a correlation between the vascular perfusion rate ratio and the mean pO_2 values ($R^2>0.7$). The initial rates of increase of $\Delta[HbO_2]$ and the slope of dynamic pO_2 response, $d(pO_2)/dt$ of well oxygenated voxels in response to hyperoxic challenge were also correlated. These results demonstrate the feasibility of simultaneous measurements using NIRS and MRI. NIR provides a noninvasive, surrogate marker for the pO_2 response to intervention for tumour tissue. As expected, the rate of pO_2 response to oxygen is primarily dependent upon the well-perfused rather than poorly perfused vasculature.

INTRODUCTION

Tumour oxygenation has been widely recognized as a pivotal factor in the efficacy of radiotherapy (Hall, 1994), photodynamic therapy (Chapman *et al*, 1991) and some chemotherapies (Brown, 1999) and patient stratification could be clinically important (Höckel *et al*, 1996; Fyles *et al*, 1998; Welch *et al*, 2003). It has been hoped that modulation of tumour oxygenation could be applied to enhance therapeutic efficacy. An attractive intervention is breathing hyperoxic gas, and indeed, several clinical trials have examined the efficacy of normobaric or hyperbaric oxygen, to improve therapeutic outcome, but often with marginal success (Overgaard and Horsman, 1996). It has been suggested that outcome might have been improved, if responsive tumours could have been identified *a priori*. Accordingly, accurate evaluation of tumour oxygenation in response to interventions at various stages of growth should provide a better understanding of tumour response to therapy, potentially allowing therapy to be tailored to individual characteristics.

Given the importance of tumour oxygenation, many techniques have been developed based on microelectrodes, optical reflectance, EPR, MRI and nuclear medicine approaches, as reviewed previously (Mason *et al*, 2002; Zhao *et al*, 2004). While each approach has unique strengths, some are highly invasive. Near-infrared spectroscopy (NIRS) has been developed in recent years as a promising non-invasive technique to quantify the concentration of tissue chromophores, such as oxygenated and deoxygenated haemoglobin, water and lipid (Sevick *et al*, 1991; Liu *et al*, 2000). Due to the deep penetration depth and biochemical specificity of NIRS, it has been widely applied for

quantitative measurements of cerebral oxygenation (Delpy and Cope, 1997; Yodh and Boas, 2003) and blood oxygenation in muscles *in vivo* (Homma *et al*, 1996). Recently, NIRS has been also used to monitor tumour vascular oxygenation with respect to interventions (Hull *et al*, 1999; van der Sanden *et al*, 1999; Liu *et al*, 2000; Gu *et al*, 2003; Wang *et al*, 2004). However, NIRS currently lacks spatial resolution, and thus, the utility of global measurements requires validation, given the well-documented heterogeneity of tumour pO_2. We have previously investigated correlates between pO_2 assessed by electrodes (Kim *et al*, 2003a; Mason *et al*, 2003) or fiber-optic probes (Gu *et al*, 2003) and NIRS. On occasion, there was a good correlation between global vascular oxygenation assessed and local pO_2 at individual locations, but often, disparate behavior was observed. Sequential MRI and NIRS suggested a better relationship based on average pO_2 from multiple locations (Kim *et al*, 2003a). We have now implemented simultaneous NIRS and ^{19}F MRI to examine the relationships further. Since NIRS is entirely non-invasive it would provide an attractive surrogate for monitoring tumour oxygenation, and hence, we seek correlations with absolute pO_2 measurements observed simultaneously by MRI.

MATERIALS AND METHODS

Animal preparation and experimental setup

Mammary adenocarcinomas 13762NF were implanted in skin pedicles (Hahn *et al.*, 1993) on the foreback of ten adult female Fisher 344 rats. When the tumours reached ~1 cm in diameter, the rats were anesthetized with ketamine hydrochloride i.p. (0.15 ml, 100

mg/ml, Aveco, Fort Dodge, IA) and were maintained under general gaseous anesthesia (air and 1% isoflurane; Baxter International Inc, Deerfield, IL). Tumour hair was trimmed to give good optical contact for NIR light transmission. Hexafluorobenzene (HFB, 50 μl, 99.9%, Lancaster Co., Pelham, NH) was administered along two or three tracks in central and peripheral regions of the tumours in a single plane (transverse to the rat's tumour, and in the region of NIR photon pathway) using a Hamilton syringe with a 32 G needle. The needle was inserted manually to penetrate across the tumour and was withdrawn ~1 mm to reduce pressure and 3~4 μl of HFB was deposited. The needle was then repeatedly withdrawn 1~2 mm and further HFB deposited at each point, as described in detail previously (Zhao *et al*, 2004).

The tumour was placed inside a size-matched Helmholtz coil, specially designed for the simultaneous MRI-NIRS study. The tumour was inserted between the two loops of the Helmholtz coil and two NIRS probes were introduced through the ends of the coil along the coil axis (Fig. 1). The rats were placed in the magnet on their side, and body temperature was maintained using a warm water blanket. Seven rats were subjected to respiratory challenge in the sequence air-oxygen-air-carbogen-air. One rat breathed air-carbogen-air-oxygen-air, one rat breathed air-carbogen-air and one rat breathed air-oxygen-air.

NIRS for measuring $\Delta[HbO_2]$

A homodyne frequency-domain system (NIM, Philadelphia, PA) was used to monitor the global change of deoxy- and oxy-haemoglobin concentration ($\Delta[HbO_2]$) in the

tumour, as described previously (Yang *et al*, 1997), though with minor modifications to ensure MR compatibility (Fig. 1). Briefly, light from 785 nm and 758 nm laser diodes (modulated at 140 MHz) was coupled into a bifurcated fiber bundle with a length of 7 m. The long fiber bundle ensured the separation of the NIRS hardware from the magnet. The probe tips (made of metal-free material for MR compatibility) were placed in good contact on opposite surfaces of the tumour. After being absorbed and scattered in the tumour tissue, the transmitted light was collected on the opposite side of the tumour by another fiber bundle (of same length) and amplified by a photomultiplier tube (PMT). An In-phase and Quadrature (IQ) demodulator chip was used to demodulate the amplitude-modulated signal from the PMT.

According to the modified Beer-Lambert law, changes of oxy- and deoxy-haemoglobin concentration, $\Delta[HbO_2]$ and $\Delta[Hb]$, respectively, can be derived from the measured amplitudes at the two wavelengths (758 nm and 785 nm) (Kim *et al*, 2003a)

$$\Delta[HbO_2] = \frac{-10.63\log(\frac{A_b}{A_t})^{758} + 14.97\log(\frac{A_b}{A_t})^{785}}{DPF \cdot d} \quad (1)$$

$$\Delta[Hb] = \frac{8.95\log(\frac{A_b}{A_t})^{758} - 6.73\log(\frac{A_b}{A_t})^{785}}{DPF \cdot d} \quad (2)$$

where A_b is the baseline amplitude, A_t is the transient amplitude during measurement, and d is the direct source-detector separation. *DPF* (differential path-length factor) is a tissue-dependent parameter and defined as the ratio between the optical path length and the physical separation between the source and detector. Since *DPF* is a variable, depending on tissue types and wavelengths, it is currently difficult to quantify *DPF* for tumours.

However, since our study focuses on dynamic changes of [HbO_2], we may include *DPF* in the unit of [HbO_2] and still obtain characteristic features of tumour oxygen dynamics (Liu *et al*, 2000). Because of un-quantitative nature of tumour *DPF* values, we will use arbitrary units (AU) to label all of the [HbO_2] data figures in this paper.

Mathematical model for blood oxygenation dynamics of tumours

We previously derived a simple mathematical model (Liu *et al*, 2000) to examine vascular dynamics relating the time constants of the biphasic features of Δ[HbO_2] to tumour blood perfusion rates by analogy to methods originally developed by Kety in the 1950's to measure regional cerebral blood flow (rCBF) with diffusible radiotracers (Kety, 1951). Our mathematical model is expressed as

$$\Delta[HbO_2(t)]^{vasculature} = \gamma H_0[1-e^{\frac{-ft}{\gamma}}] = A[1-e^{\frac{-ft}{\gamma}}] \qquad (3)$$

where Δ[HbO_2] corresponds to the changes in oxy-haemoglobin concentration from tumour vasculature measured by the NIRS, H_0 is the arterial oxygenation input, f is the blood perfusion rate, γ is the ratio of Δ[HbO_2] in the vascular bed to that in the veins and defined as vascular coefficient of the tumour.

Assuming that the tumour has two distinct perfusion regions (well-perfused and poorly perfused region), it is reasonable to define two different blood perfusion rates (f_1, f_2) with two different vascular coefficients (γ_1, γ_2) in the model. Consequently, eq. (3) can be modified to a summation of two exponential expressions, representing two regions, as

$$\Delta[HbO_2(t)]^{vasculature} = \gamma_1 H_0[1-e^{\frac{-f_1 t}{\gamma_1}}] + \gamma_2 H_0[1-e^{\frac{-f_2 t}{\gamma_2}}] = A_1[1-e^{\frac{-t}{\tau_1}}] + A_2[1-e^{\frac{-t}{\tau_2}}], \qquad (4)$$

where f_1 and γ_1 are the blood perfusion rate and the vasculature coefficient, respectively, in the well-perfused region, and f_2 and γ_2 are those representing the poorly perfused region. The two amplitudes are defined as $A_1=\gamma_1 H_0$ and $A_2= \gamma_2 H_0$, while the two time constants are defined as $\tau_1 = \gamma_1/f_1$ and $\tau_2 = \gamma_2/f_2$. Since A_1, A_2 and the two time constants can be determined by curve-fitting eq. (4) to the dynamic NIRS measurements, we arrive at the ratios for two vascular coefficients and two blood perfusion rates, as follows:

$$\frac{\gamma_1}{\gamma_2} = \frac{A_1}{A_2}, \qquad \frac{f_1}{f_2} = \frac{A_1/\tau_1}{A_2/\tau_2}, \tag{5}$$

where A_1/τ_1 and A_2/τ_2 reflect the perfusion rates of $\Delta[HbO_2]$ in the well and poorly perfused regions, respectively, and f_1/f_2 is the perfusion rate ratio of the well-perfused to poorly-perfused regions.

***FREDOM* for measuring pO_2**

MRI experiments were performed using a Varian Inova 4.7 T horizontal bore system equipped with actively shielded gradients. Shimming was performed on the tumour tissue water signal to reduce the line-width to less than 100 Hz. ^1H MRI (200.1 MHz) T1-weighted reference images were acquired with TR/TE of 150/10 ms and 40x40 mm^2 field of view. Following ^1H MRI, corresponding ^{19}F MR images (188.3 MHz) were obtained to show the distribution of HFB in the tumour. The *FREDOM* (*F*luorocarbon *R*elaxometry by *E*cho-planar imaging for *D*ynamic *O*xygen *M*apping) approach was used to measure pO_2, as described in detail previously (Hunjan *et al*, 2001). T1 maps were computed on a voxel-by-voxel basis using nonlinear least-squares data fitting by the

Gauss-Newton method. We applied a threshold to the raw T1 data in order to remove random noise, *i.e.*, voxels with T1 error >3.6 sec or T1 error/T1 >50% were disregarded. Maps of pO_2 values were obtained from the T1 maps using the equation, $pO_2 = (1/T1-0.0835)/0.001876$ (Hunjan *et al*, 2001).

Three baseline pO_2 data sets were acquired over 24 mins for all tumours, while the rats breathed air, after which the rats were repeatedly exposed to oxygen or carbogen (95% O_2 and 5% CO_2) interventions. Five pO_2 maps were obtained during each subsequent gas switch period. Typically, for a five gas-intervention sequence (*e.g.*, air-oxygen-air-carbogen-air), a total of 23 pO_2 maps were obtained over a period of 3 h. For temporal analysis, voxels were selected as only those which provided consistently reliable data for all 23 measurements over the time course with a range of 5 to 44 for the ten tumours. The slope of dynamic pO_2 changes (rate) was defined as $d(pO_2)/dt$ and $d(pO_2')/dt$ in response to increasing or decreasing inhaled FO_2 (Fraction of O_2), respectively, while pO_2 is the mean value of pO2 in all voxels in order to obtain global tumour pO_2 readings for comparison with global $\Delta[HbO_2]$ readings.

Statistical Analysis

Linear regression analysis was used to calculate the correlation between the NIRS-derived tumour hemodynamic parameters (*i.e.*, $\Delta[HbO_2]$, A_1/τ_1, A_2/τ_2, f_1/f_2) and the *FREDOM*-determined tumour parameters (*i.e.*, pO_2, $d(pO_2)/dt$, $d(pO_2')/dt$). Data are presented as mean ± standard deviation (SD) and paired Student-t tests compared the effects of oxygen and carbogen on $\Delta[HbO_2]$ and pO_2.

RESULTS

Dynamic response of $\Delta[HbO_2]$ measured by NIRS

Figure 2 shows a typical temporal profile of $\Delta[HbO_2]$ in response to oxygen and carbogen interventions for a representative 13762NF breast tumour (No.1, 1.6 cm^3), displaying apparent biphasic response to both interventions. Both single (eq. 3) and double-exponential (eq. 4) curve fitting were tested for the carbogen intervention (Fig. 3A). The maximal $\Delta[HbO_2]$ achieved with oxygen challenge was compared with that of carbogen, and revealed no significant difference between oxygen and carbogen intervention ($p>0.3$); indeed, there was a strong correlation between the maximal $\Delta[HbO_2]$ values with these two interventions ($R^2>0.75$, Fig. 3B), consistent with our previous observations (Gu *et al*, 2003). No correlation was found between the perfusion rate ratio (f_1/f_2) and tumour size ($R^2=0.16$, Fig. 3C). Vascular oxygen dynamics in response to interventions are provided for individual tumours as supplementary material in Table 2.

pO_2 measurements by *FREDOM*

Overlay of ^{19}F and ^{1}H MR images showed that HFB was distributed in both central and peripheral regions of tumour and individual pO_2 values ranged from hypoxia (< 1 torr) to 35 torr under baseline conditions (Fig. 4). Mean baseline pO_2 over all voxels ranged from hypoxia (< 5 torr) to 27 torr with a hypoxic fraction (HF_5; fractional voxels that are less than 5 torr) ranging form 0 to 100% (mean 36%) and summarized in Table 1. A strong correlation was found between mean baseline pO_2 and HF_5 ($R^2>0.85$, Fig. 5A).

Administration of oxygen or carbogen produced significant increases in tumour pO_2, as shown in the pO_2 maps, graphs and Table (Figs. 2 and 4). pO_2 response to respiratory challenge for a representative tumour, measured simultaneously by *FREDOM* and NIRS, is shown in Fig 2. Baseline measurements (breathing air) were generally stable, and altering the inhaled gas to oxygen or carbogen induced rapid and significant changes in both pO_2 and $\Delta[HbO_2]$ ($p<0.001$). Upon return to air (baseline), $\Delta[HbO_2]$ dropped quickly and significantly within 16 mins, and then more slowly, for the next 24 mins, whereas the pO_2 decrease was more gradual. Altering the inhaled gas to carbogen also produced a rapid increase in both pO_2 and $\Delta[HbO_2]$. Upon return to air breathing from carbogen both $\Delta[HbO_2]$ and pO_2 showed a similar trend to that following oxygen. As expected, all ten tumours showed a significant increase in pO_2 and decrease in hypoxic fraction (HF) in response to oxygen or carbogen inhalation. In this study, baseline pO_2 was not a good indicator of the magnitude of response (ΔpO_2) to hyperoxic gas breathing ($R^2<0.5$), but the elevated pO_2 achieved with oxygen was a function of the magnitude of the pO_2 response (ΔpO_2; Fig. 5B, $R^2>0.94$). Similarly, pO_2 achieved with carbogen was related to ΔpO_2 ($R^2>0.92$). The magnitude of response to either hyperoxic gas was correlated ($R^2>0.79$), as also the maximum pO_2 achieved with either gas ($R^2>0.83$). The rate of response to oxygen challenge, $d(pO_2)/dt$ was significantly faster than the return to baseline, $d(pO_2')/dt$ for oxygen intervention ($p<0.02$), but no difference was observed for carbogen ($p>0.1$, Fig.6). The mean pO_2 values with carbogen breathing were significantly higher than oxygen ($p<0.008$), and the tumour hypoxic fraction was generally eliminated during carbogen breathing (n = 7 of 9 tumours, Table 1).

The relationship between pO_2 and $\Delta[HbO_2]$ with respect to hyperoxic gas

Taken as a group of 10 tumours, there was no apparent relationship between the magnitude of the change in tumour vascular oxygenation ($\Delta[HbO_2]$ and pO_2 ($R^2<0.1$). However, if tumours were divided into two sub-populations, then two separate correlations were found each with similar slope (Fig. 7A), with the average of maximum $\Delta[HbO_2]$ equal to 0.18 ± 0.08 of in group 1 and 0.39 ± 0.06 in group 2. There was also a correlation ($R^2>0.7$) between the perfusion rate ratio, f_1/f_2, derived from fitting the $\Delta[HbO_2]$ curve and the mean pO_2 values of all voxels achieved with hyperoxic gas intervention (Fig.7B). Assessment of f_1/f_2 is predicated on biphasic behavior with respect to interventions, which was observed in most cases (13 of 16 measurements). There was also a positive correlation between A_1/τ_1 (the fast component of biphasic $\Delta[HbO_2]$) and the $d(pO_2)/dt$ of well oxygenated voxels (*i.e.*, those with pO_2 values > 10 torr under oxygen or carbogen intervention) ($R^2>0.5$, Fig. 8A). However, no correlation was found between $d(pO_2)/dt$ and A_2/τ_2 (the slow component, Fig. 8B).

DISCUSSION

In the present study, global average $\Delta[HbO_2]$ was measured by NIRS, and pO_2 maps were obtained simultaneously by ^{19}F MRI. We used transmission mode NIRS in order to interrogate deep tumour tissue. Utilizing our previously developed mathematical model (Liu *et al*, 2000), multiple hemo-dynamic parameters were derived for $\Delta[HbO_2]$ (A_1/τ_1, A_2/τ_2 and f_1/f_2) to be compared with pO_2. Our results demonstrate that oxygenation parameters measured from both techniques show significant and consistent elevation in

tumour oxygenation during the hyperoxic gas interventions. As reported previously, the magnitude of the vascular response was similar with both hyperoxic gases (Gu *et al*, 2003). As expected, $\Delta[HbO_2]$ increased much faster than pO_2 in all ten tumours, indicating that change in tumour vascular oxygenation precedes tumour tissue oxygenation. This observation is consistent with our previous studies in this tumour type measured simultaneously by NIRS and fiber-optic probes (Gu *et al*, 2003), as well in the Dunning prostate R3327-AT1 tumours measured sequentially by NIRS and ^{19}F MRI (Kim *et al*, 2003a).

We have previously demonstrated the application of *FREDOM* to monitor tumour oxygen dynamics in diverse rat prostate tumours (Zhao *et al*, 2001; Zhao *et al*, 2002), human tumour xenografts (Mason *et al*, 2002) and a few breast tumours (Song *et al*, 2002). Here, mean baseline was $pO_2=12 \pm 10$ torr for the 10 tumours, which is lower than reported previously (Song *et al*, 2002), but entirely consistent with the newer anesthetic protocol (air or 21% oxygen, as opposed to 33% O_2 previously). There was a strong correlation between baseline pO_2 and hypoxic fraction (Fig. 5C), as we have previously found using Dunning prostate R3327-HI tumours (Zhao *et al*, 2001). The pO_2 achieved with carbogen in this study was significantly higher than with oxygen and carbogen appeared to be more effective at eliminating the hypoxic fraction. However, carbogen was generally applied second in our experiment protocols, and it is highly likely that the initial oxygen primed the tumour. Indeed, while oxyhaemoglobin generally returned to baseline during the air breathing episode between hyperoxic gases, it is clear that pO_2 remained elevated (Fig. 2). Both ΔpO_2 and the maximum pO_2 achieved with either gas

were closely correlated. Similar behavior was reported previously based on measurements using fiber optic probes (Gu *et al*, 2003). However, in this study baseline pO_2 did not provide a good indication of response to hyperoxic gas (ΔpO_2 or pO_{2max}).

The rate of pO_2 response to either gas was similar (Fig. 6), but decrease upon return to air was significantly faster in the case of oxygen, but not carbogen. Considering the relationships between pO_2 and $\Delta[HbO_2]$ there was a significant correlation between f_1/f_2 and mean pO_2 values achieved with hyperoxic gas intervention (Fig. 7B). Furthermore, there was a significant correlation between A_1/τ_1, but not A_2/τ_2 and $d(pO_2)/dt$, provided that they were selected from well oxygenated or responsive voxels (Fig. 8). We believe these results provide further valuable insight into tumour physiology and the ability to conduct simultaneous optical and NMR measurements. A goal had been to develop a cheap, simple, fast surrogate measurement of pO2 based on NIRS of the oxygenation status of endogenous haemoglobin. It seems that no straightforward correlation exists (Fig. 7A), but there is a relationship between pO_2 and the well perfused compartments (Fig. 7B and 8A). Separation of the tumours into two groups does suggest a relationship between ΔpO_2 and $\Delta[HbO_2]$, with a tendency for the largest induced pO_2 changes to occur in those tumours with larger $\Delta[HbO_2]$ changes, but here were no obvious differences between these tumours to allow a priori stratification (Fig. 7A).

A major concern is tumour heterogeneity, as recognized throughout the literature and shown here by ^{19}F MRI (Fig. 4). Indeed, we have obtained some preliminary data using a single NIR source and three detectors placed on various regions across a tumour (Kim *et al*, 2003b). The results show that each region of the tumour responded differently to

hyperoxic gas, in terms of the extent and rate, indicating the heterogeneity of tumour vasculature. Spatial discrimination will be even more critical if such studies are transferred to human breast cancer, where the tumour is surrounded by normal tissue (Brooksby *et al*, 2003). Nevertheless, we believe this hemodynamic model and correlation between tumour vascular oxygenation and pO_2 provides valuable insight into the tumour compartment of such a mixed system and explores dynamic signatures of breast tumours, which can, in turn, enhance/assist human breast cancer diagnosis and prognosis.

In summary, by studying tumour vascular oxygenation concomitantly with changes in tumour oxygen tension, we found several significant correlations between rates and magnitudes of vascular and tissue responses. This study also demonstrates the feasibility of conducting simultaneous NIRS and MRI oximetry. We believe the correlation of tumour vascular oxygenation and tumour tissue pO_2 can provide valuable insights into tumour pathophysiology and response to interventions.

ACKNOWLEDGEMENT

This work was supported in part by the Department of Defense Pre-doctoral Research Fellowship W81XWH-04-1-0411 (MX), Breast Cancer Initiative grant DAMD17-00-1-0459 (HL), NIH R01 CA79515 (RPM) and NIH P20 CA086354 (RPM). The MR investigations were performed at the Mary Nell and Ralph B. Rogers NMR Center, a NIH BRTP facility (#P41RR02584). We are grateful to Vincent Bourke and Drs. Anca Constantinescu, Yueqing Gu and Luis Saez for valuable discussions and technical assistance.

Figure 1

Schematic of experimental setup. Z is along the bore of the magnet, and X along the axis of the rf coil.

Figure 2

Temporal profiles of $\Delta[HbO_2]$ (curve) and pO_2 (◆) in response to respiratory challenge for a representative 13762NF rat breast tumour (No. 1, 1.6 cm^3), measured simultaneously by NIRS and *FREDOM*. pO_2 is the average value of all voxels.

Figure 3

A) Dynamic responses of $\Delta[HbO_2]$ to carbogen in tumour no 1. Single exponential curve fitting yielded $\Delta[HbO_2] = 0.22\{1 - \exp[-(t-106.8)/2.5]\}$ (R^2=0.64), and double exponential fitting resulted in $\Delta[HbO_2] = 0.15\{1 - \exp[-(t-106.8)/0.58]\} + 0.13\{1 - \exp[-(t-106.8)/23.2]\}$ (R^2=0.88).

B) Relationship of maximum $\Delta[HbO_2]$ in breast tumours in response to switching from air to oxygen and to carbogen (R^2>0.75).

C) Variation of the perfusion rate ratio (f_1/f_2: well-perfused to poorly perfused regions) with tumour size (R^2=0.16) for oxygen (◆) or carbogen intervention (□).

Figure 4

Representative pO_2 maps (1.25 mm resolution) obtained using *FREDOM* with the rats A) breathing air, B) breathing 100% O_2 (fifth map after switching from the air), C) breathing carbogen (95% O_2 + 5% CO_2) (fifth map after switching from the air). Large T1 error represents T1 error > 3.6 sec or T1 error/T1 >50%.

Figure 5

A) Correlation between baseline pO_2 and hypoxic fraction (HF_5) measured using *FREDOM* (R^2>0.85).

B) Correlation between maximum pO_2 achieved while breathing oxygen and the change in pO_2 (R^2>0.94).

Figure 6

Mean $d(pO_2)/dt$ (open) and $d(pO_2')/dt$ (shaded) with error bars demonstrating the standard deviation of the mean for eight tumours with both interventions, when gas was switched from air to a hyperoxic gas and back to air, respectively. pO_2 is the mean value of all voxels appeared in the five maps during oxygen or carbogen intervention. The rates showed a significant difference with oxygen ($p<0.02$), but not with carbogen ($p>0.1$).

Figure 7

A) Correlation between maximum $\Delta[HbO_2]$ and change in pO_2 with respect to hyperoxic gas intervention for two groups of tumours (●) (group 1: #1, 2, 6, 7, 8, 9, 10; $R^2 > 0.51$) and (Δ) (group 2: #3, 4, 5; $R^2 > 0.82$).

B) Correlation between pO_2 and perfusion rate ratio (f_1/f_2) for tumours with biphasic response to intervention ($R^2 > 0.7$). pO_2 is the mean value for the final three pO_2 maps under hyperoxic intervention, selected from all voxels appearing in the final three pO_2 maps during oxygen (◆) or carbogen (□) intervention.

Figure 8

A) $d(pO_2)/dt$ vs A_1/τ_1 determined from $\Delta[HbO_2]$ for tumours with biphasic response to interventions, showing a positive correlation ($R^2 > 0.5$). pO_2 are obtained from the mean value of all well oxygenated voxels appearing in the five pO_2 maps during oxygen (◆) or carbogen (□) intervention (*i.e.*, the maximum $pO_2 > 10$ torr under oxygen or carbogen intervention)

B) $d(pO_2)/dt$ vs A_2/τ_2 from $\Delta[HbO_2]$ for tumours with biphasic response to interventions, showing lack of correlation.

REFERENCES

Benesch RE and Bensch R (1974) The mechanism of interaction of red cell organic phosphates with hemoglobin. *Adv Protein Chem* **28**: 211-237

Brooksby B, Dehghani H, Pogue BW, Paulsen KD (2003) Near infrared (NIR) tomography breast image reconstruction with a priori structural information from MRI: algorithm development for reconstructing heterogeneities. *IEEE J Select Topics Quantum Electron* **9**: 199-209

Brown JM (1999) The hypoxic cell: a target for selective cancer therapy--eighteenth Bruce F. Cain Memorial Award lecture. *Cancer Res* **59:** 5863-5870

Chapman JD, Stobbe CC, Arnfield MR, Santus R, Lee J and McPhee MS (1991) Oxygen dependency of tumor cell killing in vitro by light-activated Photofrin II. *Radiat Res* **126:** 73-79

Delpy DT and Cope M (1997) Quantification in tissue near-infrared spectroscopy. *Phil Trans R Soc Lond B* **352:** 649-659

Duncan A, Meek JH, Clemence M, Elwell CE, Tyszczuk L, Copy M and Delpy DT (1995) Optical pathlength measurements on adult head, calf and forearm and the head of the newborn infant using phase resolved optical spectroscopy. *Phys Med Biol* **40**: 295-304

Dunn J, O'Hara JA, Zaim-Wadghiri Y, Meyerand M, Grinberg O, Hou H, Hoopes P, Demidenko E and Swartz H (2002) Changes in oxygenation of intracranial tumors with carbogen: a BOLD MRI and EPR oximetry study. *J Magn Reson Imaging* **16:** 511-521.

Fyles AW, Milosevic M, Wong R, Kavanagh MC, Pintilie M, Sun A, Chapman W, Levin W, Manchul L, Keane TJ and Hill RP (1998) Oxygenation predicts radiation response and survival in patients with cervix cancer. *Radiother Oncol* **48:** 149-156

Gu Y, Bourke VA, Kim JG, Constantinescu A, Mason RP and Liu H (2003) Dynamic response of breast tumor oxygenation to hyperoxic respiratory challenge monitored with three oxygen-sensitive parameters. *Appl Opt* **42:** 2960-2967

Hahn EW, Peschke P, Mason RP, Babcock EE and Antich PP (1993) Isolated tumor growth in a surgically formed skin pedicle in the rat: a new tumor model for NMR studies. *Magn Reson Imaging* **11:** 1007-1017

Hall EJ (1994) The oxygen effect and reoxygenation. In *Radiobiology for the Radiologist,* Hall EJ (ed) pp 133-152. J. B. Lippincott: Philadelphia

Höckel M, Schlenger K, Aral B, Mitze M, Schaffer U and Vaupel P (1996) Association between tumor hypoxia and malignant progression in advanced cancer of the uterine cervix. *Cancer Res* **56:** 4509-4515

Homma S, Fukunaga T and Kagaya A (1996) Influence of adipose tissue thickness on near-infrared spectroscopic signals in the measurement of human muscles. *J Biomed Opt* **1:** 418-424

Hull EL, Conover DL and Foster TH (1999) Carbogen-induced changes in rat mammary tumour oxygenation reported by near infrared spectroscopy. *Br J Cancer* **79:** 1709-1716

Hunjan S, Zhao D, Constantinescu A, Hahn EW, Antich PP and Mason RP (2001) Tumor oximetry: demonstration of an enhanced dynamic mapping procedure using

fluorine-19 echo planar magnetic resonance imaging in the Dunning prostate R3327-AT1 rat tumor. *Int J Radiat Oncol Biol Phys* **49:** 1097-1108

Kety SS (1951) The theory and applications of the exchange of inert gas at the lungs and tissues. *Pharmacol Rev* **3:** 1-41

Kim JG, Zhao D, Song Y, Constantinescu A, Mason RP and Liu H (2003a) Interplay of tumor vascular oxygenation and tumor pO_2 observed using near-infrared spectroscopy, an oxygen needle electrode, and ^{19}F MR pO_2 mapping. *J Biomed Opt* **8:** 53-62

Kim JG, Gu Y, Constantinescu A, Mason RP and Liu H (2003b) Non-uniform tumor vascular oxygen dynamics monitored by three-channel near-infrared spectroscopy. In *Optical Tomography and Spectroscopy of Tissue V,* Chance B.(ed) pp 4955-4957. SPIE-International Society for Optical Engineering: Bellingham

Liu H, Song Y, Worden KL, Jiang X, Constantinescu A and Mason RP (2000) Noninvasive investigation of blood oxygenation dynamics of tumors by near-infrared spectroscopy. *Appl Optic* **39:** 5231-5243

Mason RP, Ran S and Thorpe PE (2002) Quantitative assessment of tumor oxygen dynamics: molecular imaging for prognostic radiology. *J Cell Biochem* **39:** 45-53

Mason RP, Hunjan S, Constantinescu A, Song Y, Zhao D, Hahn EW, Antich PP and Peschke P (2003) Tumor oximetry: comparison of ^{19}F MR EPI and electrodes. *Adv Exp Med Biol* **530:** 19-27

Overgaard J and Horsman MR (1996) Modification of hypoxia-induced radioresistance in tumors by the use of oxygen and sensitizers. *Semin Radiat Oncol* **6:** 10-21

Sevick EM, Chance B, Leigh J, Nioka S and Maris M (1991) Quantitation of time- and frequency-resolved optical spectra for the determination of tissue oxygenation. *Anal Biochem* **195:** 330-351

Song Y, Contantinescu A and Mason RP (2002) Dynamic breast tumor oximetry: the development of prognostic radiology. *Technol Cancer Res and Treat* **1:** 471-478

van der Sanden BPJ, Heerschap A, Hoofd L, Simonetti AW, Nicolay K, van der Toorn A, Colier WNJM and van der Kogel AJ (1999) Effect of carbogen breathing on the physiological profile of human glioma xenografts. *Magn Reson Med* **42**:490-499

van der Zee P, Essepreis M and Delpy DT (1992) Experimentally measured optical pathlengths for the adult head, calf and forearm and the head of the new born infant as a function of inter optode spacing. *Adv Exp Med Biol* **316**: 143-153

Vaupel P, Kelleher DK and Engel T (1994) Do changes in tumor blood flow necessarily lead to changes in tissue oxygenation and in bioenergetic status? *Adv Exp Med Biol* **361:** 607-611

Wang HW, Putt ME, Emanuele MJ, Shin DB, Glatstein E, Yodh AG and Busch TM (2004) Treatment-induced changes in tumor oxygenation predict photodynamic therapy outcome. *Cancer Res* **64:** 7553–7561

Welch MJ, Halpern H and Kurdziel KA (2003) Example of imaging solutions to multi-disease biological challenge--imaging of hypoxia. *Acad Radiol* **10:** 887-890

Yang Y, Liu H, Li X and Chance B (1997) Low-cost frequency-domain photon migration instrument for tissue spectroscopy, oximetry, and imaging. *Opt Eng* **36:** 1562-1569.

Yodh AG and Boas DA (2003) Functional imaging with diffusing light. In *Biomedical photonics handbook*, Tuan V. (ed) pp 21-1 - 21-45. CRC: Florida

Zhao D, Constantinescu A, Hahn EW and Mason RP (2001) Tumor oxygen dynamics with respect to growth and respiratory challenge: investigation of the Dunning prostate R3327-HI tumor. *Radiat Res* **156:** 510-520

Zhao D, Constantinescu A, Hahn EW and Mason RP (2002) Differential oxygen dynamics in two diverse dunning prostate R3327 rat tumor sublines (MAT-Lu and HI) with respect to growth and respiratory challenge. *Int J Radiat Oncol Biol Phys* **53:** 744-756

Zhao D, Jiang L and Mason RP (2004) Measuring changes in tumor oxygenation. *Methods Enzymol* **386:** 378-418

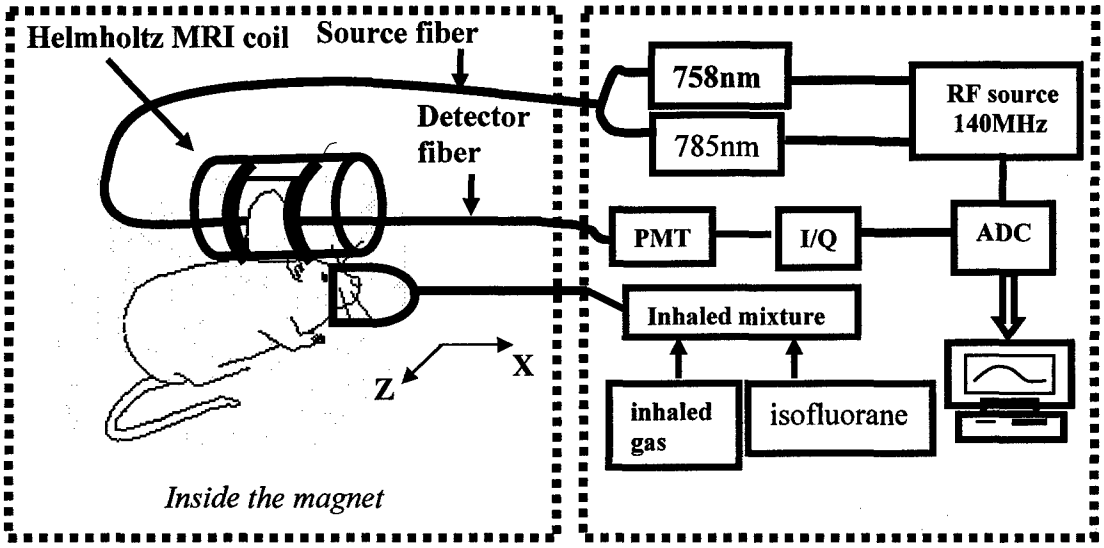
Helmholtz MRI coil
Source fiber
Detector fiber
758nm
785nm
RF source 140MHz
PMT
I/Q
ADC
Inhaled mixture
inhaled gas
isofluorane
Z
X
Inside the magnet

Figure 1

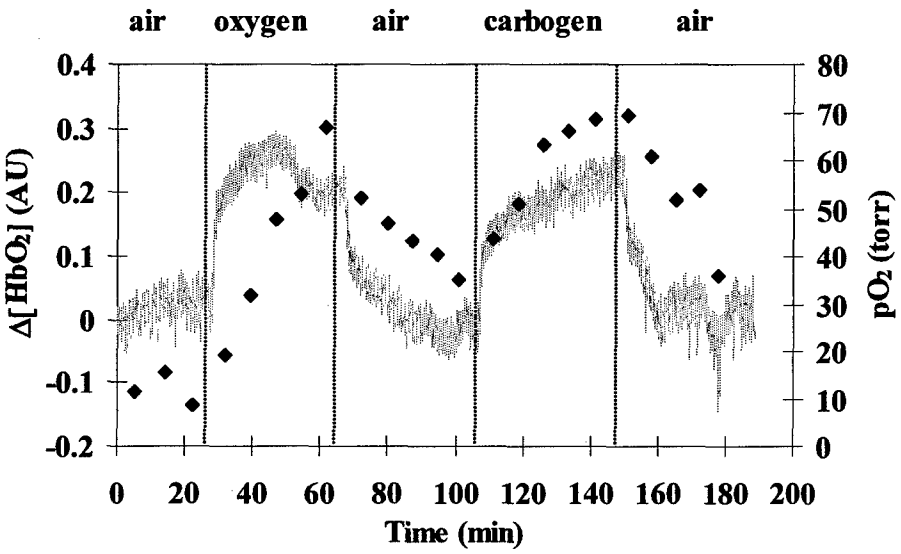
air
oxygen
air
carbogen
air
0.4
0.3
0.2
0.1
0
-0.1
-0.2
Δ[HbO2] (AU)
80
70
60
50
40
30
20
10
0
pO2 (torr)
0
20
40
60
80
100
120
140
160
180
200
Time (min)

Figure 2

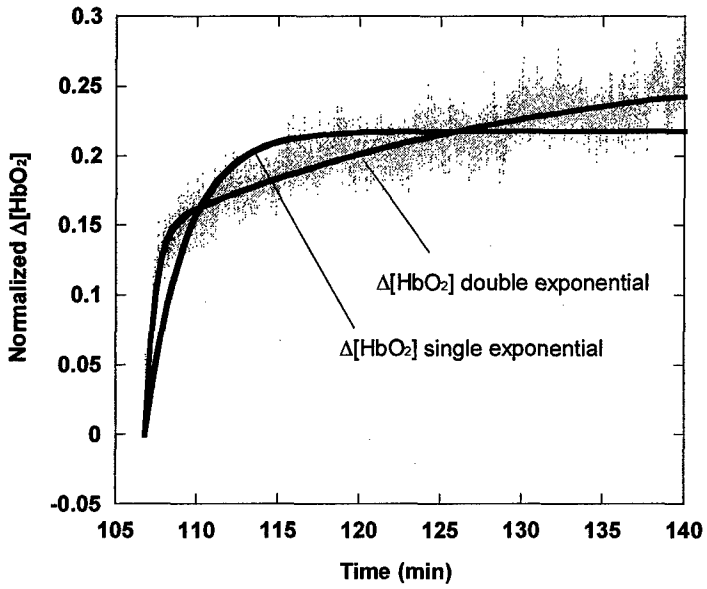

Figure 3A

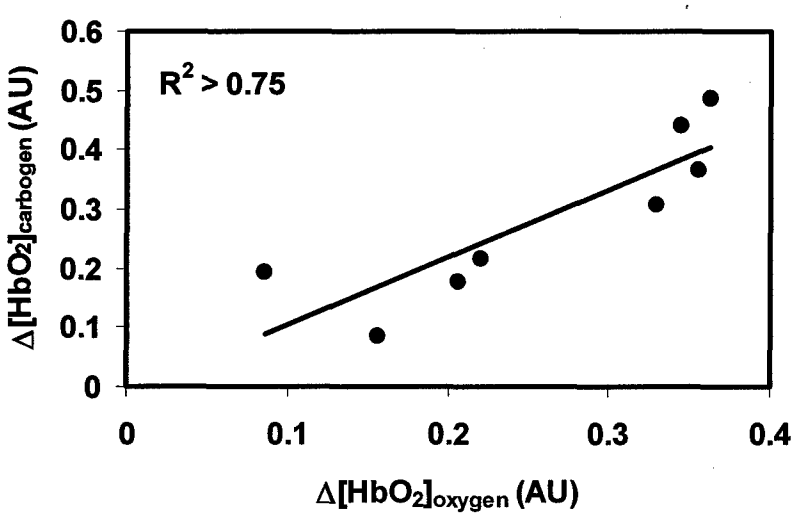

Figure 3B

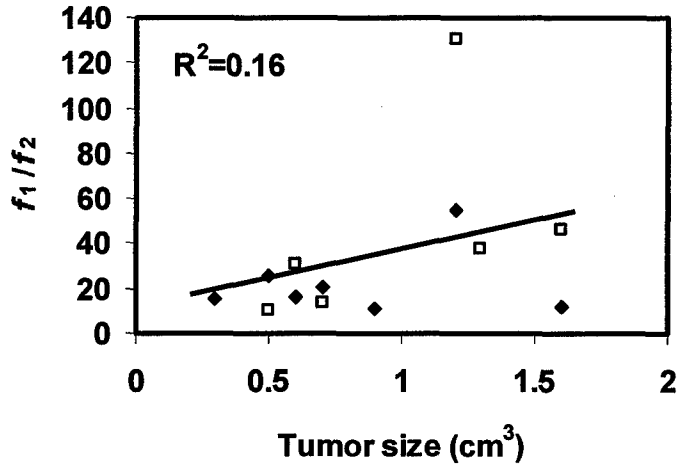

Figure 3C

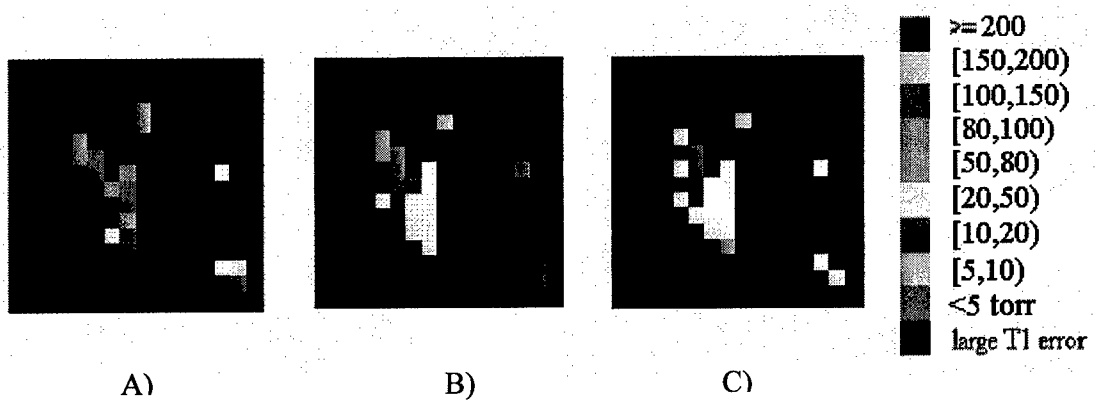
>=200
[150,200)
[100,150)
[80,100)
[50,80)
[20,50)
[10,20)
[5,10)
<5 torr
large T1 error
A)
B)
C)

Figure 4

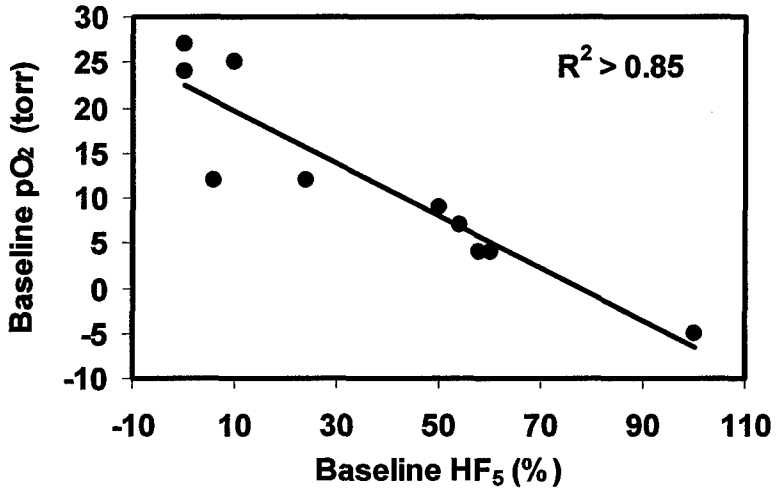

Figure 5A

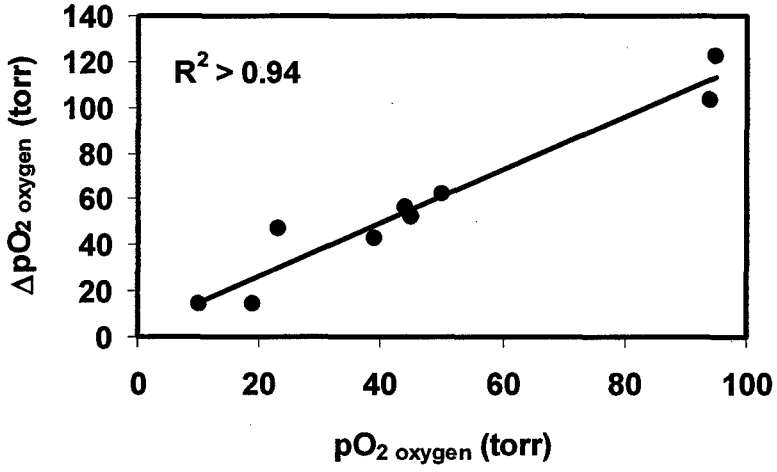

Figure 5B

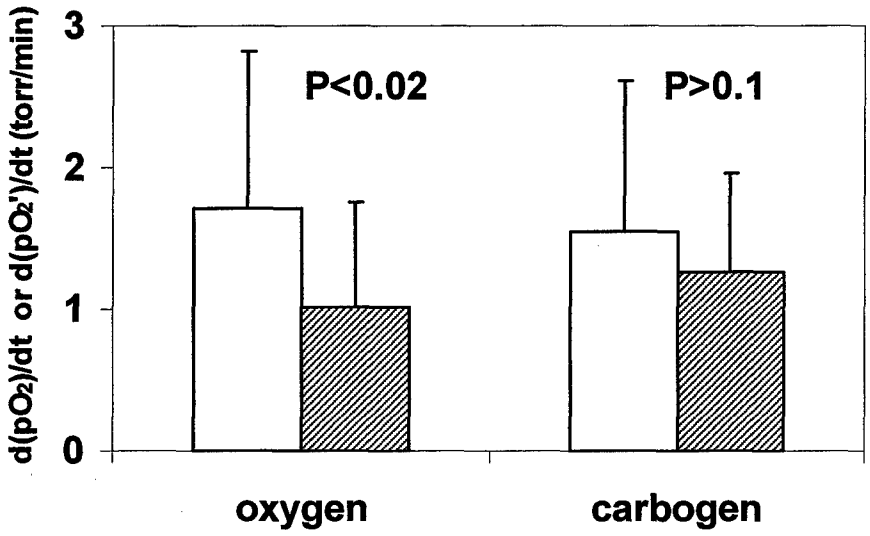

Figure 6

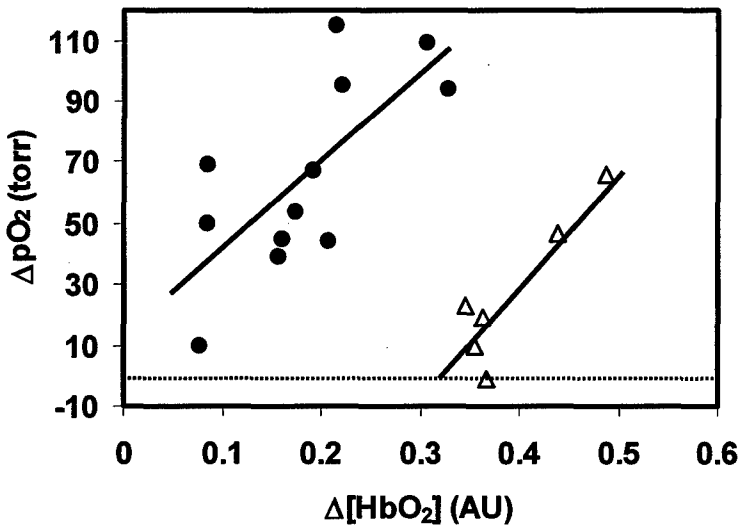

Figure 7A

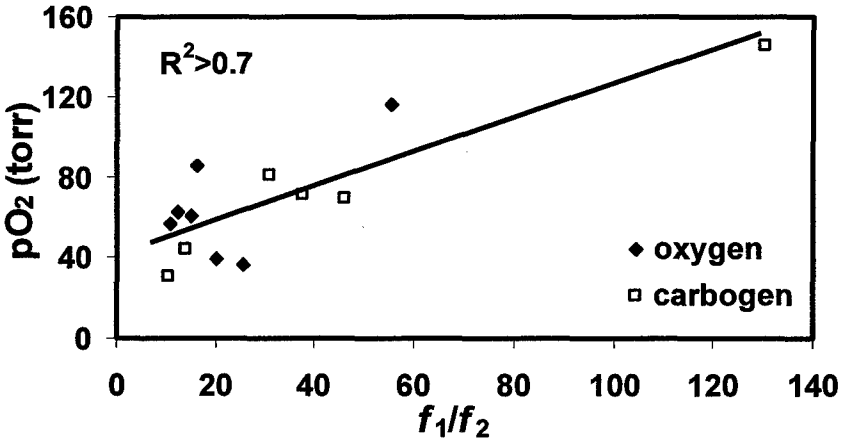

Figure 7B

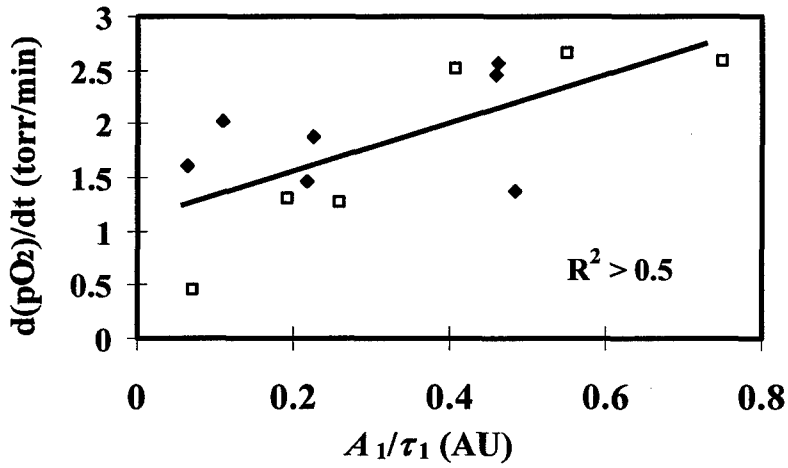

Figure 8A

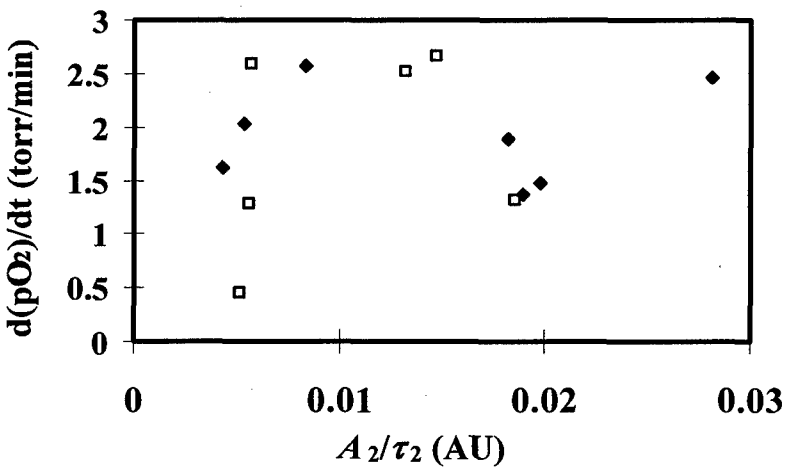

Figure 8B

Tumour			Baseline (air)			Oxygen challenge			Carbogen challenge		
No	Volume (cm^3)	*Voxels	pO_2 (Torr) Mean ± SD	HF_5 (%)	HF_{10} (%)	pO_2 (Torr) Mean ± SD	HF_5 (%)	HF_{10} (%)	pO_2 (Torr) Mean ± SD	HF_5 (%)	HF_{10} (%)
1	1.6	26	12 ± 3	24 ± 14	49 ± 15	56 ± 10	22 ± 2	29 ± 8	66 ± 3	0	0
2	0.3	10	12 ± 2	6 ± 12	53 ± 15	62 ± 15	0	0	79 ± 6	0	0
3	0.5	5	4 ± 4	60 ± 20	80 ± 0	14 ± 1	33 ± 12	53 ± 12	3 ± 1	73 ± 12	73 ± 12
4	1.3	14	< 1 torr$^+$	100 ± 0	100 ± 0	14 ± 7	19 ± 11	48 ± 30	61 ± 21	0	0
5	0.9	24	24 ± 4	0 ± 0	8 ± 4	47 ± 10	0	0	71 ± 11	0	0
6	1.2	8	4 ± 1	58 ± 7	63 ± 0	43 ± 12	50 ± 22	63 ± 0	73 ± 10	0	0
7	0.8	24	27 ± 2	0 ± 0	3 ± 2	122 ± 21	0	0	142 ± 26	0	0
8	0.6	8	9 ± 6	50 ± 22	63 ± 22	103 ± 26	0	0	118 ± 37	0	0
9	0.7	44	25 ± 1	10 ± 5	26 ± 3	----	--	--	35 ± 3	0	3 ± 3
10	0.7	8	7 ± 6	54 ± 19	75 ± 22	52 ± 18	0	0	----	--	--
Mean ± SD	0.9 ± 0.4	17 ± 12	12 ± 10	36 ± 33	52 ± 31	57 ± 36	14 ± 18	21 ± 27	72 ± 41	8 ± 24	8 ± 24

Table 1: Oxygen Tension (pO_2) in ten rat mammary 13762NF adenocarcinomas. pO_2 in baseline is the average value of all voxels in the first three maps, while pO_2 for oxygen or carbogen is the average value of all voxels in the final three pO_2 map with exposure to the hyperoxic gas intervention. Hypoxic fraction HF is the percentage of pixels with pO_2 values less than 5 torr (HF_5) or 10 torr (HF_{10}) and HF_5 and HF_{10} are the average value of final three maps in baseline, oxygen or carbogen respectively. * Number of voxels that provide acceptable data for all 23 pO_2 maps. $^+$ $p<0.01$. The mean pO_2 increased significantly with both oxygen and carbogen ($p<0.005$) and the value was significantly higher with carbogen ($p<0.008$). HF_5 was significantly reduced with oxygen or carbogen ($p<0.05$).

Supplmentray material

Tumour		Double exponential fitting				
No.	intervention	A_1 (AU)	A_2 (AU)	τ_1 (min)	τ_2 (min)	R
[a]1	oxygen	0.11 ± 0.002	0.12 ± 0.002	0.49 ± 0.02	6.6 ± 0.2	0.94
	carbogen	0.15 ± 0.001	0.13 ± 0.002	0.58 ± 0.01	23.2 ± 1.1	0.94
[a]2	oxygen	0.03 ± 0.002	0.11 ± 0.005	0.46 ± 0.18	25.6 ± 2.9	0.91
	carbogen	----	----	----	----	----
[a]3	oxygen	0.15 ± 0.001	0.38 ± 0.003	0.31 ± 0.02	20.1 ± 0.39	0.98
	carbogen	0.23 ± 0.005	0.2 ± 0.004	1.2 ± 0.04	10.8 ± 0.45	0.95
[a]4	oxygen	----	----	----	----	----
	carbogen	0.16 ± 0.002	2.3 ± 0.27	0.29 ± 0.02	155.8 ± 21	0.97
[a]5	oxygen	0.12 ± 0.002	0.23 ± 0.002	0.55 ± 0.03	11.6 ± 0.27	0.94
	carbogen	----	----	----	----	----
[a]6	oxygen	0.06 ± 0.001	0.26 ± 0.005	0.13 ± 0.01	31.2 ± 1.1	0.96
	carbogen	0.03 ± 0.001	0.08 ± 0.001	0.04 ± 0.02	13.9 ± 0.6	0.78
[a]7	oxygen	----	----	----	----	----
	carbogen	----	----	----	----	----
[b]8	oxygen	0.11 ± 0.002	0.2 ± 0.001	0.24 ± 0.02	7.1 ± 0.1	0.96
	carbogen	0.2 ± 0.002	0.12 ± 0.001	0.49 ± 0.01	9.1 ± 0.2	0.95
[c]9	carbogen	0.01 ± 0.0004	0.02 ± 0.0004	0.14 ± 0.02	3.9 ± 0.12	0.64
[d]10	oxygen	0.05 ± 0.002	0.03 ± 0.002	0.46 ± 0.05	5.6 ± 0.56	0.68
Mean ± SD	----	0.11 ± 0.068	0.32 ± 0.59	0.42 ± 0.3	24.9 ± 40.2	----

Table 2: Summary of vascular oxygen dynamics for the experimental tumours. Two amplitudes (A_1, A_2) and two time constants (τ_1, τ_2) are determined by curve-fitting the dynamic NIRS measurements using a double-exponential expression. 9 out of 10 tumours were observed to have double-exponential features with either oxygen or carbogen intervention. A_1 is significantly smaller than A_2 with oxygen ($p<0.01$), but no significant differences in carbogen ($p>0.19$).
τ_1 is significantly smaller than τ_2 in oxygen ($p<0.006$),
whereas no significant differences in carbogen ($p>0.1$).

[a]: air→O_2 →air →carbogen→air;
[b]: air → carbogen → air → O_2 → air;
[c]: air → carbogen → air;
[d]: air → oxygen → air

Investigation of breast tumor oxygen consumption by near infrared spectroscopy

Yulin Song[+ϕ], Jae G. Kim[+], Ralph P. Mason[ϕ], and Hanli Liu[+#]

[+]Joint Graduate Program in Biomedical Engineering
University of Texas at Arlington/University of Texas Southwestern Medical Center at Dallas
Arlington, TX 76019

[ϕ]Advanced Radiological Sciences, Department of Radiology
University of Texas Southwestern Medical Center at Dallas
Dallas, TX 75390

The corresponding author's information: hanli@uta.edu; phone 1 817 272-2054; fax 1 817 272-2251; Joint Program of Biomedical Engineering, P.O. Box 19138, University of Texas at Arlington, Arlington, TX, USA 76019-0167

ABSTRACT

This study develops a mathematical model for calculating tumor oxygen consumption rate and investigates the correlation between the tumor oxygen consumption rate and tumor volume. After developing the model, we used near-infrared spectroscopy (NIRS) to measure changes of oxygenated hemoglobin concentration ($\Delta[HbO_2]$) before and after potassium chloride (KCl) induced cardiac arrest. The measurements were taken from five female adult Fisher 344 rats bearing mammary adenocarcinomas 13762NF, while the anesthetized rats breathed air. After 5-10 minutes of baseline measurement of NIRS, overdose of KCl was administered through i.v. tail injection. The NIRS results from tumor measurements showed significant drop in tumor vascular oxygenation right after KCl induced cardiac arrest. The tumor oxygen consumption rate was calculated by fitting the developed model with the measured $\Delta[HbO_2]$ data, and a relationship between tumor oxygen consumption rate and tumor volume was analyzed using linear regression. It was also found that there was a strong negative linear relationship between the mean tumor oxygen consumption rate and tumor volume, indicating that the larger a tumor, the smaller the mean oxygen consumption rate. This study demonstrates that the NIRS can provide an efficient, real-time, non-invasive approach to quantify tumor oxygen consumption rate.

Key Words: Breast tumor, Tumor oxygen consumption rate, NIR Spectroscopy, Tumor Vascular Oxygenation

1. Introduction

For the past decade, substantial efforts have been made in developing techniques for measuring skeletal muscle oxygen consumption ($\dot{V}O_2$) during rest and exercise with and without vascular occlusion, and various mathematical models for computing $\dot{V}O_2$ have been proposed.[1,2,3,4] However, little has been done in determining tumor oxygen consumption in either human subjects or animal models. So far, only limited information is available about tumor oxygen consumption and its relationship to tumor kinetic parameters and tumor volume. Some studies indicated that oxygen consumption rates of breast tumors *in vivo* are intermediate between normal tissues with low metabolic rates and normal tissues with quite high activities.[5] Steen *et al.* [6] found out that the oxygen consumption rate of brain was higher than that of 9L gliosarcoma, by comparing pre-sacrifice and post-sacrifice sO_2 (hemoglobin oxygen saturation) values of rat brain and 9L tumors. No further details were provided on how the tumor oxygen consumption rate could be computed, and whether it was related to other tumor kinetic parameters and tumor volume.

To answer these important questions, we developed a simple mathematical model based on Fick's Law of diffusion to describe hemokinetics of tumor vascular oxygenated hemoglobin concentration, $[HbO_2]$, following potassium chloride (KCl) induced cardiac arrest (total global ischemia). This allowed for the description of changes in tumor oxyhemoglobin concentration, $\Delta[HbO_2]$, as a function of time. The values of $\Delta[HbO_2]$ were measured using near infrared spectroscopy (NIRS), in common with our previous work[7,8]. The mathematical model was developed in such a way that the measured $\Delta[HbO_2]$ is directly associated with the tumor oxygen consumption rate, which can be further correlated with the tumor volume. In this paper, we are going to report 1) the development of mathematical model for computing tumor oxygen

consumption rate and 2) the investigation of relationship between tumor oxygen consumption rate and tumor volume.

2. Materials and Methods

2.1 Calculations of Tumor $[HbO_2]$ and $[Hb]_{total}$

The principle of tissue NIRS is that concentrations of oxygenated hemoglobin and deoxygenate hemoglobin, $[HbO_2]$ and [Hb], respectively, are the only significant absorbing materials in tissue within the NIR range (700-900 nm). When the measured sample, such as tumor, has a mixture of oxygenated and deoxygenated hemoglobin, the modified Beer-Lambert law can be further written as[9,10,11],

$$OD^{\lambda} = \{\varepsilon_{Hb}^{\lambda}[Hb] + \varepsilon_{HbO2}^{\lambda}[HbO_2]\}\, l, \tag{1}$$

where OD^{λ} is the optical density or absorbance at wavelength λ, $\varepsilon_{Hb}^{\lambda}$ and $\varepsilon_{HbO2}^{\lambda}$ are the extinction coefficients at wavelength λ for molar concentrations of [Hb] and $[HbO_2]$, respectively, and l the optical path length. By employing two wavelengths at λ_1 and λ_2, both of $[HbO_2]$ and [Hb] can be determined by measuring the light absorbance at the two specific wavelengths, provided that the values for $\varepsilon_{Hb}^{\lambda}$ and $\varepsilon_{HbO2}^{\lambda}$ are known, as expressed below:

$$[HbO_2] = \frac{\varepsilon_{Hb}^{\lambda 2} OD^{\lambda 1} - \varepsilon_{Hb}^{\lambda 1} OD^{\lambda 2}}{l\left(\varepsilon_{Hb}^{\lambda 2}\varepsilon_{HbO2}^{\lambda 1} - \varepsilon_{Hb}^{\lambda 1}\varepsilon_{HbO2}^{\lambda 2}\right)}, \tag{2}$$

$$[Hb] = \frac{\varepsilon_{HbO2}^{\lambda 2} OD^{\lambda 1} - \varepsilon_{HbO2}^{\lambda 1} OD^{\lambda 2}}{l\left(\varepsilon_{Hb}^{\lambda 1}\varepsilon_{HbO2}^{\lambda 2} - \varepsilon_{Hb}^{\lambda 2}\varepsilon_{HbO2}^{\lambda 1}\right)}. \tag{3}$$

It follows that changes in [Hb] and $[HbO_2]$ can be consequently given as:

$$\Delta[HbO_2] = \frac{\varepsilon_{Hb}^{\lambda 2} \Delta OD^{\lambda 1} - \varepsilon_{Hb}^{\lambda 1} \Delta OD^{\lambda 2}}{l\left(\varepsilon_{Hb}^{\lambda 2}\varepsilon_{HbO2}^{\lambda 1} - \varepsilon_{Hb}^{\lambda 1}\varepsilon_{HbO2}^{\lambda 2}\right)}, \tag{4}$$

$$\Delta[Hb] = \frac{\varepsilon_{HbO2}{}^{\lambda 2}\Delta OD^{\lambda 1} - \varepsilon_{HbO2}{}^{\lambda 1}\Delta OD^{\lambda 2}}{l\left(\varepsilon_{Hb}{}^{\lambda 1}\varepsilon_{HbO2}{}^{\lambda 2} - \varepsilon_{Hb}{}^{\lambda 2}\varepsilon_{HbO2}{}^{\lambda 1}\right)}, \quad (5)$$

where ΔOD^{λ} represents a change in optical density at the specific wavelength, λ, and equals to $=\log(A_B/A_T)$. A_B and A_T correspond to light intensities measured under the baseline and transient conditions.

Equations (4) and (5) seem straight forward mathematically and have been used for several decades by biochemists to quantify $\Delta[Hb]$ and $\Delta[HbO_2]$ in laboratory spectrophotometric measurements. However, close attention needs to be paid to the values of ε for in vivo hemoglobin determination since ε values were often expressed on a heme basis, whereas a hemoglobin molecule/complex has four hemes. Therefore, there exists a factor of 4 between the commonly published ε values and the ε values to be used in equations (4) and (5) for in vivo measurements[12,13]. Furthermore, the optical pathlength, l, should be proportional to the source and detection separation, d, with a differential pathlength factor (DPF)[14,15], i.e., $l=d*DFF$. We previously utilized the ε values given by W. G. Zijlstra[16], which were expressed on a heme basis, and assumed that the DPF values were approximately constant at the two selected NIR wavelengths. Consequently, we have obtained, from eqs. (4) and (5), the following specific equations for λ_1=758 nm and λ_2=785 nm, after system calibration using liquid phantoms[8]:

$$\Delta[HbO_2] = \frac{-10.63\cdot\log(\frac{A_B}{A_T})^{758} + 14.97\cdot\log(\frac{A_B}{A_T})^{785}}{d}, \quad (6)$$

$$\Delta[Hb] = \frac{8.95\cdot\log(\frac{A_B}{A_T})^{758} - 6.73\cdot\log(\frac{A_B}{A_T})^{785}}{d}, \quad (7)$$

$$\Delta[Hb]_{total} = \Delta[Hb] + \Delta[HbO_2]$$

$$= \frac{-1.68 \cdot \log(\frac{A_B}{A_T})^{758} + 8.24 \cdot \log(\frac{A_B}{A_T})^{785}}{d}, \qquad (8)$$

Notice that for simplicity, the factor of 4 to account for the 4 hemes of ε and the DPF values are not included in the equations since little has been reported for tumor DPF. Our focus for this study is on relative changes of $\Delta[HbO_2]$ between the baseline conditions and after the KCI injection. Both of these factors are nearly constants and do not affect dynamic features of tumor $\Delta[HbO_2]$ calculations. Because of the existence of such constant factors, we used arbitrary units in this study for the units of $\Delta[Hb]$ and $\Delta[HbO_2]$. The error estimation due to the assumption of constant DPF has been given in Ref. 7.

2.2 One-Channel NIRS System

A dual-wavelength (at 758 nm and 785 nm), one-channel NIR system (NIM, Inc., Philadelphia, PA) was utilized for the animal experiment, as shown in Figure 1. A radio-frequency (rf) source was used to modulate the light intensities of two laser diodes at 140 MHz through a time-sharing system. After the light passed through a bifurcated fiber optic probe, it was transmitted through the tumor tissue and then collected by a second fiber bundle. The light was then demodulated by an In-phase and Quadrature-phase chip (I&Q chip), amplified by a photo multiplier tube (PMT), and filtered by a lowpass (LP) filter for passing only the DC components. The signals were digitized by an analog-to-digital converter (ADC) and stored in a laptop computer. The measured DC signals at the I and Q branches at the measured wavelengths, $I_{DC}(\lambda)$ and $Q_{DC}(\lambda)$, lead to the quantification of optical amplitudes, $A(\lambda)$, and phase, $\theta(\lambda)$, that passed through the tumor tissues[17]:

$$A(\lambda) = \sqrt{I(\lambda)_{DC}^2 + Q(\lambda)_{DC}^2}, \qquad (9)$$

$$\theta(\lambda) = \arctan(\frac{Q(\lambda)_{DC}^2}{I(\lambda)_{DC}^2}), \quad (10)$$

where λ represents the respective wavelengths utilized in the NIR system. Then, changes in light intensity through the tumor caused by a particular intervention were used to compute changes in tumor vascular [HbO_2] and [Hb], as described previously in Section 2.1. In this study, the measured values of θ(λ) were not particularly used for data analysis because of unclearness of direct association between θ(λ) and physiological parameters.

2.3 Animal Tumor Model and its Response to KCl Injection

Murine mammary adenocarcinomas 13762NF were implanted in skin pedicles on the forebacks of adult female Fischer 344 rats (~ 250 g, n=5), as described in details previously.[18] To identify them, each tumor was assigned a unique code and was housed separately during the course of study. The tumor model had distinct therapeutic sensitivity and metastatic characteristics. Once the tumors reached ~1 cm diameter (~ 0.5 cm^3), corresponding to a typical lower limit of tumor detected in patients, experiments were initiated. We chose to use relatively large tumors in order to ensure that the NIRS interrogated only the tumor tissue rather than the surrounding normal skin tissue. The rats were anesthetized with 200 μl ketamine hydrochloride i.p. (100 mg/ml; Aveco, Fort Dodge, IA) and were maintained under general gaseous anesthesia using a small animal anesthesia unit with air (1.0 l/min) and 1.0% isoflurane (Ohmeda PPD Inc., Fort Dodge, IA). Prior to experiments, tumor hair was cut with a pair of surgical scissors to improve the NIR light transmission. Tumor's three orthogonal diameters were measured with a caliper for estimating tumor volume. The rats were placed on their sides in an animal bed and stabilized using tape to reduce motion artifacts caused by rats' breathing movements. The body temperature was maintained at about 37 °C by a warm water blanket connected a water pump (K-

MOD 100, Baxter Healthcare Co., Deerfield, IL). A fiber optic pulse oximeter (Nonin Medical, Inc., Plymouth, MN) was placed on the hind foot to monitor arterial hemoglobin saturation (s_aO_2) and heart rate (HR), and a thermocouple (Cole-Parmer Instrument Co., Vernon Hills, IL) was inserted rectally to monitor core temperature. (Figure 1).

Following a baseline $\Delta[HbO_2]$ measurement (5 ~ 10 min), while the rats were breathing air, the rats were given an overdose of KCl (1 g/kg (Sigma) in saline) by i.v. tail injection. Care was taken so as not to disturb the position of either the light source or the detector. Changes in tumor vascular $[HbO_2]$ and total hemoglobin concentration ($[Hb]_{total}$) were continuously monitored during and after cardiac arrest for about 40 minutes by NIRS.

2.4 Data Analysis

For each tumor, the raw data were filtered and baseline corrected. The processed data were then fitted to the mathematical model to be described below to determine the kinetic parameters of the dynamic response. Tumor oxygen consumption rate $\dot{V}O_2$ and mean tumor oxygen consumption rate $\overline{\dot{V}}O_2$ were computed over 5 rat tumors, respectively, by fitting the mathematical model with the measured $\Delta[HbO_2]$. Relationships between those parameters and tumor volume were analyzed using linear regression.

3. Development of a Mathematical Model for Tumor Oxygen Consumption Rate

3.1 Dynamic Changes of Tumor $[HbO_2]$ caused by KCl Injection

In our previous report[7], we applied Kety's approach[19] to evaluate tumor hemodynamics by using HbO_2 intervention as a tracer, but we did not consider the effect of tumor oxygen consumption. In this study, we included tumor oxygen consumption rate in our hemodynamic

model. In principle, the change rate of HbO_2 in tumor vasculature should be equal to the rate at which the HbO_2 concentration is transported by arterial circulation minus the rate at which it is carried away into the venous drainage minus the rate at which tumor cells consume oxygen. In common with our previous approach[7], we assumed here a one-compartment model: tumor vasculature is well mixed with respect to oxygen so that a mass balance equation for HbO_2 can be written by the following chart. Specifically, if $[HbO_2]$ is the oxyhemoglobin concentration in the tumor at a given time t, the general conservation of mass equation for $[HbO_2]$ can be schematically depicted as follows:

Rate of decrease of oxyhemoglobin concentration in tumor vasculature	=	Inflow of oxyhemoglobin from artery	-	Outflow of oxyhemoglobin to vein	-	Consumption rate of oxyhemoglobin by tumor cells

By using Fick's Law of diffusion, the above schematic diagram can be written mathematically as

$$\frac{d[\mathrm{HbO_2}]}{dt} = f \cdot [\mathrm{HbO_2}]_A - f \cdot [\mathrm{HbO_2}]_V - \lambda \cdot [\mathrm{HbO_2}], \qquad (11)$$

where $[HbO_2] = [HbO_2](t)$ (in an arbitrary unit) is a solution to this differential equation and is a function of only time because of the one-compartment model, f is the blood perfusion rate ($ml/min/cm^3_{tissue}$), and $[HbO_2]_A$ and $[HbO_2]_V$ are oxyhemoglobin concentrations in the arterial blood and the venous blood in tumor, respectively, and λ is defined as the oxyhemoglobin dissociation constant (min^{-1}).

In Equation (11), we assumed that the oxyhemoglobin dissociation rate is equal to the tumor oxygen consumption rate at the steady state. This assumption is based on the following facts: deoxyhemoglobin and oxygen molecules normally combine to form oxyhemoglobin through a loading reaction that occurs in the lungs. Oxyhemoglobin, in turn, can be dissociated to

be deoxyhemoglobin and free oxygen molecules through an unloading process that occurs in the tissue capillaries. These two processes can be expressed as the following reversible reaction:

$$\mathrm{Hb} + \mathrm{O_2} \underset{\text{in tissue capillaries}}{\overset{\text{in lungs}}{\rightleftharpoons}} \mathrm{HbO_2}.$$

Which direction the reaction will go depends largely on two factors: 1) the pO_2 of the environment and 2) the affinity of hemoglobin for oxygen. A high value of pO_2 drives the equation to the right side of the reaction to promote oxygen loading, whereas a low pO_2 in the tissue capillaries drives the reaction to the left to promote oxygen unloading. The affinity of hemoglobin for oxygen does not change appreciably over a short period of time (minutes). Since, in our case, the rat died rapidly by KCl induced cardiac arrest, the reaction went to the left direction to unload oxygen to the plasma because of lack of oxygen supply from coming blood. The dissolved oxygen in the plasma, then, was diffused across the tumor capillary walls to the surrounding tumor tissues, where it was consumed by cellular aerobic respiration.

Let us assume that the rat died instantaneously by KCl induced cardiac arrest; thus, from this point on, the blood flow stopped, the lungs were no longer functioning, and the gas exchange between the alveolar air and the blood in pulmonary capillaries ceased. As a result, no more oxyhemoglobin molecules were transported either to or from the tumor vasculature by systemic circulation. Mathematically, this means that the tumor blood perfusion rate f is 0 after KCl administration. Equation (11), therefore, is simplified as

$$\frac{d[\mathrm{HbO_2}]}{dt} = -\lambda \cdot [\mathrm{HbO_2}], \qquad (12)$$

To find the particular solution to Equation (12), we need to know its initial condition. In this case, the initial condition is given by

$$[\mathrm{HbO_2}]\big|_{t=0} = [\mathrm{HbO_2}]_0, \tag{13}$$

where $[\mathrm{HbO_2}]_0$ is the initial baseline value (pre-KCl administration) of oxyhemoglobin concentration. Rearranging and integrating Equation (12) gives rise to an exponential solution

$$\int \frac{d[\mathrm{HbO_2}]}{[\mathrm{HbO_2}]} = -\int \lambda dt \quad \Rightarrow \quad [\mathrm{HbO_2}](t) = C \cdot e^{-\lambda t}, \tag{14}$$

where C is the constant of integration. By applying the initial condition, eq. (13), to eq. (14), we obtain the particular solution as follows:

$$[\mathrm{HbO_2}](t) = [\mathrm{HbO_2}]_0 \cdot e^{-\lambda t} \ . \tag{15}$$

Equation (15) indicates that following KCl induced cardiac arrest, tumor vascular oxyhemoglobin concentration $[\mathrm{HbO_2}]$ decreases exponentially with time, and this process is characterized by the dissociation constant λ and the initial oxyhemoglobin concentration $[\mathrm{HbO_2}]_0$, both of which can be determined by fitting eq. (15) to the experimental data.

Furthermore, it is useful to introduce the mean lifetime τ, defined as the average time that an oxyhemoglobin molecule is likely to survive before it is dissociated with oxygen. The number of oxyhemoglobin molecules that survive to time t is just $[\mathrm{HbO_2}](t)$, and the number of oxyhemoglobin molecules that dissociate between t and $t + dt$ is $|d[\mathrm{HbO_2}]/dt| \cdot dt$. Thus, the theoretical mean lifetime τ is given by

$$\tau = \frac{\int_0^\infty t \cdot |d[\mathrm{HbO_2}]/dt| \cdot dt}{\int_0^\infty |d[\mathrm{HbO_2}]/dt| \cdot dt}, \tag{16}$$

where $\int_0^\infty \left| d[\mathrm{HbO_2}]/dt \right| \cdot dt$ gives the total number of oxyhemoglobin molecules that are dissociated after KCl administration, and $\int_0^\infty \left| d[\mathrm{HbO_2}]/dt \right| \cdot dt$ is equal to $[\mathrm{HbO_2}]_0$. Evaluating Equation (16) gives

$$\tau = \frac{\int_0^\infty t \cdot [\mathrm{HbO_2}]_0 \cdot (-\lambda) \cdot e^{-\lambda t} \cdot dt}{\int_0^\infty [\mathrm{HbO_2}]_0 \cdot (-\lambda) \cdot e^{-\lambda t} \cdot dt} = \frac{\frac{1}{\lambda}\int_0^\infty (\lambda t) \cdot e^{-\lambda t} \cdot d(\lambda t)}{\int_0^\infty e^{-\lambda t} \cdot d(\lambda t)} = \frac{1}{\lambda}. \tag{17}$$

Equation (17) indicates that the mean lifetime τ is simply the inverse of the dissociation constant λ and is just the time constant of Equation (15), which, therefore, can be rewritten as

$$[\mathrm{HbO_2}](t) = [\mathrm{HbO_2}]_0 \cdot e^{-t/\tau}. \tag{18}$$

Since we only measure relative changes of $[\mathrm{HbO_2}]$ value, we can express $\Delta[\mathrm{HbO_2}]$ as:

$$\Delta[\mathrm{HbO_2}] = [\mathrm{HbO_2}] - [\mathrm{HbO_2}]_0 = -[\mathrm{HbO_2}]_0 (1-e^{-t/\tau}). \tag{19}$$

In this way, both quantities of $[\mathrm{HbO_2}]_0$ and τ can be obtained by fitting eq. (19) with the experimental data taken from the changes in $[\mathrm{HbO_2}]$ caused by KCl-induced cardiac arrest. As seen from this equation, when the measuring time is long, i.e., $t \rightarrow \infty$, the stabilized $\Delta[\mathrm{HbO_2}]$ reaches the value of $\Delta[\mathrm{HbO_2}]_0$.

3.2 Tumor Oxygen Consumption Rate $\dot{V}\mathrm{O_2}$

It is perhaps more important and significant to compute tumor oxygen consumption rate $\dot{V}\mathrm{O_2}$ from $\Delta[\mathrm{HbO_2}]$, because it reflects tumor oxygen consumption and metabolic activities. Tumor oxygen consumption rate $\dot{V}\mathrm{O_2}$ is determined by taking the first order derivative of equation (15) with respect to time t,

$$\dot{V}O_2(t) = \frac{d}{dt}\left| [HbO_2]_0 \cdot e^{-t/\tau} \right| = \frac{[HbO_2]_0}{\tau} \cdot e^{-t/\tau} = \frac{[HbO_2](t)}{\tau}, \tag{20}$$

which reflects the number of oxyhemoglobin molecules that are dissociated per unit time at a particular time t. This equation shows that the tumor oxygen consumption is proportional to the concentration of $[HbO_2]$ in our experimental case. In particular, this equation permits direct quantification of the regular tumor oxygen consumption rate, $\dot{V}O_2$ (t=0), as being $[HbO_2]_0/\tau$, which can be obtained by fitting eq. (19) to our experimental data. Furthermore, taking logarithm of eq. (20) leads to

$$ln\,(\dot{V}O_2) = -t/\tau + ln[\dot{V}O_2\,(t=0)]. \tag{21}$$

This equation demonstrates a linear relationship between the logarithm of tumor oxygen consumption rate and time after KCL injection with a slope being the inverse of time constant of $\Delta[HbO_2]$ decay after the cardiac arrest.

To facilitate the comparison of the tumor oxygen consumption rates as a function of tumor volume, we also computed a mean tumor oxygen consumption rate as follows:

$$\bar{\dot{V}}O_2 = \frac{1}{T}\int_0^T \frac{[HbO_2]_0}{\tau} \cdot e^{-t/\tau} dt \tag{22}$$

where T is the time that it takes for oxyhemoglobin concentration to drop to a steady or asymptotic minimum value. In order to evaluate the integral, we made an approximation: $T = 3\tau$ because tumor oxyhemoglobin concentration dropped to 5% of its initial value within 3τ time and the error introduced by this approximation was minimal. Evaluating eq. (22) with $T = 3\tau$ gives

$$\bar{\dot{V}}O_2 = \frac{1}{3\tau}\int_0^{3\tau} \frac{[HbO_2]_0}{\tau} \cdot e^{-t/\tau} dt \approx \frac{1}{3}\left(\frac{[HbO_2]_0}{\tau}\right). \tag{23}$$

Both eqs. (20) and (23) indicate that the quantity ($[HbO_2]_0/\tau$) has an important physiological significance, representing the transient and mean tumor oxygen consumption rate and reflects the metabolic activity of the tumor.

4. Experimental Results

Figure 2 shows the KCl effects on tumor vascular $\Delta[HbO_2]$ and $\Delta[Hb]_{total}$ for a representative mammary adenocarcinoma 13762NF (12.7 cm^3). The error bars indicate measurement uncertainties and are labeled at selected locations. (Some of them are too small to be seen.) The exponential appearance of the curves matches the solution of the mathematical model, eq. (19). As shown in the figure, $\Delta[HbO_2]$ dropped sharply and significantly by 0.8723 ± 0.0002 ($p < 0.0001$). This suggests that, first of all, the NIR system was highly sensitive to changes in tumor vascular oxygenation and was capable of providing high temporal resolution measurement. Secondly, the tumor had a relatively high oxygen consumption rate since the value of 0.8723 reflects the initial, steady-state value of tumor $[HbO_2]_0$ without KCl administration. In contrast, total hemoglobin concentration, $[Hb]_{total}$, decreased by 0.0870 ± 0.0001, only 10% of the change in $[HbO_2]$. This clearly indicates that total tumor blood volume remained relatively constant, as compared to $[HbO_2]$ during the course of the experiment. This also shows that the assumption of blood flow $f = 0$ after KCl injection was reasonable. By fitting Equation (19) to the data, $[HbO_2]_0$ and τ were found to be 0.880 ± 0.005 and 0.691 ± 0.004 (min), respectively. A careful comparison revealed that the overall shape of the $\Delta[HbO_2]$ curve was similar to those obtained by Steen *et al.*, who used subcutaneously implanted rat 9L gliosarcoma and pentobarbital overdose.[6] In addition, the τ value determined here was of the same order as reported by Steen *et al.*

Figure 3 shows the time course profiles of tumor vascular $\Delta[HbO_2]$ and $\Delta[Hb]_{total}$ for an another mammary adenocarcinoma 13762NF (15.7 cm^3). Once again, the NIR system exhibited a high sensitivity in detecting changes in $[HbO_2]$ and $[Hb]_{total}$. In this case, $\Delta[HbO_2]$ dropped even more significantly, by 1.444 ± 0.005 ($p < 0.0001$), while $\Delta[Hb]_{total}$ dropped 0.488 ± 0.002. As for the first breast tumor, the magnitude of the drop in $\Delta[Hb]_{total}$ was much less than that in $\Delta[HbO_2]$, suggesting that the decrease in $\Delta[HbO_2]$ was mainly caused by tumor oxygen consumption instead of the decrease in total tumor blood volume. The values of $[HbO_2]_0$ and τ were determined as 1.192 ± 0.008 and 1.36 ± 0.02 (min), respectively, using eq. (19).

The relationship between tumor $[HbO_2]_0$ and tumor volume for five mammary adenocarcinomas 13762NF was shown in Figure 4. The straight line is a linear regression fit to all the data, illustrating that $[HbO_2]_0$ increases linearly with an increase in tumor volume. This makes sense, intuitively, because it simply manifests the fact that the larger the tumor, the more oxygenated hemoglobin is included in the tumor volume.

Figure 5 shows the relationship between the mean lifetime or the time constant τ and tumor volume. Again, a strong linear relationship ($R > 0.91$) was obtained. This indicates that, on average, the time that an oxyhemoglobin molecule is likely to survive before it is dissociated to yield a deoxyhemoglobin molecule and four free oxygen molecules increases with increasing tumor volume. This linear relationship suggests that tumor blood perfusion is becoming increasingly poor as the tumor increases in size and, thus, tumor tissue is becoming increasingly hypoxic with increasing tumor volume.

Figure 6 shows the relationships between the tumor oxygen consumption rates $\dot{V}O_2$ as a function of time and tumor volume. To better separate the curves, only the data for the first four minutes after KCl injection were plotted. Each curve was obtained by substituting corresponding

$[HbO_2]_0$ and τ values to eq. (20). The same relationships were replotted on a semilog graph, giving straight lines of slope $1/\tau$ (see eq. (21)), as shown in Figure 7. From these two figures, it appeared that smaller tumors had greater oxygen consumption rates before and right after KCl injection. It is more significant and important to be able to estimate the tumor oxygen consumption rate when the rats were alive. Considering that the rats were alive at t = 0, $\dot{V}O_2$(alive) was determined by setting t = 0 in eq. (20). Thus, $\dot{V}O_2(\text{alive}) = \dot{V}O_2(t = 0) = [HbO_2]_0/\tau$. Figure 8 shows a strong (R = 0.86) inverse linear relationship between $\dot{V}O_2$ (0) and tumor volume, indicating clearly that the larger the tumor, the smaller its oxygen consumption rate when the rat was alive before KCl injection. Furthermore, Figure 9 shows the relationship between the mean tumor oxygen consumption rate $\overline{\dot{V}O_2}$ and tumor volume after KCl injection. Once again, a significant correlation was found (R = 0.86), suggesting that, on average, the tumor oxygen consumption rate decreases with an increase in tumor volume.

5. Discussion and Conclusion

In this study, we developed a mathematical model for computing oxygen consumption rate in the rat breast tumors and investigated the oxygen dynamics of breast tumors during the course of KCl cardiac arrest using NIRS. The NIR signal has been found to be very sensitive to changes in tissue oxygenation in small blood vessels such as arterioles, capillary, and venules.[20,21,22,23] These are the places where the oxygen is consumed by tumor/tissue cells. Since the rats died rapidly by KCl-induced cardiac arrest, the tumor metabolism or oxygen consumption was not coupled to the tumor blood flow. Under this condition, Fick's Law was applied to extract and quantify the tumor oxygen consumption from the tumor oxygenation dynamics. Time constant analysis showed that the time constant of oxygenation, τ, was related

to tumor oxygen consumption. It was found from this study that there was a strong positive linear relationship between the time constant τ of oxygenation ($\Delta[HbO_2]$) and tumor volume, suggesting that tumor perfusion or blood flow was becoming increasingly poor with an increase of tumor size. Our observation is consistent with other studies, which have reported that blood perfusion or flow rates of most rodent tumors decrease with increasing tumor size[24,25]. However, a similar relationship has not been found to be true for all human tumors. In this study, we also found that there existed a negative linear relationship between the mean tumor oxygen consumption rate $\overline{\dot{V}}O_2$ and tumor volume, indicating that the lager the tumor, the smaller the mean oxygen consumption rate due to its increase of hypoxia fraction. In other words, mean tumor oxygen consumption rate is decreasing as tumor grows since tumor cells in hypoxic region have very low oxygen consumption rate due to limited oxygen availability.

As shown in eq. (20), tumor oxygen consumption rate $\dot{V}O_2$ is an exponential function of t and is dependent on both the initial tumor oxy-hemoglobin concentration $[HbO_2]_0$ and the time constant τ. This means that tumor oxygen consumption rate $\dot{V}O_2$ decreases exponentially with time after KCl administration. This phenomenon may be explained as follows. As oxygen is being depleted by tumor cellular metabolism, oxygen concentration or oxygen tension pO_2 gradient across tumor capillaries and tissues decreases. Since oxygen diffusion is linearly proportional to its concentration gradient according to Fick's Law of diffusion, a lower oxygen concentration gradient or a lower oxygen tension gradient result in decreased oxygen diffusion and, thus, less oxygen is available for tumor cellular aerobic respiration. This, in turn, results in less oxygen consumption and even tumor cell death.

While the present study demonstrates the possibility of evaluating oxygen consumption rates of tumors by NIRS following KCl administration, the animals have to be scarified to

perform the measurements. It is possible to estimate tumor oxygen consumption rate without sacrificing rats if we are able to quantify the blood in-flow and out-flow of the tumors. This is because the same mathematical models can be utilized to assess oxygen consumption of tumors by introducing a certain respiratory challenge, such as carbogen or pure oxygen inhalation. In addition, we have used a single channel NIRS in this study, which provides us with global and mean values of tumor oxygen consumption rate. However, by using multi-channel NIRS, we will be able to show the intratumoral heterogeneity of oxygen consumption rate caused by different perfusion rates in tumors. One of our current research efforts is to develop multi-channel NIRS imaging systems to study tumor heterogeneities of static and dynamic oxygenation process under various interventions.

In summary, we have reported the NIRS results from rat breast tumor measurements and shown significant drops in tumor vascular oxygenation right after KCl induced cardiac arrest. The tumor oxygen consumption rate was calculated by fitting the developed model with the measured $\Delta[HbO_2]$ data, and a relationship between tumor oxygen consumption rate and tumor volume was analyzed using linear regression. It was also found that there was a strong negative linear relationship between the mean tumor oxygen consumption rate and tumor volume, indicating that a larger tumor has a smaller mean oxygen consumption rate. This study demonstrates that the NIRS can be an efficient, real-time, non-invasive means to quantify tumor oxygen consumption rate.

Acknowledgement:

We acknowledge the support in part by the Department of Defense Breast Cancer Pre-doctoral Research Fellowships BC962357 (YS), Breast Cancer Initiative grant DAMD17-00-1-0459 (HL), NIH R01 CA79515 (RPM) and NIH P20 CA086354 (RPM). We thank Dr. Anca Constantinescu for her technical assistance in handling animal tumors.

Figure Captions

Figure 1. Schematic experimental setup of one channel, near infrared, frequency domain IQ instrument for tumor investigation *in vivo*. Two fiber bundles were used to deliver and detect the laser light, at 758 and 785 nm, which were transmitted through the implanted tumor. The overdose of KCl was administered by i. v. tail injection after 5~10 min of $\Delta[HbO_2]$ baseline measurement.

Figure 2. Effects of overdose KCl injection on tumor vascular $\Delta[HbO_2]$ and $\Delta[Hb]_{total}$ for a representative breast tumor (12.7 cm^3). $\Delta[HbO_2]$ dropped rapidly and significantly ($p < 0.0001$). Both $\Delta[HbO_2]$ and $\Delta[Hb]_{total}$ are in arbitrary unit.

Figure 3. Effects of overdose KCl injection on tumor vascular $\Delta[HbO_2]$ and $\Delta[Hb]_{total}$ for a second breast tumor (15.7 cm^3).

Figure 4. Relationship between tumor $[HbO_2]_0$ and tumor volume for five mammary adenocarcinomas 13762NF.

Figure 5. Relationship between time constant τ and tumor volume for five mammary adenocarcinomas 13762NF.

Figure 6. Relationships between the tumor oxygen consumption rates as a function of time and tumor volume.

Figure 7. Relationships between the tumor oxygen consumption rates as a function of time and tumor volume plotted on a semilog scale.

Figure 8. Relationship between tumor oxygen consumption rate at t=0, $\dot{V}O_2$ (0) and tumor volume.

Figure 9. Relationship between the mean tumor oxygen consumption rate $\overline{\dot{V}}O_2$ and tumor volume after KCl injection.

References:

1. De Blasi, R. A., Cope, M., Elwell, C., Safoue, F., and Ferrari, M, "Noninvasive measurement of human forearm oxygen consumption by near-infrared spectroscopy", *Eur. J. Appl. Physiol.*, **67**:20-25 (1993).

2. De Blasi, R. A., Ferrari, M, Natali, A., Conti, G., Mega, A., and Gasparetto, A., "Noninvasive measurement of forearm blood flow and oxygen consumption by near-infrared spectroscopy", *J. Appl. Physiol.*, **76(3)**,1388-1392 (1994).

3. Homma, S., Eda, H., Ogasawara, S., and Kagaya, A, "Near-infrared estimation of O_2 supply and consumption ", *J. Appl. Physiol.*, **80**, 1279-1284 (1996).

4. Binzoni, T., Quaresima, V., Barattelli, G., Hiltbrand, E., Gürke, L., Terrier, F., Cerretelli, R., and Ferrari, M., "Energy metabolism and interstitial fluid displacement in human gastrocnemius during short ischemic cycles", *J. Appl. Physiol.*, **85**, 1244-1251 (1998).

5. Vaupel, P., "Vascularization, blood flow, oxygenation, tissue *p*H, and bioenergetic status of human breast cancer", *In*: Nemoto and LaManna (eds), *Oxygen Transport to Tissue XVIII*, Plenum Press: New York, 243-253 (1997).

6. Steen, R. G., Kitagishi, K., and Morgan, K., "In vivo measurement of tumor blood oxygenation by near-infrared spectroscopy: immediate effects of pentobarbital overdose or carmustine treatment", *J. Neuro-Oncol.*, **22**, 209-220 (1994).

[7] Liu, H., Song, Y., Worden K. L., Jiang X., Constantinescu, A., and Mason R. P., "Noninvasive investigation of blood oxygenation dynamics of tumors by near-infrared spectroscopy," *Applied Optics*, **39(28)**, 5231-5243 (2000).

[8] Kim, J. G., Zhao, D., Song, Y., Constantinescu, A., Mason, R. P., and Liu, H., "Interplay of tumor vascular oxygenation and tumor pO_2 observed using NIRS, oxygen needle electrode, and ^{19}F MR pO_2 mapping," *J. Biomed. Opt.*, **8(1)**, 53-62 (2003).

[9] Benesch, R., Macduff, G., and Benesch, R. E., "Determination of oxygen equilibria with a versatile new tonometer," *Anal. Biochem.*, **11**, 81-87 (1965).

[10] Benesch, R. E., Benesch, R., and Yung, S., "Equations for the spectrophotometric analysis of hemoglobin mixtures," *Anal. Biochem.*, **55**, 245-248 (1973).

[11] van Assendelft, O. W. and Zijlstra, W. G., "Extinction coefficients for use in equations for the spectrophotometric analysis of haemoglobin mixtures," *Anal. Biochem.*, **69**, 43-48 (1975).

[12] Fishkin, J. B., Coquoz, O., Anderson, E. R., Brenner, M., Tromberg, B. J., "Frequency-domain photon migration measurements of normal and malignant tissue optical properties in a human subject," *Appl. Opt.*, **36**(1), 10- (1997).

[13] "User Manual" for Near-Infrared, Non-Invasive Tissue Oximeter, ISS Inc., 1602 Newton Drive, Champaign IL 61822, USA.

[14] Sevick, E. M., Chance, B., Leigh, J., Nioka, S., and Maris, M., "Quantitation of time- and frequency-resolved optical spectra for the determination of tissue oxygenation," *Anal. Biochem.* **195,** 330–351 (1991).

[15] Delpy, D. T. and Cope, M., "Quantification in tissue near infrared spectroscopy," *Philos. Trans. R. Soc.* London B **952,** 649–659 (1997).

[16] Zijlstra, W. G., Buursma, A., and Meeuwsen-van der Roest, W. P., "Absorption spectra of human fetal and adult oxyhemoglobin, de-oxyhemoglobin, carboxyhemoglobin, and methemoglobin," *Clin. Chem.*, **37**(9), 1633-1638 (1991).

[17] Yang, Y., Liu, H., Li, X., and Chance, B., "A low cost frequency-domain photon migration instrument for tissue spectroscopy, oximetry, and imaging," *Opt. Eng.* **36**(5), 1562-1569 (1997).

18. Hahn, E. W., Peschke, P., Mason, R. P., Babcock, E. E., and Antich, P. P., "Isolated tumor growth in a surgically formed skin pedicle in the rat: a new tumor model for NMR studies", *Magn. Reson. Imaging*, **11,** 1007-1017 (1993).

19. Kety S. S., "Cerebral circulation and its measurement by inert diffusible racers," *Israel J. Med. Sci.* **23,** 3-7 (1987).

20. Chance, B., Dait, M. T., Zhang, C., Hamaoka, T., Hagerman, F., "Recovery from exercise-induced desaturation in the quadriceps muscles of elite competitive rowers", *Am. J. Physiol.*, **262** (*Cell Physiol.* 31), C766-C775 (1992).

21. Mancini, D. M., Bolinger, L, Liu, H., Kendrick, K., Chance, B., and Wilson. J. R., "Validation of near-infrared spectroscopy in humans", *J. Appl. Physiol*, **77,** 2740-2747 (1994).

22. Hampson, N. B., and Piantadosi, C. A., "Near infrared monitoring of human skeletal muscle oxygenation during forearm ischemia", *J. Appl. Physiol*, **64,** 2449-2457 (1988).

23 Liu, H., Hielscher, A. H., Tittel, F. K., Jacques, S. L., and Chance, B., "Influence of blood vessels on the measurement of hemoglobin oxygenation as determined by time-resolved reflectance spectroscopy," *Med.l Phys.* **22,** 1209-1217 (1995).

24. Jain, R. K., and Ward-Hartley, K., "Tumor blood flow: characterization, modification and role in hyperthermia", *IEEE Trans. Sonics Ultrasonics*, **SU-31,** 504-526 (1984).

25. Song, C. W., "Effect of local hyperthermia on blood flow and microenvironment", *Cancer Res.* (Suppl.), **44,** 4721s-4730s (1984).

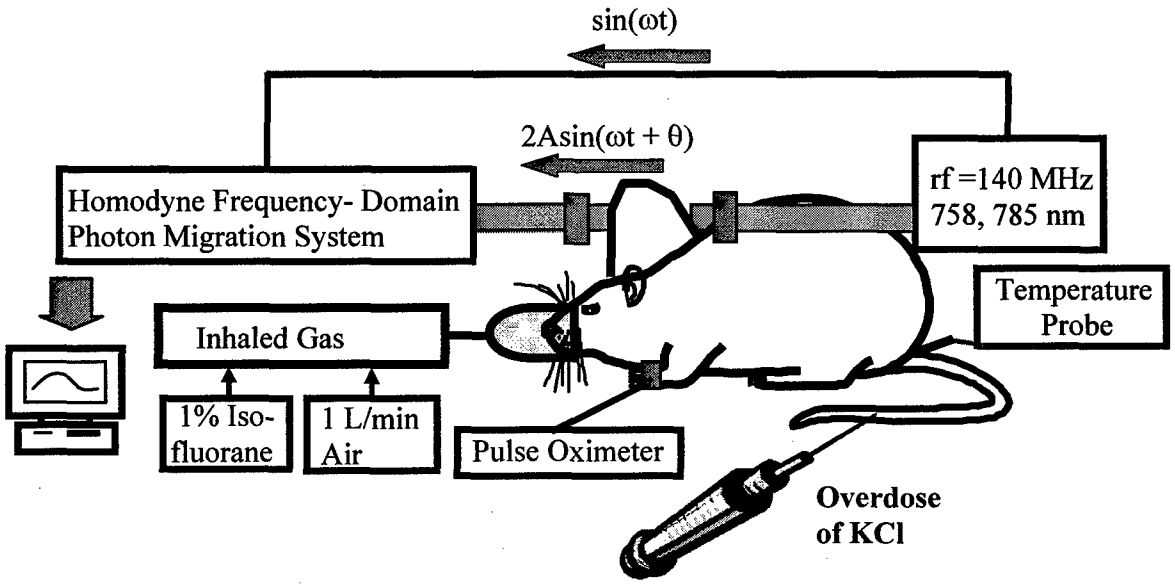
sin(ωt)
2Asin(ωt + θ)
Homodyne Frequency- Domain Photon Migration System
rf =140 MHz
758, 785 nm
Temperature Probe
Inhaled Gas
1% Iso-fluorane
1 L/min Air
Pulse Oximeter
Overdose of KCl

Figure 1

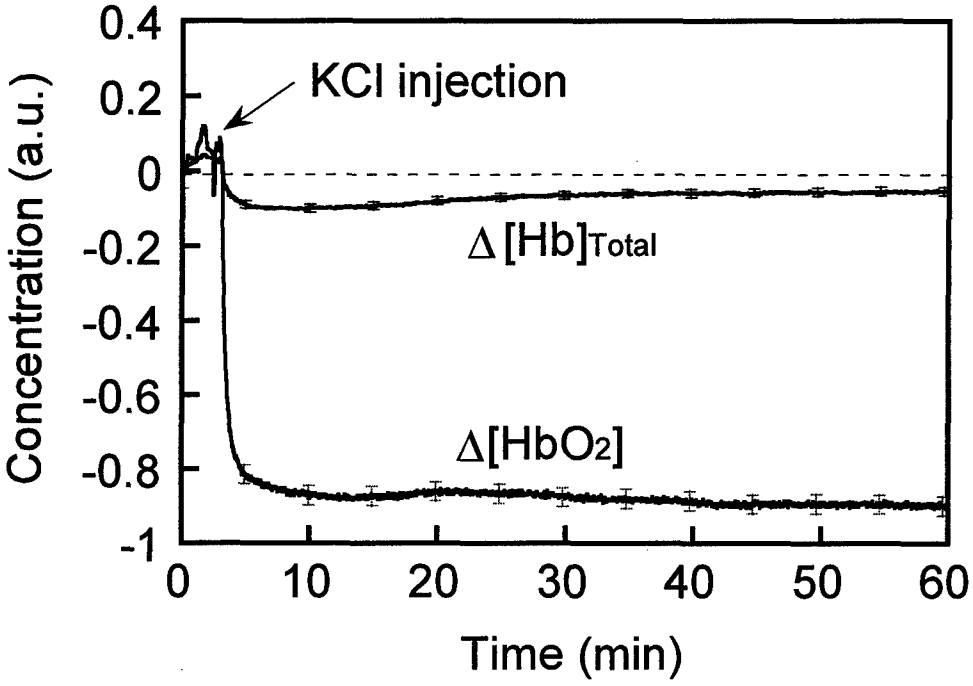
0.4
0.2
0
-0.2
-0.4
-0.6
-0.8
-1
Concentration (a.u.)
KCl injection
Δ [Hb]Total
Δ[HbO2]
0
10
20
30
40
50
60
Time (min)

Figure 2

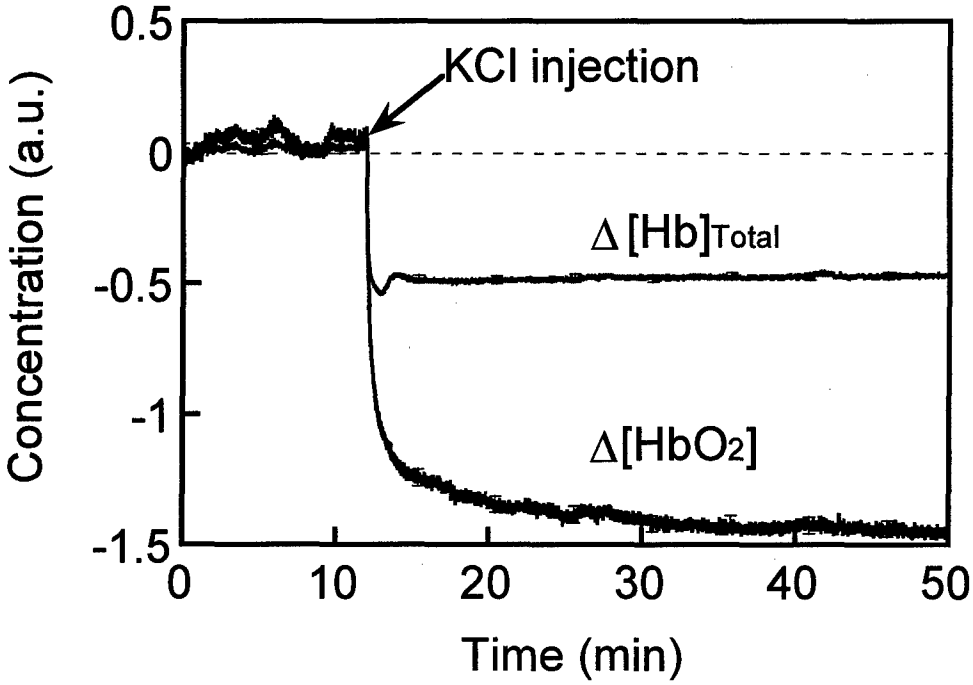
0.5
0
-0.5
-1
-1.5
Concentration (a.u.)
KCl injection
Δ [Hb]Total
Δ[HbO2]
0
10
20
30
40
50
Time (min)

Figure 3

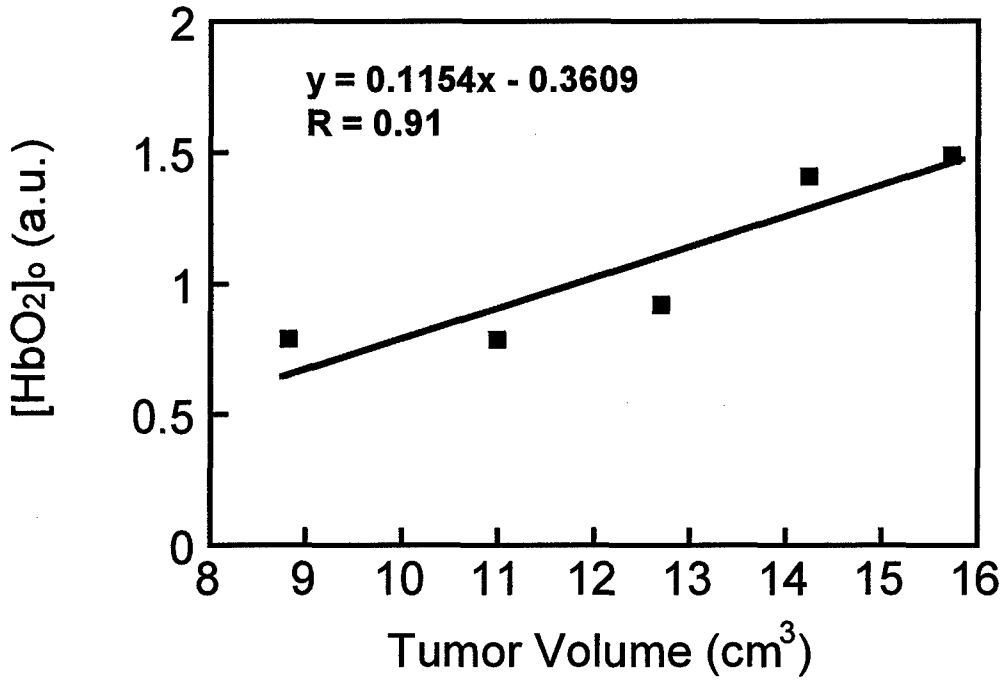
y = 0.1154x - 0.3609
R = 0.91
[HbO2]o (a.u.)
2
1.5
1
0.5
0
8
9
10
11
12
13
14
15
16
Tumor Volume (cm3)

Figure 4

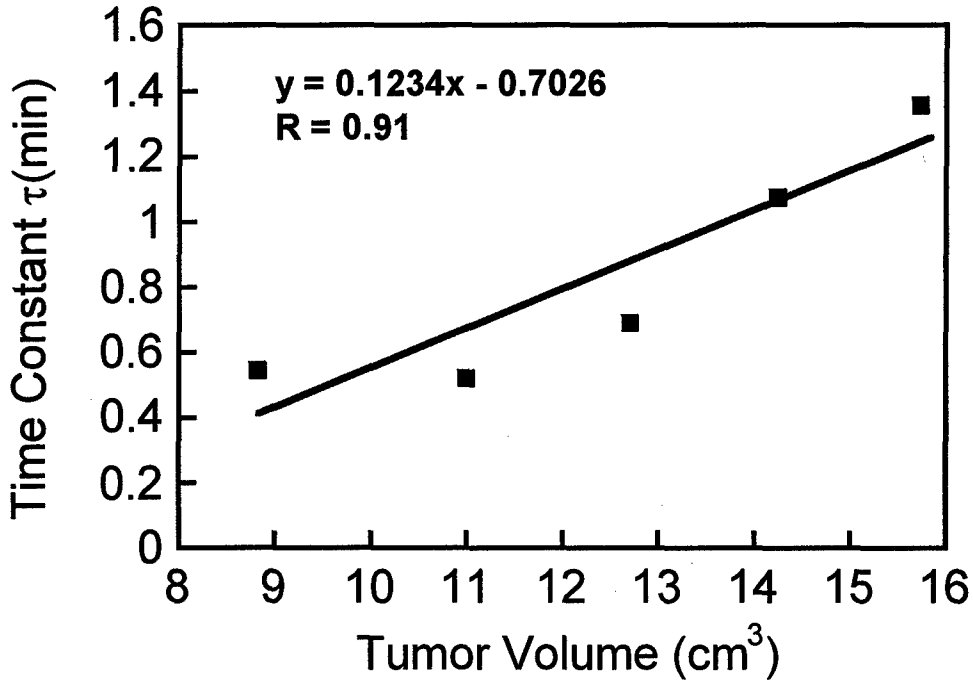
y = 0.1234x - 0.7026
R = 0.91
Time Constant τ(min)
1.6
1.4
1.2
1
0.8
0.6
0.4
0.2
0
8
9
10
11
12
13
14
15
16
Tumor Volume (cm3)

Figure 5

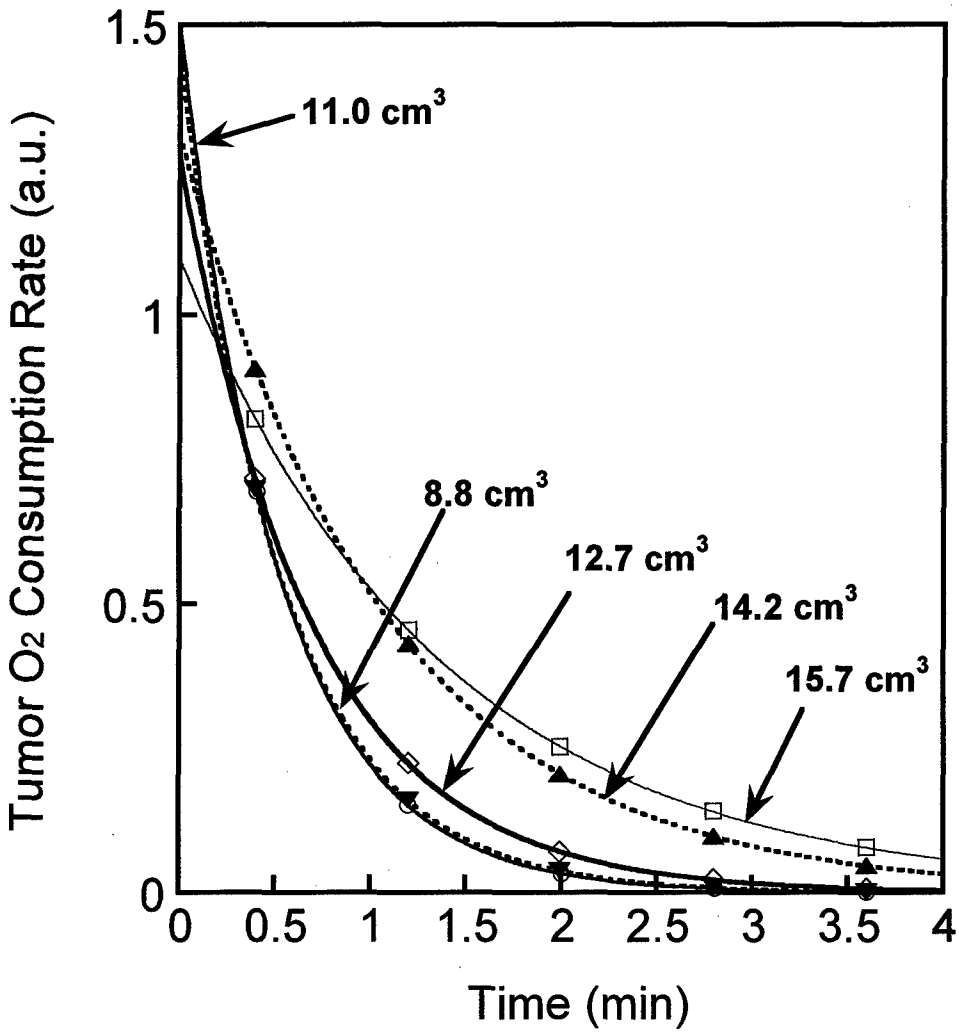
1.5
1
0.5
0
0
0.5
1
1.5
2
2.5
3
3.5
4
Tumor O2 Consumption Rate (a.u.)
Time (min)
11.0 cm3
8.8 cm3
12.7 cm3
14.2 cm3
15.7 cm3

Figure 6

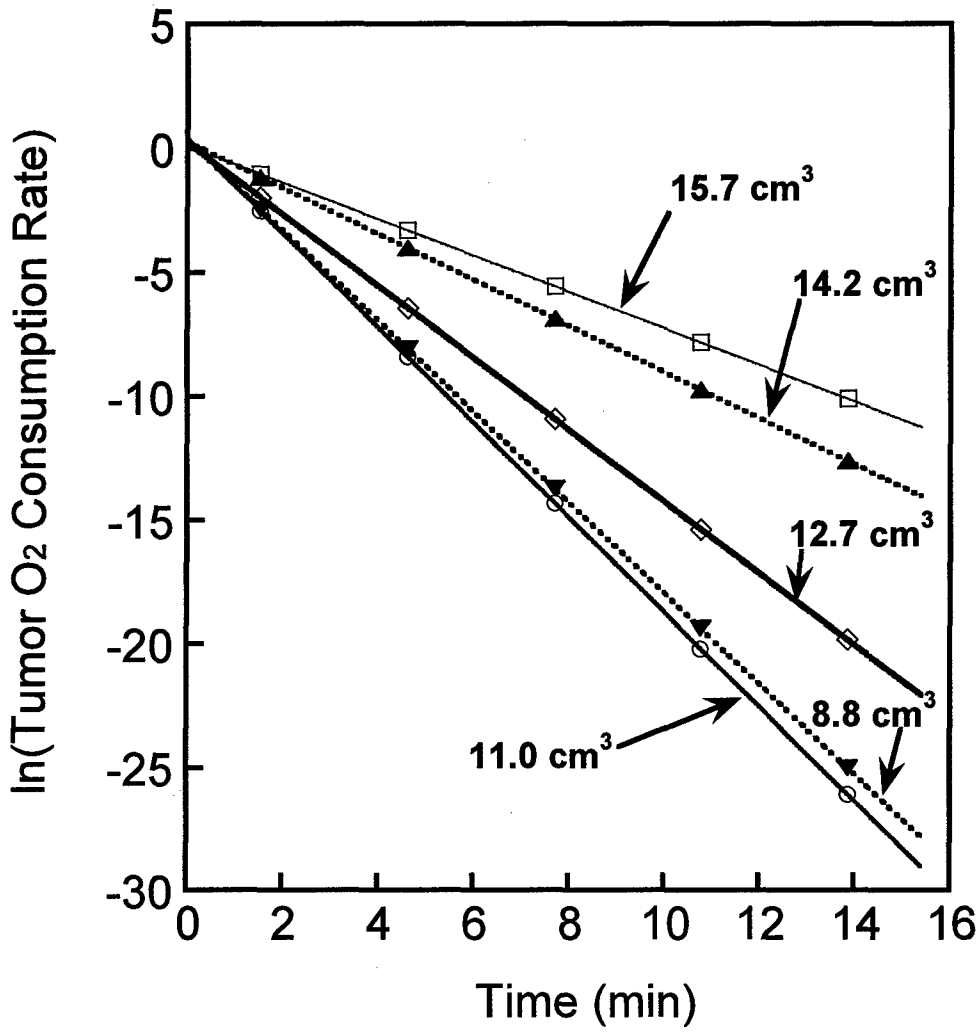
5
0
-5
-10
-15
-20
-25
-30
0
2
4
6
8
10
12
14
16
ln(Tumor O2 Consumption Rate)
Time (min)
15.7 cm3
14.2 cm3
12.7 cm3
8.8 cm3
11.0 cm3

Figure 7

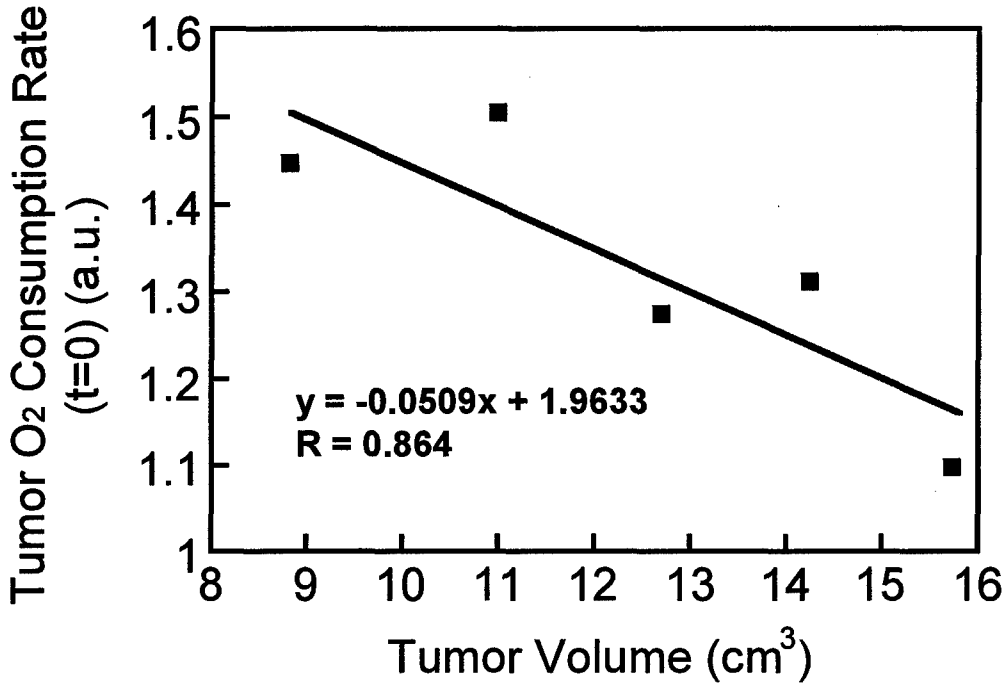
Tumor O2 Consumption Rate (t=0) (a.u.)
1.6
1.5
1.4
1.3
1.2
1.1
1
8
9
10
11
12
13
14
15
16
Tumor Volume (cm3)
y = -0.0509x + 1.9633
R = 0.864

Figure 8

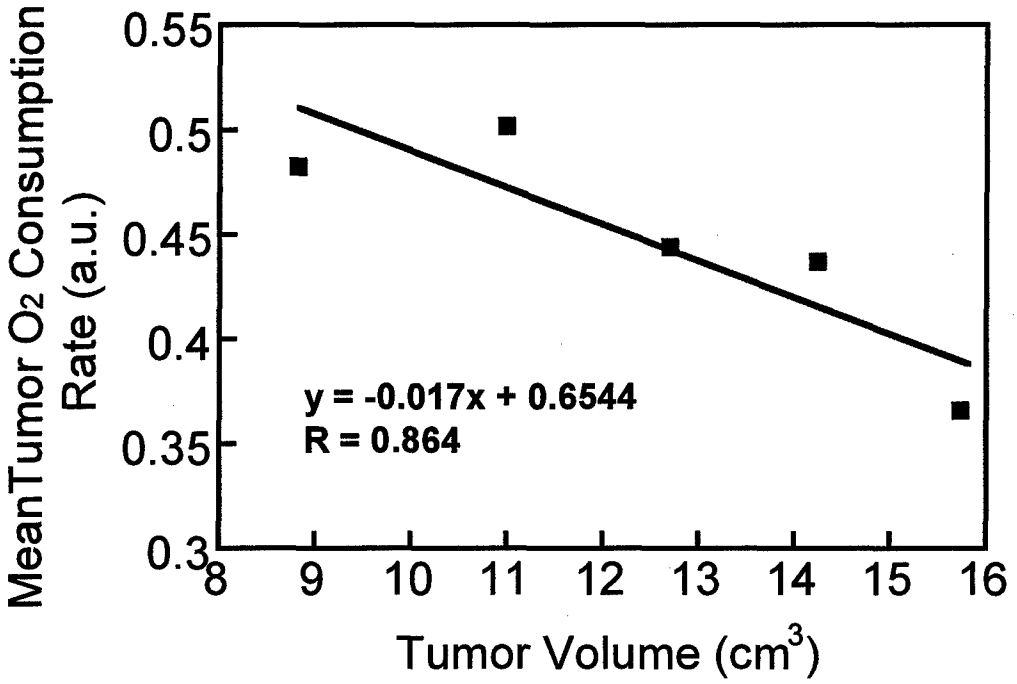
Mean Tumor O2 Consumption Rate (a.u.)
0.55
0.5
0.45
0.4
0.35
0.3
8
9
10
11
12
13
14
15
16
Tumor Volume (cm3)
y = -0.017x + 0.6544
R = 0.864

Figure 9

Investigation of breast tumor hemodynamics using tumor vascular phantoms and FEM simulations

Jae G. Kim and Hanli Liu
Joint Program in Biomedical Engineering, University of Texas Southwestern Medical Center at Dallas and University of Texas at Arlington, Arlington, Texas 76019
Tel: (817) 272-2054; FAX: (817) 272-2251; email address: ***hanli@uta.edu***

Abstract: We have developed dynamic tumor vascular phantoms and utilized the finite element method to investigate the bi-phasic behavior of oxyhemoglobin concentration increase that were observed *in vivo* from rat breast tumors during carbogen inhalation.
©2004 Optical Society of America
OCIS codes: (170.1470) blood/tissue constituent monitoring; (170.3660) Light propagation in tissues; (170.4580) Optical diagnostics for medicine; (170.6510) Spectroscopy, tissue diagnostics

1. Introduction

Solid tumors develop regions of hypoxia during their growth due to an imbalance between the rate of tumor cell proliferation and branching of the blood vessels [1,2]. Tumor hypoxia can contribute to the failure of radiotherapy [3], some forms of chemotherapy [4] and photodynamic therapy [5]. In addition, a number of clinical trials have found that patient survival measured either as tumor regression or as local control depends highly on tumor oxygenation [6]. Therefore, increasing tumor oxygenation could improve cancer therapy efficiency. As one means to improve tumor oxygenation, breathing hyperoxic gas has been used to enhance cancer treatment efficacy.

Basic on near infrared spectroscopy (NIRS) measurements, our previous *in vivo* animal study has clearly demonstrated that carbogen (95% CO_2 and 5% O_2) inhalation can improve the vascular oxygen level of breast tumors [7]. The observed changes in tumor vascular oxygenation ($\Delta[HbO_2]$) exhibited a rapid increase, followed by a gradual but significant increase, in response to carbogen intervention. To explain these biphasic behaviors of tumor hemodynamics, we established a mathematical model based on Kety's approach [8], and we formed a hypothesis that tumor vasculature is comprised with a well-perfused and poorly perfused region to explain why there are two different time constants in the $\Delta[HbO_2]$ data. The mathematical model further allows us to associate the signal amplitudes to the ratio of vascular coefficients and the ratio of the perfusion rates in the two different regions.

Even though we associated our fitting parameters of the NIR measurements mathematically with physiological factors, such as tumor vascular coefficients and perfusion rates, we did not provide solid validation for the model at the time. In this study, to further investigate breast tumor vasculature and to interpret the mathematical model, we designed and developed a tumor hemodynamic phantom for multi-channel NIRS experiments. Furthermore, we used the FEMLAB software to simulate the dynamic processes of light distribution in tumor hemodynamic phantoms, giving rise to better understanding of the association between the NIR readings and tumor physiological parameters.

2. Materials and methods

2.1 Mathematical Model of Tumor Vascular Oxygenation

The mathematical model for tumor vascular oxygenation during carbogen inhalation has been described indetails in our previous report [7]. Briefly, we followed an approach used to measure regional cerebral blood flow (rCBF) with diffusible radiotracers, as originally developed by Kety [8] in the 1950's. By applying Fick's principle and assuming that tumor has two distinct perfusion regions, the measured NIRS signal, which has a double- exponential feature observed in the rat tumor experiments, can be expressed as

$$\Delta HbO_2^{vasculature}(t) = \gamma_1 H_o[1-\exp(-f_1 t/\gamma_1)] + \gamma_2 H_o[1-\exp(-f_2 t/\gamma_2)]$$
$$= A_1[1-\exp(-t/\tau_1)] + A_2[1-\exp(-t/\tau_2)], \qquad (1)$$

where H_o is the arterial oxygenation input, f_1 and γ_1 are the blood perfusion rate and the vasculature coefficient in region 1 for the well perfused region, respectively; f_2 and γ_2 have the same respective meanings in region 2 for the poorly perfused region, and $A_1 = \gamma_1 H_o$, $A_2 = \gamma_2 H_o$, $\tau_1 = \gamma_1/f_1$, $\tau_2 = \gamma_2/f_2$. Basically, A_1, A_2, τ_1, and τ_2 can be determined from the NIRS measurements by fitting equation (1) with the experimental data. It follows thatthe ratios of two vasculature coefficients, γ_1/γ_2, and the two blood perfusion rates, f_1/f_2, can be obtained as

$$\frac{\gamma_1}{\gamma_2} = \frac{A_1}{A_2}, \quad \frac{f_1}{f_2} = \frac{A_1 / A_2}{\tau_1 / \tau_2}. \qquad (2)$$

2.2 Tumor Hemodynamic Phantom and Multi-Channel NIR Spectroscopy

To represent vascular blood vessels in tumor, we designed a vascular modeling device (VMD) by winding a small diameter tube (I.D.=0.51 mm) around a big diameter core tube (O.D.=14.4 mm). Tumor hemodynamic phantom was fabricated by embedding two VMDs into a cylindrical shape of gel, which is made of Intralipid and gelatin powder to represent tissues. The optical properties of tumor gel phantom were measured using near infrared tissue spectrometer (model: 96208, ISS Inc., Champaign, IL), and those values were close to tissue optical properties (μ_a= 0.032 cm^{-1}, μ_s'=9.2 cm^{-1} at 750 nm).

Schematic experimental setup for tumor hemodynamic phantom study is shown in Figure 1a . As shown here, NIR light at 730 nm from a multi-channel NIRS system was delivered to the tumor hemodynamic phantom, and three optical detectors were placed on the side of cylindrical phantom (D1, D2, and D3 in Fig. 1b) to collect signals, which were then processed in the computer. A certain amount of ink was injected into the two VMDs by two syringe pumps (model KDS200, KdScientific Inc., New Hope, PA), and the ink wastes were collected in the waste beaker. We used two syringe pumps so that we could control different ink flow rates for different VMDs.

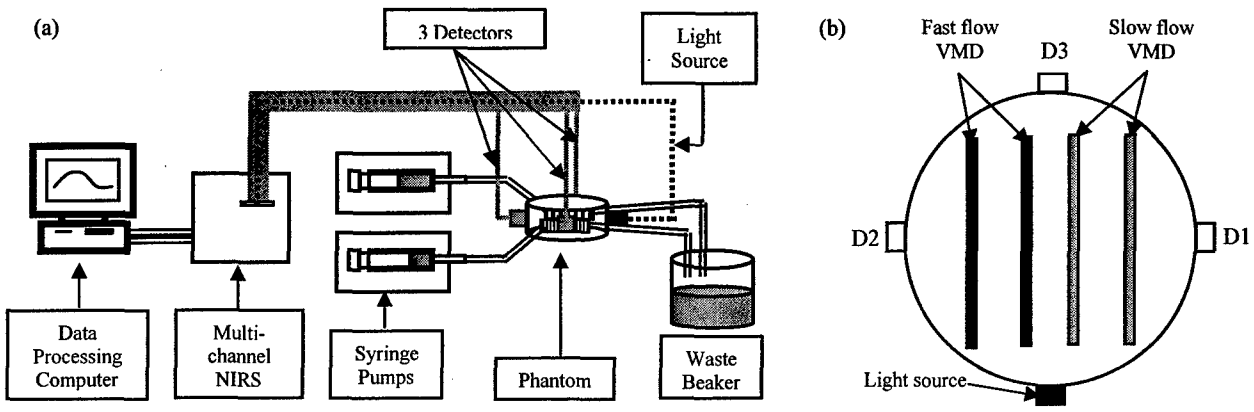

Fig. 1(a) Schematic diagram of tumor vascular phantom experimental setup. (b) The geometry of FEM simulation for tumor hemodynamic phantom.

2.3 FEM Simulation

To further investigate bi-phasic features of tumor hemodynamics, we used the FEMLAB software (COMSOL Inc. Burlington, MA), which is based on the finite element method, to simulate our dynamic tumor phantom experiments. The geometry of FEM simulations for the tumor hemodynamic phantom is shown also in Figure 1b, and it represents a 2-dimensional horizontal cross section of our tumor vascular phantom. The large circle represents the body of tumor phantom (diameter = 4 cm), and each VMD used in the dynamic phantom is represented by two thin rectangles (0.1 x 2.4 cm rectangle) within the circle as a blood vessel network: left two rectangles are for the vessels with a fast flow rate, and right two rectangles denote the vessels with a slow flow rate.

In the simulation, we used a uniform reduced scattering coefficient of 10 cm^{-1} for both the background and vasculature. Two absorption coefficients of 0.03 and 1.5 cm^{-1} were used to simulate the phantom and ink absorption in VMDs, respectively. The FEM model was performed with 1147 elements and 609 nodes and solved for the light distribution within the vascular phantom dynamically, using the stationary nonlinear solver type.

3. Results

Figure 2a shows the changes of absorption from the three detectors on the tumor hemodynamic phantom. Since two VMDs are having same inner diameter (0.51 mm), the velocities of ink in VMDs will be totally depending on the ink flow rates controlled by the two syringe pumps. The first step for this experiment was injecting ink only into left VMD with a flow rate of 20 ml/hr. As a result, D2 showed largest increase of $\Delta\mu_a$ while D1 showed smallest increase of $\Delta\mu_a$ because D1 was located quite away from the left VMD. For the second step, right VMD was injected with ink at the same flow rate of 20 ml/hr. Here, D1 showed largest increase of $\Delta\mu_a$ and D2 showed

smallest increase of $\Delta\mu_a$. Then, as the third step, the ink solution was injected into both left and right VMDs with the same flow rate (20 ml/hr). In all of the above cases, the signals from D3 showed similar profiles as the others, without clear bi-exponential patterns. For the fourth step, we injected ink into both VMDs, but with two different flow rates: 5 ml/hr for right VMD and 20 ml/hr for the left VMD. Now we can see that bi-exponential behavior appears on D3 since D3 is detecting signals from both left and right VMDs, which have two different ink flow rates.

For the further analysis, $\Delta\mu_a$ increases detected from the three detectors at step 4, as shown in Figure 2a, were fitted by using our mathematical model to obtain amplitudes and time constants values (Figure 2b). The time constant analysis shows that the $\Delta\mu_a$ increases from D1 and D2 are well fitted by the mono-exponential model, while $\Delta\mu_a$ increases from D3 is fitted well with the double exponential model, i.e., eq. (1). There exist a fast and slow time constants with $\tau_1 = 18.1 \pm 0.9$ sec and $\tau_2 = 134. \pm 11$ sec from D3, and they are well matched with τ_1 in D2 ($= 20.9 \pm 0.5$ sec) and τ_1 in D1 ($= 131. \pm 3$ sec). All of these suggest that the bi-phasic $\Delta\mu_a$ signals obtained from D3 with a fast and slow component indeed result from the dynamic changes in both left and right VMDs. We have further confirmed the same results from the FEM simulations on tumor hemodynamic phantom experiments.

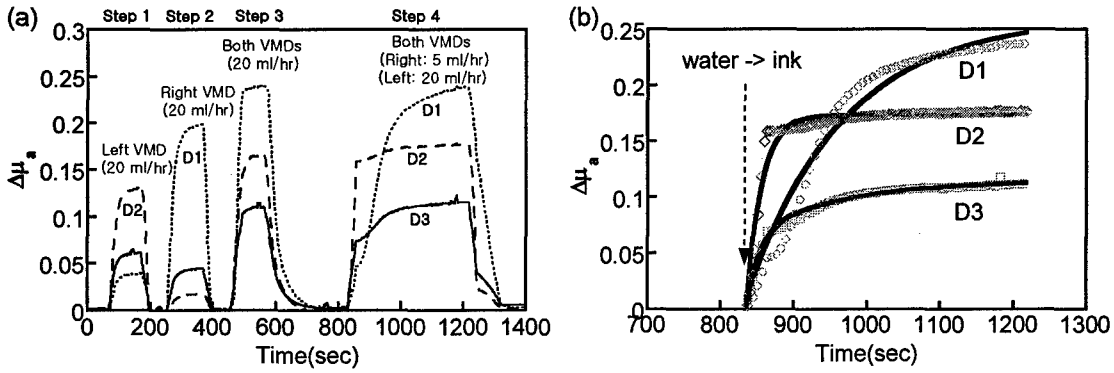

Fig. 2 (a) Effects of overdose KCl injection on tumor vascular $\Delta[HbO_2]$ and $\Delta[Hb]_{total}$ for a breast tumor (12.7 cm^3), (b) relationship between the tumor oxygen consumption rate and tumor volume.

4. Discussion and Conclusions

We have developed dynamic tumor phantom models to demonstrate our hypothesis on tumor hemodynamics during carbogen inhalation. We believe that the bi-phasic feature of tumor blood oxygenation increases during carbogen inhalation is highly associated with distinct vascular structures of the tumors, which are composed of well-perfused and poorly perfused region. We found that the two time constants in tumor hemodynamic models can result from different blood flow velocities or anything that can cause changes in blood flow velocities, such as blood vessel diameter and length. Also, the FEM simulation based on light diffusion equation was performed to simulate the tumor phantom experiments, and the results were well matched with the experiments, further supporting our previous hypothesis and the mathematical model.

5. Acknowledgements: This work was supported in part by the Department of Defense Breast Cancer Research grants of DAMD17-03-1-0353 (JGK) and BC990287 (HL).

6. References

[1] P. Vaupel, O. Thews, D. K. Kelleher, and M. Höckel, "Current status of knowledge and critical issues in tumor oxygenation", *In*: Hudetz and Bruley (eds), *Oxygen Transport to Tissue XX*, 591-602, Plenum Press, New York, 1998.
[2] P. Vaupel, "Oxygen transport in tumors: Characteristics and clinical implications", *Adv. Exp. Med. Biol.*, **388**, 341-351, 1996.
[3] R. H. Thomlinson, and L. H. Gray, "The histological structure of some human lung cancers and the possible implications for radiotherapy", *Br. J. Cancer*, **9**, 539-549, 1955.
[4] B. Teicher, J. Lazo, and A. Sartorelli, "Classification of antineoplastic agents by their selective toxicities toward oxygenated and hypoxic tumor cells", *Cancer Res.*, **41**, 73-81, 1981.
[5] J. D. Chapman, C. C. Stobbe, M. R. Arnfield, R. Santus, J. Lee, and M. S. McPhee, "Oxygen dependency of tumor cell killing *in vitro* by light activated photofrin II", *Radiat. Res.*, **126**, 73-79, 1991.
[6] A. W. Fyles, M. Milosevic, R. Wng, M. C. Kavanagh, M. Pintile, A. Sun, W. Chapman, W. Levin, L. Manchul, T. J. Keane, and R. P. Hill, "Oxygenation predicts radiation response and survival in patients with cervix cancer", *Radiother. Oncol.*, **48**, 149-156, 1998.
[7] H. Liu, Y. Song, K. L. Worden, X. Jiang, A. Constantinescu, and R. P. Mason, "Noninvasive Investigation of Blood Oxygenation Dynamics of Tumors by Near-Infrared Spectroscopy", *Applied Optics*, **39**(28), 5231-5243, 2000.
[8] S. S. Kety, "The theory and applications of the exchange of inert gas at the lungs and tissue," *Pharmacol. Rev.*, **3**, 1-41, 1951.

Non-Uniform Tumor Vascular Oxygen Dynamics Monitored By Three-Channel Near-Infrared Spectroscopy

Jae G. Kim[a], Yueqing Gu[a], Anca Constantinescu[b], Ralph P. Mason[b], Hanli Liu*[a]

[a]Joint Graduate Program of Biomedical Engineering,
University of Texas Southwestern Medical Center at Dallas/ University of Texas at Arlington
Arlington, TX 76019

[b]Advanced Radiological Sciences, Department of Radiology
University of Texas Southwestern Medical Center at Dallas
Dallas, TX 75390

ABSTRACT

In our previous report, we showed that there was a severe heterogeneity of tumor tissue oxygen dynamics even in a same tumor by using ^{19}F MR pO_2 mapping and near-infrared spectroscopy (NIRS). In this study, we applied a three channel NIRS system to reveal heterogeneity of tumor vascular oxygen dynamics during respiratory challenges. When the implanted tumor's size reached 3 cm, three photo detectors were attached on the surface of tumors in three different positions to measure changes in oxygenated hemoglobin concentration ($[HbO_2]$) while the inhaled gas was alternated between air and carbogen (95% oxygen, 5% CO2). Significant changes in tumor oxygenation were observed accompanying respiratory challenge, and these changes could be modeled with either one or two exponential components with fast and slow time constants. Time constant, amplitude, vascular coefficient, and the ratio of perfusion rate obtained from fitting curves of $\Delta[HbO_2]$ measured from three photo detectors revealed that there were indeed different responses of tumor vascular oxygenation during carbogen inhalation from three different locations. These results clearly show that tumors are highly heterogeneous in terms of vascular oxygenation response to carbogen inhalation. This study demonstrates that the NIR technology can provide an efficient, real-time, non-invasive way for monitoring tumor physiology, and it may have prognostic value and promised insight into tumor vascular development and angiogenesis.

Keywords: Tumor vascular oxygenation, tumor heterogeneity, NIR Spectroscopy, carbogen

1. INTRODUCTION

Solid tumors develop regions of hypoxia during their growth due to an imbalance between the rate of tumor cell proliferation and the proliferation and branching of the blood vessels.[1,2,3] Tumor hypoxia is responsible for the failure of radiotherapy,[4] some forms of chemotherapy,[5] and photodynamic therapy.[6] In addition, a number of clinical trials have found that patient survival measured either as tumor regression or as local control depends largely on tumor oxygenation.[7] Tumor hypoxia can occurr through diffusion-limited or chronic hypoxia and perfusion-limited or acute hypoxia.[8] Therefore, measurement of distribution of tumor perfusion rate could be important for tumor treatment planning and assessing methods designed to modulate tumor oxygenation.

Solid tumors are known to exhibit heterogeneous blood flow distribution.[9,10] There are many methods to measure tumor perfusion heterogeneity, such as Doppler ultrasound,[11] dynamic contrast MRI,[12] and the use of tumors grown in windowed chambers.[13] Intensive studies from Mason's group using ^{19}F MR pO_2 mapping have revealed intratumoral heterogeneity of pO_2 distribution and also heterogeneous response to hyperoxic gas breathing.[14,15,16] The group's findings of severe pO_2 heterogeneity in tumors can indirectly indicate the heterogeneous distribution of blood flow, since tissue pO_2 level is decided by a balance between the supply of oxygen from blood vessels and oxygen consumption by tissue cells.[17] Unlike the ^{19}F MR pO_2 mapping technique, near-infrared spectroscopy (NIRS) techniques cannot measure

pO_2 in tissue but can measure *in vivo* hemoglobin saturation and concentration. NIRS has been applied to muscle,[18,19,20] brain,[21,22,23] and tumor.[24,25,26]

In our previous study, we established a mathematical model of tumor oxygen dynamics during hyperoxic gas, such as carbogen (95% CO_2 and 5% O_2) or oxygen inhalation.[26] For our model, we formed a hypothesis that changes in oxygenated hemoglobin concentration ($\Delta[HbO_2]$) signal is composed of signals from well-perfused and poorly perfused region to explain why there are two different time constants to fit the $\Delta[HbO_2]$ data using our model. In addition to time constant, we could get amplitude of fitted curve, ratio of vascular coefficients, and ratio of perfusion rates by applying our dynamic tumor oxygenation model. Therefore, we will be able to detect intratumoral perfusion heterogeneity by applying multi-channel NIRS, since each detector's signal will come from a different region of tumor and, thus, it will show differences of curve fitting parameters among multi-detectors.

The goals of this study were to measure Δ[HbO2] in tumor vasculature during carbogen inhalation using a three channel NIRS system, and to reveal intratumoral vascular heterogeneity by fitting the Δ[HbO2] data with our mathematical model.

2. MATERIALS AND METHODS

2.1 Tumor Model and Measurement

For our study, murine mammary adenocarcinomas 13762NF grown in the hind limb of adult female Fisher 344 rats (~200 g) were used. Once these tumors reached approximately 2-3 cm in diameter, the rats were anesthetized with 0.2 ml ketamine hydrochloride (100 mg/ml; Aveco, Fort Dodge, IA) and maintained under general gaseous anesthesia using a small animal anesthesia unit with air (1 dm^3/min) and 1.3% isoflurane (Ohmeda PPD Inc., Fort Dodge, IA) through a mask placed over the mouth and nose. After anesthesia, the rat was placed on a warm blanket to maintain body temperature, which was monitored with a rectally-inserted thermal probe connected to a digital thermometer (Digi-Sense, model 91100-50, Cole-Parmer Instrument Company, Vernon Hills, IL). Tumors were shaved to improve optical contact for transmitting light, and a light source and three detectors were attached to the tumor using posts and swivel post clamps. A pulse oximeter (model: 8600V, Nonin, Inc.) was placed on the hind foot to monitor arterial oxygenation (S_aO_2) and heart rate. Figure 1 shows schematic setup for animal experiment using multi channel NIRS system.

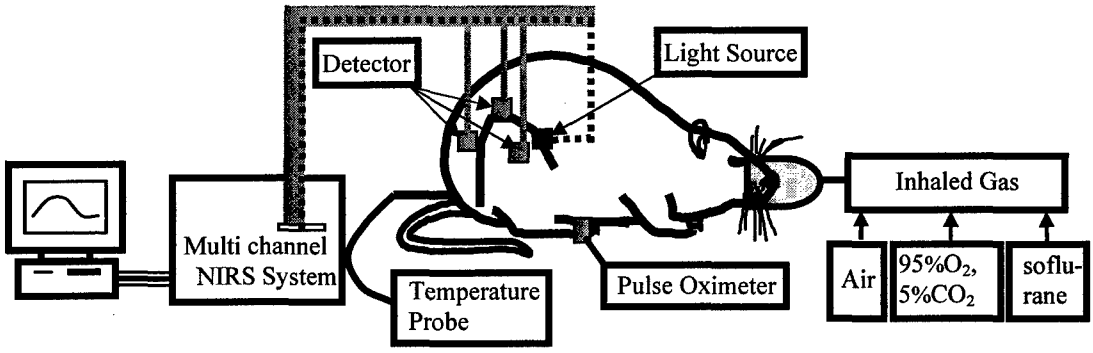

Figure 1: Schematic experimental setup of animal experiment. One of three detectors is placed opposite of the light source to detect light in transmission mode, and the other two were located in the semi-reflection mode.

All measurements were performed in the dark room, and measurements were initiated while the rats breathed air for 10 minutes to get a stable baseline. After 10 min of baseline measurement, the inhaled gas was switched to carbogen for 15 minutes, and then back to air for 15 minutes. Tumor volume V (in cm^3) was estimated as $V = (4\pi/3)\,[(L+W+H)/6]$,[27] where L, W, and H are the three respective orthogonal dimensions. Raw amplitude data from three detectors were recorded simultaneously during the experiments, and processed after the experiments to obtain the changes in

oxygenated hemoglobin concentration ($\Delta[HbO_2]$) and total hemoglobin concentration ($\Delta[Hb_{total}]$). Time constant, amplitude, γ_1/γ_2, and f_1/f_2 were calculated by fitting the data using Kaleidagraph software (Synergy Software, Reading, PA).

2.2 Multi-Channel NIR Spectroscopy

Our multi-channel NIR spectroscopy system has one light source and eight detectors to measure light signals from eight different locations, but due to tumor versus detector size constraints and to simplify the experiment, we only used three detectors to monitor tumor vascular oxygen dynamics during respiratory challenges.. In common with our previous work[26,28], we assume that oxyhemoglobin and deoxyhemoglobin are the only significant absorbance materials in the blood. The absorption coefficients comprise the extinction coefficients for deoxyhemoglobin and oxyhemoglobin multiplied by their respective concentrations (Eqs. 1 and 2).

$$\mu_a^{730} = \varepsilon_{Hb}^{730}[Hb] + \varepsilon_{HbO2}^{730}[HbO_2], \quad (1)$$
$$\mu_a^{850} = \varepsilon_{Hb}^{850}[Hb] + \varepsilon_{HbO2}^{850}[HbO_2]. \quad (2)$$

The data presented in this paper were analyzed using modified Beer-Lambert's law and amplitude values to find the changes in absorption (Eq. 3). By manipulating Equations 1-3, changes in oxygenated hemoglobin, deoxygenated hemoglobin and total hemoglobin concentrations were calculated from the transmitted amplitude of the light through the tumor (Eqs. 4, 5 and 6).

$$\mu_{aB} - \mu_{aT} = \log (A_B/A_T) / L, \quad (3)$$
$$\Delta[HbO_2] = [-0.674*\log (A_B/A_T)^{730} + 1.117*\log (A_B/A_T)^{850}] / L, \quad (4)$$
$$\Delta[Hb] = [0.994*\log (A_B/A_T)^{730} - 0.376*\log (A_B/A_T)^{850}] / L, \quad (5)$$
$$\Delta[Hb]_{total} = \Delta[Hb] + \Delta[HbO2]=[0.32*\log (A_B/A_T)^{730} + 0.741*\log (A_B/A_T)^{850}] / L, \quad (6)$$

where A_B = baseline amplitude; A_T = transition amplitude; L = optical pathlength between source/detector. The constants were computed with the extinction coefficients for oxy and deoxyhemoglobin at the two wavelengths used.[29] In principle, L should be equal to the source–detector separation, d, multiplied by a differential pathlength factor (DPF), i.e., L=d*DPF. Little is known about DPF for tumors, although a DPF value of 2.5 has been used by others.[30] Since our focus is on dynamic changes and relative values of tumor $[HbO_2]$ with respect to carbogen intervention, we have taken the approach of including the DPF in the unit, i.e., modifying eq. (4) as follows:

$$\Delta[HbO_2] = [-0.674*\log (A_B/A_T)^{730} + 1.117*\log (A_B/A_T)^{850}] / d, \quad (7)$$

where d is the direct source-detector separation in cm, and the unit of $\Delta[HbO_2]$ in Eq. (7) is mM/DPF.

2.3 Mathematical Model of Tumor Vascular Oxygenation

In our previous report,[266] we followed an approach used to measure regional cerebral blood flow (rCBF) with diffusible radiotracers, as originally developed by Kety[31] in the 1950's, to develop our model. By applying Fick's principle and defining γ as the ratio of HbO_2 concentration changes in the vascular bed to that in veins, which is equal to $(\Delta HbO_2^{vasculature})/(\Delta HbO_2^{vein})$, we could get Eq. (8) as follows:

$$\Delta HbO_2^{vasculature}(t) = \gamma H_o[1-\exp(-ft/\gamma)] = A_1[1-\exp(-t/\tau_1)] \quad (8)$$

where γ is the vasculature coefficient of the tumor, H_o is the arterial oxygenation input and f is the blood perfusion rate.

If a tumor has two distinct perfusion regions, and the measured signal is from both regions (Figure 2), then it is reasonable that we will get two different blood perfusion rates f_1 and f_2, two different vasculature coefficients γ_1 and γ_2, or all four. Therefore, Eq. (8) can be modified to double exponential expression as

$$\Delta HbO_2^{vasculature}(t) = \gamma_1 H_o[1-\exp(-f_1 t/\gamma_1)] + \gamma_2 H_o[1-\exp(-f_2 t/\gamma_2)]$$
$$= A_1[1-\exp(-t/\tau_1)] + A_2[1-\exp(-t/\tau_2)] \quad (9)$$

where f_1 and γ_1 are the blood perfusion rate and the vasculature coefficient, respectively, in region 1, f_2 and γ_2 are the same for region 2, and $A_1 = \gamma_1 H_o$, $A_2 = \gamma_2 H_o$, $\tau_1 = \gamma_1/f_1$, $\tau_2 = \gamma_2/f_2$. Then, if A_1, A_2, τ_1, and τ_2 are determined from our measurements, we can obtain the ratios of two vasculature coefficients and the two blood perfusion rates:

$$\frac{\gamma_1}{\gamma_2} = \frac{A_1}{A_2}, \qquad \frac{f_1}{f_2} = \frac{A_1/A_2}{\tau_1/\tau_2}. \quad (10)$$

With these two ratios, we will be able to understand more about tumor physiology such as vasculature and blood perfusion. In this report, we used three-channel NIR spectroscopy to explore the intratumoral heterogeneity of vasculature by obtaining A_1, A_2, τ_1, and τ_2 from three different locations on tumors.

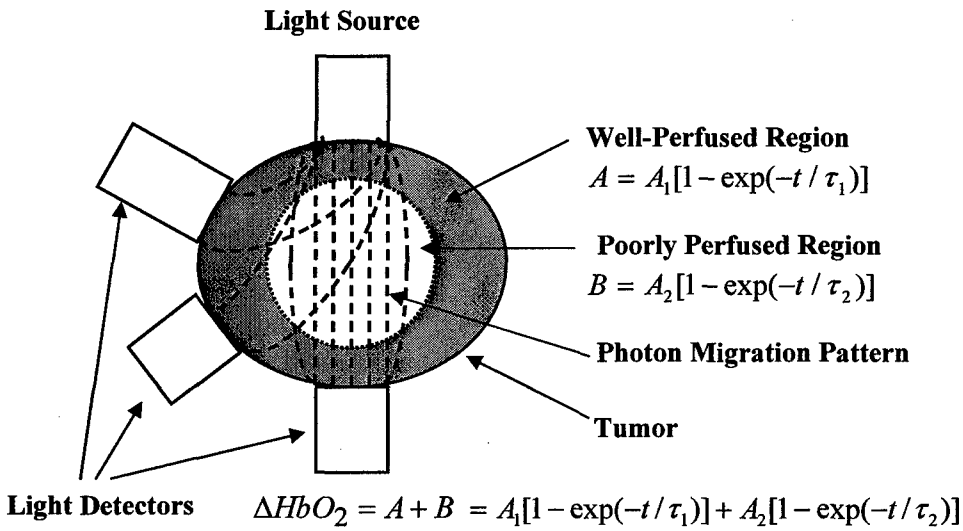

Fig. 2 Schematic diagram of two-region tumor model. If tumor has two distinct regions in terms of perfusion rate, the detector will get signal from both regions, and the signal can be fitted with double exponential expression.

3. RESULTS

Figure 3(a) shows the $\Delta[HbO_2]$ obtained from three detectors in a breast tumor (16.6 cm^3), with a source-detector separation of 1.5 cm for detector #1, 2.5 cm for detector #2, and 2.8 cm for detector #3, respectively. The measurement uncertainties are shown at only discrete locations. After 10 min of air breathing measurement as a baseline, inhaled gas was switched from air to carbogen, which caused a sharp increase in $\Delta[HbO_2]$ ($p < 0.0001$ after 1 min from gas switch) followed by a further slow, gradual, but significant, increase over the next 15 min ($P < 0.0001$).

The rising part of $\Delta[HbO_2]$ from detector #1, #2, and #3 after gas switch from air to carbogen and the fitted curves are shown in Figure 3(b) – 3(d), respectively. We used single-exponential (Eq. 8) and double-exponential expressions (Eq. 9) to fit the data of rising portion of $\Delta[HbO_2]$ and it appears that double-exponential expression gives a much better fit, as is confirmed by the respective R^2 values [0.95 ~ 0.96 versus 0.79 ~ 0.84 (not shown in the table 1)].

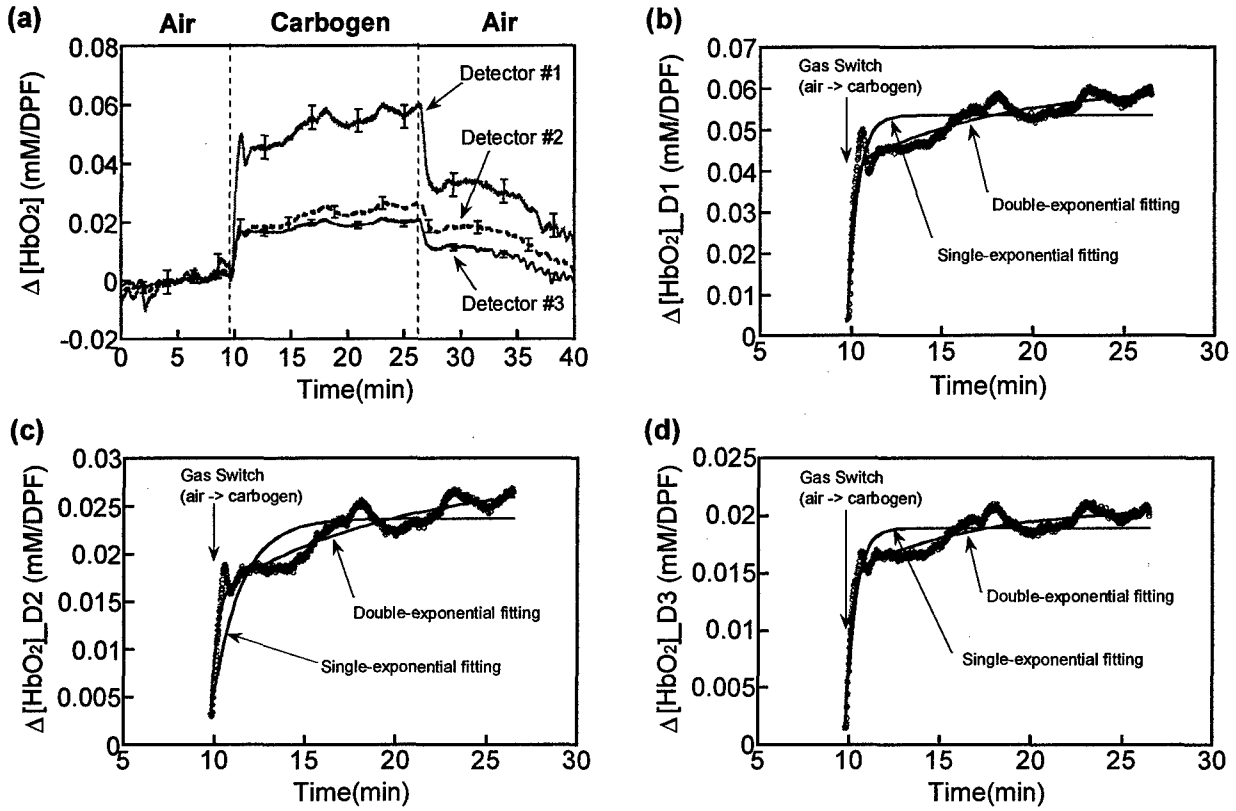

Fig. 3 Dynamic changes of $[HbO_2]$ from three detectors in a rat breast (volume: 16.6 cm^3) tumor. Dotted vertical lines mark the point when the gas was changed [Fig. 3(a)]. The rising part of $\Delta[HbO_2]$ from detectors was fitted using both single-exponential and double-exponential expressions and Fig. 3(b)-3(d) are from detector #1-#3, respectively.

Table 1. Summary of vascular oxygen dynamics from three detectors from Figure 3

Double-Exponential fitting $\Delta HbO_2 = A_1[1-\exp(-t/\tau_1)] + A_2[1-\exp(-t/\tau_2)]$			
Parameters	Detector #1	Detector #2	Detector #3
Separation: d (cm)	1.5	2.5	2.8
A_1 (mM/DPF)	0.037 ± 0.0004	0.0125 ± 0.00022	0.0134 ± 0.00016
τ_1 (min)	0.24 ± 0.011	0.3 ± 0.019	0.27 ± 0.011
A_2 (mM/DPF)	0.02 ± 0.0005	0.013 ± 0.00035	0.006 ± 0.00013
τ_2 (min)	8.27 ± 0.721	9.87 ± 0.835	7 ± 0.58
χ^2	0.0045	0.001	0.00046
R^2	0.95	0.96	0.95
$\gamma_1/\gamma_2 = A_1/A_2$	1.85 ± 0.065	0.96 ± 0.045	2.23 ± 0.08
τ_1/τ_2	0.029 ± 0.0035	0.03 ± 0.0038	0.039 ± 0.0048
$f_1/f_2 = (A_1/A_2)/(\tau_1/\tau_2)$	63.75 ± 8.83	31.58 ± 4.51	57.81 ± 8.72

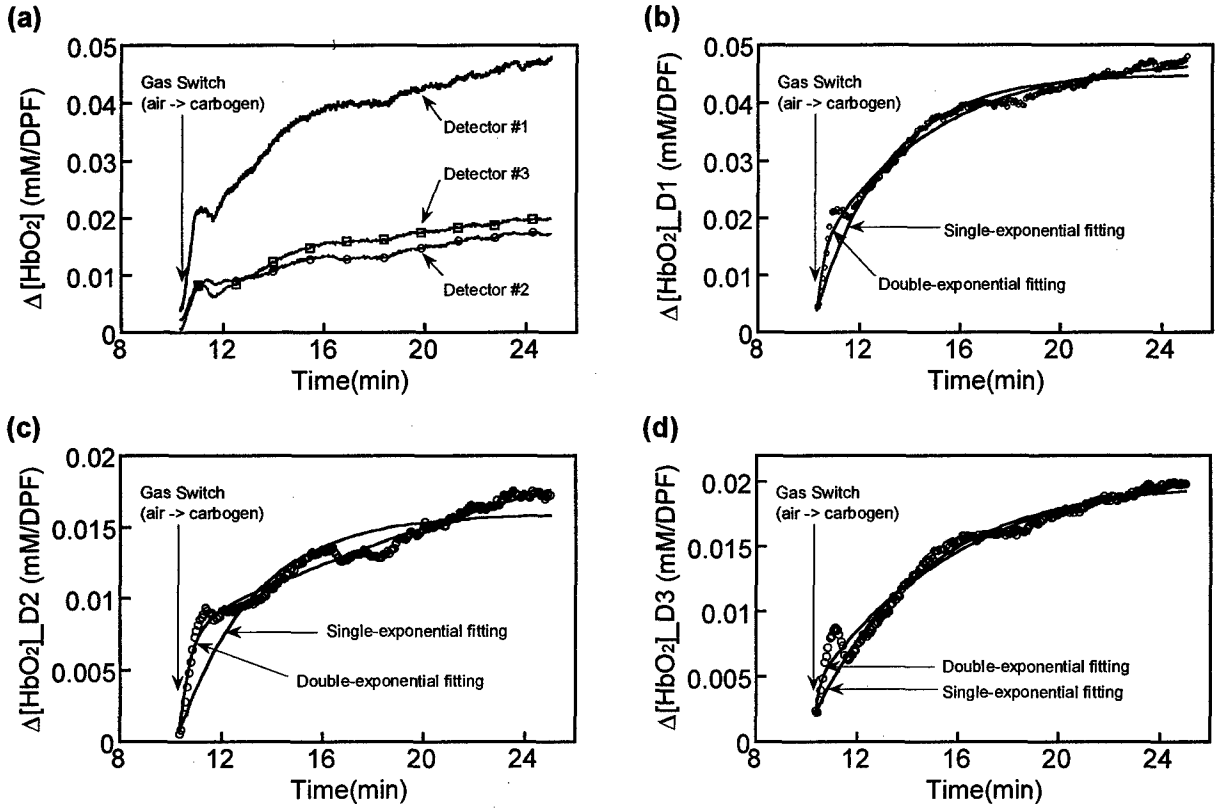

Fig. 4 Dynamic changes of $[HbO_2]$ from three detectors in another rat breast (volume: 20.6 cm^3) tumor. Dotted vertical lines mark the point when the gas was changed [Fig. 4(a)]. Figures 3(b)-3(d) show the rising part of $\Delta[HbO_2]$ after gas switch from air to carbogen, and fitted curves in detector #1-#3, respectively.

Table 2. Summary of vascular oxygen dynamics from three detectors from Figure 4

Double-Exponential fitting $\Delta HbO_2 = A_1[1-\exp(-t/\tau_1)] + A_2[1-\exp(-t/\tau_2)]$			
Parameters	Detector #1	Detector #2	Detector #3
Separation: d (cm)	2	2.5	3
A_1 (mM/DPF)	0.01 ± 0.0003	0.0072 ± 0.00012	0.0023 ± 0.00014
τ_1 (min)	0.27 ± 0.026	0.43 ± 0.02	0.16 ± 0.042
A_2 (mM/DPF)	0.033 ± 0.0003	0.021 ± 0.0017	0.017 ± 0.0001
τ_2 (min)	4.65 ± 0.1	22.98 ± 2.83	6.08 ± 0.161
χ^2	0.00093	0.00019	0.00031
R^2	0.99	0.99	0.99
$\gamma_1/\gamma_2 = A_1/A_2$	0.303 ± 0.0118	0.343 ± 0.0309	0.135 ± 0.0089
τ_1/τ_2	0.058 ± 0.0066	0.0187 ± 0.00280	$.026 \pm 0.0071$
$f_1/f_2 = (A_1/A_2)/(\tau_1/\tau_2)$	5.22 ± 0.71	18.33 ± 3.81	5.13 ± 1.32

By manipulating time constants and amplitudes, we can get physiologically meaningful parameters such as $\gamma_1/\gamma_2 = A_1/A_2$ and $f_1/f_2 = (A_1/A_2)/(\tau_1/\tau_2)$ (Eq. 10). Time constants and amplitudes from three fitted curves are summarized in the Table 1 to describe tumor vascular structure and blood perfusion. When γ_1/γ_2 is close to 1, it implies that the measured signal results equally from both region 1 and 2 [Figure 3(c)], and if $\gamma_1/\gamma_2 > 1$, then the measured signal results more from region 1 than region 2 [Figure 3(b) and 3(d)]. All the ratios of f_1/f_2 in Figure 3(b) – 3(d) are much greater than 1, which indicate the blood perfusion rate in region 1 is much higher than that in region 2.

Figure 4 depicts $\Delta[HbO_2]$ obtained from another breast tumor (20.6 cm^3). The fast and significant increases of $\Delta[HbO_2]$ after switching gas from air to carbogen are similar to those from tumor in Figure 3, and also double-exponential fitting shows better fitness compared to single-exponential expression. However, as can be seen from Table 2, this tumor has several different characteristics compared to tumor in Figure 3. First, this tumor has very different values of time constants between detectors, while the tumor in Figure 3 has close values of time constants between detectors. Fast time constants in Figure 3 are 0.24, 0.3, and 0.27 min, and slow time constants in Figure 3 are 8.27, 9.87, and 7 min, which are close to each other between detectors, but tumor in Figure 4 shows very different values of time constant between detectors. Fast time constants in Figure 4 are 0.27, 0.43, and 0.16 min, and slow time constants in Figure 4 are 4.65, 22.98, and 6.08 min. In addition to time constants, the γ_1/γ_2 and f_1/f_2 are also very different from those in the Table 1. Figures 4(b)-4(d) have $\gamma_1/\gamma_2 <1$ while only Figure 3(c) has $\gamma_1/\gamma_2 <1$, which implies that signals from all three detectors in Figure 4 are mainly from region 2 rather than region 1. The ratios of perfusion rate in Figure 4, f_1/f_2, are also much smaller than those from tumor in Figure 3.

4. DISCUSSION

We have seen intrtumoral heterogeneity in terms of tissue pO_2 using ^{19}F MR pO_2 mapping via reports from Dr. Mason's research group.[14,15,16] ^{19}F MR pO_2 mapping technique clearly showed that tumor tissue has a wide distribution of pO_2, and also different responses to respiratory challenges even within a tumor. Tissue pO_2 is mainly decided by the balance between the supply of oxygen from blood vessels and the oxygen consumption by tissue cells. With assumption of constant oxygen consumption during gas switch from air to carbogen, tumor tissue pO_2 will be mainly dependent of blood oxygen level changes.

NIRS is a portable, low cost, and real time measurement system that can measure changes of blood oxygen level by using two wavelengths. We have used a NIRS system that has one light source and one detector so that we could have global measurement of $\Delta[HbO_2]$ and $\Delta[Hb_{total}]$ in tumor during respiratory challenges.[26,28] Through our previous experiments, we have found that most of tumors have bi-phasic behavior of $\Delta[HbO_2]$ increase (rapid increase followed by a slow and gradual increase) after switching the gas from air to carbogen or air to 100% oxygen. To explain this bi-phasic behavior, we formed a hypothesis that the bi-phasic behavior of $\Delta[HbO_2]$ increase during carbogen or oxygen inhalation results from two different regions in tumors in terms of blood perfusion rate and vascular structure, and we developed a mathematical model to get physiologically meaningful parameters from experimental data.

The region in tumor that has fast blood perfusion rate, f_1, and high ratio of $\Delta[HbO_2]^{vasculature}$ and $\Delta[HbO_2]^{vein}$, γ_1, is called region 1, while region 2 represents the region that has slow blood perfusion rate, f_2, and low ratio of $\Delta[HbO_2]^{vasculature}$ and $\Delta[HbO_2]^{vein}$, γ_2. Thus, the ratio of γ_1 and γ_2 can be simply thought of as a ratio of region 1 volume to region 2 volume. In other words, when $\gamma_1/\gamma_2 \approx 1$, it implies that the light penetrated tumor volume consists of 50% well-perfused region and 50% poorly perfused region. If γ_1/γ_2 is smaller than 1 or larger than 1, this means the measured signal results mostly from poorly perfused region, or well-perfused region, respectively. Therefore, by looking at these two ratios between detectors from Table 1 and 2, we can find the intratumoral heterogeneity in terms of blood perfusion rate and proportion of either well-perfused region or poorly perfused region.

For instance, γ_1/γ_2 from detector #2 is the lowest value among three detectors in Figure 3, which means that the light transmitted tumor volume between light source and detector #2 has less well perfused region than those volumes detected by detector #1 and #3. Detector #2 also has lowest f_1/f_2 compare to two other detectors. These implies that tumor volume detected by detector #2 in Figure 3 has relatively low portion of well oxygenated region compare to those detected by detector #1 and #3, and it caused lowest f_1/f_2 among three detectors. Table 2 also can show the intratumoral

heterogeneity in Figure 4. However, in this case, detector #2 shows highest γ_1/γ_2 and f_1/f_2 among three detectors, which means that tumor volume detected by detector #2 in Figure 4 has more well oxygenated region than those detected by detector #1 and #3. Both detector #2s in the Figures 3 and 4 are placed on tumors in semi transmittance mode, but their detected tumor volumes have totally different vasculature.

Additionally, we can also find the heterogeneity between two different tumors by comparing those fitted parameters. For instance, a large proportion of tumor in Fig. 3 consists of well-perfused region (γ_1/γ_2 = 0.96 ~ 2.23) while tumor in Figure 4 is mostly composed of poorly perfused region (γ_1/γ_2 = 0.135 ~ 0.343). In the case of tumor in Figure 3, the blood perfusion rate in the well-perfused region is much faster than in the poorly perfused region, while the ratio of blood perfusion rate between well-perfused region and poorly perfused region from tumor in Figure 4 (f_1/f_2 = 5.13 ~ 18.33) is not as high as tumor in Figure 3 (f_1/f_2 = 31.58 ~ 63.75). All of these results show that tumor vasculature vary significantly in terms of perfusion rate between each tumor and also within each individual tumor.

5. CONCLUSION

We applied a three channel NIRS system to show the heterogeneity of tumor vasculature in terms of blood perfusion rate and vascular coefficients. All detectors on tumor showed a sharp increase of $\Delta[HbO_2]$ that was followed by slow and gradual increase. However, the differences between the signals from three detectors could be found by applying our mathematical model to fit the $\Delta[HbO_2]$ data during carbogen inhalation. Although all signals from three detectors in both Figures 3 and 4 showed bi-phasic behavior of $\Delta[HbO_2]$, their time constants and ratio of γ_1/γ_2 and f_1/f_2 revealed that tumor vasculature is not homogeneous and, indeed, it is heterogeneous with respect to blood perfusion rate and proportion of well-perfused region in tumor. Our future study will be conducted to prove our hypothesis on the bi-phasic behavior of $\Delta[HbO_2]$ during carbogen inhalation and to learn more about meaning of time constant, amplitude, γ_1/γ_2, and f_1/f_2 from our mathematical model.

ACKNOWLEDGEMENTS

This work was supported in part by The American Cancer Society RPG-97-116-010CCE (RPM), NIH RO1 CA79515 (RPM), and the Department of Defense Breast Cancer Initiative grants BC990287 (HL).

REFERENCES

[1] P. Vaupel, O. Thews, D. K. Kelleher, and M. Höckel, "Current status of knowledge and critical issues in tumor oxygenation", *In*: Hudetz and Bruley (eds), *Oxygen Transport to Tissue XX*, 591-602, Plenum Press, New York, 1998.

[2] P. Vaupel, "Vascularization, blood flow, oxygenation, tissue *p*H, and bioenergetic status of human breast cancer", *In*: Nemoto and LaManna (eds), *Oxygen Transport to Tissue XVIII*, 243-253, Plenum Press, New York, 1997.

[3] P. Vaupel, "Oxygen transport in tumors: Characteristics and clinical implications", *Adv. Exp. Med. Biol.*, **388**, 341-351, 1996.

[4] R. H. Thomlinson, and L. H. Gray, "The histological structure of some human lung cancers and the possible implications for radiotherapy", *Br. J. Cancer,* **9**, 539-549, 1955.

[5] B. Teicher, J. Lazo, and A. Sartorelli, "Classification of antineoplastic agents by their selective toxicities toward oxygenated and hypoxic tumor cells", *Cancer Res.*, **41**, 73-81, 1981.

[6] J. D. Chapman, C. C. Stobbe, M. R. Arnfield, R. Santus, J. Lee, and M. S. McPhee, "Oxygen dependency of tumor cell killing *in vitro* by light activated photofrin II", *Radiat. Res.*, **126**, 73-79, 1991.

[7] A. W. Fyles, M. Milosevic, R. Wng, M. C. Kavanagh, M. Pintile, A. Sun, W. Chapman, W. Levin, L. Manchul, T. J. Keane, and R. P. Hill, "Oxygenation predicts radiation response and survival in patients with cervix cancer", *Radiother. Oncol.*, **48**, 149-156, 1998.

[8] J. H. Kaanders, J. Bussink, and A. J. van der Kogel, "ARCON: a novel biology-based approach in radiotherapy", *Lancet Oncol.*, **3**(12), 728-37, 2002.

[9] R. J. Gillies, P. A. Schornack, T. W. Secomb, and N. Raghunand, "Causes and effects of heterogeneous perfusion in tumors," *Neoplasia*, **1** (3), 197-207, 1999.

[10] D. R. Tailor, H. Poptani, J. D. Glickson, J. S. Leigh, and R. Reddy, "High-Resolution Assessment of Blood Flow in Murine RIF-1 Tumors by Monitoring Uptake of H_2 ^{17}O With Proton $T_1\rho$-Weighted Imaging," *Magn. Reson. Med.*, **49**, 1–6, 2003.

[11] J. C. Acker, M. W. Dewhirst, G. M. Honore, T. V. Samulski, J. A. Tucker, and J. R. Oleson, "Blood perfusion measurements in human tumors, evaluation of laser Doppler methods," *Int. J. Hypertherm*, **6**, 287-304, 1990.

[12] J. Griebel, N. A. Mayr, A. de Vries, M. V. Knopp, T. Gneiting, C. Kremser, M. Essig, H. Hawighorst, P. H. Lukas, and W. T. Yuh, "Assessment of tumor microcirculation: a new role of dynamic contrast MR imaging," *J. Magn. Reson. Imaging*, **7**, 111-119, 1997.

[13] M. W. Dewhirst, C. Gustafson, J. F. Gross, and C. Y. Tso, "Temporal effects of 5.0 Gy radiation in healing subcutaneous microvasculature of a dorsal flap window chamber", *Radiat. Res.*, **112**, 581-591, 1987.

[14] R. P. Mason, A. Constantinescu,S. Hunjan,D. Le,E. W. Hahn,P. P. Antich,C. Blum,and P. Peschke, "Regional tumor oxygenation and measurement of dynamic changes." *Radiat. Res.*, **152**, 239-249, 1999.

[15] D. Zhao, A. Constantinescu, E. W. Hahn and R. P. Mason. "Tumor oxygenation dynamics with respect to growth and respiratory challenge: Investigation of the Dunning prostate R3327-HI tumor," *Radiat. Res.*, **156**(5), 510-520, 2001.

[16] S. Hunjan, D. Zhao, A. Constantinescu, E. W. Hahn, P. Antich, and R. P. Mason, "Tumor oximetry: demonstration of an enhanced dynamic mapping procedure using fluorine-19 echo planar magnetic resonance imaging in the dunning prostate R3327-AT1 rat tumor," *Int. J. Radiat. Oncol. Biol. Phys.*, **49**, 1097-1108, 2001.

[17] M. Höckel, P. Vaupel, "Tumor hypoxia: definitions and current clinical, biologic, and molecular aspects", *J Natl Cancer Inst.*, **93**, 266–76, 2001.

[18] B. Chance, S. Nioka, J. Kent, K. McCully, M. Fountain, R. Greenfield, and G. Holtom, "Time resolved spectroscopy of hemoglobin and myoglobin in resting and ischemic muscle", *Anal. Biochem.*, **174**,698-707, 1988.

[19] S. Homma, T. Fukunaga,, and A. Kagaya, "Influence of adipose tissue thickness on near infrared spectroscopic signals in the measurement of human muscle", *J. Biomed. Opt.*, **1**(4), 418-424, 1996.

[20] M. Ferrari, Q. Wei, L. Carraresi, R. A. De Blasi, and G. Zaccanti, "Time-resolved spectroscopy of the human forearm", *J. Photochem. Photobiol. B: Biol.*, **16**,141-153, 1992.

[21] B. Chance, E. Anday, S. Nioka, S. Zhou, L. Hong, K. Worden, C. Li, T. Murray, Y. Ovetsky, D. Pidikiti, and R. Thomas, "A novel method for fast imaging of brain function non-invasively with light", *Optics Express*, **2**(10), 411-423 1998.

[22] R. Wenzel, H. Obrig, J. Ruben, K. Villringer, A. Thiel, J. Bernarding, U. Dirnagl, and A. Villringer, "Cerebral blood oxygenation changes induced by visual stimulation in humans", *J. Biomed. Opt.*, **1**(4),399-404, 1996.

[23] M. Cope, and D. T. Delpy, "A system for long term measurement of cerebral blood and tissue oxygenation in newborn infants by near infrared transillumination", *Med. Biol. Eng. Comp.*, **26**, 289-294, 1988.

[24] R. G. Steen, K. Kitagishi, and K. Morgan, "In vivo measurement of tumor blood oxygenation by near-infrared spectroscopy: immediate effects of pentobarbital overdose or carmustine treatment", *J. Neuro-Oncol.*, **22**, 209-220, 1994.

[25] H. D. Sostman, S. Rockwell, A. L. Sylvia, D. Madwed, G. Cofer, H. C. Charles, R. Negro-Vilar, and D. Moore, "Evaluation of BA1112 rhabdomyosarcoma oxygenation with microelectrodes, optical spectrophotometry, radiosensitivity, and magnetic resonance spectroscopy", *Magn. Reson. Med.*, **20**, 253-267, 1991.

[26] H. Liu, Y. Song, K. L. Worden, X. Jiang, A. Constantinescu, and R. P. Mason, "Noninvasive Investigation of Blood Oxygenation Dynamics of Tumors by Near-Infrared Spectroscopy", *Applied Optics*, **39**(28), 5231-5243, 2000.

[27] T. Y. Reynolds, S. Rockwell, and P. M. Glazer, "Genetic instability induced by the tumor microenvironment," *Cancer Res.*, **56**, 5754–5757, 1996.

[28] Jae G. Kim, Dawen Zhao, Yulin Song, Anca Constantinescu, Ralph P. Mason, and Hanli Liu, "Interplay of tumor vascular oxygenation and tumor pO_2 observed using near-infrared spectroscopy, an oxygen needle electrode, and ^{19}F MR pO_2 mapping", *J. Biomed. Opt.*, **8**(1), 53-62, 2003.

[29] M. Cope, "The application of near infrared spectroscopy to non invasive monitoring of cerebral oxygenation in the newborn infant", PhD thesis, University College London, 1991.

[30]. R. G. Steen, K. Kitagishi and K. Morgan, " *In vivo* measurement of tumor blood oxygenation by near-infrared spectroscopy: Immediate effects of pentobarbital overdose or carmustine treatment", *J. Neuro-Oncol.*, **22**, 209-220, 1994.

[31] S. S. Kety, "Cerebral circulation and its measurement by inert diffusible racers," *Israel J. Med. Sci.*, **23**, 3-7, 1987.